Heteroatom (N/S) Doped Graphitic Carbon Coordinated with Transition Metals (Fe/Co) as Platinum-free Electrocatalysts for Energy Applications

Thesis Submitted to AcSIR
For the Award of the Degree of

DOCTOR OF PHILOSOPHY
IN
CHEMICAL SCIENCES

AcSIR

By
Mr. Siddheshwar N. Bhange
Registration Number: 10CC17J26036

Under the guidance of
Dr. Sreekumar Kurungot

CSIR-National Chemical Laboratory, Pune-411008,
India

May 2020

CERTIFICATE

This is to certify that the work incorporated in this Ph.D. thesis entitled **"HETEROATOM (N/S) DOPED GRAPHITIC CARBON COORDINATED WITH TRANSITION METALS (Fe/Co) AS PLATINUM-FREE ELECTROCATALYSTS FOR ENERGY APPLICATIONS"** submitted by **Mr. Siddheshwar N. Bhange** to Academy of Scientific and Innovative Research (AcSIR) in fulfillment of the requirements for the award of the Degree of Doctor of Philosophy, embodies original research work under my guidance. I further certify that this work has not been submitted to any other University or Institution in part or full for the award of any degree or diploma. Research materials obtained from other sources has been duly acknowledged in the thesis. Any text, illustration, table etc., used in the thesis from other sources, have been duly cited and acknowledged.

It is also certified that this work done by the student, under my supervision, is plagiarism free.

Siddheshwar N. Bhange

(Student)

Dr. Sreekumar Kurungot

(Supervisor)

DECLARATION

I, hereby declare that all the experiments in thesis entitled **"HETEROATOM (N/S) DOPED GRAPHITIC CARBON COORDINATED WITH TRANSITION METALS (Fe/Co) AS PLATINUM-FREE ELECTROCATALYSTS FOR ENERGY APPLICATIONS"** submitted for the degree of Doctor of Philosophy in Chemical Sciences to the Academy of Scientific and Innovative Research (AcSIR) have been carried out by me at the Physical and Materials Chemistry Division, CSIR-National Chemical Laboratory, Pune-411008, India, under the supervision of **Dr. Sreekumar Kurungot**. This work is original and has not been submitted to any other University or Institution in part or full for the award of any degree or diploma.

Mr. Siddheshwar N. Bhange   Date: 07-05-2020

Physical and Materials Chemistry Division,

CSIR- National Chemical Laboratory

Pune-411008, India.

Acknowledgement

First and foremost, praises and thanks to God, the Almighty, for His showers of blessings throughout my research work to complete the research successfully.

I would like to express my deepest and sincere gratitude to all the people involved directly or indirectly in the completion of my Ph.D. It is very difficult for me to express my feelings and thoughts into words, nevertheless, I will try to make a genuine effort to thank all the people whose assistance was a milestone in the completion of this research.

Firstly, I would like to express my sincere gratitude from bottom of my heart to my thesis adviser, Dr. Sreekumar Kurungot, for giving me this opportunity to do research and for the continuous support for my Ph.D. study and related research, for his patience, motivation, immense knowledge and guidance. His guidance helped me in all the time of research and writing of this thesis. His positive criticism and valuable guidance helped me to improve myself in the professional sphere. I wish to thank him for providing all essential facilities which were very important for my research work. I am thankful to him for involving me in every part of the fuel cell system development, discussions and interactions with the industry partner. I will always remember this great time to work with him and his helpful nature during my research work. I could not have imagined having a better advisor and mentor for my Ph.D. study.

I want to express my sincere gratitude to the former Director of NCL, Dr. Sourav Pal, and current Director, Professor Ashwini Kumar Nangia, for providing the great and a big platform, infrastructure and valuable support to do research work. I also want to thank the former Head of the Physical and Materials Chemistry Division, Dr. P. A. Joy, for allowing me to avail the facilities of the Department. I am also thankful to Dr. B. L. V. Prasad for his support as the current Head of the Physical and Material Chemistry Division and also as the Chairman of SAO.

I am very much thankful to the former SAO Chairman Dr. Mysore Shashidhar, AcSIR chairman Dr. Mahesh J. Kulkarni, and employees Mrs. Pornima Kolhe, Mr. Purushouthaman, Ms. Harshita, Mrs. Vaishali, Ms. Komal, Mrs. Poornima, Mr. Santosh and others for processing my documents on time.

I would like to thank my DAC members Dr. Syed G Dastager, Dr. T. G. Ajithkumar and Dr. Jayaraj Nithyanandhan for their valuable guidance and fruitful discussions during the DAC meetings.

I would like to thank Dr. Ashish Lele, Dr. Ulhas Kharul, Dr. Neelima Bulakh, Dr. Harshawardhan Pol, Mr. Vivek Borkar and Swapnil Aherrao for their helping hand during the fuel cell project-related activities.

I would like to thank Dr. Rahul Banerjee, Dr. R. Nandini Devi and their students, Himadri and Jijil, respectively, for the fruitful collaborations.

I am thankful to Mr. Gholap, Ms. Pooja, Mr. Shrinivas Deo, Mr. Venkitesh, Mr. Thushar, Mrs. Sheetal, and Mrs. Rupali, who rendered their help in the characterization of various samples at the Center of Materials Characterization (CMC).

I also take this opportunity to thank my seniors, Dr. Sreekuttan M. Unni, Dr. Bihag Anothumakkool, Dr. Palaniselvam Thangavelu, Dr. Vishal M. Dhavale, Dr. Harshita B. A., Dr. Joyashish Debgupta, Dr. Dhanraj Shinde and Dr. Vrushali, for their monitoring and care during my initial days.

I would like to express my special thanks to all my friends in the Lab, Rajith, Sachin G., Pandiraj, Pritish, Santosh K. Singh, Roby Soni, Varchaswal Kashyap, Ajinkya, Smita, Sharad, Maya, Pranav, Vidyanand, Ayesha, Sachin K., Narugopal, Meena, Dr. Raji V, Dr. Debasree, Dr. Gaurav, Dr. Shilpa, Dhiraj, Aniket, Geeta, Swati, Ajmal, Mariya, Abdul and Mahesh for all their affection, help and support.

I wish to thank my NCL friends, Pradip, Shahaji, Shekhar, Nagesh, Arun Toris, Vinaya, Sachin, Babasaheb, Sagar Patil, Digamber, Manik, Satej, Sandip, Gaurav, Harshal, Vedi and Ashwini, for providing me excellent working ambiance during the course of this work.

I wish to acknowledge the extensive help from Dr. Sreekuttan, Dr. Harshita, Dr. Soni, Dr. Gaurav, Dr. Santosh and Rajith during my research in NCL.

I am grateful to Dr. Jayaraj Nithyanandhan and Dr. Vaidhyanathan Ramanathan (IISER Pune) for giving their valuable time to evaluate my work during the fellowship upgradations.

I wish to express my special feelings and thoughts to my friends and family who directly and indirectly helped and motivated me to complete my research successfully. I want to express special thanks to my Mom and Dad, whose love, blessings and trust have been my strength. I am grateful to have such a family and all my family members, my wife Snehal, sister Latika, brother Somnath, brother-in-law Ramdas, sister-in-law Sheetal and nephews, Shivansh, Rohit and Ratnadeep, who were always providing me motivations, inspirations and supports during this research. My family gives me strength, hopes and confidence to work hard in life. Their patience and sacrifices are inspirations for me in my life.

Though many are not mentioned, none is forgotten.

Siddheshwar N. Bhange

List of Abbreviations

Abbreviation	Expansions
AFC	Alkaline Fuel Cell
AEMFCs	Anion Exchange Membrane Fuel Cells
ADT	Accelerated Durability Test
BET	Brunauer–Emmett–Teller
CNF	Carbon Nanofiber
CNT	Carbon Nanotube
CA	Chronoamperometry
CP	Chronopotentiometry
CE	Counter Electrode
CV	Cyclic Voltammetry
CO	Carbon Monoxide
C_{dl}	Double layer Capacitance
CNH	Carbon Nanohorn
CP	Conducting Polymers
DOE	Department of Energy
DFT	Density Functional Theory
DMFC	Direct Methanol Fuel Cell
EDAX	Energy Dispersive X-ray Analysis
ECSA	Electrochemical Surface Area
ESR	Equivalent Series Resistance
EDLC	Electrical Double Layer Capacitance

EDOT	3,4-Ethylene dioxythiophene
EIS	Electrochemical Impedance spectroscopy
FESEM	Field Emission Scanning Electron Microscope
GC	Glassy Carbon
Gr	Graphene
HOR	Hydrogen Oxidation Reaction
HRTEM	High Resolution Transmission Electron Microscopy
K-L	Koutecky-Levich
LSV	Linear Sweep Voltammetry
MEA	Membrane Electrolyte Assembly
MFCF	Molten Carbonate Fuel Cell
MWCNT	Multi-walled Carbon Nanotubes
NGr	Nitrogen doped Graphene
OCV	Open Circuit Voltage
PAFC	Phosphoric Acid Fuel Cell
PBI	Polybenzimidazole
PEMFC	Polymer Electrolyte Membrane Fuel Cell
PGM	Platinum Group Metal
PANI	Polyaniline
PEDOT	Poly(3,4-ethylene dioxythiophene)
PTFE	Polytetraflouroethylene
RE	Reference Electrode
RHE	Reversible Hydrogen Electrode

RDE	Rotating Disc Electrode
RRDE	Rotating Ring Disk Electrode
SAED	Selected Area Electron Diffraction
SEM	Scanning Electron Microscopy
SOFC	Solid Oxide Fuel Cell
SSA	Specific Surface Area
SWCNT	Single-walled Carbon Nanotube
TEM	Transmission Electron Microscope
TGA	Thermogravimetric Analysis
WE	Working Electrode
XRD	X-ray Diffraction
ZAB	Zinc-air Battery
ZIF	Zeolitic Imidazolate Framework
1D	One Dimensional
2D	Two Dimensional
3D	Three Dimensional

Table of contents

Chapter 2

Single Cell Fabrication of CNT Strung ZIF-derived Electrocatalyst as Cathode Material in Alkaline Fuel Cell and Metal-air Battery

Chapter 3

Chapter 4

Chapter 5

Chapter 6

Preface

The growing population and industrialization create a concomitant increase in the global energy demand, which is expected to be increased even rapidly in future. Currently, a significant amount of energy is being produced from fossil fuels such as petroleum, natural gases, coal, *etc*.; these energy sources might get depleted after a few decades. Along with this, the major problem associated with the fossil fuel based energy sources is environmental pollution. The combustion of fossil fuels generate greenhouse gases, which can create a substantial ecological impact on the living organisms in the planet. To avoid such adverse impact of the fossil fuels to the planet and to give a safe and healthy life in the future, it is necessary to replace the non-renewable sources of energy to appropriate renewable systems and technologies. Few green energy devices and technologies are already developed and are being implemented, such as those harvesting tidal energy, solar energy, geothermal energy, electrochemical energy, *etc*., which can provide power without creating any environmental issues. However, the problem of these naturally available energy sources is that they are intermittent in nature, and the availability of these energy sources is not adequate and reliable to solve the real issues. In this context, the electrochemical means of energy production from sustainable sources has become a potential and promising alternative, and this has gained substantial momentum in the domain of energy research. Among the various electrochemical systems explored, polymer electrolyte membrane fuel cells (PEMFCs) and zinc-air batteries (ZABs) are being identified as the two prominent systems which can offer wide applications considering the power and energy density considerations for various practical requirements.

The development and commercialization of PEMFCs and ZABs have been firmly stuck due to the high cost and stability of the electrode materials. In the case of the PEMFCs, it consumes hydrogen gas and produces electricity with heat and water as the by-products. The primary significant cathode reaction in the PEMFCs is oxygen reduction reaction (ORR), and it suffers from sluggish kinetics and thus needs a strong catalyst to facilitate the reaction. Currently, the platinum (Pt) based catalysts like Pt/C are being used to facilitate ORR, which give high output energy from PEMFCs. This forces to use Pt as an inevitable catalyst on the electrodes of PEMFCs, which ultimately becomes as the main factor in making the PEMFC systems commercially expensive. The poor stability and high price of the Pt-based electrocatalysts hamper the commercialization prospects of PEMFCs. The efficiency of the fuel cell strongly

depends on the cathode catalyst, and the cathode is considered as the heart of the fuel cell. Similar challenges are existing in the case of ZABs as well owing to the same nature of the cathode reaction, where again the Pt based systems are known to work well to facilitate ORR. To tackle the catalyst issues related to cost and durability, a systematic study has been performed by designing various active and stable Pt-free electrocatalysts, and the present dissertation covers a discussion on the progress made in this direction. The strategy adopted here is primarily focused onto modify the morphology, surface area, nature and coordination of the reactive sites and conductivity to achieve a favourable modulation in terms of the ORR activity of the noble metal-free electrocatalysts. The outcome of the individual chapters are highlighted below:

Chapter 1 gives a detailed discussion about the importance of the different electrochemical devices like PEMFCs, ZAB, *etc*. and the factors limiting the development and commercialization of these sustainable technologies. The chapter covered a discussion on the working principles of these energy devices and it also included a literature review on the development of the various Pt-free electrocatalysts for ORR applications. The obtained activity and the major drawbacks associated with the existing electrocatalysts developed by various research groups are described systematically. Further, the general strategies adopted to improve the electrocatalytic activity of the non-precious metal-based materials and their generally adopted synthesis methodologies also have been discussed in this chapter. Lastly, the scope and objectives of the thesis are stated at the end of the chapter.

Chapter 2 deals with the development of a highly porous cobalt based ZIFs (Co-ZIF-67) stringed along the highly conducive CNT backbone using a simple one pot technique at room temperature, which was then utilized to derive porous, corrosion resistant, Co nanoparticle embedded ORR electrocatalysts. Followed by a detailed structural and electrochemical characterization of the catalysts, for the first time, the single cell performance of the best Co-ZIF-67 derived electrocatalyst (CoNC-900) has been evaluated by fabricating Membrane Electrode Assemblies (MEAs) of Alkaline Exchange Membrane Fuel Cell (AEMFC) and Zinc–Air Battery (ZAB) systems. A maximum power density of 296 mW cm^{-2} (*vs*. 317 mW cm^{-2} of 40 wt. % Pt/C) and 60 mW cm^{-2} (*vs*. 64 mW cm^{-2} of 40 wt. % Pt/C) in the single cells of ZAB and AEMFC systems, respectively, establishes the practical proficiency of the homemade electrocatalysts for the cathode applications during the realistic system level validations.

Chapter 3 focuses on the synthesis of a Pt-free oxygen reduction electrocatalyst based on nitrogen and sulphur co-doped crumbled graphene with trace amounts of iron. The co-doped crumbled graphene structure was obtained by simple oxidative polymerization of ethylenedioxythiophene in aqueous solution followed by an annealing process under an inert atmosphere. The electrocatalyst displays improved oxygen reduction activity and electrochemical stability under acidic conditions. The half-cell reaction of the 1000 ºC annealed system (PF-1000) displays only 0.10 V overpotential in both the onset and half-wave potentials compared to the state-of-the-art Pt/C in an acidic environment for ORR. More importantly, the limiting current of PF-1000 clearly surpasses the limiting current displayed by Pt/C. This indicates that the crumbled assembly of the graphene flakes helps the system to expose the active sites and the porous network of the material matrix ensures extended accessibility of the active sites to the electrolyte and reagent. The dioxygen reduction kinetics of PF-1000 appear similar to those of Pt/C and the system accomplishes the reduction of the dioxygen molecule through the recommended 4-electron reduction pathway. The improved activity and electrochemical stability of PF-1000 are mainly attributed to the enriched and well accessible active reaction centres such as graphitic nitrogen, sulphur, and iron coordination and the peculiar morphology of the system. Further, a single cell evaluation of an MEA based on PF-1000 as the cathode catalyst delivered a maximum power density of 193 mW cm^{-2} at a cell temperature of 60 ºC using Nafion as the proton-conducting membrane.

Chapter 4 summarizes the works related to the development of a graphene based electrocatalyst possessing the Fe and S coordinated active sites, which can facilitate ORR under acidic and basic pH conditions. Here, a Pt-free, iron and S-doped, scrolled graphene (P12-900) system was prepared *via* annealing of polyethylenedioxythiophene (PEDOT) as a potential oxygen reduction electrocatalyst which could perform exceptionally well under acidic and basic electrolyte conditions. The residual iron chloride retained by the polymer matrix, which was employed as the oxidizing agent for the polymerization reaction, plays a vital role in generating the potential ORR active sites based on the Fe- and S-doped graphene in the system. The composition designated as P12-900 displays ORR activity with substantially reduced overpotential in both acidic and basic electrolyte conditions, which is a unique feature reported in this class of materials. In the basic medium, P12-900 displays an ORR activity which is similar to that for the performance of 40 wt. % Pt/C. Under acidic conditions, the in-house system displays only an 80 mV overpotential in the onset potential compared to its Pt counterpart. Single-cell demonstration of a Nafion-based PEMFC by employing the P12-900

catalyst as the cathode delivered the maximum power density (PD) of 345 mW cm^{-2} at 60 °C. Equally, when tested as the air electrode for a ZAB with KOH electrolyte, the cell displayed a maximum power density of 320 mW cm^{-2} and a maximum current density of 685 mA cm^{-2}, which are comparable to the performance of the system based on the *state-of-the-art* Pt/C (322 mW cm^{-2} and 649 mA cm^{-2} respectively) cathode. Thus, the prepared precious metal-free catalyst performs as a promising candidate for the replacement of the noble metal catalyst for PEMFCs and ZAB systems with its unique capability to facilitate the electrode reactions under acidic and basic electrolyte conditions.

Chapter 5 is dedicated for developing a Pt-free electrocatalyst which can perform well under acidic pH conditions considering the need of such systems to implement in the *state-of-the-art* PEMFCs based on proton exchange membranes. In line with this requirement, a catalyst for facilitating ORR could be prepared with simultaneous incorporation of both Fe-N and Fe-S active sites on *in situ* generated carbon sheets which are spatially separated by a network created by means of carbon nanotube (CNT). This catalyst shows ability to perform under both the acidic and basic conditions. This has been achieved by growing a polyethylenedioxythiophene polymer network in the presence of CNT and melamine followed by its pyrolysis under inert atmosphere. The catalyst formed at 900 °C (PMCNT-900) displays an onset potential of 0.94 V for ORR under acidic electrolyte conditions, which corresponds to 60 mV overpotential compared to its 40 wt % Pt/C counterpart. Interestingly, in single cell demonstration of a Nafion-based PEMFC with PMCNT-900 as the cathode catalyst, the system delivered a maximum power density (PD) of 500 and 275 mW cm^{-2} at 60 °C under H$_2$-O$_2$ and H$_2$-Air feed conditions, respectively. On the other hand, in a single cell test in the anion exchange membrane fuel cell (AEMFC) mode, a maximum power density of 65 mW cm^{-2} at 50 °C could be achieved with the same cathode catalyst, which is a comparable value obtained while employing Pt/C as the cathode. These results, thus, infer to the efficiency of the catalyst to facilitate ORR under the extreme pH conditions, and, particularly, its performance under acidic condition reveals its prospect as a potential Pt-free electrocatalyst to serve in the Nafion-based systems.

Chapter 6 gives a summary of the important observations and outcomes of each chapter of the thesis. A brief overview of the different strategies adopted and the major technological leads achieved in each case are included in this chapter. Finally, the future prospects of the ideas, technologies and strategies as evolved from the various work components of this thesis are included in the last part of this chapter.

Chapter-1

Introduction: Oxygen Reduction Reaction Electrocatalysts for Polymer Electrolyte Membrane Fuel Cell and Metal-air Battery Applications

This chapter briefly describes the global energy consumption scenario followed by the development of electrocatalysts for the oxygen reduction reaction (ORR) in the polymer electrolyte membrane fuel cell (PEMFC) and zinc-air battery (ZAB) applications. A discussion on the working principle of PEMFC and ZAB, their components, advantages, and issues associated with the development is given. Also, a discussion on the ORR mechanism and the
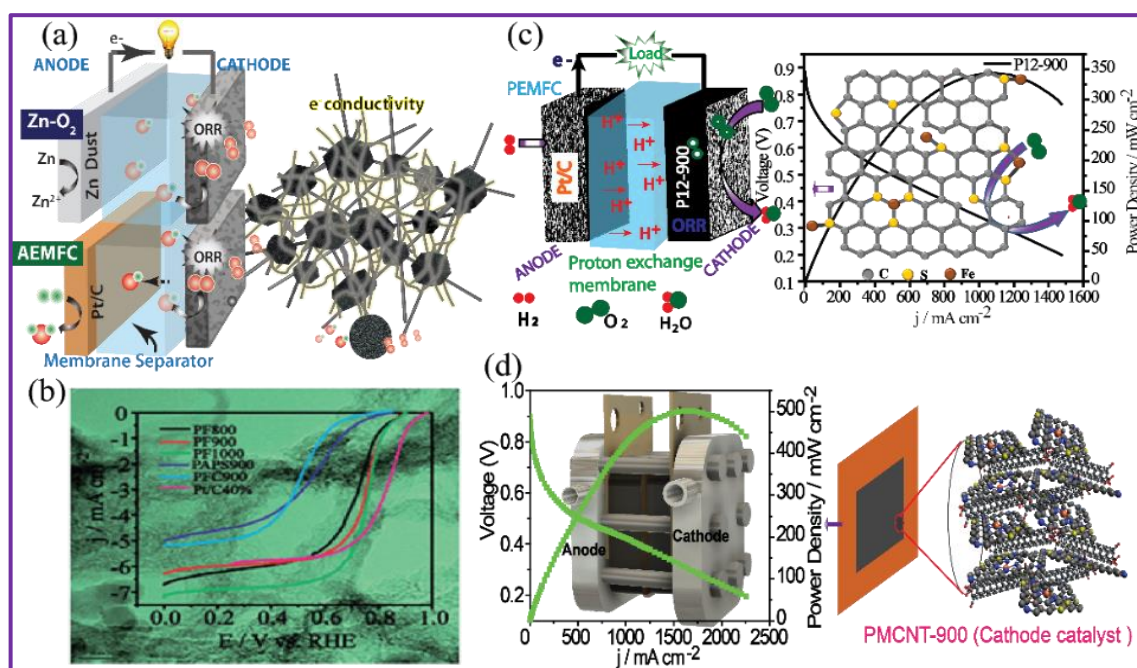
Scheame 1.1. Combination of the TOCs of the working chapter.

development of the platinum-free (Pt-free) electrocatalyst, followed by a literature review on the catalyst design with heteroatom doped graphitic carbon and metal nitrogen coordination (M-Nx) on carbon supports are included. The importance of the heteroatom type and heteroatom-doped carbon allotropes for the development of high potential electrocatalyst has been discussed. Finally, the objective and scope of the present thesis work are listed at the end of this chapter.

1.1 Introduction

An increase in the global population has resulted in an unprecedented increase in energy demand. To cope with the rising energy needs of the ever-increasing global community, we must increase our present rate of energy production to a high level. Currently, we are mainly dependent on fossil fuel for energy requirements. We rely mostly on coal (25.1%), natural gas (20.9 %), and oil (34.3 %) for energy (**Figure 1.1a**). With the development of new efficient technologies and energy conversion devices,[1, 2] the worldwide energy demand will be doubled in the middle of the century and tripled at the end of the century.[3] the combustion of fossil fuel generates greenhouse gases leading to global warming impacts the human health.[4-5] To resolve the environmental pollution, global warming, and the energy crisis of the world, the development of advanced renewable energy technologies is necessary.[6]

To develop alternative technologies, sunlight, tides, waves, and geothermal heat energy can be used as the energy sources. The generated power can be used in different areas like electricity generation, air heating, cooling, and transportation.[7] In this respect, few green energy devices and technologies have been developed, such as tidal energy,[8] solar cells,[9] geothermal energy, electrochemical energy,[10] *etc*.[11-14] These devices would provide energy without damaging the environment. However, the problem of these naturally available energy sources is their intermittent nature, and the availability of these energy sources cannot solve the real issues. The electrochemical energy sources have great potential to address these issues. The electrochemical energy devices such as the fuel cells and metal-air batteries can convert the chemical energy into electrical energy whereas the lithium-ion batteries, supercapacitors, *etc*. can store the chemical energy.[15-20] Among these electrochemical devices, fuel cell and zinc-air battery (ZAB) have tremendous potential to replace the fossil fuel-based energy sources.

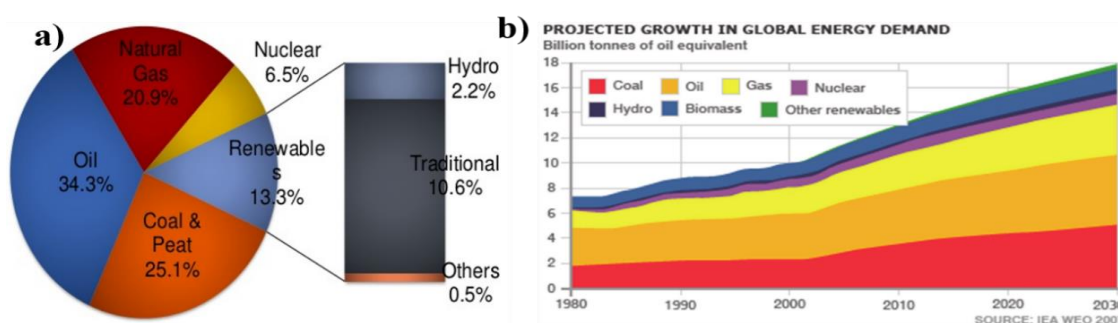***Figure 1.1.*** *Global energy scenario: a) sources of the energy used, and b) the projected growth in the global energy demand (**Source**: www.iea.org, https://www.researchgate.net/figure/Global-energy-demand-projections Source_fig2_323783427).*

The fuel cell has the advantages of higher efficiency than diesel engines, does not emit greenhouse gases, and the only by-product is water. Similarly, ZAB having advantage of high energy density with low expensive materials and excellent shelf-life. Whereas, the fuel cell is a green energy technology which consumes hydrogen (H_2) as fuel and oxygen (O_2) as an oxidant to produce electricity and forms water as a by-product without producing any noise. The bottleneck in the commercialization of PEMFC and ZAB is the high cost and poor durability of the commercial Pt/C used as an ORR catalyst. The ORR reaction has sluggish kinetics which needs high loading of the Pt/C catalyst to facilitate the reaction. For improving the ORR kinetics, and reduce the cost of the catalyst, recently, there has been a distinct shift on the development of the non-noble metal electrocatalysts for ORR. Therefore, the current thesis is devoted on the development of noble metal-free electrocatalysts for ORR and the development of methodologies to make cost-effective PEMFCs and ZABs. The following section discusses the fundamentals of fuel cells, with prime focus on PEMFC, and ZABs.

1.2 Fuel Cells

A fuel cell is an electrochemical conversion device that can convert chemical energy into electrical energy. In a fuel cell, H_2 and the other small organic molecule such as methanol, ethanol, formic acid, *etc*., are used as fuels, and the oxidant is air or O_2. The fuel cell is different from the battery, and it needs a continuous flow of fuel to produce electricity unlike batteries. In the case of the batteries, the chemicals react with each other and generate electricity; once it gets finished, the battery dies out.[21, 22] The fuel cell is a more viable option in the energy market because of its high electrical conversion efficiency, environmental friendly nature, and safety. The fuel cells are highly scalable; they can be scaled up from a small single cell to a multicell stack according to the required power output. Theoretically, the open-circuit voltage (OCV) of the fuel cell is 1.23 V and it possesses a thermodynamic efficiency of ~85% based on the higher heating value of the hydrogen. However, the practical efficiency of the fuel cell is close to 40-60 %,[23] whereas the diesel engines show approximate efficiency of ~37%. Among the various types of fuel cells, PEMFC has emerged as the matured technology due to its advantages for low-temperature and applications related to both stationary and automobile operations. The membrane electrode assembly (MEA) in the case of a PEMFC is called the heart of the cell, which consists of three different parts, *i.e*., the anode, cathode, and membrane. At the anode and cathode, Pt supported on carbon (Pt/C) is generally employed to facilitate the respective electrocatalytic reactions. At the anode, the hydrogen oxidation reaction (HOR) occurs where H_2 is oxidized to protons (H^+) releasing electrons. The protons will move towards the cathode

through the proton exchange membrane; at the cathode, they combine with the reduced oxygen and produce water. The electron moving in the outer circuit is harnessed for electrical work. There are different types of fuel cells;[24] the classification of fuel cell has been done depending on the type of the electrolyte used and the operating temperature of the cells (**Figure 1.2**).

1.2.1 Polymer Electrolyte Membrane Fuel Cells (PEM fuel cells)

PEM fuel cell is known as membrane fuel cell, where the membrane separates the gases and transport the proton or anion through the membrane. Depending on the transport of proton (H^+) and the anion (OH^-), a PEM fuel cell can be classified into two categories (i) proton exchange membrane fuel cell (PEMFC) and (ii) anion exchange membrane fuel cell (AEMFC). These fuel cells generally operate below 100 ^{o}C and also the system needs membrane humidification to transport ions efficiently. These fuel cells have gained enormous market attention as a profitable alternative.

1.2.2 Proton Exchange Membrane Fuel Cell (PEMFC)

The PEMFC consists of three components, *i.e.*, the anode, cathode, and the proton-conducting electrolyte membrane. The proton-conducting membrane is solid, impermeable to the gases,
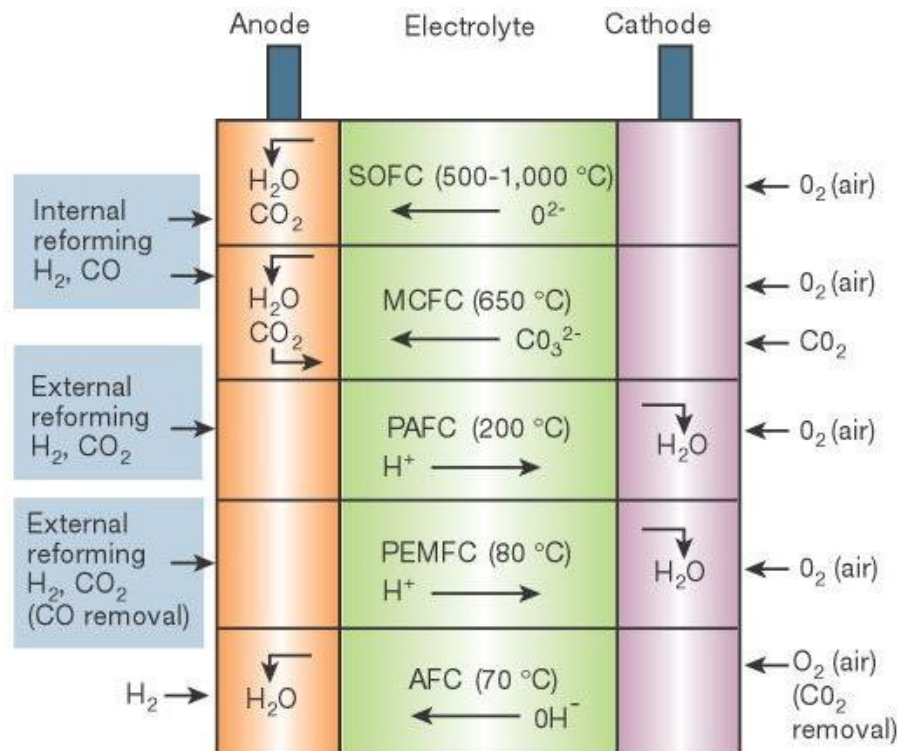
*Figure 1.2. Types of fuel cells. (Reproduced with the permission of **Springer Nature, License Number: 4810801505308**, Copyright © 2001, Springer Nature).*

nonporous and electrically insulating. The proton conduction can occur through either Grothuss hopping or vehicular mechanism. Depending on the operating temperature, there are two different types of PEMFCs, the low-temperature fuel cell (LT-PEMFCs) and high-temperature fuel cells (HT-PEMFCs).[25-27] The HT-PEMFC operates at 160-200 °C, where phosphoric acid doped polybenzimidazole (PBI) membrane is generally being used as an electrolyte.[28-30] In the case of LT-PEMFCs, the proton conduction through the membrane needs humidification, and the cell operates below 100 °C. Also, LT-PEMFC allows a quick start-up (less warm-up time). The presence of CO impurities in the fuel can act on the Pt surface and poison the catalyst on the electrode surface.[31-34] In PEMFCs, the higher loading of Pt/C increases the cost of the fuel cell. Also, the poor durability of Pt/C acts as the bottleneck for achieving durable performance. The reactions at the electrodes in a PEMFC are mentioned below:
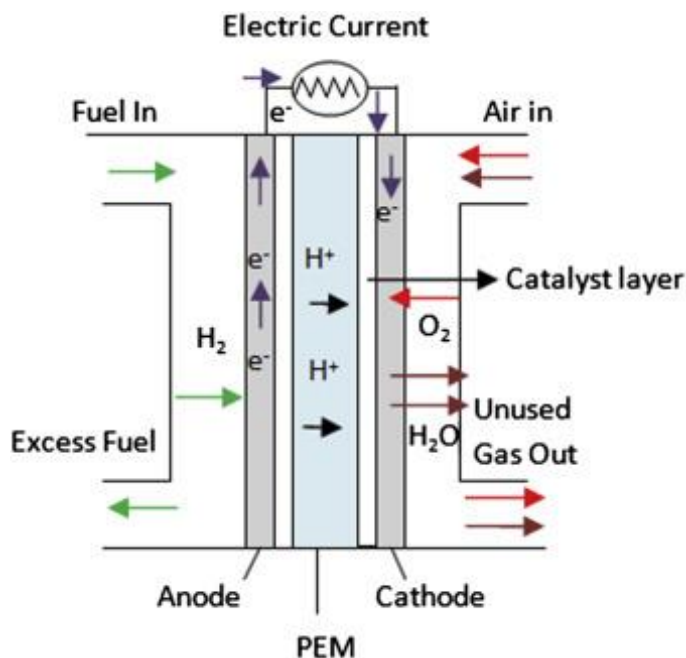
Figure 1.3. *Schematic representation of a PEMFC. (Reproduced with the permission of Elsevier, License Number: 4810740283953, Copyright © 2019 Elsevier).*

Anode:

$$2H_2 \rightarrow 4H^+ + 4e^-, \qquad E = 0.0 \ V \ vs \ SHE \qquad (1.1)$$

Cathode:

$$O_2 + 4H^+ + 4e^- \rightarrow 2H_2O, \quad E = 1.23 \ V \ vs \ SHE \qquad (1.2)$$

Overall reaction:

$$2H_2 + O_2 \rightarrow 2H_2O, \qquad E = 1.23 \ V \ vs \ SHE \qquad (1.3)$$
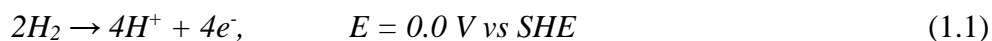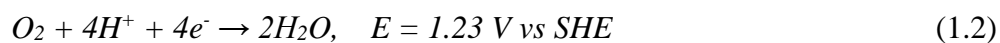
1.2.3 Anion Exchange Membrane Fuel Cell (AEMFC)

In AEMFC, the hydroxyl ion (OH⁻) is transported through the anion exchange membrane (AEM). At the cathode, oxygen is reduced, and thus produced OH⁻ ions move through the AEM and reach to the anode side. At the anode, HOR will occur and produces H⁺ and electrons. The H⁺ will combine with OH⁻ and forms water. The generated electrons will flow through the outer circuit of the cell as electricity. In AEMFC, water is produced at the anode side of the cell. As compared to PEMFCs, the electrode reaction of the AEMFC is kinetically faster in an alkaline medium. Therefore, Pt-based electrocatalysts can be replaced with suitable non-precious metal-based electrocatalysts for obtaining better activity and efficiency. The cell reactions of AEMFC are given below:
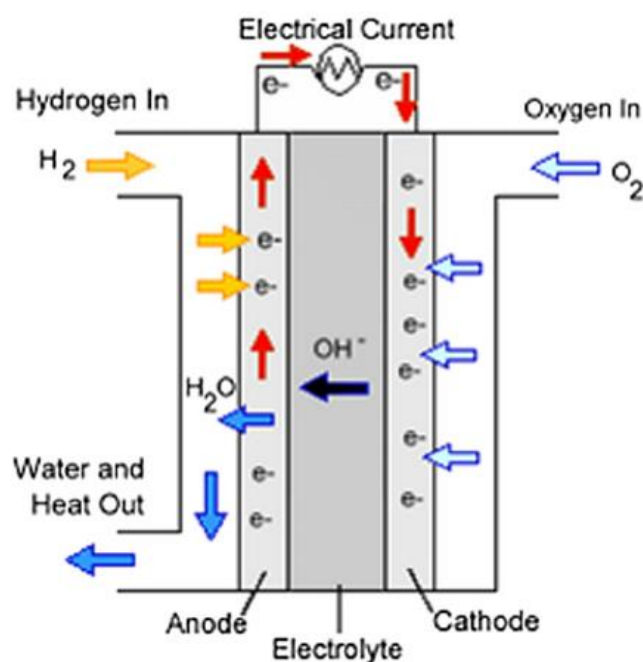
Figure 1.4. *Schematic diagram of an alkaline membrane fuel cell (AEMFC). (Reproduced with permission of **Springer Nature, License Number: 4810781491954**, Copyright © 2013, Springer Nature).*

Anode:

$$2H_2 + 4OH^- \rightarrow 4H_2O + 4e^-, \qquad E = -0.83 \ V \ vs \ SHE \qquad (1.4)$$

Cathode:

$$O_2 + 2H_2O + 4e^- \rightarrow 4OH^-, \qquad E = 0.4 \ V \ vs \ SHE \qquad (1.5)$$

Overall reaction:

$$2H_2 + O_2 \rightarrow 2H_2O, \qquad E = 1.23 \ V \ vs \ SHE \qquad (1.6)$$
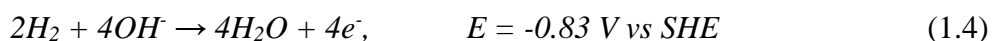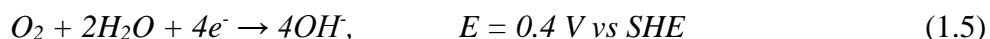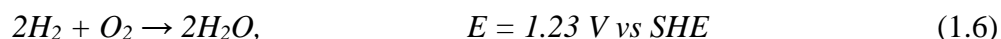
1.3 Zinc-Air Battery (ZAB)

ZAB has the highest capability to store energy among the primary battery systems available in the marketplace. The anodes in these systems typically use the zinc electrode with high surface area for meeting the high power requirements. To make high surface area zinc electrodes the dendritic powder is electrodeposited from the alkaline electrolyte. The dendritic powder can also be pressed and formed into a solid plate without gelling due to the mechanical inter-locking among branches of powder particles. On the other hand, if we look at the cathodic component of ZAB, there is a need for highly active and durable air electrocatalysts having high-performance and non-precious metal-based nanomaterials for facilitating ORR.[35-38] **Figure 1.5** schematically illustrates the basic structure of a primary ZAB.[39] It consists of a negative zinc electrode, a membrane separator, and a positive air electrode assembled in an alkaline electrolyte. The atmospheric oxygen can diffuse into the porous cathode by the difference in oxygen pressure between the outside and inside of the cell. The ORR catalyst facilitates the reduction of oxygen to hydroxyl ions (OH$^-$) at the cathode in the alkaline condition. The electrons would be generated from the oxidation of zinc metal at the anode. The generated OH$^-$ ions at the cathode migrate to the anode to complete the cell reaction. The OCV of ZAB is 1.59 V; however, the sluggish kinetics of ORR at the cathode resulting in high overpotential and reduces this obtained OCV. For achieving the high OCV, the cathode catalyst should have higher ORR activity. For making rechargeable ZAB, the cathode catalyst should also show the oxygen evolution reaction (OER) activity.
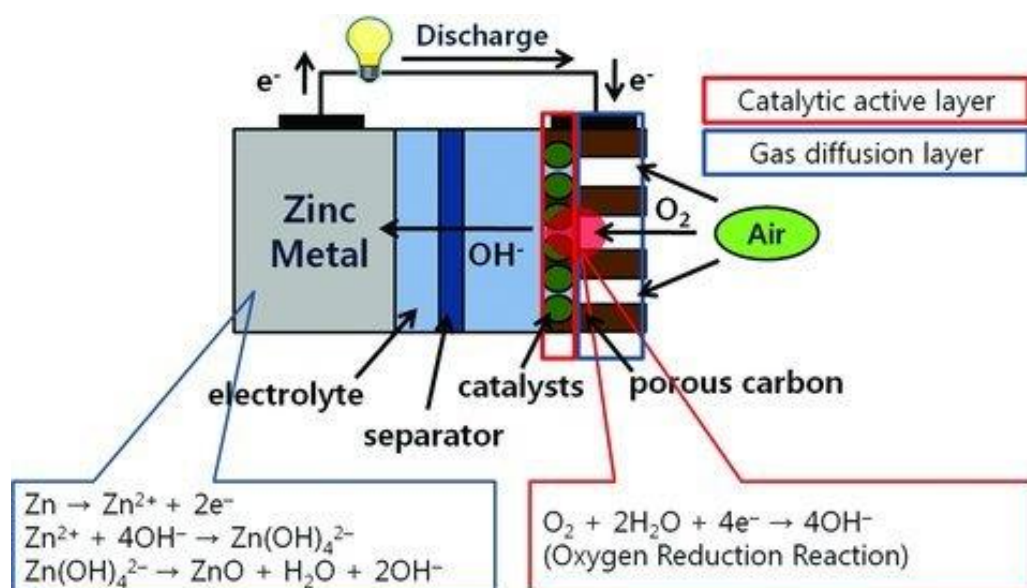
Figure 1.5. *Schematic for the working principle of the zinc-air battery (ZAB), (Reproduced with the permission of **John Wiley and Sons, License Number. 4810730242505**).*

Discharge:

Anode: $Zn + 4OH^- \rightarrow Zn\,(OH)_4{}^{2-} + 2e^-$ $(E_0 = -1.25\ V)$ (1.7)

          $Zn\,(OH)_4{}^{2-} \rightarrow ZnO + H_2O + 2OH^-$ (1.8)

Cathode: $O_2 + 2H_2O + 4e^- \rightarrow 4OH^-$ $(E_0 = 0.34\ V\ pH= 11)$ (1.9)

Overall reaction:

          $2Zn + O_2 \rightarrow 2ZnO$ $(E_0 = 1.59\ V)$ (1.10)

Parasitic reaction: $Zn + 2H_2O \rightarrow Zn\,(OH)_2 + H_2$ (1.11)

Recharge:

Anode: $ZnO + H_2O + 2OH^- \rightarrow Zn\,(OH)_4{}^{2-}$ (1.12)

          $Zn\,(OH)_4{}^{2-} + 2e^- \rightarrow Zn + 4OH^-$ (1.13)

Cathode: $4OH^- \rightarrow O_2 + 2H_2O + 4e^-$ (1.14)

Overall reaction: $2ZnO \rightarrow 2Zn + O_2$ (1.15)
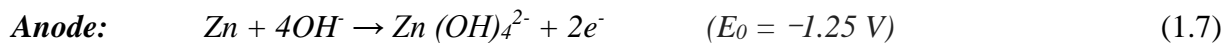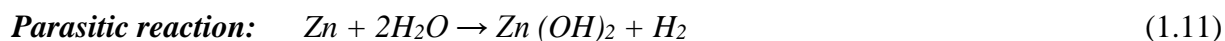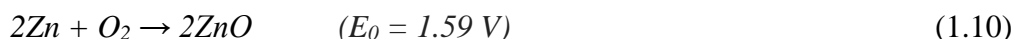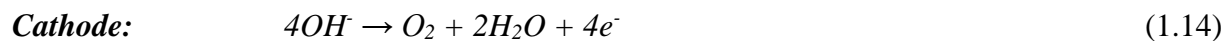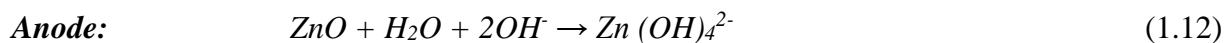
The commercialization of ZAB is facing the problem of low efficiency because of the slow ORR kinetics on the air cathode. Also, it needs improvement regarding performance and rechargeability. During discharge of the ZAB, it forms non-conducting zinc oxide at the anode and on recharge, it is again converted to zinc metal. The cathode catalyst should also have a bifunctional nature that can display both the ORR and OER during discharge and charging, respectively. The cell reactions in ZAB during charging and discharging can be represented as below:

1.4 Electrocatalysts for PEMFCs

The electrocatalysts used for facilitating HOR and ORR at the anode and the cathode, respectively, in PEMFCs is platinum carbon (Pt/C).[40-42] The fuel cell performance mainly depends on the electrode reactions; HOR is more facile as compared to ORR. The overpotential of HOR is less than 50 mV in the Pt-based catalysts. If the fuel changes from hydrogen to

methanol or any other alcohol, the *state-of-the-art* Pt/C catalysts show the poor activity.[40] Due to slow kinetics of ORR, substantially high loading of Pt is required to achieve significant current densities which inadvertently increases the fuel cell cost. Moreover, the carbon corrosion during PEMFC operation leads to the agglomeration of Pt nanoparticles which ultimately decreases the performance of PEMFCs. Hence, the development of highly active and stable electrocatalysts for ORR is a major task for the advancement of PEMFCs. Up to now, various metallic, non-metallic,[43-45] alloys,[46-48] and core-shell[49-51] kind of electrocatalysts have been investigated for ORR. Still, the developed Pt-free catalysts have not been able to meet the performance of Pt/C. Further improvements in the activity of the aforementioned systems are necessary to develop better ORR catalysts. Many strategies, such as the heteroatom doping on the carbon matrix, building transition metal coordinations with a heteroatom, developments of catalysts based on metal oxides, and metal chalcogenide are explored extensively.

1.5 Electrocatalyst Development Strategy

The development of high-performance and cost-effective electrocatalysts is challenging to meet the requirements for practical applications. To improve the activity, two different approaches
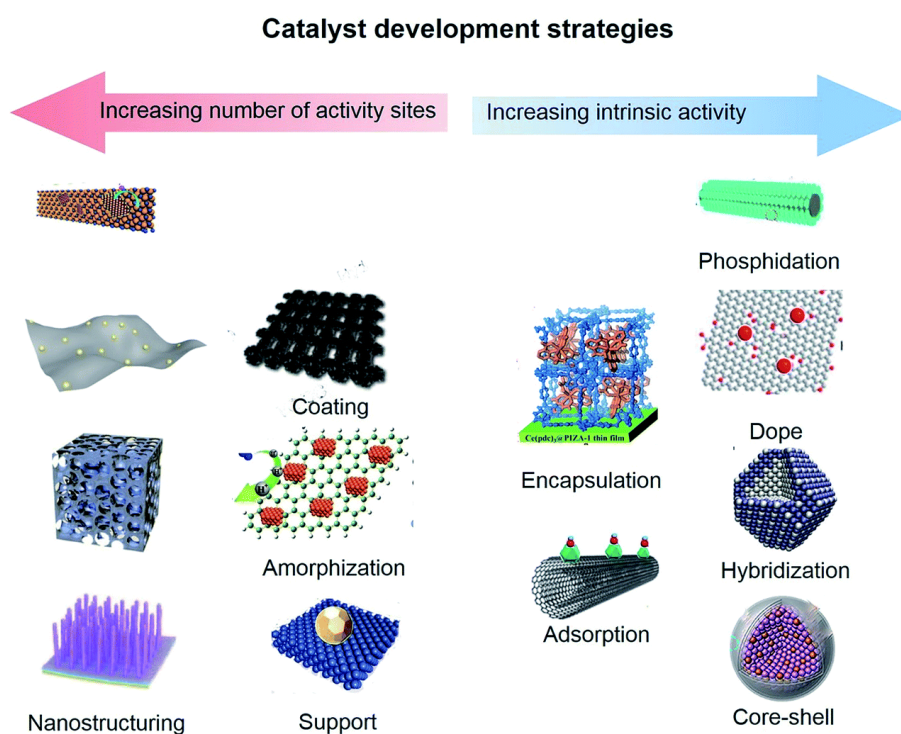
Figure 1.6. Schematic representation of the catalyst development strategies adopted for increasing the number of the active sites and intrinsic activity (reproduced with the permission from Royal Society of Chemistry, Copyright 2019).[53]

can be adopted; one is to increase the number of active sites in the catalyst, and the other is to increase the intrinsic activity of the catalyst.[52, 53] To achieve high current densities, high loading of the catalyst is usually employed in the electrodes; however, the increased catalyst loading can cause mass-transport polarization at high current densities. Therefore thin electrode coatings are always desired. To achieve thinner coatings, the catalyst must have high intrinsic activity. By tuning the inherent morphological features and increasing the number of active sites in the catalyst simultaneously, the issues related to the mass-transport and kinetic polarization can be effectively addressed.

1.6 Oxygen Reduction Reaction (ORR)

The cathode reaction of the PEM fuel cell is ORR, which is the limiting reaction in the fuel cell due to sluggish kinetics of oxygen reduction. The sluggish ORR kinetics causes higher overpotential in the platinum-group-metal (PGM) based catalysts in PEMFC and AEMFC.[52] In ORR, the transfer of electron increases the bond length between the O-O bond and reduces the bond order, which is then converted to different products depending on the electrolyte used.[54] Depending on the number of electrons transferred during the reduction of dioxygen molecules, ORR follows 2e⁻ pathway and 4e⁻ pathway.[55, 56] The desirable pathway in the acidic medium is 4e⁻ pathway as the 2e⁻ pathway leads to the significant formation of the peroxide during the reaction. In the cell, the 2e⁻ pathway leads to hydrogen peroxide formation,[56] which can lead to the degradation of the membrane and carbon support. Also, the 2e⁻ pathway would affect the potential of the fuel cell. The pathways of ORR in the acidic and basic media are given below:

In acidic medium

4e⁻ pathway:

$$O_2 + 4H^+ + 4e^- \rightarrow 2H_2O \qquad E_o = 1.23\ V \qquad (1.16)$$

2e⁻ pathway:

$$O_2 + 2H^+ + 2e^- \rightarrow H_2O_2 \qquad E_o = 0.70\ V \qquad (1.17)$$

$$H_2O_2 + 2H^+ + 2e^- \rightarrow 2H_2O \qquad E_o = 1.76\ V \qquad (1.18)$$
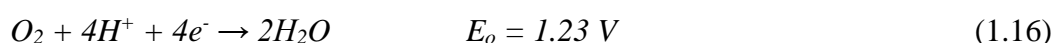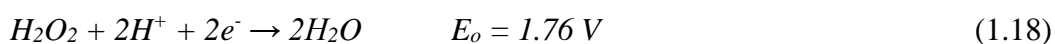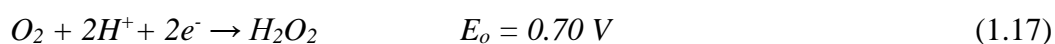
The peroxide molecules in (1.17) also produce water and oxygen molecules:

$$2H_2O_2 \rightarrow 2H_2O + O_2 \qquad (1.19)$$

In alkaline medium

4e⁻ pathway:

$$O_2 + 2H_2O + 4e^- \rightarrow 4OH^- \qquad E_o = 0.401\ V \qquad (1.20)$$

2e⁻ pathway:

$$O_2 + H_2O + 2e^- \rightarrow HO_2^- + OH^- \qquad E_o = -0.065\ V \qquad\qquad (1.21)$$

$$HO_2^- + H_2O + 2e^- \rightarrow 3OH^- \qquad E_o = 0.867\ V \qquad\qquad (1.22)$$
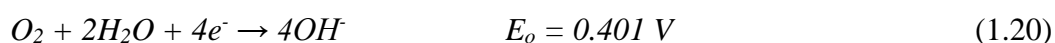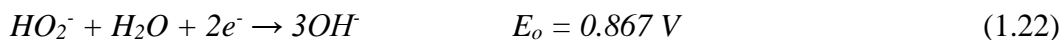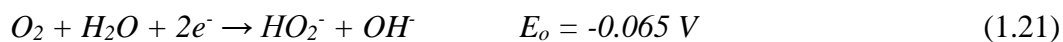
The OH_2^- species produced in (1.21) also produces OH^- and oxygen as follows:

$$HO_2^- \rightarrow 2OH^- + O_2 \qquad\qquad (1.23)$$

1.6.1 ORR Mechanism on Pt

The ORR mechanism on Pt has been studied extensively, and it involved multi-electron processes.[56] Based on the theoretical studies on the electronic structure, two mechanistic pathways have been predicted; one is the direct four-electron transfer reaction producing water, and the other is the two-electron transfer process forming H_2O_2. Moreover, the associative and dissociative mechanisms can occur on the Pt surface. The associative pathway occurs at higher current density. Whereas the dissociative pathway occurs at a lower current density. The five steps associated with the associative mechanism are listed below:

Associative mechanism:

$$Pt + O_2 \rightarrow Pt\text{-}O_{2\ (\text{-}ads)} \qquad\qquad (1.24)$$

$$Pt\text{-}O_{2\ (\text{-}ads)} + H^+ + e^- \rightarrow Pt\text{-}HO_{2\ (\text{-}ads)} \qquad\qquad (1.25)$$

$$Pt\text{-}HO_{2\ (\text{-}ad)} + H^+ + e^- \rightarrow H_2O + Pt\text{-}O_{(ad)} \qquad\qquad (1.26)$$

$$Pt\text{-}O_{(ad)} + H^+ + e^- \rightarrow Pt\text{-}OH_{(ad)} \qquad\qquad (1.27)$$

$$Pt\text{-}OH_{(ad)} + H^+ + e^- \rightarrow H_2O + Pt \qquad\qquad (1.28)$$
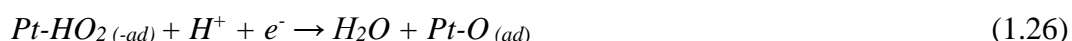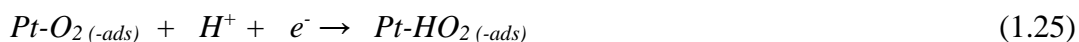
Dissociative mechanism:

The splitting of O_2 occurs on the catalytic surface and the species gets protonated to give OH moiety, which further reacts to form H_2O. This mechanism gives an idea about the direct (4e⁻) pathway for ORR.

The steps associated with the dissociative mechanism are listed below:

$$Pt + \tfrac{1}{2} O_{2\ (ad)} \rightarrow Pt\text{-}O_{(ad)} \qquad\qquad (1.29)$$

$$Pt\text{-}O_{(ad)} + H^+ + e^- \rightarrow Pt\text{-}OH_{(ad)} \qquad\qquad (1.30)$$

$$Pt\text{-}OH_{(ad)} + H^+ + e^- \rightarrow H_2O + Pt \qquad\qquad (1.31)$$

ORR is kinetically multifaceted and the proper mechanism is not yet confirmed.

1.7 Pt-based Electrocatalysts for ORR

PEMFCs and ZABs are the promising alternatives for the future energy production; however, their widespread commercialization is hindered by the sluggish kinetics of ORR. At present, Pt is used as the catalyst for the oxygen reduction on the cathode. Even though Pt is the *state-of-the-art* catalyst for ORR, the improvement in the activity of the Pt-based catalysts can be achieved by adopting the strategies like the structural modification, modification of the shape of the Pt nanocrystals, alloying, making core-shell structures etc. It is well known that the activity of Pt for ORR varies with the exposed plane of the Pt. The (110) plane of the Pt is more active for ORR in perchloric acid. Only surface atoms are active for the catalytic activity and the inside atoms are inactive. In the quest to reduce the quantity of Pt, alloying of Pt with other catalyst has been attempted to produce systems such as Pt_3Co, Pt_3Fe, and Pt3Ni. Among different alloys, Pt_3Ni shows ~2-3 times higher specific activity compared to Pt/C.[57]
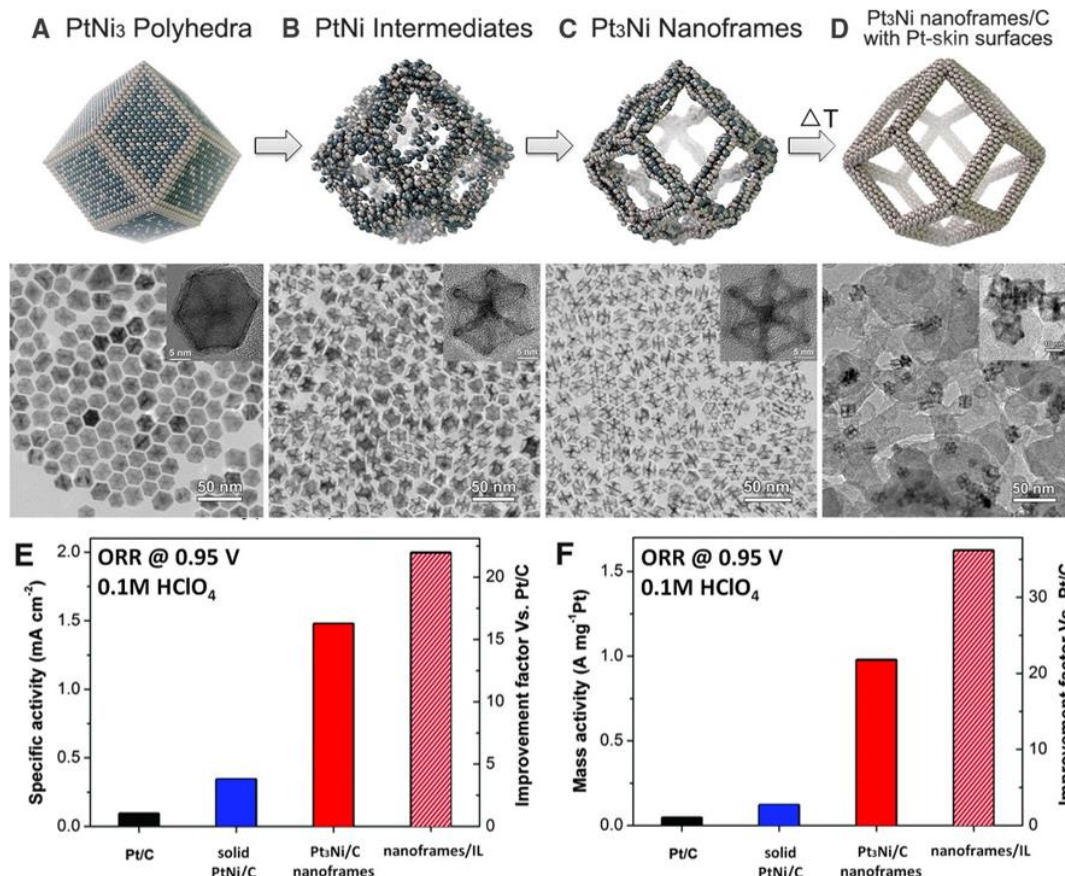
Figure 1.7. *A-D) Synthesis steps involved for making the Pt₃Ni nanoframe/C with Pt-skin surface from the PtNi₃ polyhedra, E) specific activities and F) mass activities. (Reproduced with the permission of Copyright © 2014, American Association for the Advancement of Science, **License Number. 4812501203782**).*

Chen *at el*. have prepared 3D Pt_3Ni nanoframes/C with Pt-skin surface from the crystalline $PtNi_3$ polyhedra through interior leaching in solution (**Figure 1.7**).[58] The edges of the Pt_3Ni nanoframes are Pt-rich; the catalyst showed a 36 times increment in mass activity and 22 times in specific activity compared to the Pt/C catalyst. The activity and stability of the nanoframe structure were found to be excellent in acidic conditions without any deformation of the structure. The enhancement of the activity of such a system is mainly due to the change in the electronic structure. Further, the leaching of the transition metals in the alloy catalysts leads to the decrement of the ORR activity. This issue can be solved by forming a thin layer coating of the Pt on the non-Pt metals as the core. Many core-shell materials have been introduced, such as Cu@Pt, Pd@Pt, Ni@Pt, etc., which show better stability and durability.[59-62] However, the synthesis of such alloy and core-shell materials with proper composition and a thin layer on a support is a challenging task. Also, Pt is a high-cost material, making the fuel cell less cost-competitive in the market. Therefore, the development of suitable Pt-free electrocatalysts for ORR is essential.

1.8 Pt- free Electrocatalysts for ORR

Widespread commercialization of PEMFCs could be made by replacing the Pt catalysts with earth-abundant materials. Achieving high durability and performance is a challenging task for the researchers in the field of the Pt-free catalysts. For the development of non-precious electrocatalysts for ORR, the transition metals and mixtures of them can be used. The transition metals like Fe, Co, Ni, Zn, Mn, Cu, and Cr have studied as the oxygen reduction electrocatalysts so far. The Fe, Co, Ni, and Mn have great potential in the development of cost-effective electrocatalysts for ORR.[63-65] The heteroatom (N, S, B, P, and F) doped-carbons have great potential for ORR due to their electronic structure which gives catalytic activity comparable to the *state-of-the-art* Pt/C.[66-69] Some conducting polymers and the metal-organic frameworks (MOF) have also shown activity towards ORR.[70-72] Even the combination of the heteroatom doped-carbon with transition metal gives promising activity in basic as well as the acidic electrolytes. Also, the M-N-C (M-transition metals) coordination catalysts show excellent activity for ORR in both the electrolytes.

1.8.1 Metal-free Electrocatalysts for ORR

Various carbon structures and morphologies have been used to make a cost-effective ORR catalyst. Carbon materials such as graphene, CNTs, and ordered mesoporous carbons have attracted a lot of attention for their use in fuel cells. These carbon materials have beneficial

properties like high conductivity, high mechanical and chemical stability, and high surface area which make them ideal for the designing of the electrocatalysts. However, these materials are not stable in an acidic environment. Also, ORR follows the 2e- pathway on these materials. Hence, further improvement of the ORR activity and stability is achieved by the incorporation of heteroatom into the carbon matrix. The commonly used heteroatoms in carbon are N, S, B, and P. Also, co-doping improves the ORR activity.

1.8.1.1 Nitrogen Doping (N-doping)

Several literature reports are available on nitrogen-doped carbon morphologies as catalysts for ORR. The electronegativity of nitrogen (3.04) is higher than the carbon (2.55) in the nitrogen-doped carbon framework.[67] The difference in the electronegativity creates positive

Figure 1.8. Schematic representation of the nitrogen-doped graphene with various kinds of doped-N coordinations. (Reproduced with the permission of Elsevier, Copyright © 2017, Elsevier).[76]

charge density on the carbon atom, which results in the favorable adsorption of O_2. Also, nitrogen makes an exclusive electronic structure by the conjugation of the lone pair of electrons with the delocalized pi-electrons of carbon. The size of nitrogen is small, and the doping of nitrogen in the carbon matrix is most straightforward through the post-treatment method. Nitrogen doping in the carbon structures and morphologies like graphene, CNT and CNF can be obtained through different routes such as chemical vapor deposition (CVD), hydrothermal method, and annealing the mixture of the nitrogen precursors with carbon at a high temperature in an inert atmosphere. Typically, melamine, urea, NH_3, nitrogen-containing conducting polymers, *etc*., are used as the nitrogen sources for the synthesis of nitrogen-doped carbon morphologies.[73-75] In the graphene framework, the doped nitrogen can be classified as pyridinic-

N, pyrrolic-N, and graphitic-N.[76] Klaus Mullen *et al.* [77] have reported an N-doped micro/mesoporous carbon catalyst which is highly active in alkaline media synthesized through a hard templating method with N-enrich polymer and colloidal silica followed by NH_3 activation.[77]
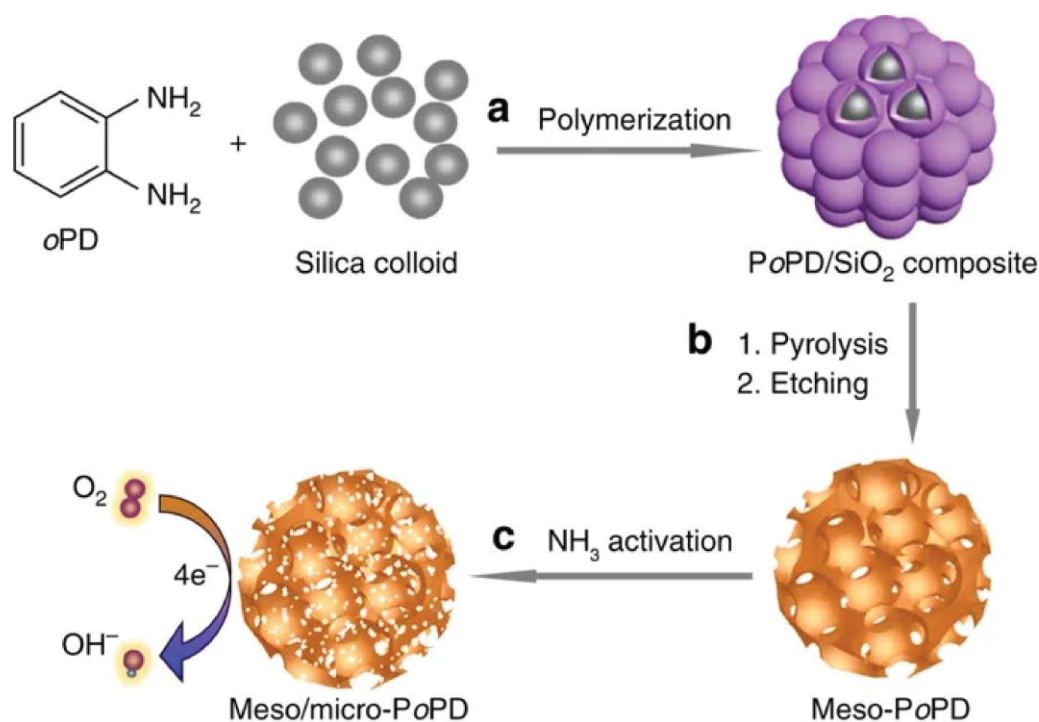
Figure 1.9. *Schematic of the synthesis of N-doped micro/mesoporous electrocatalyst: a) the polymerization of oPD with silica colloid by ammonium persulphate, b) pyrolysis of the composite followed by etching of SiO₂ in NaOH solution and c) NH₃ activation of the composite to form the final catalyst. (Reproduced with the permission from **Nature publishing group, License Number: 4810630943099**, Copyright © 2014, Springer Nature).*

The material showed the half-wave potential of 0.85 V in alkaline media. The enhancement of the activity is credited to the highly porous structure and N-doping which influence the electronic property of the catalysts. Further, the prepared material was used as a cathode catalyst for the fabrication of the primary ZAB. Gupta *et al*. reported N-doped graphene oxide prepared through a simple solvent and electrochemical method for ORR. It had a 3-D structure with more defects in the graphitic sheet, causing the enhanced the ORR activity.[78] To understand the mechanism of the ORR reaction on the N-doped carbon, Liang Yu *et al*. carried out significant work.[79] They reported that the N-doped graphene shows good activity for ORR and also, using DFT calculations, the two dissociative and associative mechanisms are investigated as follows:

Associative

$$O_2 \rightarrow O_{2\ (ad)} \tag{1.32}$$

$$O_{2\ (ad)} + H_2O + e^- \rightarrow OOH_{\ (ad)} + OH^- \tag{1.33}$$

$$OOH_{\ (ad)} + e^- \rightarrow O_{\ (ad)} + OH^- \tag{1.34}$$

$$O_{\ (ad)} + H_2O + e^- \rightarrow OH_{\ (ad)} + OH^- \tag{1.35}$$

$$OH_{\ (ad)} + e^- \rightarrow OH^- \tag{1.36}$$

Dissociative

$$\tfrac{1}{2}\ O_2 \rightarrow O_{\ (ad)} \tag{1.37}$$

$$O_{\ (ad)} + H_2O + e^- \rightarrow OH_{\ (ad)} + OH^- \tag{1.38}$$

$$OH_{\ (ad)} + e^- \rightarrow OH^- \tag{1.39}$$
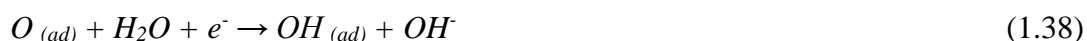
The associative mechanism is more favorable than the dissociative.

1.8.1.2 Sulphur Doping (S-doping)

The sulphur doping (S-doping) in the carbon morphologies is less investigated compared to the nitrogen. From the theoretical studies, it has been shown that the S-doping in the carbon matrix is comparatively tricky than nitrogen doping. Researchers believe that the change in the electronegativity due to doping of the nitrogen or other heteroatom in the carbon would change the positive charge density and this can help for ORR. In the case of S-doping, the difference in electronegativity of the sulphur (2.58) and carbon (2.55) is negligible.[67] The electronegativities are almost similar; also, the size of the sulphur atom is larger than the carbon. Hence, Zhang *et al.* introduced a new concept known as spin density.[73] The activity is affected by the mismatch of the outer orbital of sulphur and carbon; the positively charged sulphur atom is viewed as an active centre for ORR. Yang *et al.,*[67] have developed S-doped graphene as a catalyst through a simple method by taking a mixture of graphene oxide (GO), and benzyl disulphide (BDS), which was subsequently annealed under an argon atmosphere (**Figure 1.9**). The activity of the catalyst was tested in an alkaline medium and this catalyst showed better ORR activity compared to the commercial Pt/C. Recently, sulphur containing polymers (polythiophene, PEDOT, *etc*.) have been used as precursors for preparing the S-doped electrocatalysts for ORR.[81-85] The S-doped graphene shows excellent activity toward ORR, even though the atomic percentage of sulphur in the carbon is relatively low. The low content

of the sulphur can be attributed to the loss of sulphur from the carbon matrix at high temperatures. Further improvement in the activity of the catalyst can be achieved through the co-doping of heteroatoms.
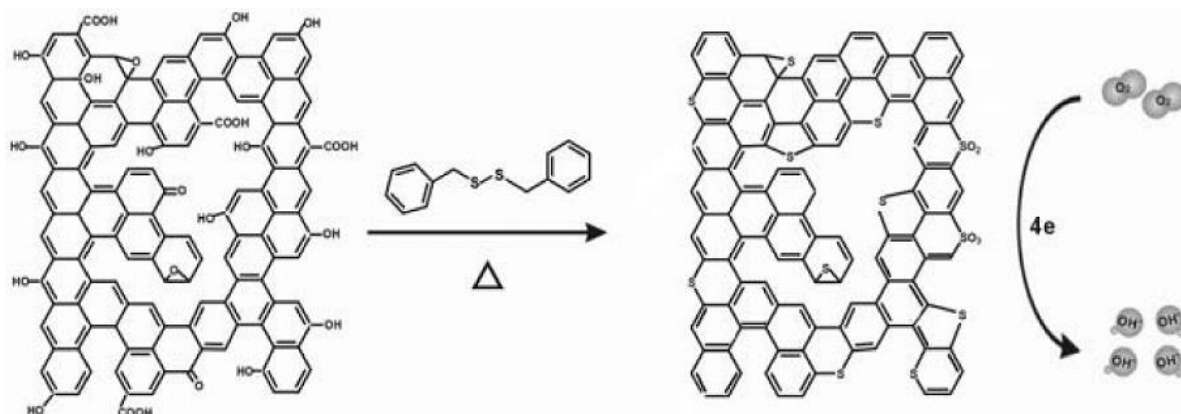
Figure 1.10. *Schematic illustration of the sulfur doped graphene (S-graphene) preparation. (Reproduced with permission from ACS, Copyright © 2012, American Chemical Society).*[67]

1.8.1.3 Nitrogen and Sulphur co-doping

Qiao *et al*. [80] had first demonstrated the N and S co-doped system *via* the thermal treatment of a mixture of melamine and benzyl disulphide as the N and S source, respectively, with GO. The ORR activity of the N and S co-doped graphene is higher compared to the individual N-doped

Atom Number	Spin Density	Charge Density
C1	0.43	0.23
C2	-0.03	0.28
C3	-0.03	0.28
C4	0.16	-0.22
C5	0.16	-0.22
N	0.06	-0.88
S	0.09	0.21

Figure 1.11. *Spin and charge density of the graphene network; C1 has very high spin density, C2 and C3 have high positive charge density, and C4 and C5 have moderately high positive spin densities. (Reproduced with permission from **Jhon Wiley and Sons, License Number: 4810300201848**)*

and S-doped graphene systems.[86-89] Due to the co-doping, it is found from the DFT calculations that the change in charge and spin density induces higher ORR (**Figure 1.10**). The N-S-G showed an onset potential of -0.06 V *vs*. Ag/AgCl compared to the commercial Pt/C, which showed a value of -0.03 V *vs*. Ag/AgCl in the alkaline electrolyte.[80] Hence, the N and S co-doping synergistically helped to improve ORR activity. Also, using a single precursor for N and S, Wang *at el*.[90] prepared a metal-free electrocatalyst for ORR, which shows high current density and good onset potential, involving a direct 4e- transfer reaction.[90]

1.8.2 Non-precious Metal-based Electrocatalysts for ORR

The high cost and poor durability of the precious Pt-based catalyst and its alloy electrocatalysts restrict the commercialization of the electrochemical devices such as PEMFCs and ZABs. To solve the problem of activity of the existing electrocatalysts and cost, low-cost transition metals and their coordination with heteroatom in the carbon morphologies are attracting attention. The developed catalyst is also expected to be a promising candidate for the replacement of the high-cost Pt-based catalysts. There are several literature reports on the non-precious metal-based catalysts,[91-96] where the catalysts show lower activity compared to the commercial Pt/C catalyst. The inferior activity of these catalysts is caused by the low number of active sites. The non-precious metal-doped or heteroatom doped-coordinated graphitic carbon matrix can increase th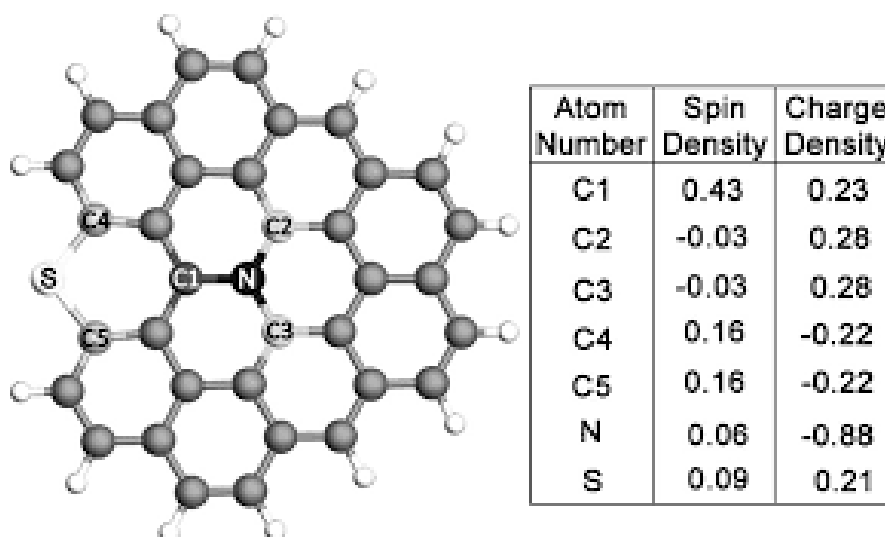e number of active sites in the catalyst.[97-100] Also, by making the metal-N or metal-S coordination in the graphene framework, the enhancement in the ORR activity can be achieved. Further, to accomplish the improvement in the activity, the atomic dispersion of the active metal coordination with heteroatom helps to increase the number of the active sites in the carbon morphology. Zelenay *et al.,*[101] have synthesized the M-N-C based catalysts using polyaniline as both the nitrogen and carbon precursor by annealing at higher temperatures with the incorporation of iron and cobalt metal salts. The prepared catalyst has Fe and Co in the N-doped carbon as active centers, which act as the ORR active sites. The catalyst shows a shift in the half-wave potential value by 60 mV compared to the Pt/C catalyst in the acidic environment. In a single-cell analysis, the catalyst delivered 550 mW cm^{-2} power density with the durability of 700 h at 0.40 V cell voltage in the hydrogen-air condition (**Figure 1.12**). Zelenay *et al.,*[102] have also demonstrated a single-step synthesis process of highly ORR active catalysts by using the cyanamide as a nitrogen and carbon source and iron acetate as an iron source. The derived catalyst shows excellent ORR activity in the basic medium and even performed better than the Pt/C catalyst while displaying high durability.
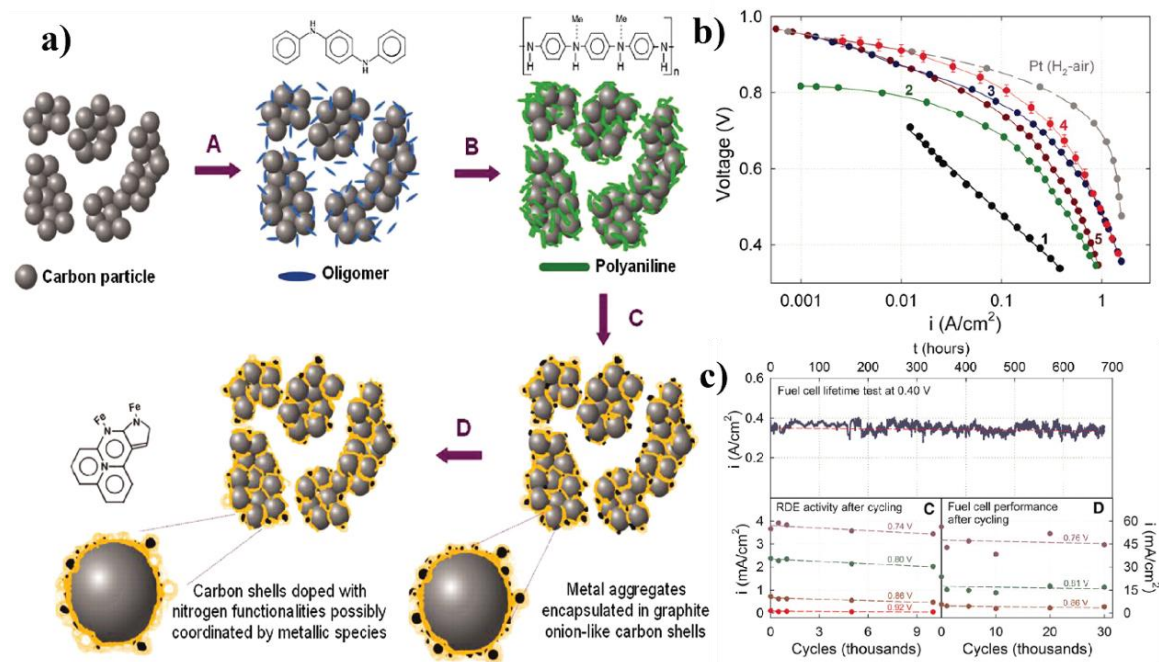
Figure 1.12. *a) Schematic representation of the synthesis of PANI-M-C catalysts, b) the polarization plots of various PANI derived cathode catalysts recorded in H_2-O_2 atmosphere: 1, PANI-C; 2, PANI-Co-C; 3, PANI-FeCo-C (1); 4, PANI-FeCo-C (2); and 5, PANI-Fe-C, c) the long term durability data of PANI-FeCo-C(1) as a cathode catalyst at a constant potential of 0.4 V in H_2-air at a cell operating temperature of 80 °C (Reproduced from the permission of the **Science, License Number: 4810600466724**, Copyright © 2011, American Association for the Advancement of Science).*

Chung *et al.* [103] have prepared micro/mesoporous iron nitrogen carbon catalysts using two nitrogen precursors, which have nitrogen coordinated with iron (FeN_4) embedded carbon as active sites for ORR. The Fe-N_4 active site showed a maximum power density of 940 mW cm^{-2} in H_2-O_2 conditions in a single cell analysis of PEMFC with a 4 cm^2 electrode active area. Kara Strickland *et al.*,[104] introduced a new type of material for ORR. They prepared iron encapsulated by the carbon nitride skin, which creates more active site density. Also, it can eliminate any Fenton kind of processes during the ORR reaction. Recently, Wu *et al.*,[105] have developed a system based on single atomic dispersed iron coordinated nitrogen in the carbon matrix-forming Fe-N_x complex, which acts as active ORR sites in acidic media. The catalyst was prepared by the thermal decomposition of the zeolite imidazole framework (ZIF) in the presence of iron under an inert atmosphere. The material shows a 30 mV higher shift in the half-wave potential compared to the Pt/C catalysts in acidic media while displaying excellent durability. The enhancement in the activity is due to the formation of Fe-N_x active sites (**Figure**

1.13). Also, Li *et al.*,[106] demonstrated a system consisting of atomically isolated Fe in sulphur and nitrogen-doped carbon morphologies for the improved ORR activity. XAFS and DFT studies indicate that the low electronegativity of the S creates a positive charge on the nitrogen to facilitate ORR. Fe-N-C based non-precious metal-based electrocatalysts are promising candidates for the replacement of the Pt-based electrocatalysts in PEMFCs, but show low activity in acidic conditions. Further, to improve the activity of the Fe-N-C system, Wang *at el*.[107] have introduced S-doping in the Fe-N-C system. The S-doped Fe-N-C catalyst showed ~0.83 V half-wave potential, which is ~50 mV lesser compared to the commercial Pt/C.[107] The Fe, N, and S codoped highly porous hollow carbon nanorods prepared by Lin *at el*. displayed improved ORR performance.[108]
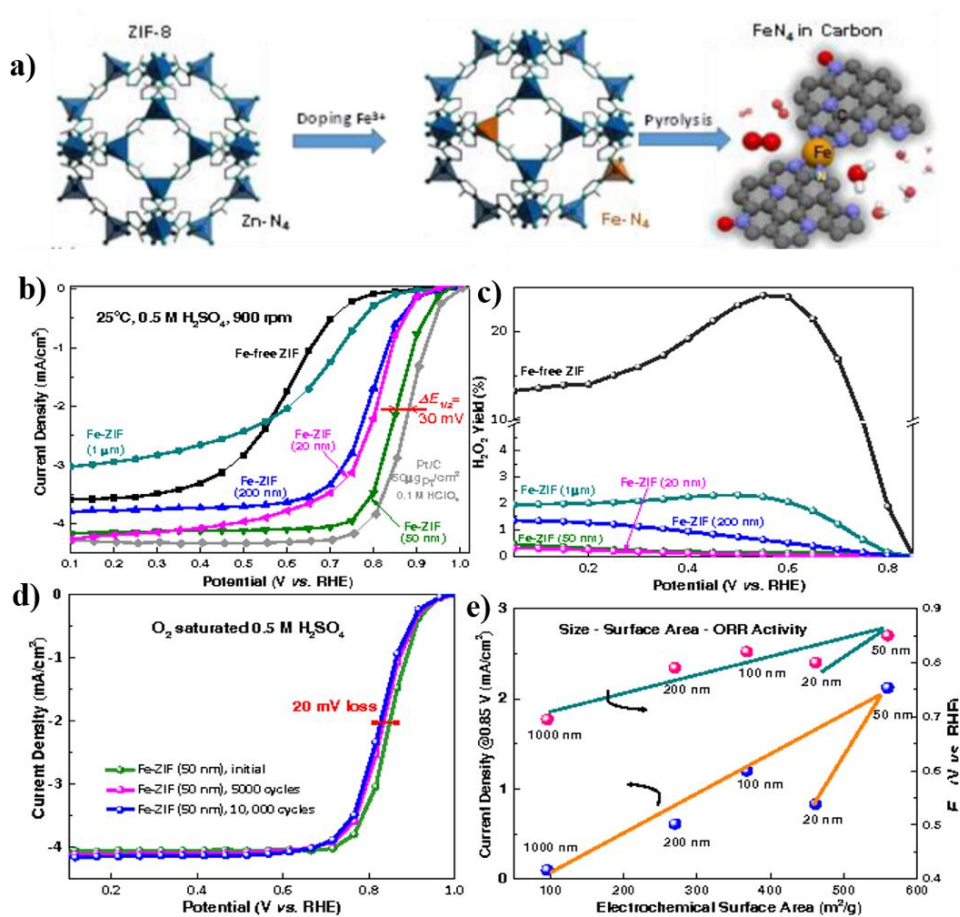

Figure 1.13. *a) Schematic illustration of the Fe-doped ZIF-derive electrocatalysts, b) linear sweep voltammograms (LSVs) of the ZIP-derived catalysts in 0.5M H₂SO₄, c) hydrogen peroxide formation of the ZIP-derives catalysts, d) ADT and e) the correlation of the ORR activity with the surface area. (Reproduced with permission ACS, Copyright © 2017, American Chemical Society).[105]*

1.9 Scope and Objectives of the Present Thesis

After the detailed literature survey, it is understood that highly efficient and cost-effective electrocatalysts are urgently required for the widespread use of the electrochemical energy devices such as PEMFCs and ZABs. The existing PEMFCs and ZABs are facing issues of low performance, high-cost, and lower widespread applicability. The exorbitant cost of the *state-of-the-art* Pt/C catalysts make these systems highly expensive and, thus, hamper the commercial prospects in the energy market. Hence, development of low-cost Pt-free electrocatalysts as substitutes for the *state-of-the-art* Pt/C catalyst is an important need of the time. To tackle the catalyst issues related to cost and durability, a systematic study needs to be performed by designing various active and stable Pt-free electrocatalysts, and the present dissertation is an effort to develop viable Pt-free electrocatalysts, which can serve as potential replacements for their Pt-based counterparts for both PEMFC and ZAB. The literature review presented in this chapter gives the current status of the development of the metal-free, heteroatom-doped, and non-noble metal-based electrocatalysts for ORR. It also highlights the various strategies adopted for increasing the number of the active sites and tackle the issues related to reaction kinetics, mass transport and ORR overpotentials. However, the present Pt-free systems require significant improvement in terms of both performance and durability, and this still remains as a challenging task irrespective of whatever advancements have been made in this direction so far. In view of this, the present dissertation is intended to develop innovative solutions for realizing practically feasible noble metal-free ORR electrocatalysts. The strategy adopted here is primarily focused on modifying the morphology, surface area, nature and coordination of the reactive sites and conductivity to achieve a favourable modulation in terms of the ORR activity of the noble metal-free electrocatalysts.

The specific objectives of this thesis are listed below:

1. In any electrochemical system involving gaseous reactants like the PEMFC and metal-air battery systems, the active catalytic site must have simultaneous and liberal access to the three-phase interface, *i.e.*, gas, electron-conducting medium, and proton-conducting medium. Therefore, an ideal electrode configuration should concurrently balance the transport process of all these three phases effectively. Thus, it is very likely that the key requisites of a fuel cell electrocatalyst are high porosity, surface area, high conductivity, strong ORR activity and good electrochemical stability. Hence, one important objective here is to develop an electrocatalyst possessing all the vital requisites of an ideal electrode material *viz.*, high porosity, high conductivity, along with high intrinsic electrochemical activity which play decisive role in determining the

activity of the triple phase boundary in the energy devices like PEMFCs and ZABs. In this direction, a cobalt based ZIF stringed CNT is proposed to be prepared which can be a potential electrode material for realistic system level applications.

2. Non-precious dioxygen reduction electrocatalysts have attracted significant attention currently for the development of stable, cost-effective PEMFCs. In line with this requirement, a Pt-free oxygen reduction electrocatalyst based on nitrogen and sulphur co-doped crumbled graphene with trace amounts of iron could is expected to be a potential system. Hence, development of a noble metal-free electrocatalyst possessing micro/mesoporous crumbled graphene morphology with high surface area and accessible nitrogen and sulphur dual doped active sites is a targeted objective of the present thesis. A realistic system level validation of a PEMFC based on the catalyst as the cathode also is an objective of the work.

3. Another objective is the development of an ORR electrocatalyst comprised of S-doped graphene enriched with the $Fe-S_x$ coordinated sites, which can display high activity in both acidic and basic environments. This can be prepared *via* annealing of PEDOT, which builds the $Fe-S_x$ coordination sites originated by the intervention of the residual iron chloride retained by the polymer matrix, which will be employed as the oxidizing agent for the polymerization reaction. System level evaluation of both PEMFC (acidic environment) and ZAB (basic environment) by employing this catalyst for the cathode of the systems is another objective of the work.

4. Development of an ORR electrocatalyst comprising of co-existing FeNx/FeSx active site bearing carbon sheets which are spatially separated by a network of carbon nanotubes (CNTs) for facilitating ORR both under acidic and basic pH conditions is another objective here considering the need of modulation of both the morphological features and the active site co-ordinations. This is targeted to be prepared form PEDOT in the presence of CNT and melamine with controlled pyrolysis under an inert atmosphere, which is expected to facilitate the formation of an electrocatalyst having the desirable characteristics of spatial separation of the active site-bearing carbon sheets with the help of the CNT network.

1.10 References

1. K. Gregory and H.-H. Rogner, *Mitigation and Adaptation Strategies for Global Change*, 1998, **3**, 171-230.

2. S. Al-Hallaj and K. Kiszynski, 2011, **79**.

3. J.-E. Lane, *Earth Science Research*, 2018, **7**, 1.

4. M. Isaac and D. P. van Vuuren, *Energy Policy*, 2009, **37**, 507-521.

5. E. L. Etnier and A. P. Watson, *Environmental Management*, 1981, **5**, 409-425.

6. R. M. Rotty, *Energy*, 1979, **4**, 881-890.

7. M. Z. Jacobson and M. A. Delucchi, *Energy Policy*, 2011, **39**, 1154-1169.

8. C. J. Fox, S. Benjamins, E. A. Masden and R. Miller, *Renewable and Sustainable Energy Reviews*, 2018, **81**, 1926-1938.

9. V. Devabhaktuni, M. Alam, S. Shekara Sreenadh Reddy Depuru, R. C. Green, D. Nims and C. Near, *Renewable and Sustainable Energy Reviews*, 2013, **19**, 555-564.

10. J. Hou, Y. Shao, M. W. Ellis, R. B. Moore and B. Yi, *Physical Chemistry Chemical Physics*, 2011, **13**, 15384-15402.

11. F. O. Rourke, F. Boyle and A. Reynolds, *Renewable and Sustainable Energy Reviews*, 2010, **14**, 1026-1036.

12. R. Tiron, F. Mallon, F. Dias and E. G. Reynaud, *Renewable and Sustainable Energy Reviews*, 2015, **43**, 1263-1272.

13. S. D. Pohekar, D. Kumar and M. Ramachandran, *Renewable and Sustainable Energy Reviews*, 2005, **9**, 379-393.

14. J. M. Giussi, M. L. Cortez, W. A. Marmisollé and O. Azzaroni, *Chemical Society Reviews*, 2019, **48**, 814-849.

15. L. Lu, X. Han, J. Li, J. Hua and M. Ouyang, *Journal of Power Sources*, 2013, **226**, 272-288.

16. V. Mehta and J. S. Cooper, *Journal of Power Sources*, 2003, **114**, 32-53.

17. S. R. C. Vivekchand, C. S. Rout, K. S. Subrahmanyam, A. Govindaraj and C. N. R. Rao, *Journal of Chemical Sciences*, 2008, **120**, 9-13.

18. A. Kraytsberg and Y. Ein-Eli, *Nano Energy*, 2013, **2**, 468-480.

19. W. G. Hardin, D. A. Slanac, X. Wang, S. Dai, K. P. Johnston and K. J. Stevenson, *The Journal of Physical Chemistry Letters*, 2013, **4**, 1254-1259.

20. A. K. Shukla and T. Prem Kumar, *WIREs Energy and Environment*, 2013, **2**, 14-30.

21. O. Gröger, H. Gasteiger and P. Suchsland, *Journal of The Electrochemical Society*, 2015, **162**, A2605-A2622.

22. J. Stempien and S. H. Chan, *Journal of Power Sources*, 2016, **340**, 347.

23. J. A.J, A. Abdulkareem, A. Jimoh and A. Afolabi, *Advances in Materials Science and Applications*, 2015, **4**, 63-75.

24. G. Gautier and S. Kouassi, *International Journal of Energy Research*, 2015, **39**, 1-25.

25. A. Chandan, M. Hattenberger, A. El-kharouf, S. Du, A. Dhir, V. Self, B. G. Pollet, A. Ingram and W. Bujalski, *Journal of Power Sources*, 2013, **231**, 264-278.

26. M. Mamlouk, T. Sousa and K. Scott, 2011.

27. W. J. Zhou, B. Zhou, W. Z. Li, Z. H. Zhou, S. Q. Song, G. Q. Sun, Q. Xin, S. Douvartzides, M. Goula and P. Tsiakaras, *Journal of Power Sources*, 2004, **126**, 16-22.

28. Q. Li, R. He, J. O. Jensen and N. J. Bjerrum, *Fuel Cells*, 2004, **4**, 147-159.

29. S. Simon Araya, F. Zhou, V. Liso, S. Sahlin, J. Vang, S. Thomas, X. Gao, C. Jeppesen and S. Kær, *International Journal of Hydrogen Energy*, 2016, **41**.

30. S. Bose, T. Kuila, T. X. H. Nguyen, N. H. Kim, K.-t. Lau and J. H. Lee, *Progress in Polymer Science*, 2011, **36**, 813-843.

31. J. J. Baschuk and X. Li, *International Journal of Energy Research*, 2003, **27**, 1095-1116.

32. C. M. Pedersen, M. Escudero-Escribano, A. Velázquez-Palenzuela, L. H. Christensen, I. Chorkendorff and I. E. L. Stephens, *Electrochimica Acta*, 2015, **179**, 647-657.

33. J. J. Baschuk and X. Li, *International Journal of Energy Research*, 2001, **25**, 695-713.

34. H. Ju, K.-S. Lee and S. Um, *Journal of Mechanical Science and Technology*, 2008, **22**, 991-998.

35. Y. Li, M. Gong, Y. Liang, J. Feng, J.-E. Kim, H. Wang, G. Hong, B. Zhang and H. Dai, *Nature Communications*, 2013, **4**, 1805.

36. Z. Chen, A. Yu, R. Ahmed, H. Wang, H. Li and Z. Chen, *Electrochimica Acta*, 2012, **69**, 295-300.

37. V. Neburchilov, H. Wang, J. J. Martin and W. Qu, *Journal of Power Sources*, 2010, **195**, 1271-1291.

38. X. Liu, M. Park, M. G. Kim, S. Gupta, X. Wang, G. Wu and J. Cho, *Nano Energy*, 2016, **20**, 315-325.

39. J.-S. Lee, S. Tai Kim, R. Cao, N.-S. Choi, M. Liu, K. T. Lee and J. Cho, *Advanced Energy Materials*, 2011, **1**, 34-50.

40. X. Ren, Q. Lv, L. Liu, B. Liu, Y. Wang, A. Liu and G. Wu, *Sustainable Energy & Fuels*, 2020, **4**, 15-30.

41. P. Chandran, A. Ghosh and S. Ramaprabhu, *Scientific Reports*, 2018, **8**, 3591.

42. S. Sui, X. Wang, X. Zhou, Y. Su, S. Riffat and C.-j. Liu, *Journal of Materials Chemistry A*, 2017, **5**, 1808-1825.

43. R. Ma, G. Lin, Y. Zhou, Q. Liu, T. Zhang, G. Shan, M. Yang and J. Wang, *npj Computational Materials*, 2019, **5**, 78.

44. L. Yang, J. Shui, L. Du, Y. Shao, J. Liu, L. Dai and Z. Hu, *Advanced Materials*, 2019, **31**, 1804799.

45. L. Dai, *Current Opinion in Electrochemistry*, 2017, **4**, 18-25.

46. M. Escudero-Escribano, P. Malacrida, M. H. Hansen, U. G. Vej-Hansen, A. Velázquez-Palenzuela, V. Tripkovic, J. Schiøtz, J. Rossmeisl, I. E. L. Stephens and I. Chorkendorff, *Science*, 2016, **352**, 73-76.

47. J. Greeley, I. E. L. Stephens, A. S. Bondarenko, T. P. Johansson, H. A. Hansen, T. F. Jaramillo, J. Rossmeisl, I. Chorkendorff and J. K. Nørskov, *Nature Chemistry*, 2009, **1**, 552-556.

48. E. Antolini, J. R. C. Salgado, M. J. Giz and E. R. Gonzalez, *International Journal of Hydrogen Energy*, 2005, **30**, 1213-1220.

49. V. Di Noto and E. Negro, *Fuel Cells*, 2010, **10**, 234-244.

50. J. Jiang, H. Gao, S. Lu, X. Zhang, C.-Y. Wang, W.-K. Wang and H.-Q. Yu, *Journal of Materials Chemistry A*, 2017, **5**, 9233-9240.

51. Y. Xiong, L. Xiao, Y. Yang, F. J. DiSalvo and H. D. Abruña, *Chemistry of Materials*, 2018, **30**, 1532-1539.

52. J. K. Nørskov, J. Rossmeisl, A. Logadottir, L. Lindqvist, J. R. Kitchin, T. Bligaard and H. Jónsson, *The Journal of Physical Chemistry B*, 2004, **108**, 17886-17892.

53. J. Wang, X. Xiao, Y. Liu, K. Pan, H. Pang and S. Wei, *Journal of Materials Chemistry A*, 2019, **7**, 17675-17702.

54. S. K. Singh, K. Takeyasu and J. Nakamura, *Advanced Materials*, 2019, **31**, 1804297.

55. V. P. Zhdanov and B. Kasemo, *Electrochemistry Communications*, 2006, **8**, 1132-1136.

56. T. Li and P. B. Balbuena, *Chemical Physics Letters*, 2003, **367**, 439-447.

57. V. R. Stamenkovic, B. S. Mun, M. Arenz, K. J. J. Mayrhofer, C. A. Lucas, G. Wang, P. N. Ross and N. M. Markovic, *Nature Materials*, 2007, **6**, 241-247.

58   C. Chen, Y. Kang, Z. Huo, Z. Zhu, W. Huang, H. L. Xin, J. D. Snyder, D. Li, J. A. Herron, M. Mavrikakis, M. Chi, K. L. More, Y. Li, N. M. Markovic, G. A. Somorjai, P. Yang and V. R. Stamenkovic, *Science*, 2014, **343**, 1339-1343

59   R. Ferrando, J. Jellinek and R. L. Johnston, *Chemical Reviews*, 2008, **108**, 845-910.

60   R. Ghosh Chaudhuri and S. Paria, *Chemical Reviews*, 2012, **112**, 2373-2433.

61   V. M. Dhavale, S. M. Unni, H. N. Kagalwala, V. K. Pillai and S. Kurungot, *Chem Commun (Camb)*, 2011, **47**, 3951-3953.

62   S. J. Hwang, S. J. Yoo, J. Shin, Y.-H. Cho, J. H. Jang, E. Cho, Y.-E. Sung, S. W. Nam, T.-H. Lim, S.-C. Lee and S.-K. Kim, *Scientific Reports*, 2013, **3**, 1309.

63.   U. Martinez, S. Komini Babu, E. F. Holby, H. T. Chung, X. Yin and P. Zelenay, *Advanced Materials*, 2019, **31**, 1970224.

64.   Q. Hu, G. Li, J. Pan, L. Tan, J. Lu and L. Zhuang, *International Journal of Hydrogen Energy*, 2013, **38**, 16264-16268.

65.   Y. Liu, Y. Wang, X. Xu, P. Sun and T. Chen, *RSC Advances*, 2014, **4**, 4727-4731.

66.   H. Jiang, J. Gu, X. Zheng, M. Liu, X. Qiu, L. Wang, W. Li, Z. Chen, X. Ji and J. Li, *Energy & Environmental Science*, 2019, **12**, 322-333.

67.   Z. Yang, Z. Yao, G. Li, G. Fang, H. Nie, Z. Liu, X. Zhou, X. a. Chen and S. Huang, *ACS Nano*, 2012, **6**, 205-211.

68.   R. Sibul, E. Kibena-Põldsepp, U. Mäeorg, M. Merisalu, A. Kikas, V. Kisand, A. Treshchalov, V. Sammelselg and K. Tammeveski, *Electrochemistry Communications*, 2019, **109**, 106603.

69.   L. Feng, Z. Qin, Y. Huang, K. Peng, F. Wang, Y. Yan and Y. Chen, *Science of The Total Environment*, 2020, **698**, 134239.

70.   G. Wu, Z. Chen, F. Garzon and P. Zelenay, *ECS Transactions*, 2008, **16**.

71.   J. Quílez-Bermejo, C. González-Gaitán, E. Morallón and D. Cazorla-Amorós, *Carbon*, 2017, **119**, 62-71.

72.   S. Gonen and L. Elbaz, *Data in Brief*, 2018, **19**, 281-287.

73.   F. Pan, J. Jin, X. Fu, Q. Liu and J. Zhang, *ACS Applied Materials & Interfaces*, 2013, **5**, 11108-11114.

74.   Z.-H. Sheng, L. Shao, J.-J. Chen, W.-J. Bao, F.-B. Wang and X.-H. Xia, *ACS Nano*, 2011, **5**, 4350-4358.

75.   B. Zheng, Y. Chen, P. Li, Z. Wang, B. Cao, F. Qi, J. Liu, Z. Qiu and W. Zhang, 2017, **6**, 259.
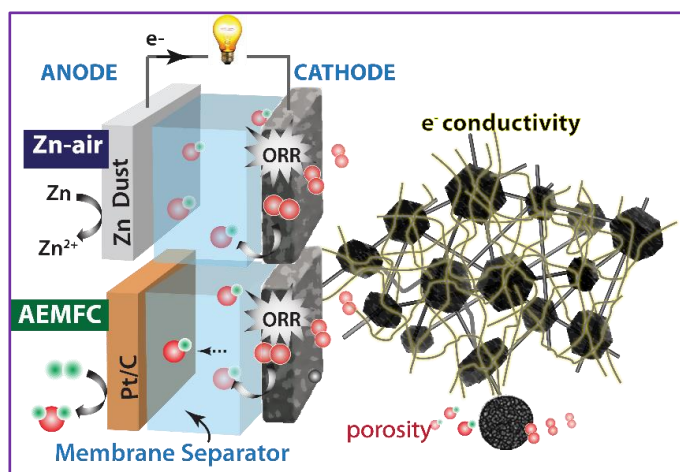
76. R. Yadav and C. K. Dixit, *Journal of Science: Advanced Materials and Devices*, 2017, **2**, 141-149.

77. H.-W. Liang, X. Zhuang, S. Brüller, X. Feng and K. Müllen, *Nature Communications*, 2014, **5**, 4973.

78. J. H. Dumont, U. Martinez, K. Artyushkova, G. M. Purdy, A. M. Dattelbaum, P. Zelenay, A. Mohite, P. Atanassov and G. Gupta, *ACS Applied Nano Materials*, 2019, **2**, 1675-1682.

79. L. Yu, X. Pan, X. Cao, P. Hu and X. Bao, *Journal of Catalysis*, 2011, **282**, 183-190.

80. J. Liang, Y. Jiao, M. Jaroniec and S. Z. Qiao, *Angewandte Chemie International Edition*, 2012, **51**, 11496-11500.

81. C. Jin, T. C. Nagaiah, W. Xia, M. Bron, W. Schuhmann and M. Muhler, *ChemSusChem*, 2011, **4**, 927-930.

82. S. K. Singh, X. Crispin and I. V. Zozoulenko, *The Journal of Physical Chemistry C*, 2017, **121**, 12270-12277.

83. M. Zhang, W. Yuan, B. Yao, C. Li and G. Shi, *ACS Applied Materials & Interfaces*, 2014, **6**, 3587-3593.

84. Z. Guo, H. Liu, C. Jiang, Y. Zhu, M. Wan, L. Dai and L. Jiang, *Small*, 2014, **10**, 2087-2095.

85. J. A. Vigil, T. N. Lambert and K. Eldred, *ACS Applied Materials & Interfaces*, 2015, **7**, 22745-22750.

86. S.-A. Wohlgemuth, R. J. White, M.-G. Willinger, M.-M. Titirici and M. Antonietti, *Green Chemistry*, 2012, **14**, 1515-1523.

87. W. Ai, Z. Luo, J. Jiang, J. Zhu, Z. Du, Z. Fan, L. Xie, H. Zhang, W. Huang and T. Yu, *Advanced Materials*, 2014, **26**, 6186-6192.

88. J. Xu, G. Dong, C. Jin, M. Huang and L. Guan, *ChemSusChem*, 2013, **6**, 493-499.

89. Y. Su, Y. Zhang, X. Zhuang, S. Li, D. Wu, F. Zhang and X. Feng, *Carbon*, 2013, **62**, 296-301.

90. X. Wang, J. Wang, D. Wang, S. Dou, Z. Ma, J. Wu, L. Tao, A. Shen, C. Ouyang, Q. Liu and S. Wang, *Chemical Communications*, 2014, **50**, 4839-4842.

91. P. Lang, N. Yuan, Q. Jiang, Y. Zhang and J. Tang, *Energy Technology*, 2020, **8**, 1900984.

92. S. Kim, S. Kato, T. Ishizaki, O. L. Li and J. Kang, *Nanomaterials (Basel)*, 2019, **9**, 742.

93. M. Sun, H. Liu, Y. Liu, J. Qu and J. Li, *Nanoscale*, 2015, **7**, 1250-1269.

94. M.-R. Gao, J. Jiang and S.-H. Yu, *Small*, 2012, **8**, 13-27.

95.   H.-J. Zhang, Q.-Z. Jiang, L. Sun, X. Yuan, Z. Shao and Z.-F. Ma, *International Journal of Hydrogen Energy*, 2010, **35**, 8295-8302.

96.   Y. Dong, Y. Deng, J. Zeng, H. Song and S. Liao, *Journal of Materials Chemistry A*, 2017, **5**, 5829-5837.

97.   X. Wang, H. Zhang, H. Lin, S. Gupta, C. Wang, Z. Tao, H. Fu, T. Wang, J. Zheng, G. Wu and X. Li, *Nano Energy*, 2016, **25**, 110-119.

98.   M. Wang, Y. Yang, X. Liu, Z. Pu, Z. Kou, P. Zhu and S. Mu, *Nanoscale*, 2017, **9**, 7641-7649.

99.   Z. Guan, X. Zhang, W. Chen, J. Pei, D. Liu, Y. Xue, W. Zhu and Z. Zhuang, *Chemical Communications*, 2018, **54**, 12073-12076.

100.   R. Jäger, P. E. Kasatkin, E. Härk, P. Teppor, T. Romann, R. Härmas, I. Tallo, U. Mäeorg, U. Joost, P. Paiste, K. Kirsimäe and E. Lust, *Journal of Electroanalytical Chemistry*, 2018, **823**, 593-600.

101.   G. Wu, K. L. More, C. M. Johnston and P. Zelenay, *Science*, 2011, **332**, 443-447.

102.   H. T. Chung, J. H. Won and P. Zelenay, *Nature Communications*, 2013, **4**, 1922. 116

103.   H. T. Chung, D. A. Cullen, D. Higgins, B. T. Sneed, E. F. Holby, K. L. More and P. Zelenay, *Science*, 2017, **357**, 479-484.

104.   K. Strickland, E. Miner, Q. Jia, U. Tylus, N. Ramaswamy, W. Liang, M.-T. Sougrati, F. Jaouen and S. Mukerjee, *Nature Communications*, 2015, **6**, 7343.

105.   H. Zhang, S. Hwang, M. Wang, Z. Feng, S. Karakalos, L. Luo, Z. Qiao, X. Xie, C. Wang, D. Su, Y. Shao and G. Wu, *Journal of the American Chemical Society*, 2017, **139**, 14143-14149.

106   Q. Li, W. Chen, H. Xiao, Y. Gong, Z. Li, L. Zheng, X. Zheng, W. Yan, W.-C. Cheong, R. Shen, N. Fu, L. Gu, Z. Zhuang, C. Chen, D. Wang, Q. Peng, J. Li and Y. Li, *Advanced Materials*, 2018, **30**, 1800588.

107   Y.-C. Wang, Y.-J. Lai, L. Song, Z.-Y. Zhou, J.-G. Liu, Q. Wang, X.-D. Yang, C. Chen, W. Shi, Y.-P. Zheng, M. Rauf and S.-G. Sun, *Angewandte Chemie International Edition*, 2015, **54**, 9907-9910.

108   Y. Wang, C. Zhu, S. Feng, Q. Shi, S. Fu, D. Du, Q. Zhang and Y. Lin, *ACS Applied Materials & Interfaces*, 2017, **9**, 40298-40306.

Chapter-2

Single Cell Fabrication of CNT Strung ZIF-derived Electrocatalyst as Cathode Material in Alkaline Fuel Cell and Metal-air Battery

The present chapter deals with the development of an electrocatalyst possessing all the vital requisites of an ideal electrode material *viz.*, high porosity, high conductivity, along with high intrinsic electrochemical activity which play decisive role in determining the activity of the triple phase boundary in the energy devices like polymer electrolyte membrane fuel cells and metal-air batteries. In the present work, the highly porous cobalt based ZIFs (Co-ZIF-67) are stringed along the highly conducive CNT backbone using a simple one pot technique at room temperature, which is then utilized to derive porous, corrosion resistant, Co nanoparticle embedded electrocatalysts. Followed by a detailed structural and electrochemical characterization of the catalysts, for the first time, the single cell performance of the best Co-ZIF-67 derived electrocatalyst (CoNC-900) has been evaluated by fabricating Membrane Electrode Assemblies (MEAs) of Alkaline Exchange Membrane Fuel Cell (AEMFC) and Zinc–Air Battery (ZAB) systems. A maximum power density of 296 mW cm^{-2} (*vs*. 317 mW cm^{-2} of 40 wt. % Pt/C) and 60 mW cm^{-2} (*vs*. 64 mW cm^{-2} of 40 wt. % Pt/C) in the single cells of ZAB and AEMFC systems, respectively, establishes the practical proficiency of the homemade electrocatalysts for the cathode applications during the realistic system level validations.

2.1 Introduction

The inception of Oxygen Reduction Reaction (ORR) activity in alkaline medium is vividly foreseen as an overarching reaction, considering the working pH of many electrochemical energy systems *viz*., alkaline fuel cells, metal-air batteries, chlor-alkali electrolyzers etc.[1-2] Under the ORR conditions, the performances of the standard Pt/C catalysts are often limited by the catalyst degradation or carbon support corrosion during the course of long term operation.[3] Moreover, their high cost and scarcity further necessitate the need to lookout for more cost-effective, durable and competitive electrocatalysts.[4-5] Therefore, many metal/metal-free nanostructured systems have been developed and tried as non-precious ORR electrocatalysts.[6-7] Of all, the carbon-based systems have been the most preferred contenders considering the synthetic flexibility available to tune their morphology, surface area, porosity, degree of graphitization etc .[8-9] The electronic properties of these systems can also be tuned by means of heteroatom doping into the neutral carbon matrix.[10] This process is believed to augment the electron-donating ability of the nearby carbon, alter its spin density and reinforce charge distribution in the basal carbon matrix, thereby increasing the reactivity.[11] Carbon research largely focuses on the template based synthesis to yield highly porous carbons.[12-13] In this direction, Metal-Organic Frameworks (MOFs) are popular as 'self-sacrificial hard templates' for synthesizing porous carbon nanostructures without the aid of any secondary carbon source/pore-forming agents.[14] In particular, the MOFs containing heteroatoms and transition metal ions are known to result into functional metal oxide/metal-containing porous carbon composites, which are often demonstrated to catalyze energetic electrochemical reactions with lesser activation energy.[15] It is noteworthy that apart from high active site density, the presence of high structural integrity and electrical conductivity is also one of the prime requisites of a typical ORR electrocatalyst.[16] However, the high porosity of these MOF-derived carbons often compromises their graphitization and in turn, the electrical conductivity.[17] Thus, in the present work, cobalt-based ZIF (Co-ZIF-67) derived carbon is stringed along electrically conductive graphitic multiwalled CNTs in order to fabricate a highly structured, corrosion-resistant and integrated electrocatalysts (Scheme 2.1). The as obtained nanostructured catalyst is observed to effectively catalyze ORR showing remarkably on par performance with that of the commercial 40% Pt/C catalyst when employed in both Alkaline Exchange Membrane Fuel Cell (AEMFC) and Zinc–Air Battery (ZAB) systems .

The Co-ZIF-67/CNT composite is synthesized using a simple one-pot procedure by mixing methanolic solutions of functionalized MWCNTs and $Co(NO_3)_2.6H_2O$ with 2-methylimidazole (2-mIm), followed by stirring at room temperature for 1 h and drying at 60 ˚C for 6 h. The

MWCNT is pre-functionalized using conc. HNO_3:conc. H_2SO_4 (3:1) mixture to ensure site-specific nucleation of the Co-ZIF-67 structure.

2.2 Experimental Section
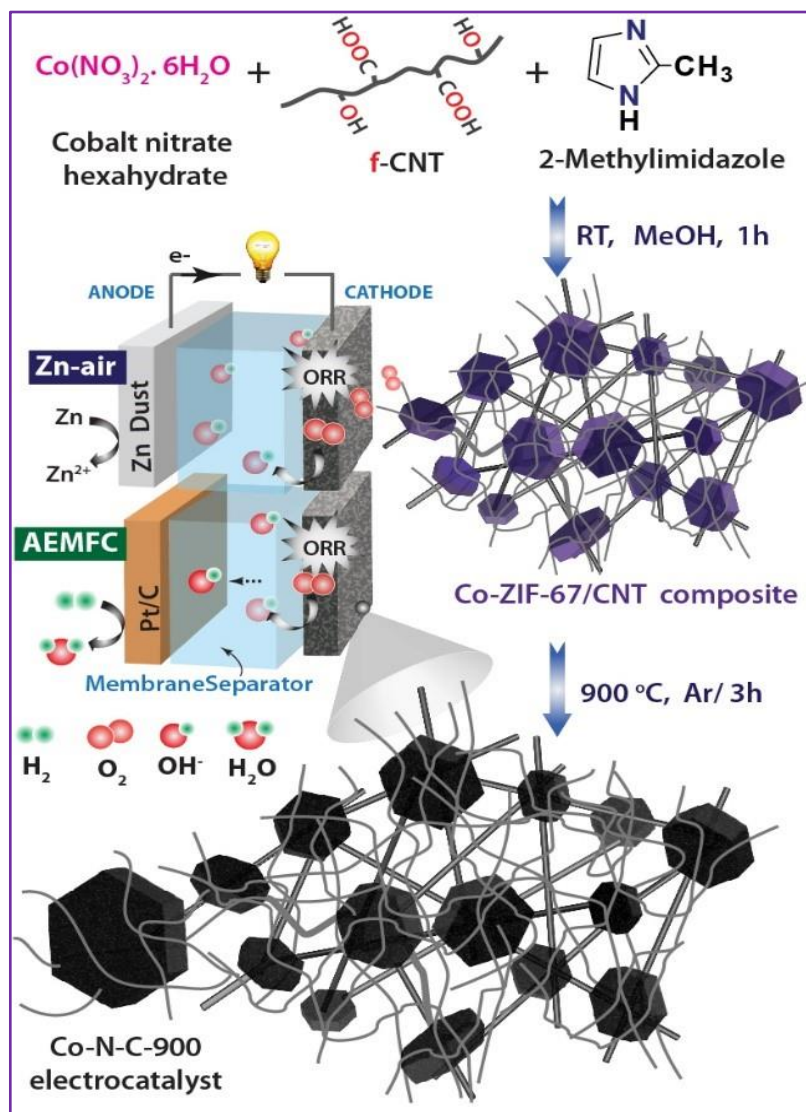
Scheme 2. 1 Schematic representation of the synthesis of CoNC-900 electrocatalyst and its utilization as an ORR electrocatalyst in anion exchange membrane fuel cell and Zn-air battery system.

2.2.1 Functionalization of MWCNT

1000 mg of the pristine MWCNT was dispersed in conc. HNO_3:conc. H_2SO_4 (3:1) mixture and refluxed at 90 °C for 3 h. The MWCNT was checked for functionalization and then washed in DI water, filtered and eventually dried overnight at 60 ˚C.

2.2.2 Synthesis of Co-ZIF-67/CNT Composite

Solution A: 1.53 g of 2-methyl imidazole was dissolved in 100 ml of methanol. Solution B: 70 mg of the functionalized Carbon Nanotube (CNT) was homogenized in 100 mL methanolic solution of cobalt (II) nitrate (containing 996 mg of $(Co (NO_3)_2).6 H_2O$ in 100 ml) using a probe sonicator for 15 min. [the amount of MWCNT was varied between 70 g (1×)–140 g (2×)–210 g (3×) to optimize the amount of CNT loading in the composite]. Solution A was slowly added drop-wise into Solution B and stirred for 1 h at room temperature. The precipitate obtained was then filtered immediately and dried at 60 ˚C. In the case of Co-ZIF-67 synthesis, the addition of MWCNTs was omitted.

2.2.3 Pyrolysis of Co-ZIF-67/CNT Composite

An alumina boat containing Co-ZIF-67/CNT composite was placed inside the tube furnace and heated at different temperatures (800-1000 ^oC) under argon flow at a ramp of 5 ˚C min^{-1} for 3 h each and then cooled naturally to room temperature.

2.3 PXRD, FTIR, TGA, Microscopy and N$_2$ Sorption Experiment Details

The Thermo Gravimetric Analysis (TGA) was carried out using a SDT Q600 TG-DTA analyzer in an oxygen atmosphere from 25–900 °C at a heating rate of 10 °C/min. The Fourier Transform Infrared (FT-IR) spectra were recorded in the 400-4000 cm^{-1} region on a Bruker Optics ALPHA-E spectrometer equipped with universal ZnSe ATR (attenuated total reflection) accessory. The SEM images were obtained using tungsten filament as electron source using Zeiss DSM 950 Scanning Electron Microscope and FEI, QUANTA 200 3D Scanning Electron Microscope operating at 10 kV. The TEM images were obtained using FEI Tecnai G2 F20 XTWIN TEM at an accelerating voltage of 200 kV. The samples were dispersed in isopropanol and sonicated prior to their drop-casting onto the copper grids. The N$_2$ adsorption experiments (from 0 to 1 bar) were carried out using the automatic Quantachrome Quadrasorb instrument.

2.4 Half-cell Study

The electrochemical half-cell study was performed in a standard three-electrode configuration using a BioLogic electrochemical workstation. A graphite rod (Alfa Aesar, 99.9995%) and Hg/HgO (1 M KOH) electrode were used as the counter electrode and the reference electrode, respectively.

The catalytic ink was prepared by homogenizing the pyrolyzed sample in isopropanol:water (3:2) mixture. Then 10 µl of this mixture was coated onto the freshly polished glassy carbon

electrode surface (geometrical area=0.196 cm^2) and 5 µl of 0.5% Nafion binder solution was added on it. The electrode was then dried at 60 ^{o}C for ~1 h and thereafter used for the studies. The electrochemical studies were performed at ambient temperature (298 K) using 0.1 M KOH solution and the electrode potentials were converted to the RHE. E_o (Hg/HgO (0.87 V) was determined using hydrogen saturated 0.1 M KOH as the electrolyte. The LSV was performed at a scan rate of 1.0 mV s^{-1} in a three-electrode system using a Pt rode as the working electrode, graphite rod as the counter electrode and Hg/HgO as the reference electrode, respectively. The potential at which the current crosses zero in the polarization plot was taken as the thermodynamic potential (*vs* Hg/HgO) for the hydrogen electrode.[31]

2.5 RRDE Study

In this study, the LSV pertaining to the disc electrode (coated with the electrocatalyst) was recorded at 10 mV s^{-1}, while the ring electrode was held at a constant potential of 0.40 V (*vs.* Hg/HgO). Prior to the study, the collection coefficient of the ring electrode was determined using K$_3$Fe(CN)$_6$ solution. It was found to be 0.37, which is in agreement with the value provided by the manufacturer. Thereafter, the apparent number of electrons involved in catalyzing ORR (n) and the corresponding amount of H$_2$O$_2$ produced in each case during the ORR were calculated using the following relations:

$$n = \frac{4 \times I_D}{I_D + {I_R}/{N}}$$

$$H_2O_2\% = \frac{200 \times \frac{I_R}{N}}{I_D + \frac{I_R}{N}}$$

wherein, I_D is the Disk current, I_R is the Ring current and N is the collection coefficient of the ring electrode.

2.6 Acid Washing of CoNC-900

The acid washing of the best catalyst in the study, CoNC-900, was carried out in 0.5 M H$_2$SO$_4$ for 8 h at 80 ^{o}C to remove the cobalt nanoparticles. The sample was then washed with copious amount of DI water followed by ethanol and finally dried at 60 ^{o}C overnight using a programmed oven. The acid wash sample is referred as CoNC-900-AW in the study.

2.7 Single-cell Polarization Study

2.7.1 Fabrication of Zinc-air Single Cell

The Zn-air single cell was fabricated and tested in a home-built electrochemical cell using Zn dust as the anode and CoNC-900 coated carbon paper as the cathode. Initially, the cathode was prepared by brush coating the catalyst ink [loading of 2 mg cm^{-2}, comprising of CoNC-900 + Fumion® binder (20%)] onto the porous carbon paper (35 CC-SGL with 15% PTFE content). The electrodes were then sandwiched between a Celgard® membrane soaked in 6 M KOH.

2.7.2 Fabrication of Membrane Electrode Assembly (MEA) of AEMFC using CoNC-900 and Pt/C

The standard PEMFC protocol was used for fabricating MEA of AEMFC single-cell. Initially, the electrodes were prepared by brush coating the catalyst ink [comprising of CoNC-900 or Pt/C catalyst (Johnson Matthey) + Fumion® binder (10%)] onto the porous carbon paper (35 CC-SGL with 15% PTFE content). The electrodes (CoNC-900 as the cathode and Pt/C as the anode) were then sandwiched between Fumapem (R) AA membrane using Kapton as gasket and cold-pressed by applying 1000 kgN pressure for 2 min. The MEA was then arranged onto the graphite plates using an FRT gasket for single-cell assembly (active area = 4 cm^2, Fuel Cell Technologies, USA).

The single-cell test fixture used for fuel cell polarization study consists of the following components:

- Aluminium end-plates
- Graphite monopolar plates provided with integrated O-ring gasket and serpentine gas flow field
- Cathode loading: 2.0 mg/cm^2; F/C: 0.40; electrode thickness: 325 μm
- Anode loading: 0.80 mg/cm^2; F/C: 0.40; electrode thickness: 320 μm
- Gas flow: 50 sccm and 100 sccm at anode and cathode respectively
- Operating temperature: 50 ^{o}C
- Membrane pellet thickness: 55 μm
- Uncompressed MEA thickness: 700 μm
- Compressed MEA thickness: 538 μm
- Percentage of the compression: 23 %
- Thickness of the gasket used: 190 μm

2.7.3 *In-situ* Impedance Measurement

The *in-situ* impedance measurements were carried out on the Zn-air and AEMFC single-cell using a two-electrode configuration and Autolab electrochemical work station in the frequency range of 1 MHz−100 Hz and an input voltage amplitude of 10 mV. During the measurement, O_2 was passed through the cathode (used as a working electrode) and H_2 was passed through the anode (used as both counter and reference electrode).

2.7.4 Determination of Ionic Conductivity of the Anion Exchange Membrane

The membrane resistance was initially determined using the high-frequency intercept of the Nyquist plots obtained using EIS measurement at the OCV condition. The ionic conductivity of the Fumapem®FAA membrane was then determined using the following relation:

$$\sigma = l / (R \times A)$$

wherein, σ = ionic conductivity (S/cm), l = pellet thickness (cm), R = membrane resistance (Ω) and A = area of the membrane (cm^2).

2.8 Results and Discussion
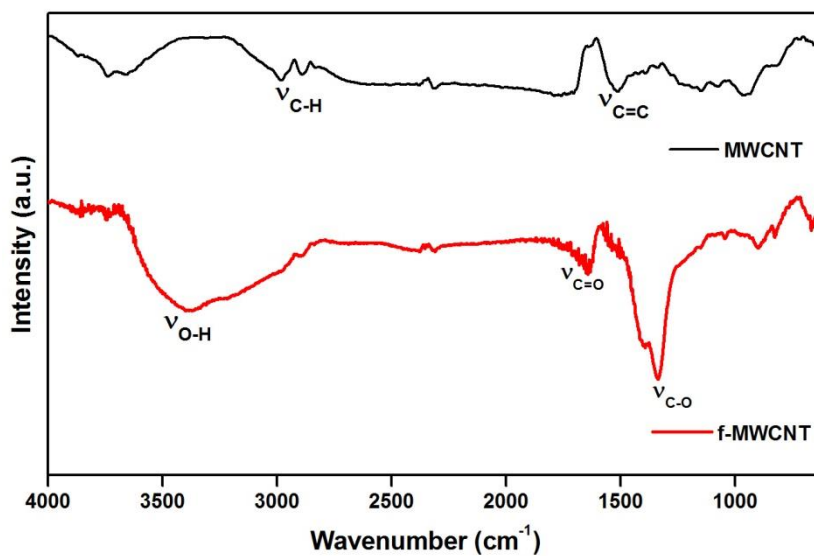
2.8.1 FTIR Analysis

Figure 2.1 Comparative FTIR spectra of pristine and functionalized MWCNT.

The comparative FTIR spectra study indicates the introduction of carboxylic acid functional groups after the functionalization of MWCNT (**Figure 2.1**). The peaks at ~1338, ~1636 and ~3383 cm^{-1} indicate the characteristic signatures of the carboxylic acid functional groups.[29-30]

These groups act as the anchoring sites for the ZIF seeding process during the preparation of the CNT-MOF composite material.

2.8.2 XRD Analysis
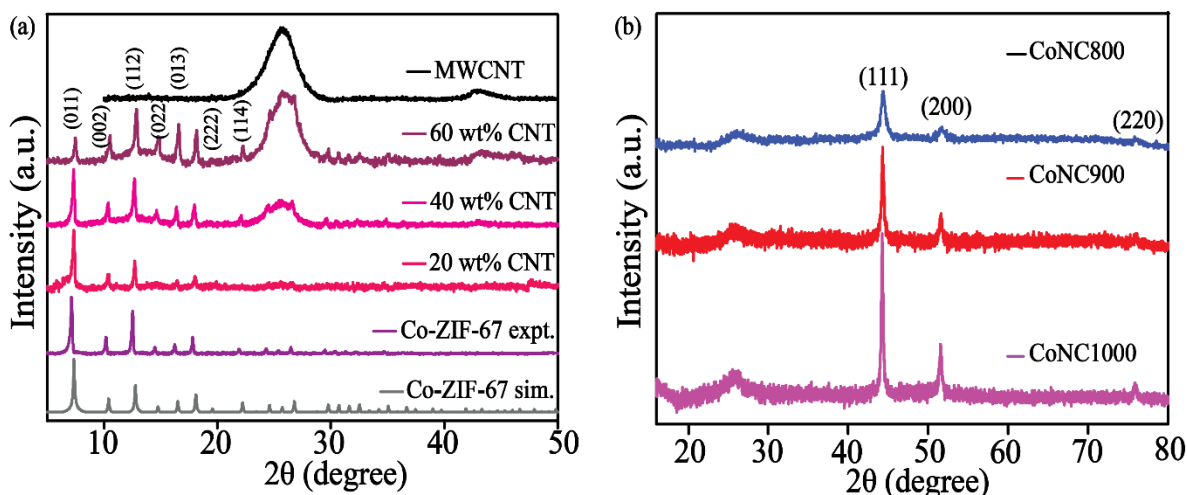
Figure 2.2 Comparative PXRD spectra of MWCNT, ZIF-67, and their composites.

The formation of Co-ZIF-67 on the CNT surface is verified by comparing the powder X-ray diffraction (PXRD) patterns of Co-ZIF-67, MWCNT, and the Co-ZIF-67/CNT composites (**Figure 2.2a**). The presence of the (111) and (200) planes of the cobalt nanoparticles was verified by the PXRD analysis of the pyrolyzed composites (**Figure 2.2b**). The spectra also indicate the presence of the (002) plane of the graphitized carbon species at the 2θ value of 26˚.

2.8.3 SEM and TEM

The amount of CNT was initially varied to determine the amount needed to wholly string the Co-ZIFs besides ensuring uniform nucleation and consistency in the size of the crystals. The Transmission Electron Microscopy (TEM) and Scanning Electron Microscopy (SEM) images of the Co-ZIF-67/CNT composite indicate the formation of uniform Co-ZIF-67 polyhedrons on the functionalized MWCNT surface (**Figure 2.3a, b**). On composite formation, the size of the Co-ZIF-67 polyhedrons is found to decrease from ~1 μm to ~200 nm, possibly due to the increased number of nucleation sites on the functionalized MWCNTs (**Figure 2.3c-e**).
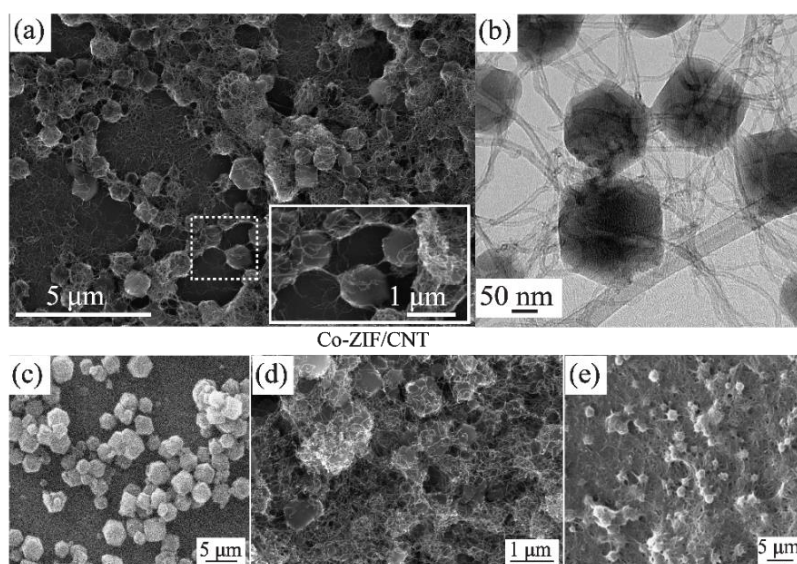
Figure 2.3 (a) SEM and (b) TEM images evidencing the synthesis of CNT stringed Co-ZIF-67 composites; SEM images of (c) ZIF-67 crystals, (d) 10 wt.% CNT loading and (e) 40 wt.% CNT loading.
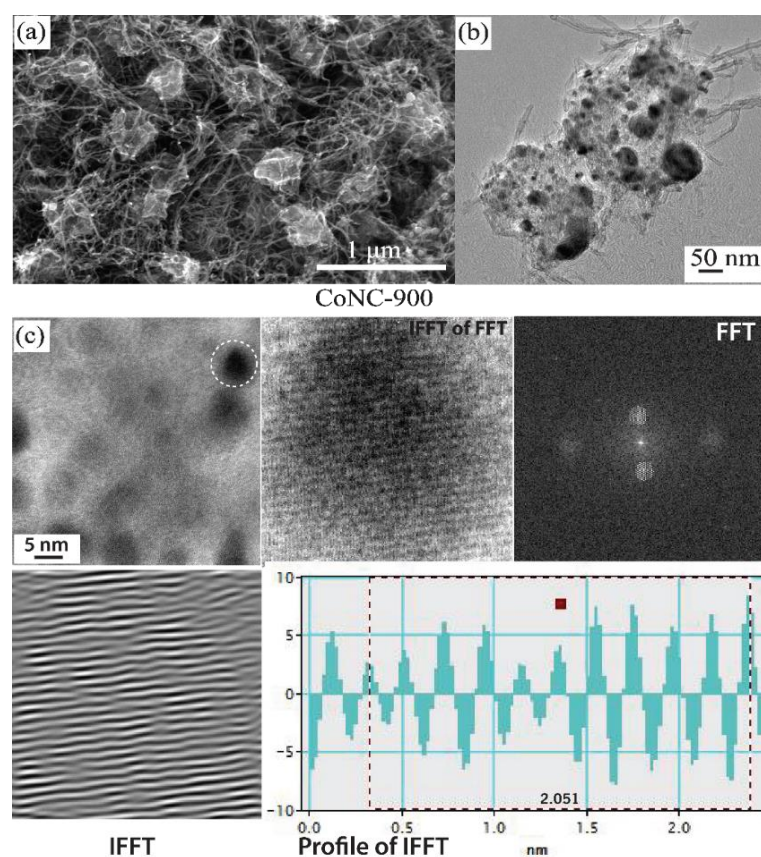
Figure 2.4 (a) SEM image, (b) TEM image indicating the retention of the parent morphology after pyrolysis at 900 °C and (c) Enlarged TEM image and the corresponding FFT and IFFT images of CoNC-900 showing the lattice fringe and d-spacing corresponding to the Co (111) plane.

However, it is also worthy to note that changes in the surface texture and porosity can also be observed following the annealing procedure (**Figure 2.4a, b**). The high-resolution TEM image further specifies the presence of the lattice planes corresponding to the d-spacing value of 0.205 Å, indicating the presence of the Co(111) planes in the pyrolyzed composite (CoNC-900) (**Figure 2.4c**). The Energy Dispersive X-ray Spectroscopy (EDS) mapping of CoNC-900 indicates a homogeneous dispersion of the constituting elements (C, O, N and Co) in the composite pyrolyzed at 900 $^{\circ}$C (**Figure 2.5**). During the pyrolysis in the inert atmosphere, Co-ZIF-67 undergoes self-sacrificial decomposition resulting in the formation of cobalt nanoparticle embedded porous carbon. The retention in the morphology of the parent Co-ZIF-67/CNT composite can be largely substantiated from the SEM study of the pyrolyzed samples.

| CoNC900 | C | O | N | Co |
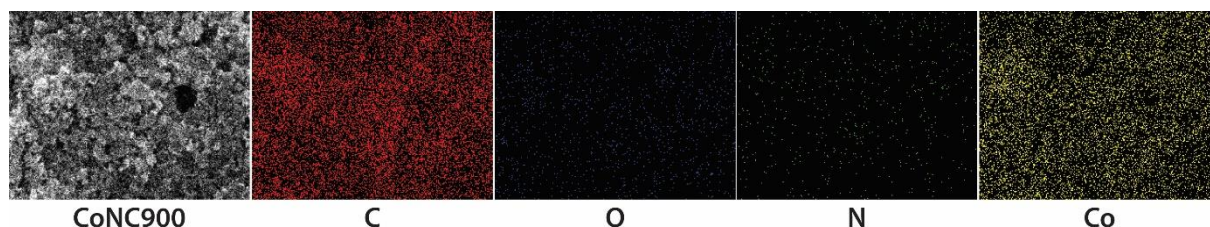
Figure 2.5. Elemental mapping images of CoNC-900 indicating the presence of Co and N in the carbon matrix.

2.8.4 TGA Analysis

The Thermogravimetric Analysis (TGA) of the samples carried out at inert atmosphere indicates that the optimized Co-ZIF-67/CNT composite contains~ 20 wt. % of MWCNTs (**Figure 2.6**). The as-obtained Co-ZIF-67/CNT (containing 20 wt. % MWCNTs) is then pyrolyzed at different temperatures (800-1000 $^{\circ}$C) in the O_2 atmosphere for 3 h each (Yield~ 60-70%).
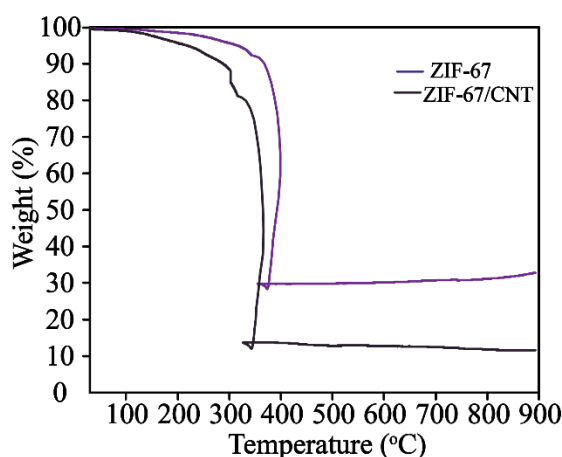
Figure 2.6 TGA plots of ZIF-67 and ZIF-67/CNT composite in O_2 atmosphere.

2.8.5 BET Surface Area Analysis
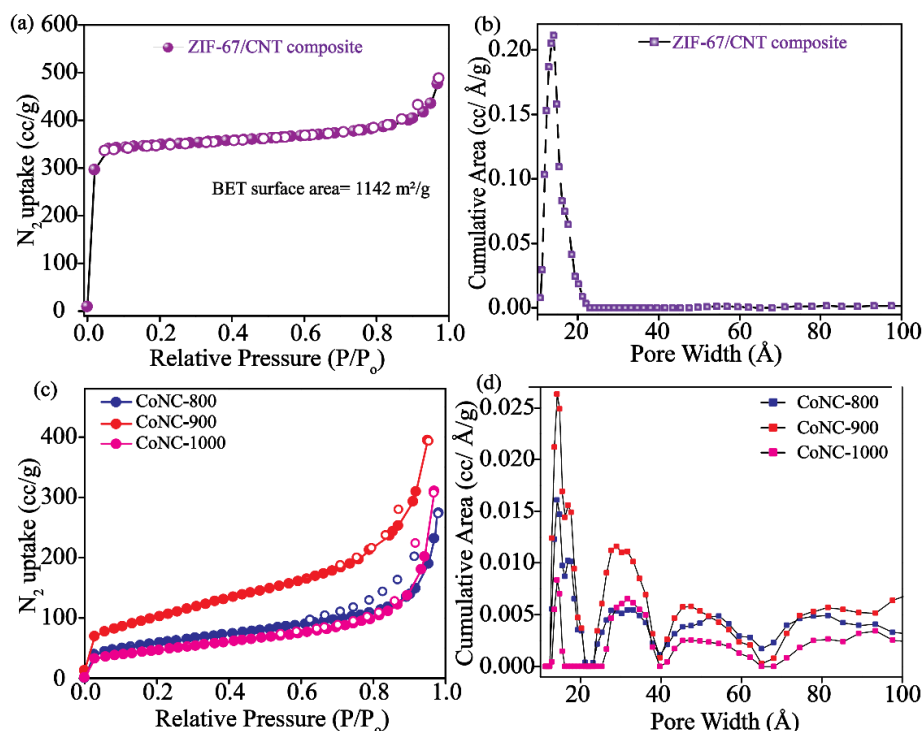
Figure 2.7 (a) N_2 adsorption isotherm and (b) pore size distribution plot of ZIF-67/CNT composite; (c) combined N_2 adsorption isotherms of the pyrolyzed Co-ZIF-67/CNT composites and (d) combined pore size distribution plots of the pyrolyzed samples.

The N_2 adsorption study of the Co-ZIF-67/CNT composite (containing 20 wt. % of MWCNT) indicates a Brunauer, Emmett and Teller (BET) surface area of 1140 m^2 g^{-1}. The pore size distribution study indicates the presence of substantial microporosity in the composite (**Figure 2.7a, b**). Interestingly, on pyrolysis, the surface area of the composite is found to decrease to 210 m^2 g^{-1} (CoNC-800), 364 m^2 g^{-1} (CoNC- 900) and 168 m^2 g^{-1} (CoNC-1000) respectively (**Figure 2.7c**). This is believed to be a consequence of the change in the pore structure (evolution of mesopores) during the strenuous pyrolysis condition (**Figure 2.7d**).[18] The increase in the adsorptive capacity from CoNC-800 to CoNC- 900 is believed to be an effect of the improved thermal activation.[19] However, the reduction in the specific surface area of CoNC-1000 is a detrimental effect of the pore shrinkage (as evident from the pore size distribution plot (**Figure 2.7d**)), which is possibly enforced by the thermal breakdown of the pores at 1000 ºC.

2.8.6 XPS Analysis
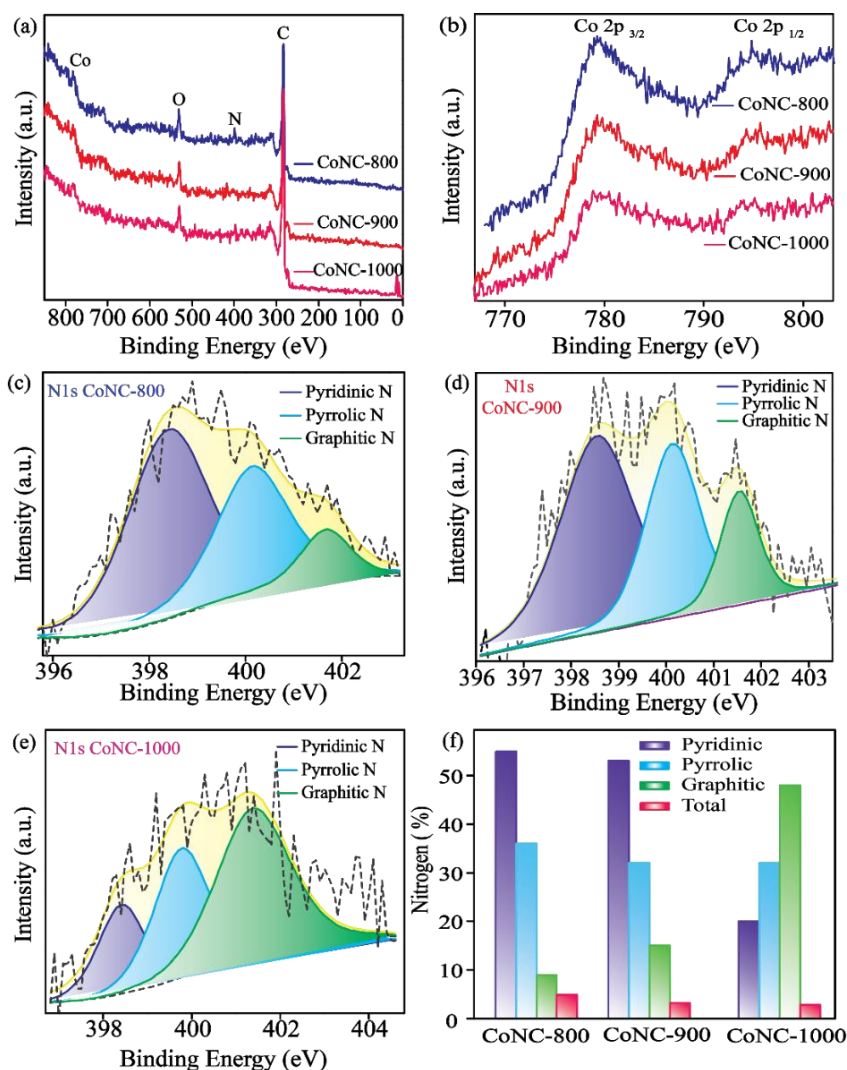
Figure 2.8 (a) Compiled Survey Spectra; (b) combined Co2p spectra of the composites pyrolyzed at different temperatures; (c) deconvoluted N1s XPS spectra of CoNC-800; (d) N 1s spectra of CoNC-900 indicating the nature of the N functionalities; (e) CoNC-1000 indicating the nature of N functionalities present in the system; and (f) estimated amount of different types of nitrogen functionalities in the pyrolyzed samples.

The surface sensitive X-ray Photoelectron Spectroscopy (XPS) survey spectra confirm the presence of Co, N, O, and C in the final pyrolyzed composites (**Figure 2.8a**). The Co 2p XPS spectrum specifies the existence of cobalt moieties in the pyrolyzed samples. The XPS analysis of CoNC-900 indicates the existence of metallic Co (at 778.0 eV) along with the presence of CoN$_x$ (at 780.4 eV) moieties in the pyrolyzed samples (**Figure 2.8b**).[23] The N1s spectral study indicates the presence of pyridinic (at 398.5 eV), pyrrolic (at 400.1 eV) and graphitic (at 401.5 eV) forms of nitrogen in the pyrolyzed composites (**Figure 2.8c-e**).[20, 21, 22] A notable increase

in the pyridinic N from CoNC-800 to CoNC-900, and the gradual decrease in the amount of graphitic N with an increase in the pyrolysis temperature is observed in **Figure 2.8f**.

2.8.7 Four Probe Conductivity Study

In order to determine the influence of the presence of CNT, the electrical conductivity of the carbons derived from Co-ZIF-67 (named carbonized Co-ZIF-67) and Co-ZIF-67/CNT composite (CoNC-900) was analyzed using the four-probe conductivity study. On the introduction of highly conductive MWCNTs, a remarkable 16-fold increase in the electrical conductivity of the pyrolyzed composites is observed (**Figure 2.9**). This study thereby ascertains the need for stringing the ZIFs on the CNT before pyrolysis.
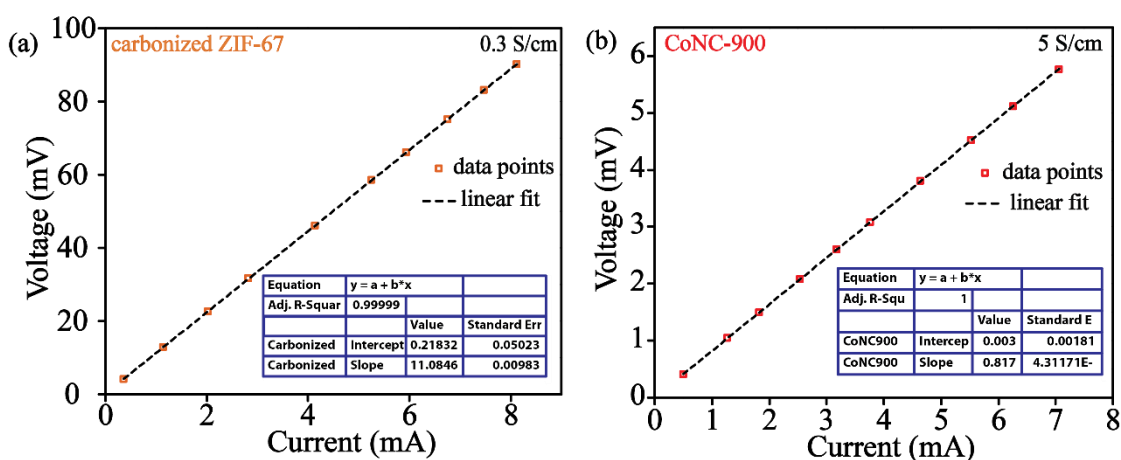
Figure 2.9 I-V profiles of the carbonized (a) ZIF-67 (without CNT) and (b) ZIF-67/CNT composite.

2.8.8 Electrochemical Analysis

In order to test the electrocatalytic activities of the pyrolyzed Co-ZIF-67/CNT composites, the Rotating Disk Electrode (RDE) and Rotating Ring Disk Electrode (RRDE) studies were conducted in 0.1 M KOH solution. The electrode potentials are quoted with respect to that of the Reversible Hydrogen Electrode (RHE) in this study. In the O_2-saturated electrolyte, the Linear Sweep Voltammograms (LSVs) of the pyrolyzed samples indicate the presence of a well-defined cathodic peak, corresponding to the reduction of the dissolved molecular oxygen species in the electrolyte. The combined LSVs of all the pyrolyzed samples with respect to the commercial 40 wt. % Pt/C catalyst, recorded at an electrode rotation rate of 1600 rpm, are shown in **Figure 2.10a**. Among all, CoNC-900 (onset, 0.94 V *vs*. RHE) is found to show an ORR activity relatively closer to that of the commercial 40 wt. % Pt/C, with a half-wave potential difference of just 30 mV (**Table 2.1**). In addition, the plot derived from the Rotating Ring Disk Electrode (RRDE) studies also indicates that the composite pyrolyzed at 900 °C follows the desired direct four-electron pathway (**Figure 2.10b**). The studies also conclude that

among all the pyrolyzed samples, CoNC-900 comparatively yields lesser H_2O_2 while catalyzing ORR (**Figure 2.10c**). In order to get a better estimate of the reaction kinetics, the Tafel plot analyses are carried out. The study indicates that, of all, CoNC-900 shows much smaller Tafel slope value (61 mV/decade), even smaller than that of Pt/C (79 mV/decade) (**Figure 2.10d**).

Table 2.1 Comparison survey of the performance of the pyrolyzed electrocatalysts reported in the present work in 0.1 M KOH.

Sample	Onset Potential (in V)	Half-wave potential (in V)	Tafel slope (in mV/decade)
Carbonized ZIF-67	0.80	0.61	123
CoNC-800	0.88	0.75	68
CoNC-900	0.94	0.81	61
CoNC-1000	0.91	0.78	66
40 wt.% Pt/C	1.00	0.84	79
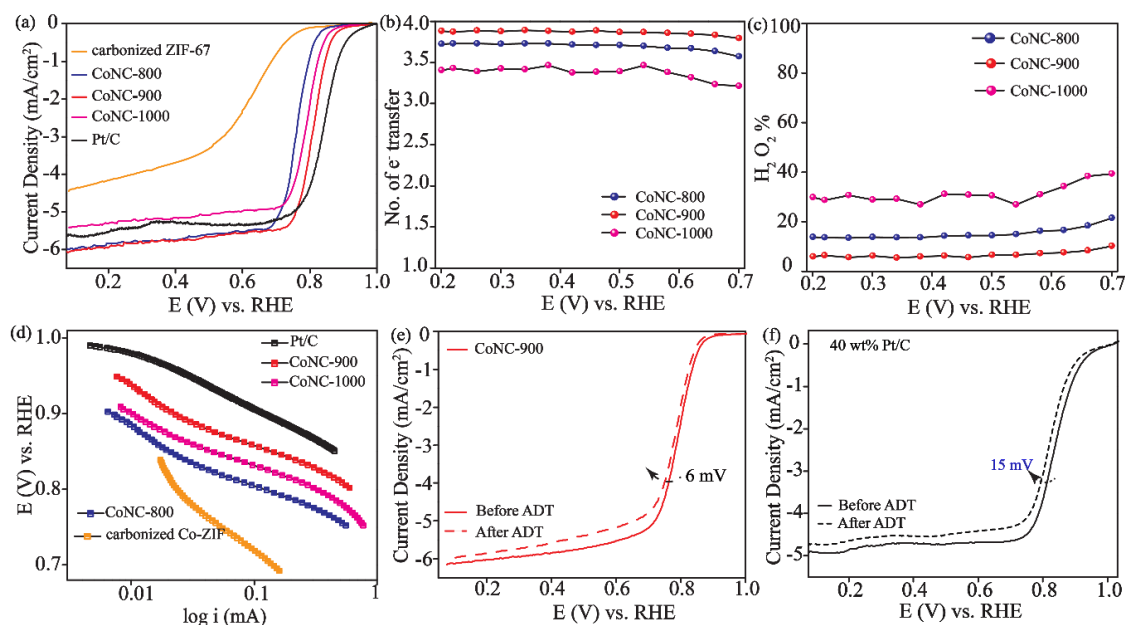
Figure 2.10. (a) LSV plots of the pyrolyzed Co-ZIF-67/CNT composite at different temperatures in 0.1 M KOH solution; (b) number of electrons transfer involved in ORR; (c) RRDE derived plots indicating the comparative amount of H_2O_2 produced in cases of Co-ZIF-67/CNT composite pyrolyzed at different temperatures; (d) combined Tafel plots; (e) LSV plots of CoNC-900 before and after the Accelerated Durability Test (ADT); (f) LSVs of 40 wt.% Pt/C before and after ADT.

The electrocatalytic stability of CoNC-900 was tested *via* Accelerated Durability Test (ADT) carried out by potential scanning over 0.40 V potential window at 100 mV/s scan rate between -0.30 to 0.10 V (*vs.* Hg/HgO) in O_2-saturated 0.1M KOH for 5000 cycles. The tests indicate that CoNC-900 shows excellent catalytic stability even after 5000 cycles of scanning over 0.40 V potential window at 100 mV/s scan rate. The small negative shift of just 6 mV (compared to 15 mV of Pt/C, **Figure 2.10e and 2.10f**) at the end of ADT reveals the superior support stability of the CNTs over that of the Vulcan carbon support in Pt/C. The stand out performance of CoNC-900 could be observed to be a beneficial effect of its high surface area (which is expected to assist facile mass diffusion and ready access to the active sites) and the superior support stability provided by the CNTs.[24] It could also be a contributing effect of the presence of CNT in the backbone, which is known to be a better electron conductor and corrosion resistor than the Vulcan® XC-72 carbon support used in the commercial Pt/C.[25] The superior activity could also be ascribed to comparatively large proportions of the pyridinic and graphitic forms of N functionalities in CoNC-900, which are supposedly responsible for the intrinsic ORR activity in N-doped carbons.[26] Further, in order to ascertain the exact role of the Co nanoparticles on the catalytic activity, CoNC-900 was acid washed to remove the metal nanoparticles (**details in Section 2.6**).

Equation	y = a + b*x	
Weight	No Weighting	
Residual Sum of Squares	0.00852	
Pearson's r	0.99999	
Adj. R-Square	0.99997	
	Value	Standard Err
B Interce	0.0146	0.0281
Slope	2.5668	0.00508
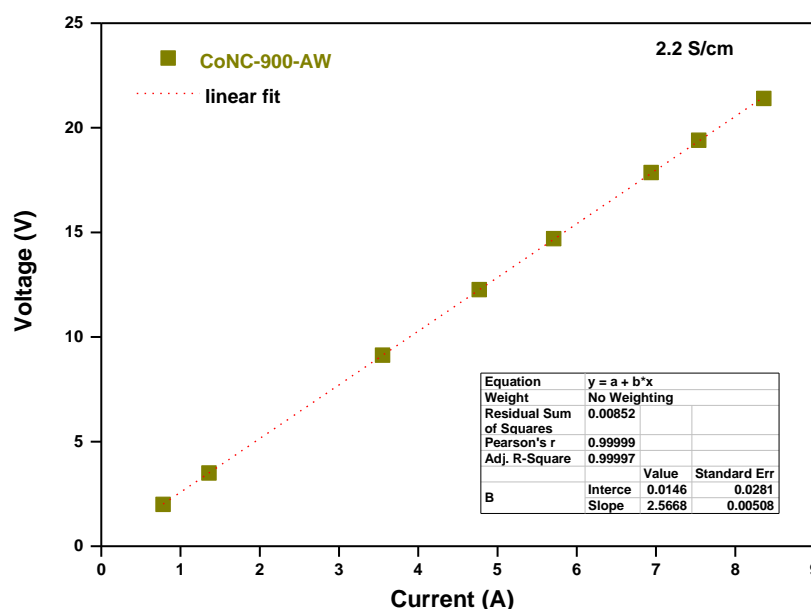
Figure 2.11. I-V profile of CoNC-900-AW.

The four-probe electrical conductivity of the sample obtained after the acid wash (CoNC-900-AW) is found to be decreased from 5 to 2.2 S cm^{-1}, **Figure 2.11**. Interestingly, the PXRD and the XPS spectra have confirmed the retention of the CoN_x moieties (at 780.4 eV) in the acid-washed CoNC-900-AW (**Figure 2.12a, b**). The acid-washed sample shows a decrease in

the BET surface area from 364 to 295 m^2 g^{-1}, (**Figure 2.12c**). But, the ORR activity of the acid-washed samples indicates a decrease in the limiting current with the onset potential remaining largely unchanged (**Figure 2.12d**). This hints at the retention of the ORR active sites despite the rigorous chemical treatment procedure. Also, from these results, it can be presumed that the Co-N_x species are the main ORR active sites in the composite, while the Co moieties help in preserving the structural integrity of the electrocatalyst besides contributing to the conductivity of the material.
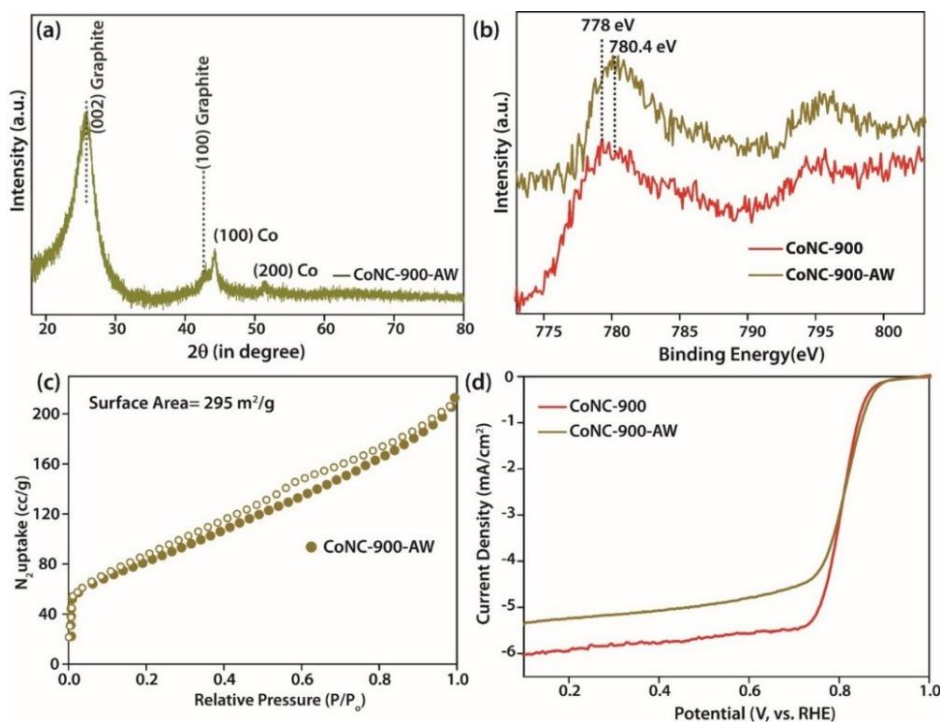
Figure 2.12 (a) PXRD pattern; (b) comparative Co 2p XPS spectra; (c) N_2 adsorption isotherm; (d) comparative LSV plots of CoNC-900 before and after the acid wash treatment.

The high positive ORR onset, high surface area and high electrical conductivity of CoNC-900 instigated the testing of its practical utility as electrocatalysts for ZAB and AEMFC systems. The ZAB cell was fabricated and tested in a home-built electrochemical cell using Zn dust as the anode and CoNC-900 coated carbon paper as the cathode. Initially, the cathode was prepared by brush coating the catalyst ink (loading of 2.0 mg cm^{-2}; comprising of CoNC-900 and Fumion® binder (20%)) onto the porous carbon paper (35 CC-SGL with 15% PTFE content). The electrodes were then sandwiched between the Celgard® membrane soaked in 6 M KOH. Similarly, another MEA constituting of 40 wt. % Pt/C coated GDL (as the cathode) and Zn dust (as the anode) was also fabricated for comparison. On using CoNC-900 as a cathode material, the fabricated primary Zn-air battery system is observed to show an OCV of 1.47 V

(as against 1.52 V of the Pt/C based cell) (**Figure 2.13a**). The single-cell study indicates a peak power density of 296 mW cm^{-2} (*vs.* 317 mW cm^{-2} of the Pt/C system) and maximum current density of 612 mA cm^{-2} (*vs.* 650 mW cm^{-2} of the Pt/C system). The metric performance of the CoNC-900 based system is very close to that of the benchmark Pt/C catalyst-based system and in effect, comparable to the *state of the art* non-Pt catalyst based systems reported till date. The galvanostatic discharge profile at 50 mA cm^{-2} shows a stable flat rate of discharge, with the working voltage stabilized at 1.1 V, thereafter indicating negligible decay in the performance up to ~2 h of operation (**Figure 2.13b**). This further ascertains the consistency in the catalytic activity and integral stability of the fabricated assembly during the course of prolonged operation. This could be mainly attributed to the porous structure of CoNC-900, which assists facile diffusion of the reactant O$_2$ molecules and OH$^-$ ions from the active sites.
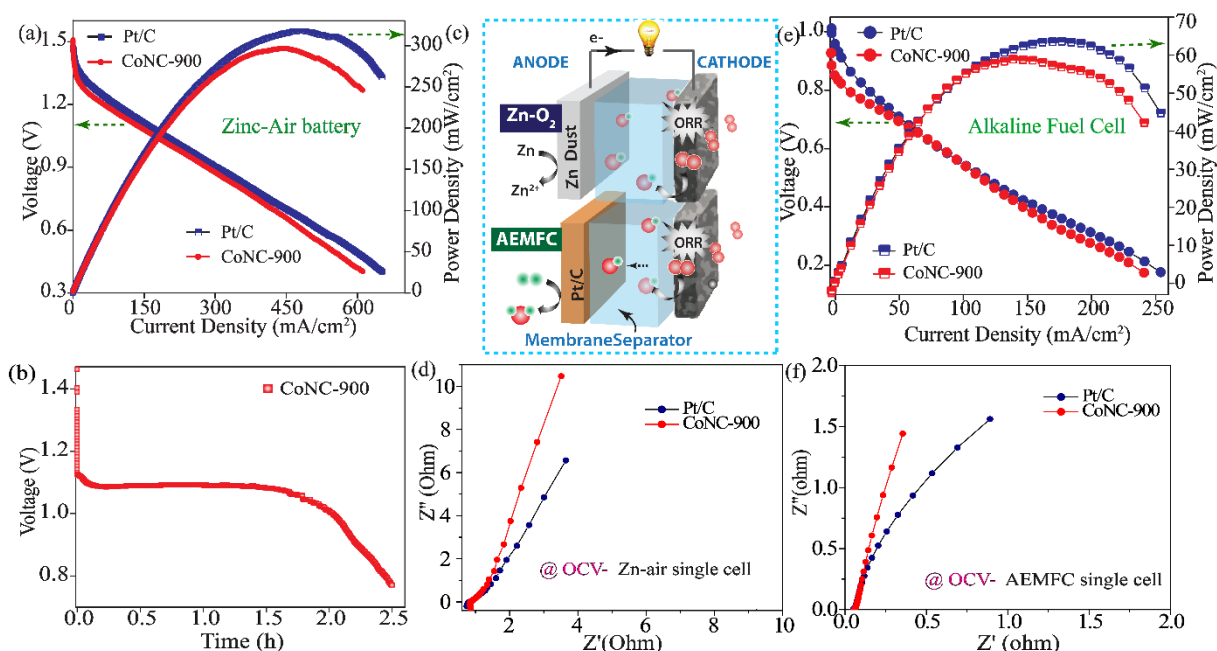
Figure 2.13 (a) Comparative polarization plots of the Zn-air battery systems fabricated using CoNC-900 and Pt/C as the air-cathode electrocatalysts; (b) time dependent galvanostatic discharge curve of the Zn-air battery fabricated using CoNC-900 as the air catalyst at 50 mA cm^{-2}; (c) schematic representation of the Zn-air/AEMFC single cell assemblies fabricated using CoNC-900 as cathode electrocatalyst; (d) EIS spectra of the Zn-air single cells based on CoNC-900 and Pt/C as the cathode electrocatalysts; (e) steady-state polarization plots of the AEMFC fabricated using CoNC-900 and Pt/C as the cathode electrocatalysts recorded at 50 °C; (f) EIS spectra of the AEMFC single cell assemblies based on CoNC-900 and Pt/C as the cathode electrocatalysts recorded at OCV.

Furthermore, CoNC-900 was used as the cathode electrocatalyst to fabricate the Membrane Electrode Assembly (MEA) of an Anion Exchange Membrane Fuel Cell (AEMFC). The standard PEMFC protocol was used for fabricating MEA of the AEMFC single cell. Initially, the electrodes were prepared by brush coating the catalyst ink (comprising of CoNC-900 or 40 wt. % Pt/C catalyst (Johnson Matthey®) and Fumion® binder (10%)) onto the porous carbon paper (35 CC-SGL with 15% PTFE content). The electrodes (CoNC-900 as the cathode and Pt/C as the anode) were then sandwiched between the Fumapem® AA membrane using Kapton as the gasket and cold-pressed by applying 1000 kgN pressure for 2 min. The MEA was then arranged onto the graphite plates using FRT gasket for single-cell assembly (active area = 4 cm^2, Fuel Cell Technologies, USA). Likewise, another MEA constituted entirely of 40 wt. % Pt/C coated GDL (as both anode and cathode) was also fabricated for comparison. The MEA comprising of CoNC-900 as the cathode is found to show an OCV of 0.92 V (as against 1.01 V of the Pt/C based cell) (**Figure 2.13e**). The steady-state polarization plot of the MEA constituting the CoNC-900 cathode shows characteristics very similar to that of the MEA based on the standard Pt/C electrocatalyst. At 0.60 V, the CoNC-900 system is found to display a current density of 80 mA cm^{-2}, which is comparable to that of the cell based on Pt/C (80 mA cm^{-2}). Most importantly, the in-house system is found to deliver a maximum of 60 mW cm^{-2} power density (against 64 mW cm^{-2} of the Pt/C system). Interestingly, although the MEA constituting CoNC-900 shows a larger initial activation loss, the activity resurrects to compete with the system based on standard Pt/C in the ohmic region. This behaviour is presumably a beneficial effect of the presence of CNTs in CoNC-900, whose highly conducting nature possibly resurrects the activity of CoNC-900 in the ohmic polarization region (as verified from the four-probe conductivity studies, **Figure 2.9b**). It is important to note that unlike the PEMFC systems, the performance of an AEMFC is largely restricted by the OH- conductivity of the separating membrane. [27] In the present study, *in-situ* impedance measurements were carried out to determine the ion conductivity of the anion exchange membrane in the frequency range of 1 MHz-100 Hz and an input voltage amplitude of 10 mV. The high-frequency intercept of the Nyquist plots indicates an OH- conductivity of 2.5×10^{-2} S cm^{-1}, which is an order lesser than that of the Nafion® based systems (**Figure 2.13f**).[28] Overall, from the above observations, it could be observed that the single-cell performance of the as-synthesized CoNC-900 system is found to perform better than most of the non-Pt based AEMFC cathode systems reported till date.

2.9 Conclusions

Overall, the present work proposes a proficient way to synthesize less expensive MOF derived electrocatalysts possessing the critical requisites of an ideal electrode material *viz.*, high porosity, and high conductivity besides high intrinsic electrochemical activity. Herein, the Co-based ZIF acts as a non-precious 'self-sacrificial' template for deriving Co-embedded highly porous carbon while the MWCNT is found to largely impart high electrical conductivity and corrosion resistance to the catalyst system. Most convincingly, the CoNC-900 electrocatalyst is found to consistently perform in par with that of the standard Pt/C electrocatalyst when implemented in both Zn air battery and AEMFC systems. This study thereby underscores a simple route to derive a highly porous and conducting nonprecious ORR electrocatalyst, which could be foreseen as a potential candidate for fabricating other energy devices like Li-air, Al-air battery systems etc.

2.10 Reference

[1]. Y. Li and H. Dai, Chem. *Soc. Rev.* **2014**, 43, 5257- 5275.

[2]. Z.-L. Wang, D. Xu, J.-J. Xu and X.-B. Zhang, *Chem. Soc. Rev*. **2014**, 43, 7746 - 86.

[3]. S.-E. Jang and H. Kim, J. *Am. Chem. Soc*. **2010**, 132, 14700 - 14701.

[4]. J. Wu and H. Yang, *Acc. Chem. Res*. **2013**, 46, 1848 -1857.

[5]. Y. Bing, H. Liu, L. Zhang, D. Ghosh and J. Zhang, *Chem. Soc. Rev*. **2010**, 39, 2184 - 202.

[6]. M. Lefèvre, E. Proietti, F. Jaouen, J.-P. Dodelet, Science, **2009**, 324, 71-74.

[7]. R. Bashyam and P. Zelenay, Nature. **2006**, 443, 63-66.

[8]. C. Zhu, H. Li, S. Fu, D. Du and Y. Lin, *Chem. Soc. Rev*. **2016**,45, 517-535.

[9]. M. Zhou, H.-L. Wang and S. Guo, *Chem. Soc. Rev*. **2016**, 45, 1273 -307.

[10]. J. Zhang and L. Dai, ACS *Catal*. **2015**, 5, 7244 -7253.

[11]. S. Yang, L. Zhi, K. Tang, X. Feng, J. Maier and K. Müllen, *Adv. Funct. Mater.* **2012**, 22, 3634 -3640.

[12]. T.-Y. Ma, L. Liu and Z.-Y. Yuan, *Chem. Soc. Rev*. **2013**, 42, 3977-4003.

[13]. S. Pandiaraj, H. B. Aiyappa, R. Banerjee and S. Kurungot, *Chem Commun*. **2014**, 50, 3363 - 3366.

[14]. H. B. Aiyappa, P. Pachfule, R. Banerjee and S. Kurungot, *Cryst. Growth Des*. **2013**, 13, 4195 -4199.

[15]. S. Gadipelli, T. Zhao, S. A. Shevlin and Z. Guo, *Energy Environ. Sci*. **2016**, 9, 1661 - 1667.

[16]. J.-C.Li, S.-Y. Zhao, P.-X. Hou, R. -P. Fang, C. Liu, J. Liang, J. Luan, X.- Y.Shan and H.-M. Cheng, *Nanoscale*, **2015**, 7, 19201 -19206.

[17]. J. Liang, X. Du, C. Gibson, X. W. Du, and S. Z. Qiao, *Adv. Mater*. **2013**, 25, 6226 -6231.

[18]. G. Wu, C. M. Johnston, N. H. Mack, K. Artyushkova, M. Ferrandon, M.Nelson, J. S. Lezama-Pacheco, S. D. Conradson, K. L. More, D. J. Myersd and P. Zelenay, *J. Mater. Chem*. **2011**, 21, 11392 -11405.

[19]. X.Wang, J. S. Lee, C. Tsouris, D. W. DePaoli and S. Dai, *J. Mater. Chem,* **2010**, 20, 4602 -4608.

[20]. R. L. Liu, D. Q. Wu, X. L. Feng, K. Müllen, *Angew Chem. Int. Ed*. **2010**, 49, 2565 -2569.

[21]. Y. Wang, Y. Y. Shao, D. W. Matson, J. H. Li, Y. H. Lin, *ACS Nano*. **2010**, 4,1790 -1798.

[22]. S. Yang, L. Zhi, K. Tang, X. Feng, J. Maier, and K. Müllen, *Adv. Funct. Mater.* **2012**, 22, 3634 -6340.

[23]. Y. Hou , Z. Wen, S. Cui , S. Ci , S. Mao , and J. Chen, Adv. Funct. Mater. 2015, 25, 872 –882.

[24]. L. Shang, H. Yu, X. Huang, T. Bian, R. Shi, Y. Zhao, G. I. N. Waterhouse, L.-Z. Wu, C.-H. Tung, and T. Zhang, *Adv. Mater*. **2016**, 28, 1668 -1674.

[25]. K. Gong, F. Du, Z. Xia, M. Durstock and L. Dai, *Science*, **2009**, 323, 760 -764.

[26]. S. M. Unni, S. N. Bhange, R.Illathvalappil, N. Mutneja, K.R.Patil, and S.Kurungot, *small*, **2015**, 11,352 -360.

[27]. T. Palaniselvam, V. Kashyap, S. N. Bhange, J.-B. Baek, and S. Kurungot, *Adv. Funct. Mater*. **2016**, 26, 2150 -2162.

[28]. K. A. Mauritz and R. B. Moore, *Chem. Rev*. **2004**,104, 4535 -4586.

[29]. P. Molla-Abbasi, R. Ghaffarian, E. Danesh, *Smart Mater. Struct.* **2011,** 20, 105012.

[30]. I. Ovsiienko, T. Len, L. Matzui, V. Tkachuk, I. Berkutov, I. Mirzoiev, Y. Prylutskyy, N. Tsierkezos, U. Ritter, *Mat.-wiss. U. Werkstofftech.* **2016,** 47, 2-3.

[31]. R. Illathvalappil, V. M. Dhavale, S. N. Bhange and S. Kurungot, *Nanoscale*, **2017**, 9, 9009-9017.

Chapter-3

Nitrogen and sulphur co-doped Crumbled Graphene for the Oxygen Reduction Reaction with Improved Activity and Stability in Acidic Medium

Non-precious oxygen reduction electrocatalysts have attracted great attention nowadays for the development of stable, cost-effective proton exchange membrane fuel cells (PEMFCs). In line with this requirement, this chapter deals with the synthesis of a Pt-free oxygen reduction electrocatalyst based on nitrogen and sulphur co-doped crumbled graphene with trace amounts of iron. The co-doped crumbled graphene structure was obtained by simple oxidative polymerization of ethylenedioxythiophene in aqueous solution followed by an annealing process under inert atmosphere. This new electrocatalyst displays improved oxygen reduction activity and electrochemical stability under acidic conditions. The half-cell reaction of the 1000 °C annealed system (PF-1000) displays only 0.10 V overpotential in both the onset and half-wave potentials compared to state-of-the-art Pt/C in an acidic environment for ORR. More importantly, the limiting current of PF-1000 clearly

surpasses the limiting current displayed by Pt/C. This indicates that the crumbled assembly of the graphene flakes helps the system to expose the active sites and the porous network of the material matrix ensures extended accessibility of active sites to the electrolyte and reagent. The oxygen reduction kinetics of PF-1000 is found to follow a mechanistic pathway which is similar to that of Pt/C and the system accomplishes the reduction of the dioxygen molecule through the recommended 4-electron reduction pathway. The improved activity and electrochemical stability of PF-1000 are mainly attributed to the enriched and well accessible active reaction centres such as graphitic nitrogen, sulphur, and iron coordination and the peculiar morphology of the system. Further, a single cell evaluation of a membrane electrode assembly (MEA) based on PF-1000 as the cathode catalyst delivered a maximum power density of 193 mW cm^{-2} at a cell temperature of 60 °C using Nafion as the proton-conducting membrane.
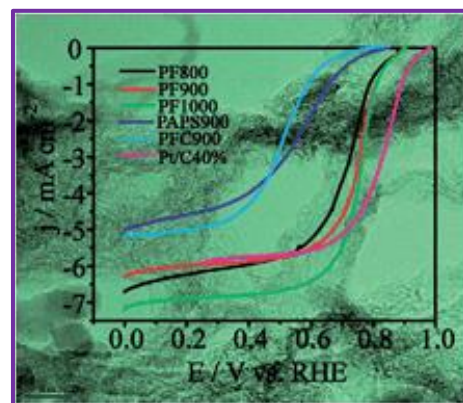
Content of this chapter is published in: **J. Mater. Chem. A, 2016, 4, 6014**. * *Reproduced with permission from Royal Society of Chemistry, Copyright 2016n (J. Mater. Chem. A, 2016, **4**, 6014).*

3.1 Introduction

Development of non-precious metal-based electrocatalysts with comparable oxygen reduction reaction (ORR) activity to that of the state-of-the-art platinum (Pt) systems is an emerging area of research for the development of cost-effective polymer electrolyte membrane fuel cells (PEMFCs).[1,2] In particular, the ability of a system to perform in a wide range of electrolyte pH has been considered as an important advantage as PEMFCs can be operated by using proton and anion exchange membranes.[3,4] Chemically modified carbon allotropes, especially heteroatom (mainly nitrogen) doped graphene nanosheets, proved to be better choices as efficient ORR electrocatalysts at the PEMFC cathode.[5-8] Among the different synthesis routes available for the preparation of nitrogen-doped graphene (NGr), high-temperature annealing of a mixture of graphene oxide (GO) and a suitable nitrogen source is usually employed for the bulk synthesis.[5,6,9-12] Such nanosheets usually display low surface area with limited reactive edges due to the restacking of the graphene sheets.[13] To allow for efficient adsorption and reduction of the dioxygen molecules, the active reaction centres of the carbon-based electrocatalysts require the reactive edges exposed on the surface of the carbon.[14-18] The approaches, such as employing hard and soft templates to impart porosity to the graphene sheet (to improve the reactive edges), gravely affect its electrical conductivity, which in turn reduces the ORR activity.[19]

The ability of graphene sheets to accomplish morphological re-arrangements can be taken as an effective strategy for creating more exposed and active surface reaction centres by enhancing the reactive edges as well as the surface area.[2,20] Many morphological re-arrangements of graphene sheets, such as three-dimensional arrangements, loosely bound tubular arrangements, etc. have resulted in improved ORR activity.[2,8,21,22] However, the ORR activity of such graphene sheets is constrained to alkaline conditions and the reports on their acidic variants are relatively scarce.[2,23-25] This suggests that, along with the morphological re-arrangement, the density of the active sites on the graphene sheets plays a crucial role in determining the ORR activity by improving the adsorption and reduction of the dioxygen molecules irrespective of the pH of the electrolytes. However, in the case of single atom doping, such as nitrogen doping, there exists an optimum level of doping. An amount beyond this threshold level can bring in other issues which can mask the ORR performance.[26,27] There are some recent studies which reveal that when the atomic percentage of nitrogen doping exceeds an optimum level, the capacitive nature of the material increases.[28] This indicates that the preferred nitrogen coordination in carbon morphologies is more important compared to the total

nitrogen atom percentage in order to improve the active reaction site density and, thereby, the ORR activity.

Considering benefits from synergistic interactions and stabilization effects, dual doping has been recently considered as an appropriate strategy for improving active reaction centres.[2,5,6,29] However, accomplishing both structural modification and dual doping of graphene sheets concomitantly is practically difficult and it can only be achieved through an *in situ* process using a single precursor.[30] Herein, a simple strategy is disclosed for the synthesis of N and S doped crumbled graphene sheets from a single precursor, polyethylenedioxythiophene (PEDOT), for facilitating ORR under acidic conditions (**Scheme 3.1**).

3.2 Experimental

3.2.1 Materials

Ethylenedioxythiophene (EDOT), cetyl triethylammonium bromide (CTAB), iron chloride hexahydrate, and ammonium persulfate were purchased from Sigma Aldrich. HCl and H_2SO_4 were purchased from Thomas Baker, India. All the chemicals were used as received without any further purification.

3.2.2 Synthesis of PEDOT-Fe

2 ml of EDOT monomer was dissolved in 80 ml of 1 M HCl solution using 1 g of CTAB as the surfactant at room temperature. 5 g of ammonium persulfate in 20 ml of 1 M HCl was added drop by drop to the EDOT solution for the polymerization of EDOT. It was followed by the addition of 9.1 g of iron chloride hexahydrate solution into 20 ml of 1 M HCl solution. This mixture was kept for a period of 24 h with constant stirring. The suspension containing the polymer and transition metal salt was dried at 80 °C with stirring. This product is termed as PEDOT-Fe. PEDOT-Fe was annealed for 1 h (at 800, 900, and 1000 °C) in an argon atmosphere for carbonization. The resulting black coloured powder was dispersed in 0.5 M H_2SO_4 and stirred at 80 °C for 8 h. The acid-washed sample was further annealed for 1 h in an argon atmosphere to get the final product. The products named as PF-800, PF-900, and PF-1000 represent the annealed PEDOT-Fe at 800, 900 and 1000 °C, respectively. Similarly, for comparison purpose, two more control samples were prepared. (1) The EDOT monomer was polymerized using ammonium persulfate without the addition of iron chloride; the resulting polymer was annealed at 900 °C and 1000 °C in an argon atmosphere for 1 h and the samples are named as PAPS-900 and PAPS-1000, respectively. (2) The EDOT monomer was polymerized using iron chloride without the addition of ammonium persulfate; the resulting

polymer was annealed at 900 ºC and 1000 ºC in an argon atmosphere for 1 h and the samples are named as PFC-900 and PFC-1000, respectively.
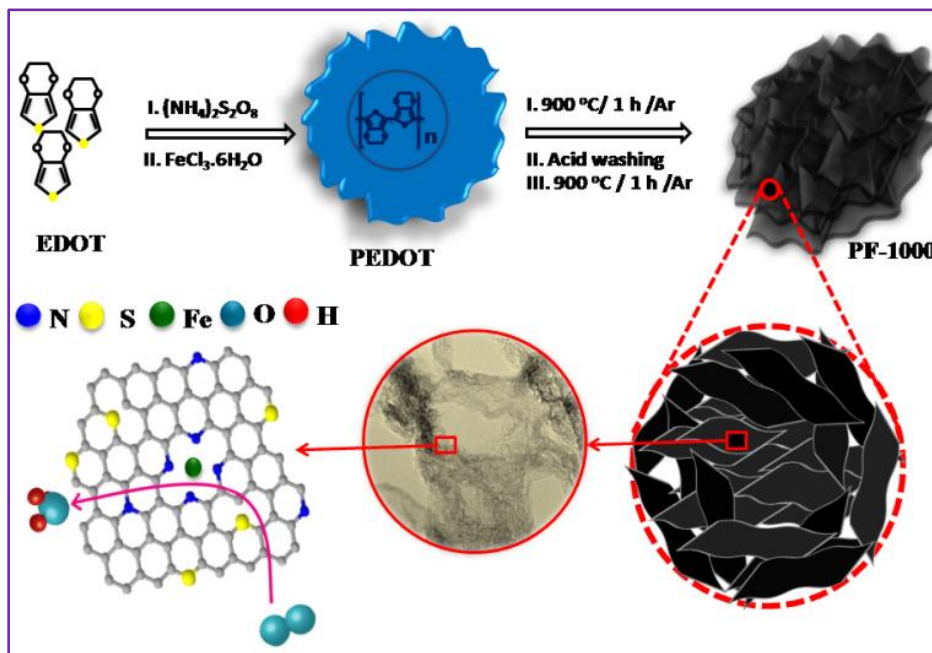
Scheme 3.1 A schematic representation of the synthesis of PF-1000, which is an assembly of crumbled graphene flakes, containing N and S heteroatoms directly doped on the carbon sites along with the active sites formed by the coordination of N with Fe.

3.3 Material Characterization

The morphology of the synthesized materials was analyzed using a transmission electron microscope (TEM) Tecnai-T 20 model at an acceleration voltage of 200 kV. TEM sample was prepared by drop coating of a well-dispersed catalyst sample in isopropyl alcohol solution onto a carbon-coated Cu grid followed by drying. Rigaku Smartlab diffractometer was used for X-ray diffraction (XRD) of the samples at a scan rate of $2°$ min^{-1}, for Cu Kα radiation ($\lambda = 1.5406$ Å). VG Microtech Multilab ESCA 3000 spectrometer (Mg Kα X-ray source (hν = 1.2536 keV)) was used for X-ray photoelectron spectroscopy (XPS) of the catalysts. Raman analysis was performed using an HR 800 Raman spectrometer (Jobin Yvon, Horiba, France) at 632 nm red laser (NRS 1500 W).

3.4 Electrochemical Studies

The electrochemical analysis was carried out in a BioLogicSP-300 Potentio-Galvanostat using a three-electrode system with a glassy carbon electrode (GCE) as the working electrode, graphite rod and Hg/HgSO$_4$ as the counter and the reference electrode, respectively. For the

preparation of the catalyst ink, 10 mg of the material was dispersed in 1 ml solution of 3:1 ratio of IPA:water and 40 µl of 5 wt. % Nafion solution and sonicated for 1 h using a bath sonicator. For preparing the working electrode, 10 µl of the catalyst ink was drop coated on the glassy carbon electrode and dried under an IR lamp to get the uniform coating on the electrode surface. The total catalyst loading on the glassy carbon electrode is 0.5 mg cm^{-2}. 40 wt. % Pt/C with a catalyst loading of 0.2 mg cm^{-2} was used for the comparison purpose in the half cell studies. The linear sweep voltammetry (LSV) was carried out in oxygen saturated 0.5 M H$_2$SO$_4$ at a scan rate of 10 mV s^{-1} with an electrode rotation rate of 1600 rpm.

3.5 Rotating Ring Disc Electrode (RRDE) Analysis

RRDE study was performed in oxygen saturated 0.5 M H$_2$SO$_4$ at a scan rate of 10 mV s^{-1} with an electrode rotation speed of 1600 rpm. The ring potential was held at 1.5 V with respect to RHE. The collection efficiency of the ring was measured to be 0.37 using K$_3$Fe(CN)$_6$ solution. The following equations were used to calculate the hydrogen peroxide percentage (mol %) and the number of electrons:

$$H_2O_2\% = \frac{\frac{200 \times I_R}{N}}{I_D + \frac{I_R}{N}}$$

$$n = \frac{(4 \times I_D)}{(I_D + \frac{I_R}{N})}$$

where, I$_D$ is the disc current, I$_R$ is the ring current, and N is the collection efficiency.

3.6 Single-cell Analysis

Nafion 212 membrane was used as the proton-conducting membrane and the membrane pre-treatment was performed as reported earlier.[41] A conventional brush coating method was adopted for the preparation of the electrodes. For the cathode, catalyst slurry was prepared by mixing PF-1000 and Nafion 20 wt. % (DuPont, USA) in isopropyl alcohol. The carbon to Nafion ratio in the catalyst was fixed as 0.50. The catalyst slurry was applied onto the gas diffusion layer (SGL, Germany) until a total loading of the catalyst reached as 3 mg cm^{-2}. For the anode, Pt/C (40 wt. %) was used as the catalyst with a Pt loading of 0.50 mg cm^{-2}. For comparison purpose, an MEA with the cathode comprising the standard Pt/C (40 wt. %) catalyst was also prepared by maintaining a Pt loading of 0.50 mg cm^{-2}. The membrane electrode

assembly (MEA) with 4 cm^2 active electrode area was prepared by keeping the membrane in between the electrode and hot-pressing at a temperature of 130 °C with a pressure of 0.25 ton for 1 min. The prepared MEA was assembled using a standard fixture (Fuel Cell Technologies, USA) and the testing was performed by using a fuel cell test station (Fuel Cell Technologies Inc.). Hydrogen and oxygen gas were used as the fuel and oxidant, respectively. These gases were delivered at a flow rate of 0.3 slpm for H$_2$ and 0.5 slpm for O$_2$ in the anode and cathode compartments, respectively, of the single cell. The single-cell was analyzed at a cell temperature of 65 °C and 100 % humidity without applying any backpressure.

3.7 Results and discussion

3.7.1 XRD and Raman Analysis
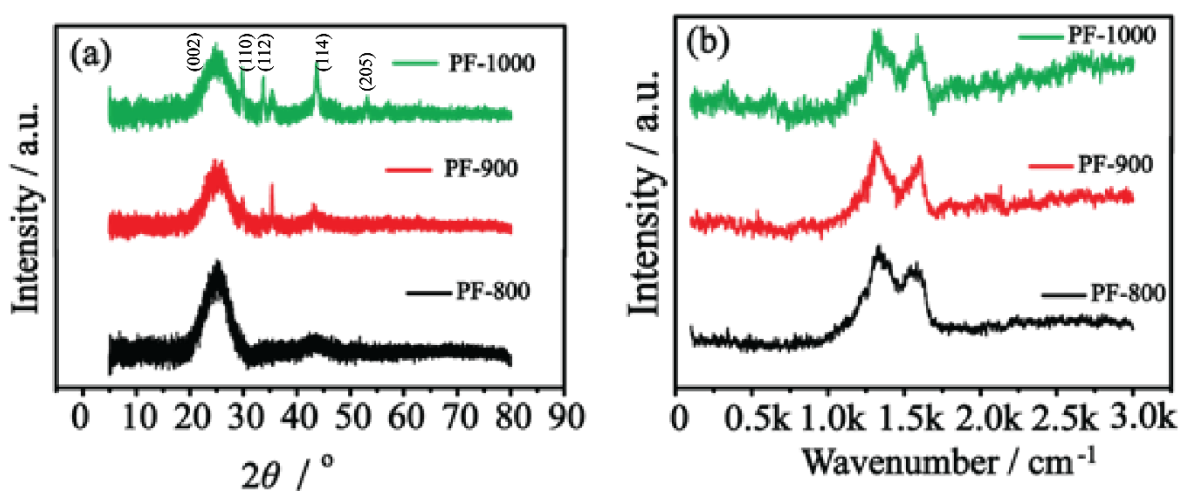
Figure 3.1. (a) X-ray diffraction (XRD) profiles and (b) Raman spectra of the PF electrocatalysts.

Strong evidence for the graphitization of the polymer matrix was obtained from the X-ray diffraction (XRD) patterns of the high temperature annealed PF catalysts (**Figure 3.1a**). In all the cases, there is a broad peak at the 2θ value of 25.26° corresponding to the (002) plane of the graphitic carbon. In addition to this graphitic plane, PF-900 and PF-1000 show peaks at the 2θ values of 29.8°, 33.7°, 43.8° and 52.9°, which are corresponding to the (110), (112), (114) and (205) phases of the hexagonal FeS particles, respectively,[31] and are absent in the case of PF-800. Even though XRD shows the presence of FeS particles in the PF catalysts, Raman spectra (**Figure 3.1b**) do not show any characteristic vibrations (usually observed below 500 cm^{-1})[32] corresponding to the FeS nanoparticles. This indicates that the FeS nanoparticles are well encased inside the carbon sheets. However, all the three annealed samples display peaks at 1317 cm^{-1} and 1599 cm^{-1}, respectively, for the D (defective) and G (graphitic) bands of the carbon

framework.[33] The intensity ratio of the D and G band (I_D/I_G), a representation of the disorder in the carbon matrix,[34] of all three samples is in the order of PF-900 (1.011) < PF-800 (1.019) < PF-1000 (1.021). Even though the I_D/I_G ratios of all the three annealed samples differ marginally, PF-1000 shows a relatively higher I_D/I_G ratio, which indicates the presence of more defects on it. This stands out as strong evidence on the structural modification incurred on the PEDOT derived carbon as the annealing temperature increases.

3.7.2 SEM and TEM Analysis

Figure 3.2 (a) SEM image of PF-1000, indicating the crumbled nature of the PEDOT derived graphene flakes. (b-d) TEM images of PF-1000 at different magnifications; the red arrows in Figure (d) indicate the graphene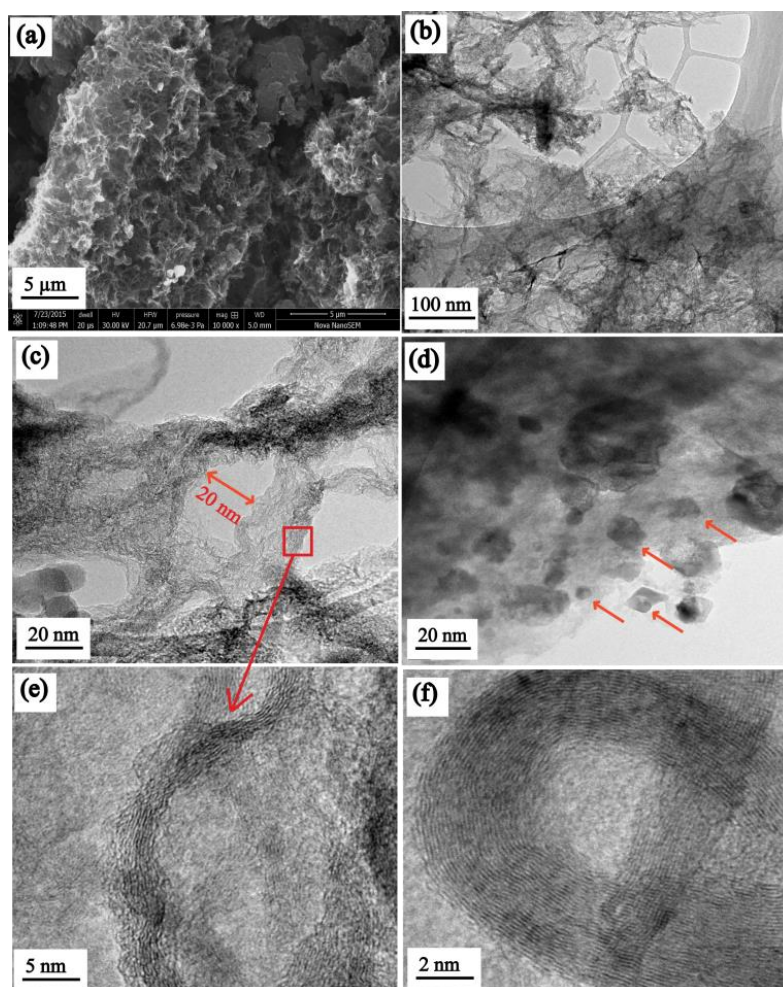 layer wrapping around the FeS nanoparticles. Figure (e and f) represent the HRTEM images of the graphene sheets; the graphene layers and their buckled nature are clearly evident from these images

The evidence for the crumbled nature of the graphene sheets was observed from the scanning electron microscopy (SEM) image of PF-1000 (**Figure 3.2a**), which displays the highly porous nature of the material. It looks like the nanoflakes of graphene sheets are assembled in an interconnected fashion, leading to the establishment of open pores in the matrix. Further evidence for the crumbled graphene type morphology is obtained from the transmission electron microscopy (TEM) images presented in **Figure 3.2b–d**. At some locations (**Figure 3.2b and c**), the graphene layers have pulverized nature and the small crumbled layers are generally interconnected. Still, the layered nature of the graphene structure is clearly evident in the image presented in **Figure 3.2c**. Overall, the structure retains good intrinsic porosity with exposure of the greater extent of the surface, which is expected to be holding more number of accessible active sites on the surface. This makes a significant difference compared to the conventional graphene structures, where the restacking of the sheets tend to make a large proportion of the active sites inaccessible. The crumbled graphene also contains Fe–S nanoparticles encased within the graphene sheets, as evident from **Figure 3.2d**. The graphene cases around the Fe–S nanoparticles are marked with red arrows for ease of understanding. This result is in accordance with the Raman data, which do not indicate the characteristic vibrations corresponding to the Fe–S moiety due to the encapsulation effect. Moreover, the high-resolution TEM (HRTEM) images (**Figure 3.2e and f**) of the crumbled graphene show distorted lattice fringes compared to pure sp^2 graphene. These buckled or disordered fringes of the crumbled graphene indicate the effective doping of the heteroatoms in the carbon matrix.[37] Moreover, the selected area electron diffraction (SAED) pattern (**Figure 3.3**) of PF-1000 shows a clear hexagonal pattern, which indicates the different orientations of the crystalline plane due to the crumbling of the multi-layered graphene sheets.[35,36]

As mentioned previously, the SEM image displays the crumbled nature of the graphene sheets and the flakes are assembled to give a highly porous appearance of the matrix. The nanoflakes of the graphene sheets hold uniformly distributed N, Fe and S atoms with a greater chance of getting exposed due to the peculiar porous architecture of the material. The uniform distribution of the N, Fe, and S atoms on the surface of the graphene sheets is clearly evident from the elemental mapping (**Figure 3.4**). The SEM images of PF-800 and PF-900 differ much from that of PF-1000 (**Figure 3.5**). The conversion of the bulk carbon mass to the sheet-like morphology depends on the annealing temperature.
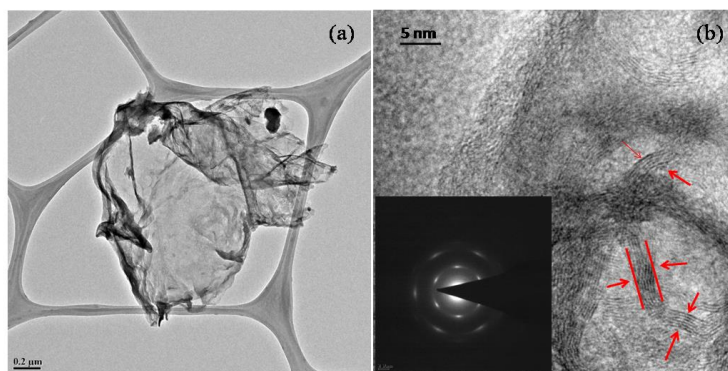
Figure 3.3 Transmission Electron Microscopic (TEM) images of the PF-1000 electrocatalyst recorded at different magnifications: (a) 0.2 µm and (b) 5 nm scale bar. The inset of (b) shows the selected area electron diffraction pattern of PF-1000.
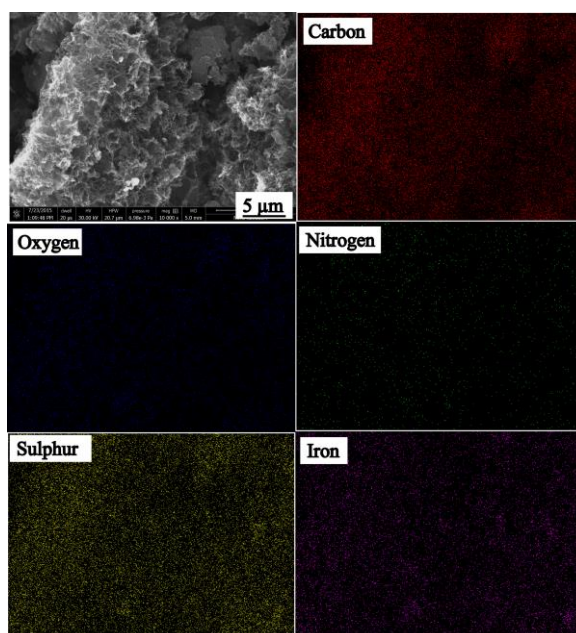

Figure 3.4 Elemental mapping of PF-1000 using SEM.
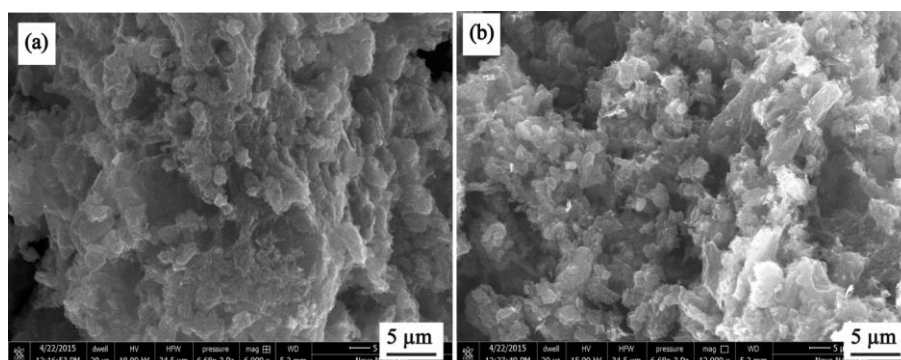
Figure 3.5 Scanning Electron Microscopic (SEM) images of (a) PF-800 and (b) PF-900.

3.7.3 Surface Area Analysis

This is supported by the Brunauer–Emmett–Teller (BET) surface area values for all the electrocatalysts (**Figure 3.6**). The surface area of the PF catalysts increases with the increase in the annealing temperature in the order of PF-800 (324 m^2 g^{-1}) < PF- 900 (632 m^2 g^{-1}) < PF-1000 (800 m^2 g^{-1}). The enhanced surface area with respect to the increase in the annealing temperature is directly connected to the morphological changes incurred by the PF samples while heating from 800 to 1000 $^{\circ}$C. Along with this, the pore size distribution analysis (**Figure 3.6b**) indicates that the PF catalysts have a mixed micro- and mesoporosity. However, most of the pore diameter was measured to be below 4 nm and it is interesting that the pore volume increases with the increase in the annealing temperature. PF-800 has the least pore volume compared to PF-900 and PF-1000 and this trend is exactly matching with the change in the BET surface area with respect to the annealing temperature.
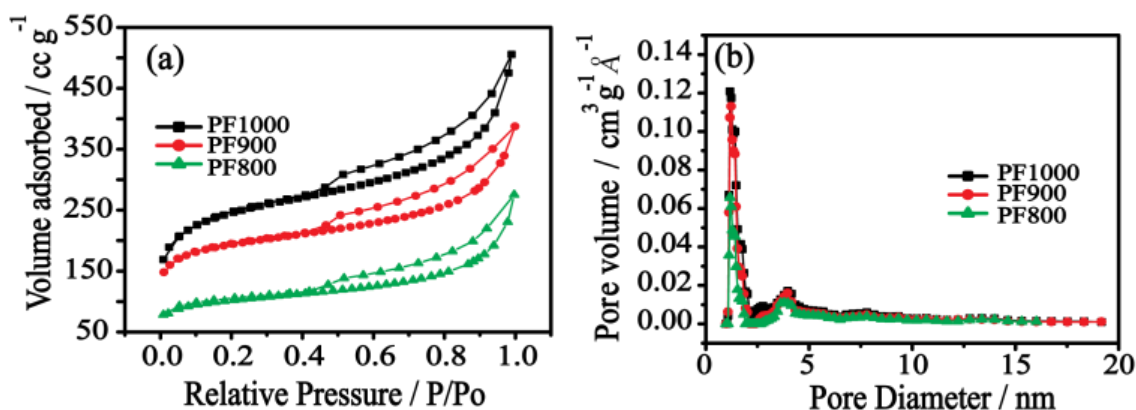
Figure 3.6 (a) Nitrogen adsorption-desorption isotherms and (b) pore size distribution profiles of PF-800, PF-900, and PF-1000.

3.7.4 XPS Analysis

X-ray photoelectron spectroscopy (XPS) reveals the presence of carbon, nitrogen, oxygen, iron, and sulphur (**Table 3.1**) on the surface of the graphene sheets, which is supported by the elemental mapping. Improved graphitization with respect to the annealing temperature is evidenced by the increased carbon to oxygen ratio. As expected, the atomic percentage (atom %) of the doped nitrogen decreases with the annealing temperature. It is assumed that the unreacted oxidant $(NH_4)_2S_2O_8$ and the surfactant (cetyl ammonium bromide, CTAB) are the main sources for nitrogen doping, whereas sulphur is generated exclusively from PEDOT. The annealing temperature induces decomposition of these moieties and some portion of the generated nitrogen and sulphur will be harvested by the concomitantly generated graphene flakes.

Table 3.1: Surface elemental composition of the PF electrocatalysts calculated from XPS.

	C (atom %)	O (atom %)	N (atom %)	S (atom %)	Fe (atom %)
PF-800	80.86	12.02	4.39	2.47	0.24
PF-900	82.45	11.19	4.20	1.91	0.23
PF-1000	85.31	10.08	2.63	1.77	0.18

Since the formation of the graphene framework and the doping process occur simultaneously under annealing conditions, an efficient doping of the heteroatom moieties is expected to occur in the system. Since the structure retains inherent porosity due to the interconnected nature of the crumbled graphene flakes, the pores can act as trapping sites for the evolving gases and can subsequently ensure a homogenous and surface enriched doping of both nitrogen and sulphur. It is interesting to note that the atomic % of sulphur is comparatively lower than that of nitrogen in the PF samples even though the carbon framework is generated exclusively from the sulphur enriched polymer called PEDOT.
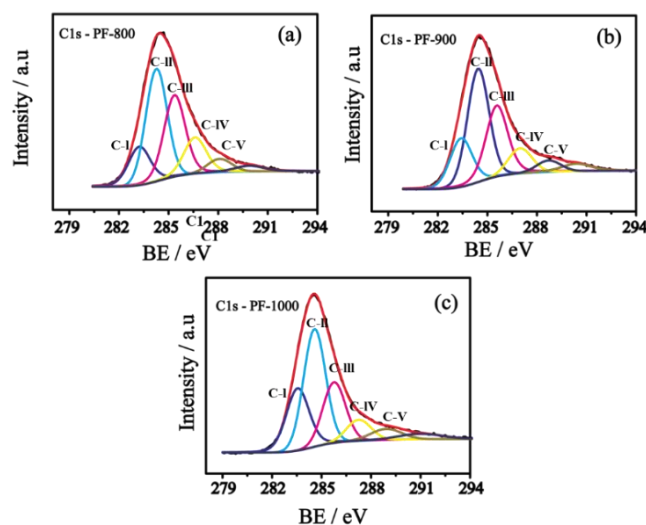
Figure 3.7 Fitted C1s spectra of (a) PF-800, (b) PF-900, and (c) PF-1000. The different carbon species are marked as C-I (metal carbide), C-II (C=C), C-III (C-N), C-IV (C-S) and C-V (-O-C=O).

A detailed discussion on the deconvoluted spectra of the individual components is given in the following sections. The C 1s spectrum of PF-1000 was fitted to get an insight on the different types of carbon bonding on the surface (**Figure 3.7c**). A peak designated as C-I appeared at 283.5 eV is corresponding to the metal carbide and the peak represented as C-II at 284.5 eV is attributed to the C=C interaction. Moreover, the indication of the nitrogen and sulphur doping could also be obtained from the peaks marked as C-III and C-IV at the binding energies of 285.7 and 287.3 eV, respectively. The peak denoted as C-V at 288.6 eV of the fitted C1s spectra also

provides information about the -O-C=O type interaction of the carbon. The similar peaks are also observed in the case of the PF-800 and PF-900 samples.

The fitted N1s spectra of all the three PF catalysts show the presence of pyridinic (398.3 eV), pyrrolic (399.6 eV), graphitic (400.7 eV) and oxide (402–405 eV) forms of nitrogen (**Figure 3.8**).[38] More interestingly, a peak observed at a binding energy of 397.0 eV in the fitted N1s spectrum confirms the presence of iron nitride.[39] Since the XRD spectra do not show any characteristic peak of the iron nitride, it may be assumed that such nanoparticles are relatively low in concentration on the graphene surface. The pyridinic nitrogen content in the PF catalysts decreases with the increase in the annealing temperature in the order of PF-800 (27.74%) > PF-900 (19.24%) > PF-1000 (12.50%). Because of the poor thermal stability, the pyridinic nitrogen is either converted into the pyrrolic or graphitic form with increasing the annealing temperature.[40] The graphitic to the pyridinic ratio of the PF catalysts increases in the order of PF-800 (0.95) < PF-900 (1.27) < PF-1000 (2.24), indicating that more graphitic nitrogen is present on the surface of PF-1000. It is already known that the presence of graphitic nitrogen improves the ORR current density by facilitating a favourable four-electron ($4e^-$) transfer reaction.[40]
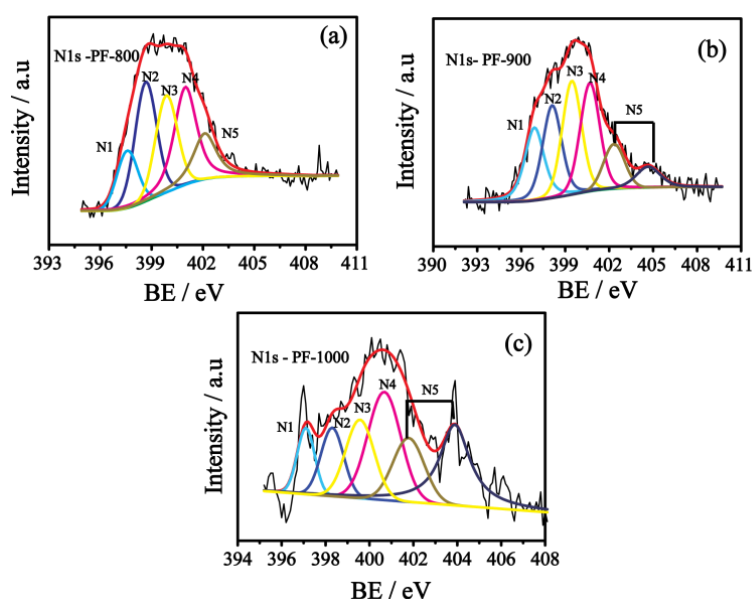
Figure 3.8 Fitted N1s spectra of (a) PF-800, (b) PF-900 and (c) PF-1000. Different nitrogen species are marked as N1 (nitride), N2 (pyridinic), N3 (pyrrolic), N4 (graphitic) and N5 (oxide).

The atom % of the iron in the PF catalysts is found to be relatively low (< 0.25%) and the fitted Fe 2p spectrum shows the presence of both Fe^{II} and Fe^{III} states (**Figure 3.9**). The peaks at 711.10 and 725.05 eV represent the $2p_{3/2}$ and $2p_{1/2}$ orbitals, respectively, of Fe^{II}. Similarly, the peaks at 714.02 and 726.09 eV correspond to the $2p_{3/2}$ and $2p_{1/2}$ orbitals, respectively, of Fe^{III}. The doped

nitrogen may coordinate to iron with the binding energies similar to the pyridinic coordination in the fitted nitrogen N1s spectrum. A clear peak observed at 398.0 eV in the fitted N1s spectrum of the PF catalysts confirms the formation of the Fe–N_x type interaction along with the pyridinic nitrogen on the electrocatalysts.[41]
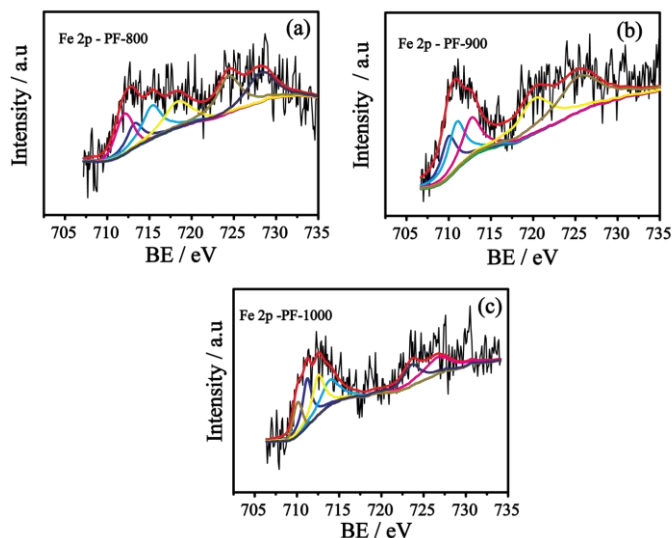
Figure 3.9 Fitted Fe 2p spectra of (a) PF-800, (b) PF-900, and (c) PF-1000.
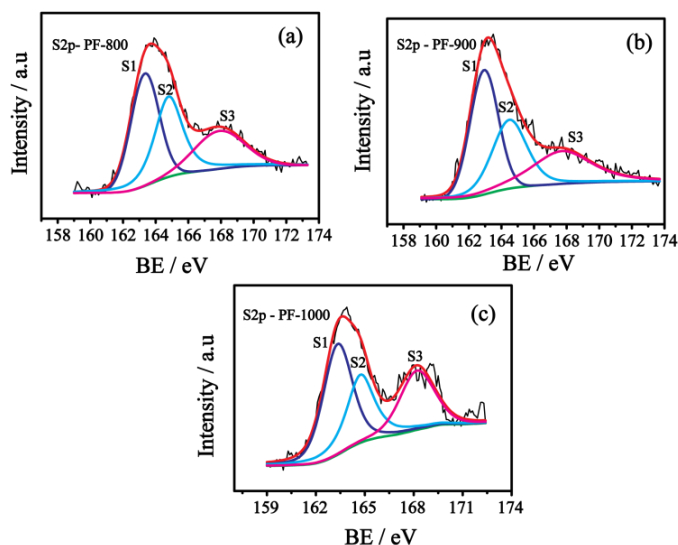
Figure 3.10 Fitted S2p spectra of (a) PF-800, (b) PF-900, and (c) PF-1000. Different sulphur species are marked as S1 (C-S-C, $2p_{3/2}$), S2 (C-S-C, $2p_{1/2}$) and S3 (C-SO_x-C).

The fitted sulphur 2p spectrum of the PF catalysts shows the C–S–C peaks at 163.5 eV ($2p_{3/2}$) and 164.5 eV ($2p_{1/2}$) with an intensity ratio of 1:2 (**Figure 3.10**). The atom% of sulphur decreases with the increase in the annealing temperature in the order of PF-800 (2.47%) > PF-900 (1.91%) > PF-1000 (1.77%). It is also important to note that all the PF catalysts show a peak at 168.0 eV corresponding to the C–SO_x–C interaction.[42] However, the absence of thiol

groups (~160.0 eV) in the XPS spectra indicates that most of the sulphur dopants are residing at the edges and this rules out the chances of doping by creating coordination similar to that of the graphitic nitrogen.[43] Also, the thermal stability of the sulphur species such as its oxide is very poor at high temperature and this also can contribute to reducing the sulphur content in the PF catalysts, which is found to be below 2.5 atom %. The outer orbital mismatch between the carbon and sulphur creates spin density changes and contributes towards facilitating the ORR. Similarly, the C–SO$_x$–C centres will also assist in efficient adsorption of the oxygen molecules.[42] XPS analysis suggests that the prepared catalysts are enriched with three different types of reaction centres, *viz.*, graphitic nitrogen, sulphur–carbon coordination, and coordinated iron, which in turn reflects on the activity and stability characteristics of the PF catalysts as evident from the following sections.

3.7.5 Electrochemical Analysis

The ORR activity of the PF catalysts was evaluated in oxygen saturated 0.5 M H$_2$SO$_4$ using both rotating disc electrode (RDE) and rotating ring disk electrode (RRDE) techniques. The linear sweep voltammogram (LSV) was recorded at different electrode rotation speeds at a scan rate of 10 mV s^{-1}. A graphite rod and a reversible hydrogen electrode were employed as the counter and reference electrodes, respectively. Replacement of the conventional Pt counter electrode with the graphite rod ensures elimination of possible contamination of the Pt-free working electrode with the deposition of Pt ions, which can be leached out from the counter electrode if a Pt rod is used. **Figure 3.11a** shows LSVs of the different samples recorded at an electrode rotation speed of 1600 rpm. A close inspection of the LSV profiles shows similar onset (0.89 V) and half-wave (0.75 V) potentials for both PF-900 and PF-1000. This indicates similar intrinsic activity and active reaction site density in PF-900 and PF-1000. However, the oxygen reduction current density at higher overpotential is higher for PF-1000 than that for PF-900. Compared to 40 wt. % Pt/C, PF-1000 and PF-900 experience an overpotential of 0.10 V in both the onset and half-wave potentials. However, the ORR activity displayed by PF-900 and PF-1000 catalysts is superior to that of some of the recently reported non-precious ORR catalysts under acidic conditions. There are many reports on the matching performance of the non-precious metal-based catalysts with that of the state-of-the-art Pt/C catalysts in basic media, but similar reports under acidic conditions are rare.[1,2,12] PF-800 shows an overpotential of 15 mV on the onset potential (0.875 V) and 30 mV on the half-wave potential compared to PF-900 and PF-1000. This further confirms the critical role played by dual doping in generating
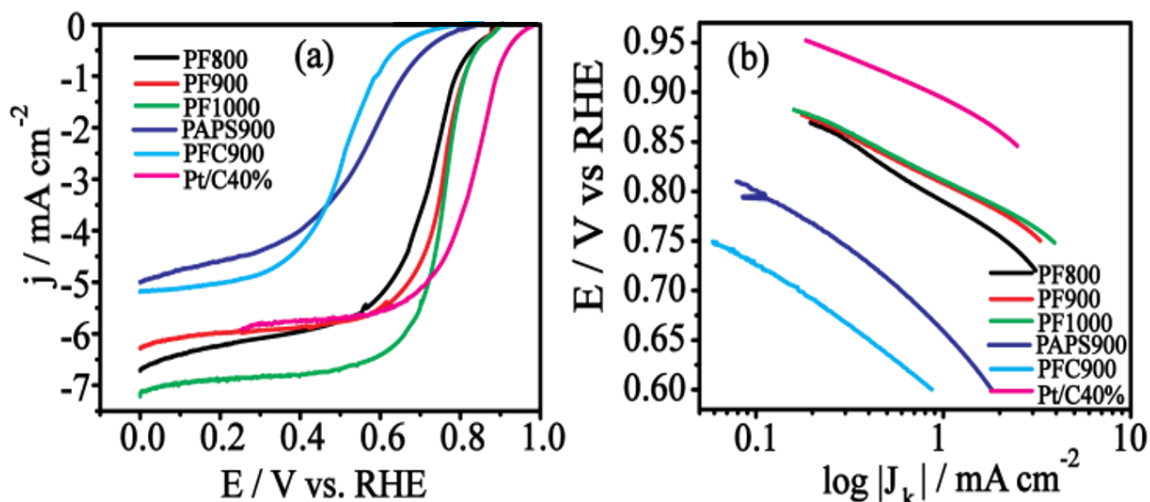
Figure 3.11 (a) LSVs of the different electrocatalysts recorded at an electrode rotation rate of 1600 rpm and a voltage scan rate of 10 mV s^{-1} in oxygen saturated 0.5 M H$_2$SO$_4$, (b) Tafel plots of the PF electrocatalysts derived from the LSVs.

the active reaction centres with significantly redefined performance characteristics compared to the sites generated from the corresponding mono-dispersed entities. A similar Tafel slope of 93 mV per decade for PF-900 and PF-1000 (**Figure 3.11b**) indicates similar oxygen reduction mechanisms in both these systems, which appeared to be closely following that for Pt/C (88 mV decade^{-1}). The PF-800 (116 mV decade^{-1}), PFC-900 (131 mV decade^{-1}) and PAPS-900 (126 mV decade^{-1}) show much higher Tafel slopes, which indicates the involvement of a different reduction mechanism in these samples compared to PF-900 and PF-1000. Even though PF-900 and PF-1000 show similar ORR mechanisms, the mass activity of PF-1000 at 0.85 V is superior to that of PF-900 and PF-800.

Table 3.2: Electrochemical performance of the PF electrocatalysts in 0.5 M H$_2$SO$_4$ in comparison with Pt/C (40 wt.%).

	Onset potential (V vs RHE)	Half-wave potential (V vs RHE)	Tafel slope (mV/decade)	Mass activity @ 0.85 V (A/g)
PF-1000	0.890	0.75	93	0.78
PF-900	0.890	0.75	94	0.70
PF-800	0.870	0.72	116	0.60
PFC-900	0.794	0.50	131	0.00
PAPS-900	0.843	0.56	126	0.00
Pt/C (40 wt.%)	0.989	0.83	88	11.50

The mass activity of the PF electrocatalysts at 0.85 V is in the order of PF-1000 (0.78 A g^{-1}) > PF-900 (0.70 A g^{-1}) > PF-800 (0.60 A g^{-1}). The ORR activities of the control samples such as PAPS-900, PFC-900, PAPS-1000, and PFC-1000, were compared with those of PF-1000 and PF-900. PAPS-900 (E onset 0.83 V, E$_{1/2}$ 0.56 V) and PFC-900 (E onset 0.77 V, E$_{1/2}$ 0.50) experience high overpotential compared to PF-1000 and PF-900. However, PAPS-1000 (E onset 0.83 V, E$_{1/2}$ 0.64 V) and PFC-1000 (E onset 0.77 V, E$_{1/2}$ 0.58 V) display less overpotential in the half-wave potential values with respect to their 900 $^{\circ}$C annealed samples. Still, the ORR activity of PAPS-1000 and PFC- 1000 is less compared to that of PF-1000 (**Figure 3.12**).

The hydrogen peroxide yield (% H$_2$O$_2$) and electron transfer number during the ORR were measured using an RRDE (**Figure 3.13**). RRDE measurements were performed at an electrode rotation speed of 1600 rpm and a voltage scan rate of 10 mV s^{-1} in oxygen saturated 0.5 M
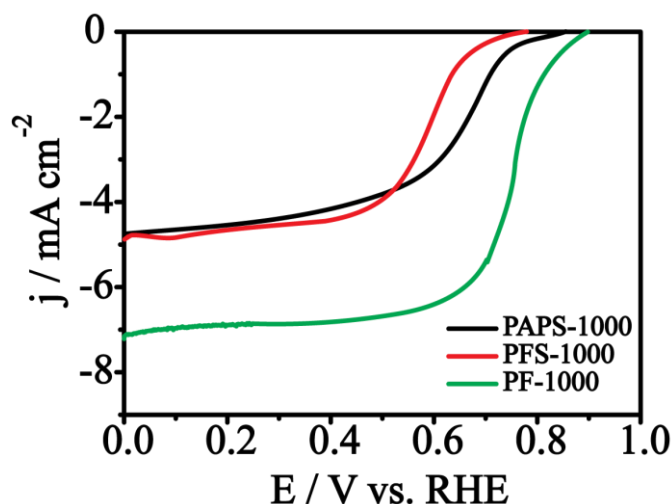
Figure 3.12 LSVs of PAPS-1000, PFC-1000, and PF-1000 recorded at an electrode rotation rate of 1600 rpm at 10 mV s^{-1} scan rate in oxygen saturated 0.5 M H$_2$SO$_4$.
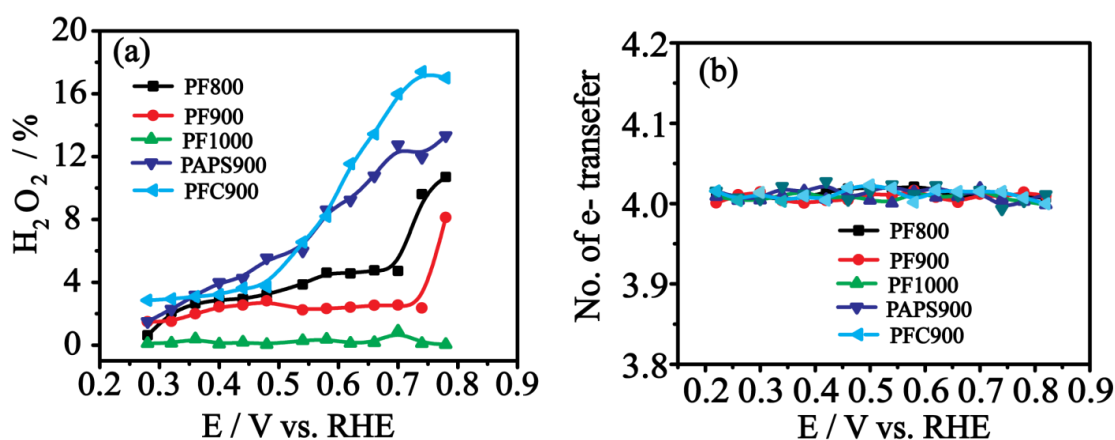
Figure 3.13 (a) Hydrogen peroxide yield and (b) the number of the electrons transferred in the case of the PF electrocatalysts at different potentials in 0.5 M H$_2$SO$_4$ calculated from RRDE.

H_2SO_4. The ring potential was kept at 1.5 V *vs.* RHE. The collection efficiency of the ring electrode was measured to be 0.37. During the electrode reactions, the oxygen molecule gets reduced at the glassy carbon disc electrode to form water and peroxide. The formed peroxide molecule gets further oxidized at the platinum ring electrode and forms water. The corresponding disc and ring currents were recorded and used for calculating the peroxide yield during the electrode process. The calculated H_2O_2 yield is <4% for PF-900 and PF-1000. This shows that both the catalysts reduce dioxygen predominantly to water through the preferred $4e^-$ transfer reaction. Even though PF-900 and PF-1000 have similar half-wave and onset potentials, the mass activity and reduction current density at higher overpotential are higher for PF-1000. XPS analysis confirms the higher atom % of the graphitic nitrogen in PF-1000. Recent literature suggests that the presence of graphitic nitrogen assists in improving the ORR current density.[40] In view of this, the higher content of the graphitic nitrogen in PF 1000 is responsible for its improved mass activity and reduction current density. Even though the surface composition of sulphur, iron, and nitrogen of PF-1000 is comparatively less than that of PF-900, the high surface area with microporosity of the system improves the distribution and accessibility of the active reaction sites on PF-1000. The high surface area with the crumbled morphology of PF-1000 helps to improve the mass transfer through the catalysts. Thus, the reactant gases far more easily reach the active centres such as graphitic nitrogen, C–S–C and Fe–N_x. Overall, the high density of the active reaction centres accomplished through the spin density changes by the dual doping and Fe–N_x coordination with a high surface area and better accessibility help PF-1000 to perform as a better electrocatalyst for ORR at low pH.
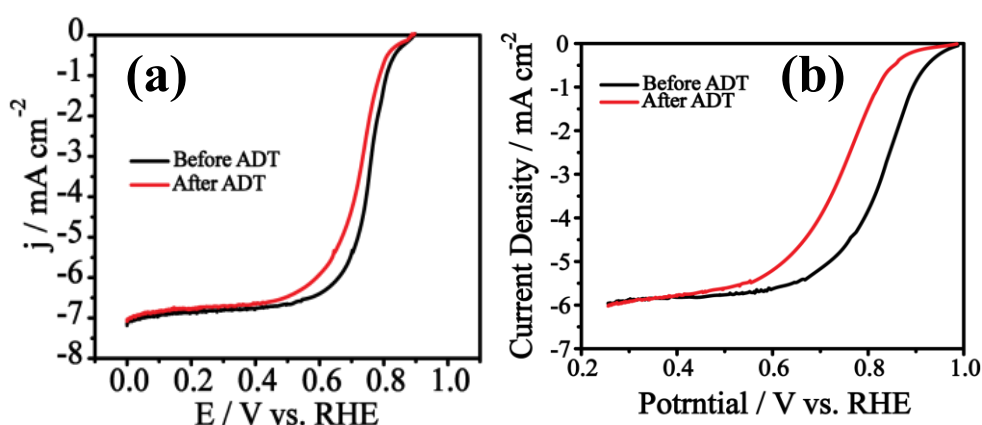
Figure 3.14 (a) LSVs of PF-1000 before and after 5000 potential cycling, (b) LSVs of Pt/C before and after 5000 potential cycling.

The stability of PF-1000 was studied using an accelerated durability test (ADT) (**Figure 3.14a**). LSVs, with an electrode rotation rate of 1600 rpm, were obtained before and after 5000 potential cycles (potential window of 0.60–1.0 V, scan rate of 100 mV s^{-1}). The main purpose of ADT is to facilitate forced corrosion of the carbon substrate at the high positive potential in oxygen saturated 0.5 M H_2SO_4. The forced corrosion will cause the leaching of the dopants such as nitrogen, sulphur and metal coordinated centres leading to the reduction in surface density of the active reaction centres of the carbon catalysts. Therefore, ADT provides clear evidence for the electrochemical stability of the carbon catalysts. Subsequent to ADT, in the LSV, PF-1000 suffers a negative shift in the half-wave potential by 27 mV apparently without making any change in its intrinsic activity since the onset potential is found to be more or less same before and after ADT. However, Pt/C experiences a performance degradation of 81 mV in the half-wave potential (**Figure 3.14b**). These observations indicate that, compared to Pt/C, PF-1000 appears to be a highly durable electrocatalyst at lower pH. Since the graphene framework in the present catalyst appears to be stable, the active centres (doped N, S, and Fe–N_x) also greatly benefit in terms of the electrochemical durability under acidic pH conditions.

Since PF-1000 shows higher ORR activity and stability under acidic conditions, we have taken the material for a realistic validation in a single cell mode by fabricating a membrane electrode assembly (MEA). The MEA with an active area of 4 cm^2 was constructed by using PF-1000 as the cathode catalyst and Pt/C as the anode catalyst. The electrodes were fabricated by coating slurry of the catalyst in Nafion by maintaining a Nafion to carbon ratio of 0.50. The anode and cathode catalyst loadings were maintained as 0.50 and 3.0 mg cm^{-2}, respectively. The electrodes were sandwiched with a Nafion 212 (DuPont, USA) proton conducting membrane. The testing was performed by connecting the single cell with a fuel cell test station (Fuel Cell Technologies Inc., USA) and by collecting the current density (mA cm^{-2}) and voltage (V) points by supplying hydrogen in the anode (0.3 slpm) and oxygen in the cathode (0.2 slpm) compartments. Data acquisition was performed by using LabVIEW 5.1 software. The PF-1000 based single-cell displays an open circuit voltage (OCV) of 0.73 V, which is 0.153 V lower than that observed in the half-cell analysis. A well-featured polarization plot could be obtained covering the activation, ohmic and mass transfer polarization regions, indicating the ability of the cathode catalyst to perform the electrode reaction under varying power demanding conditions. The system displayed a maximum power density of 193 mW cm^{-2} without applying any back-pressure (**Figure 3.15**). Even though the fuel cell performance of PF-1000 is less compared to that of Pt/C (maximum power density of 600 mW cm^{-2}), considering as a totally
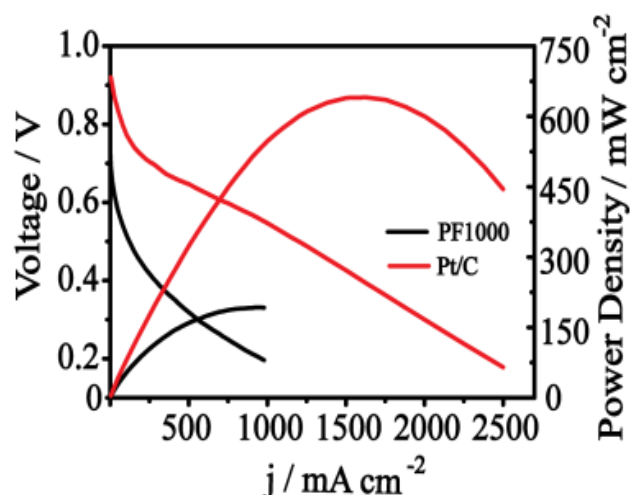
Figure 3.15 Single-cell polarization plots of the MEAs based on PF-1000 (3 mg cm^{-2}) and Pt/C (0.50 mg cm^{-2}) as the cathode catalysts. Pt/C was used as the anode catalyst (0.50 mg cm^{-2}) in both the MEAs. Nafion® 212 membrane was used as the proton-conducting membrane for the MEA preparation. Hydrogen and oxygen gases were used as the fuel and oxidant with flow rates of 0.3 and 0.5 slpm, respectively. The single-cell was analyzed without applying any back-pressure at a cell temperature of 65 °C with 100 % humidity.

Pt-free cathode electrode system, this value is comparable to many values reported in the literature.[44,45] Actually, the electrode preparation in the case of the Pt-free systems requires different levels of optimizations owing to the molecular level distribution of the active sites compared to the Pt-based systems, where the active centres are considered to be the surface of the Pt nanoparticles. The ionomer to carbon ratio and viscosity of the catalyst ink are crucial in this case, as the active ionomer interface (in this case Nafion) should be created without clogging the pores of the crumbled graphene structures. Optimization studies targeting an improved protocol are currently in progress in our laboratory. Overall, the single-cell performance of PF-1000 goes in line with the promisingly high intrinsic ORR activity detected through the half-cell experiments.

3.8 Conclusions

Micro/mesoporous nitrogen and sulphur dual doped crumbled graphene possessing a high surface area and accessible active sites could be prepared from a single precursor, PEDOT, through high-temperature annealing under an inert atmosphere. PEDOT annealed at 1000 °C (PF-1000) displays a surface area of 800 m^2 g^{-1}, which is higher compared to that of the PEDOT annealed at 900 and 800 °C. XPS analysis reveals the presence of three different types of active

reaction centres, *viz.* graphitic nitrogen coordination, sulphur-carbon interaction and Fe-Nx. Both PF-900 and PF-1000 show similar onset and half-wave potentials in 0.5 M H_2SO_4, and the overpotential with respect to 40 wt. % Pt/C is only 0.1 V. Tafel analysis depicts the oxygen reduction kinetics of PF-1000 and PF-900, similar to that of Pt/C. However, the mass activity calculated at 0.85 V and the ORR reduction current density at higher negative potentials are higher for PF-1000 compared to PF-900. Only 27 mV reduction in the half-wave potential is observed for PF-1000, compared to 80 mV shift in the case of Pt/C, after 5000 ADT cycles. This validates the better electrochemical stability possessed by PF-1000. Finally, a single-cell analysis using PF-1000 as the cathode catalyst provides a well-defined voltage-current polarization plot with a maximum power density of 193 mW cm^{-2} without applying any back-pressure. Thus, the intrinsic activity as measured through the half-cell measurements of PF-1000 could be fairly well translated in terms of a single cell performance under realistic cell testing conditions.

3.9 Reference

[1]. Y. Nie, L. Li, and Z. Wei, *Chem. Soc. Rev.*, 2015, **44**, 2168-2201.

[2]. L. Dai, Y. Xue, L. Qu, H.-J. Choi and J.-B. Baek, *Chem. Rev.*, 2015, **115**, 4823-4892.

[3]. G. Merle, M. Wessling and K. Nijmeijer, *J. Membr. Sci.*, 2011, **377**, 1-35.

[4]. S. J. Peighambardoust, S. Rowshanzamir, and M. Amjadi, *Int. J. Hydrogen Energy*, 2010, **35**, 9349-9384.

[5]. X.-K. Kong, C.-L. Chen and Q.-W. Chen, *Chem. Soc. Rev.*, 2014, **43**, 2841-2857.

[6]. X. Wang, G. Sun, P. Routh, D.-H. Kim, W. Huang, and P. Chen, *Chem. Soc. Rev.*, 2014, **43**, 7067-7098.

[7]. X. Zhou, J. Qiao, L. Yang, and J. Zhang, *Adv. Energy Mater.*, 2014, DOI: 10.1002/aenm.201301523.

[8]. C. Zhu, H. Li, S. Fu, D. Du, and Y. Lin, *Chem. Soc. Rev.*, 2016.

[9]. H. Wang, T. Maiyalagan and X. Wang, *ACS Catal.*, 2012, **2**, 781-794.

[10]. Z. Yang, J. Ren, Z. Zhang, X. Chen, G. Guan, L. Qiu, Y. Zhang and H. Peng, *Chem. Rev.*, 2015, **115**, 5159-5223.

[11]. C. K. Chua and M. Pumera, *Chem. Soc. Rev.*, 2014, **43**, 291-312.

[12]. M. Zhou, H.-L. Wang and S. Guo, *Chem. Soc. Rev.*, 2016.

[13]. B. Zhao, P. Liu, Y. Jiang, D. Pan, H. Tao, J. Song, T. Fang, and W. Xu, *J. Power Sources*, 2012, **198**, 423-427.

[14]. Y. Zheng, Y. Jiao, M. Jaroniec, Y. Jin, and S. Z. Qiao, *Small*, 2012, **8**, 3550-3566.

[15]. J. Benson, Q. Xu, P. Wang, Y. Shen, L. Sun, T. Wang, M. Li, and P. Papakonstantinou, *ACS Applied Materials and Interfaces*, 2014, **6**, 19726-19736.

[16]. T. Ikeda, Z. Hou, G.-L. Chai and K. Terakura, *J. Phys. Chem. C*, 2014, **118**, 17616-17625.

[17]. G.-L. Chai, Z. Hou, D.-J. Shu, T. Ikeda and K. Terakura, *J. Am. chem. Soc.*, 2014, **136**, 13629-13640.

[18]. I.-Y. Jeon, H.-J. Choi, S.-M. Jung, J.-M. Seo, M.-J. Kim, L. Dai and J.-B. Baek, *J. Am. chem. Soc.*, 2013, **135**, 1386-1393.

[19]. T.-m. Sun, L.-m. Dong, C. Wang, W.-l. Guo, L. Wang, and T.-x. Liang, *New Carbon Materials*, 2013, **28**, 349-354.

[20]. D.-S. Yang, D. Bhattacharya, M. Y. Song, F. Razmjooei, J. Ko, Q.-H. Yang and J.-S. Yu, *ChemCatChem*, 2015, **7**, 2882-2890.

[21]. Z. Liu, H. Nie, Z. Yang, J. Zhang, Z. Jin, Y. Lu, Z. Xiao and S. Huang, *Nanoscale*, 2013, **5**, 3283-3288.

[22]. Q. Li, P. Xu, W. Gao, S. Ma, G. Zhang, R. Cao, J. Cho, H.-L. Wang and G. Wu, *Adv. Mater.*, 2014, **26**, 1378-1386.

[23]. M. Shao, *Electrocatalysis in Fuel Cells: A Non- and Low- Platinum Approach*, Springer London, 2013.

[24]. Z. Chen, D. Higgins, A. Yu, L. Zhang, and J. Zhang, *Energy Environ. Sci.*, 2011, **4**, 3167-3192.

[25]. F. Jaouen, E. Proietti, M. Lefevre, R. Chenitz, J.-P. Dodelet, G. Wu, H. T. Chung, C. M. Johnston and P. Zelenay, *Energy Environ. Sci.*, 2011, **4**, 114-130.

[26]. X. Feng, *Nanocarbons for Advanced Energy Conversion*, Wiley, 2015.

[27]. J. D. Wiggins-Camacho and K. J. Stevenson, *J. Phys. Chem. C*, 2011, **115**, 20002-20010.

[28]. J. D. Wiggins-Camacho and K. J. Stevenson, *J. Phys. Chem. C*, 2009, **113**, 19082-19090.

[29]. S.-A. Wohlgemuth, R. J. White, M.-G. Willinger, M.-M. Titirici and M. Antonietti, *Green Chem.*, 2012, **14**, 1515-1523.

[30]. J. Zhu, S. P. Jiang, R. Wang, K. Shi and P. K. Shen, *J. Mater. Chem. A*, 2014, **2**, 15448-15453.

[31]. M. Akhtar, M. A. Malik, F. Tuna, and P. O'Brien, *J. Mater. Chem. A*, 2013, **1**, 8766-8774.

[32]. C. Remazeilles, M. Saheb, d. Neff, E. Guilminot, K. Tran, J.-A. Bourdoiseau, r. Sabot, M. Jeanin, H. Matthiesen, P. Dillmann and P. Refait, *Journal of Raman Spectroscopy*, 2010, **41**, 1425-1433.

[33]. V. M. Dhavale, S. S. Gaikwad and S. Kurungot, *J. Mater. Chem. A*, 2014, **2**, 1383-1390.

[34]. S. K. Singh, V. M. Dhavale and S. Kurungot, *ACS Applied Materials & Interfaces*, 2015, **7**, 442-451.

[35]. H. Huang, Y. Xia, X. Tao, J. Du, J. Fang, Y. Gan and W. Zhang, *Journal of Materials Chemistry*, 2012, **22**, 10452-10456.

[36]. I.-Y. Jeon, H.-J. Choi, S.-Y. Bae, D. W. Chang, and J.-B. Baek, *Journal of Materials Chemistry*, 2011, **21**, 7820-7826.

[37]. T. Palaniselvam, R. Kannan and S. Kurungot, *Chem. Commun.*, 2011, **47**, 2910-2912.

[38]. 38.   J. R. Pels, F. Kapteijn, J. A. Moulijn, Q. Zhu and K. M. Thomas, *Carbon*, 1995, **33**, 1641-1653.

[39]. X. Wang, W. T. Zheng, H. W. Tian, S. S. Yu, W. Xu, S. H. Meng, X. D. he, J. C. Han, C. Q. Sun and B. K. Tay, *Appl. Surf. Sci.*, 2003, **220**, 30-39.

[40]. L. Lai, J. R. Potts, D. Zhan, L. Wang, C. K. Poh, C. Tang, H. Gong, Z. Shen, J. Lin, and R. S. Ruoff, *Energy Environ. Sci.*, 2012, **5**, 7936-7942.

[41]. S. M. Unni, R. Illathvalappil, S. N. Bhange, H. Puthenpediakkal, and S. Kurungot, *ACS Appl. Mater. Interface*, 2015, 7, 24256-24264.

[42]. S. Bag, B. Mondal, A. K. Das and C. R. raj, *Electrochimi. Acta*, 2015, **163**, 16-23.

[43]. Z.-S. Wu, S. Yang, Y. Sun, K. Parvez, X. Feng and K. Müllen, *J. Am. Chem. Soc.*, 2012, **134**, 9082-9085.

[44]. R. Bashyam and P. Zelenay, *Nature*, 2006, **443**, 63-66.

[45]. H.-C. Huang, I. Shown, S.-T. Chang, H.-C. Hsu, H.-Y. Du, M.-C. Kuo, K.-T. Wong, S.-F. Wang, C.-H. Wang, L.-C. Chen and K.-H. Chen, *Adv. Funct. Mater.*, 2012, **22**, 3500-3508.

Chapter-4

Graphene with Fe and S Coordinated Active Centers: An Active Competitor for the Fe-N-C Active Center for Oxygen Reduction Reaction

This chapter deals with the development of Pt-free electrocatalysts which can work under both acidic and basic pH conditions. Here, a Pt-free, iron and sulphur-doped, scrolled graphene (P12-900) system was prepared *via* annealing of polyethylenedioxythiophene (PEDOT) as a potential oxygen reduction electrocatalyst which could perform exceptionally well under acidic and basic electrolyte conditions. The residual iron chloride retained by the polymer matrix, which was employed as the oxidizing agent for the polymerization reaction, plays a vital role in generating the potential oxygen reduction reaction (ORR) active sites based on the iron and sulphur-doped graphene in the system. The composition designated as P12-900 displays ORR activity with substantially reduced overpotential in both acidic and basic electrolyte conditions, which is a unique feature reported in this class of materials. In the basic medium, P12-900 displays an ORR activity which is similar to that for the performance of 40 wt. % Pt/C. Under acidic conditions, the in-house system displays only an 80 mV overpotential in the onset potential compared to its Pt counterpart. Single-cell demonstration of a Nafion based PEMFC by employing the P12-900 catalyst as the cathode delivered the maximum power density (PD) of 345 mW cm^{-2} at 60 °C. Equally, when tested as the air electrode for a zinc-air battery with KOH electrolyte, the cell displayed a maximum power density of 320 mW cm^{-2} and a maximum current density of 685 mA cm^{-2}, which are comparable to the performance of the system based on the state-of-the-art Pt/C (322 mW cm^{-2} and 649 mA cm^{-2} respectively) cathode. Thus, the prepared precious-metal-free catalyst performs as a promising candidate for the replacement of the noble metal catalyst for PEMFCs and zinc-air battery systems with its unique capability to facilitate the electrode reactions under acidic and basic electrolyte conditions.
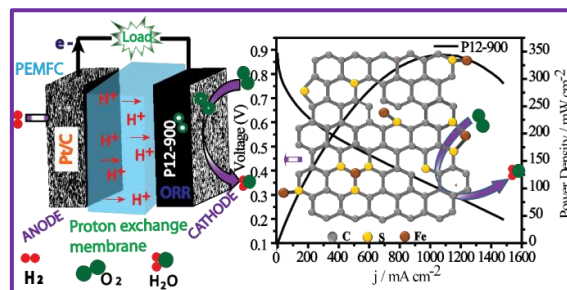
4.1 Introduction

The green renewable energy devices such as proton exchange membrane fuel cells (PEMFCs) and metal-air batteries have attracted much research attention in recent days in view of the increasing global energy demand and environmental impact of the traditional energy sources.[1-4] The cathodic oxygen reduction reaction (ORR) in these energy devices plays a key role in determining the energy efficiency.[5] The high kinetic barriers of ORR at low temperature demand the need for precious metal electrocatalysts (e.g., Pt/C).[6] However, the high cost, along with poor stability and intolerance to fuel crossover of noble metals impedes the widespread commercialization potential of a futuristic energy system such as PEMFCs.[7] A splendid study has been conducted to develop low-cost alternatives to the Pt group metals (PGM). In pursuit of the development of nonprecious electrocatalysts, the heteroatom doped carbon morphologies (dopants such as N, S, B, P, etc.) have received wide attention because some possess the ability to display ORR activity comparable to that for Pt/C in a basic medium.[8-12] The literature deals with quite extensive information on the promising ORR activity of N- or S-doped carbons in an alkaline medium.[51] However, the majority of such systems fail to perform in an acidic medium owing to the high overpotential incurred by the reaction under the low pH conditions.[13-15] Also, reports are available for the codoping of S and N or N and B or N and P in the carbon framework to enhance the overall ORR activity.[16-19] One important factor which decides the overall ORR activity in terms of the achievable current density from the doped carbon catalysts is the number density of the active reaction sites responsible for dioxygen adsorption and its subsequent reduction.[20,21] Even with several structural modifications practiced to improve the surface density of such active centers, the general trend is that the heteroatom doped carbon catalysts display poor performance in an acidic medium compared to a basic environment.[22] One effective way to overcome this limitation is by coordinating the doped heteroatom centers with 3d transition metals such as iron or cobalt. There are reports highlighting the promising ORR activities displayed by such systems in acidic conditions.[23,24]

Fe-N_x doped carbon usually shows reasonable ORR activity in acidic condition (still experiences higher overpotential compared to Pt/C) and excellent activity in alkaline conditions.[25-27] Experimental and theoretical studies have been carried out extensively to understand the improved performance displayed by such systems.[25,28-30] It is found that there exists a cooperative interaction by which Fe increases the O-O bond length through back-bonding with adsorbed oxygen, whereas the doped nitrogen moieties activate the neighbouring carbon atoms through charge density/spin density changes.[31] Apart from the Fe-N_x type active centers, Fe-P type interactions also proven to be catalysing the reduction of dioxygen molecule

in the acidic environment that has been reported.[31] However, the ORR activity of the Fe-P systems is low in comparison to the Fe-N_x counterparts. Moreover, improvement in the ORR activity of the Fe-N_x doped carbon has also been observed with additional doping of S atoms in the carbon matrix.[32,33] The exact role of S in such systems is still unclear, but this moiety is expected to incur activation of the carbon atoms through spin density changes as reported by Yang *et al.*[34]

In the ongoing efforts to develop an ORR catalyst that can work well in both acidic and basic electrolyte conditions, the iron pyrite (FeS_2) systems are found to be displaying ORR activity in both alkaline and acidic conditions. However, they were found to offer lesser activity compared to the Fe-N_x type coordination. This lesser activity contribution originates primarily from the poor electrical conductivity of the pyrite type materials.[35] The ORR activity modulation in systems based on the Fe-S bonding is possible by adopting a strategy through which a strong interaction between the doped-S and Fe can be achieved on the carbon surface. This work is based on such a strategy, wherein we could prepare Fe and S-doped graphene with enriched Fe-S coordination sites in the graphene matrix *via* a simple process involving annealing of polyethylenedioxithiophene (PEDOT) subsequent to its formation from ethylenedioxythiophene as the monomer and $FeCl_3$ as the oxidizing agent. The Fe moieties present in the system establish the Fe-S_x coordination with a fraction of the doped S species in the graphene matrix which are formed during the pyrolysis of PEDOT (**Scheme 4.1**). The catalyst shows substantially improved ORR activity compared to the Fe-N_x type catalysts in both the acidic and basic medium, positioning it as a strong competitor for the Fe-N_x type systems to serve as an alternate to Pt/C in both acid and alkaline conditions. The work also demonstrates the practical system-level application of the present catalysts by testing the single cells of the PEMFC and Zn-air battery, which are based on acidic (Nafion) and basic (KOH) electrolytes, respectively.

4.2 Experimental Section

4.2.1 Materials

Ethylenedioxythiophene (EDOT), anhydrous iron chloride ($FeCl_3$), and potassium hydroxide were procured from Sigma-Aldrich. Sulfuric acid, acetonitrile, and zinc dust were obtained from Thomas Baker, India. All the chemicals were used without any further purification.

4.2.2 Synthesis

400 mg of the EDOT monomer was mixed with 40 mL of acetonitrile in a beaker while maintaining stirring of the mixture. A solution of $FeCl_3$ (5.475 g) in acetonitrile (20 mL) was added dropwise into the monomer solution. The ratio of the monomer to $FeCl_3$ was maintained as 1:12. The mixture was continuously stirred for 24 h at room temperature to ensure complete polymerization of the EDOT monomer into PEDOT. The polymer was dried at 80 °C and then annealed at different temperatures such as 800, 900, and 1000 °C for 1 h in an argon atmosphere. This was followed by an acid wash using 0.5 M H_2SO_4 at 80 °C for 8 h to remove the surface metal oxide impurities. It was then filtered and washed several times with deionized water (DI) and dried overnight at 80 °C. A second annealing in an inert atmosphere was performed on the acid-washed carbon recovered from the first annealing process for 1 h at 800, 900, and 1000 °C. Thus, obtained final carbon samples after the second pyrolysis process are respectively named as P12-800, P12-900, and P12-1000. For the purpose of comparison, PEDOT was also prepared without using $FeCl_3$ to obtain the catalyst which is free from Fe. This was achieved by preparing PEDOT through electrochemical deposition on a conducting substrate (FTO). The main purpose of the electrochemical method of EDOT polymerization is to avoid the presence of any kind of nitrogen impurities in the polymer. Lithium perchlorate and the EDOT monomer were used as the supporting electrolyte and monomer, respectively, in an acetonitrile solution. The electrochemical deposition on the FTO plate was performed at 10 mA cm^{-2} current density. The as-deposited PEDOT on FTO was washed with the acetonitrile solution and dried under an IR lamp. After drying, the PEDOT layer was scratched out from the FTO plate and annealed at 900 °C in an inert atmosphere for 1 h. The annealed sample was subjected to acid washing at 80 °C in 0.5 M H_2SO_4 for 8 h. After drying, it was again annealed for 1 h at 900 °C in an argon atmosphere. Thus obtained control sample is named as P-900. To make an activity comparison of Fe-Sx with Fe-N$_x$ type coordination, we prepared Fe-N$_x$ doped carbon (FeN/C-900) as another control sample by following the procedure reported by Zelenay *et al.* for comparing the ORR activity.[36]
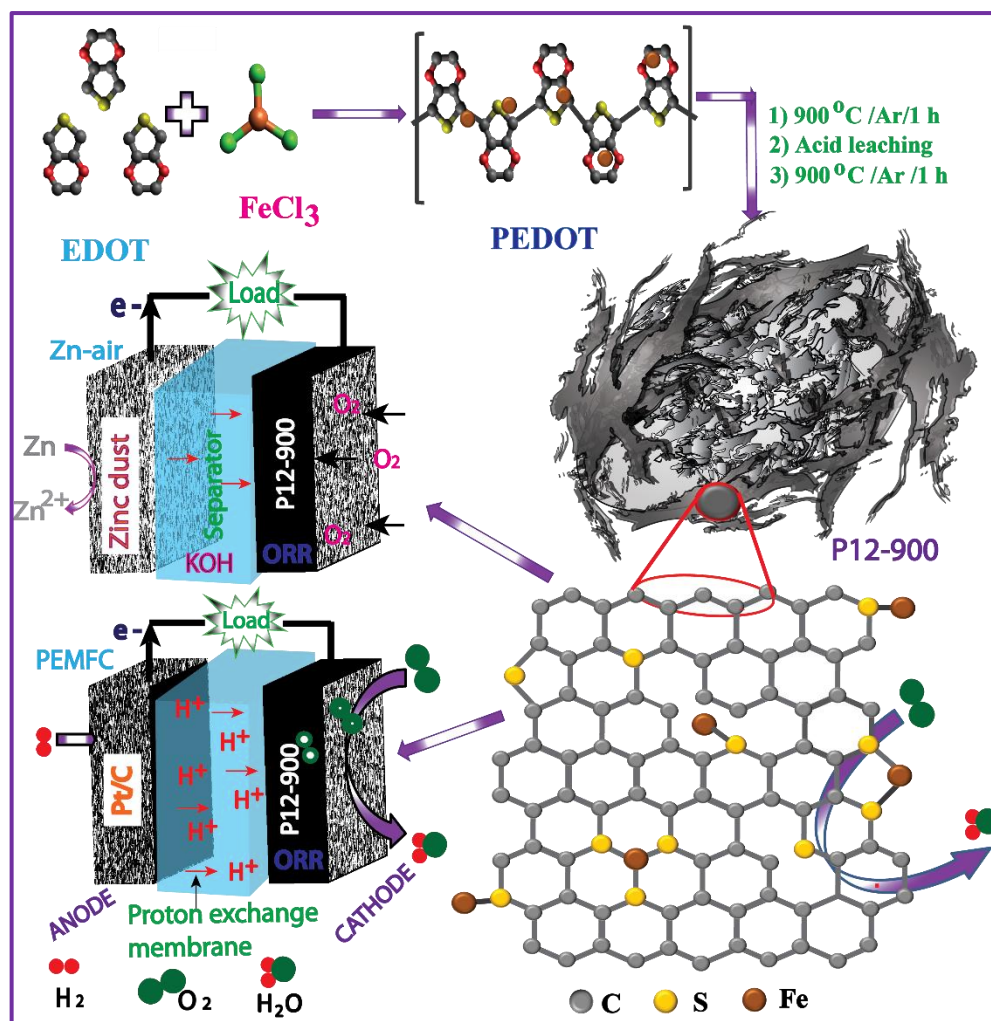
Scheme 4.1 A schematic representation of the synthesis of P12-900, showing the Fe and S-doped graphene sheets where the C-S and Fe-S surface moieties work as the catalytically active centres for facilitating electrochemical oxygen reduction reaction (ORR) in both acidic and alkaline pH conditions. The scheme also shows the demonstration of the catalyst as the cathode electrode material for PEMFC (acidic condition) and Zn-air battery (basic condition).

4.2.3 Synthesis of FeN/C-900

200 mg of Vulcan carbon was dispersed in 40 ml of 1 M HCl using a bath sonication for 30 min by maintaining the temperature below 10 ºC. 1 ml of aniline in 10 ml of 1 M HCl was added into the above dispersed solution. 2.5 g of ammonium persulphate was taken in 20 ml of 1 M HCl and the solution was kept for cooling. Subsequently, the solution was added dropwise into the above suspension with constant stirring. 4.55 g of iron chloride hexahydrate taken in 20 ml of 1 M HCL was added in the above suspension and the mixture was kept for constant stirring for 24 h. Followed by this, the recovered material was dried at 80 ºC and the powdered sample was pyrolyzed at 900 ºC for 1 h in inert atmosphere followed by acid washing in 0.5 M

H_2SO_4 for 8 h at 80 °C. It was filtered and washed with DI water several times and dried at 80 °C for 12 h. A second round of pyrolysis was carried out at 900 °C for 1 h and the catalyst is named as FeN/C-900.

4.3 Physical Characterization

Transmission electron microscope (TEM) Tecnai-T 20 model at an acceleration voltage of 200 kV was used for the analysis of the morphology of the synthesized materials. Sample for the TEM scanning was prepared by dispersing the catalyst sample in isopropyl alcohol and drop coating on the carbon coated Cu grid followed by drying. For X-ray diffraction, a Rigaku Smartlab diffractometer was used and the scan rate was maintained as 2° min^{-1} (Cu Kα radiation (λ=1.5406 Å)). A VG Microtech Multilab ESCA 3000 spectrometer (Mg Kα X-ray source (hν=1.2536 keV)) was used for the X-ray photoelectron spectroscopic (XPS) investigation of the catalysts. Raman analysis was performed using an HR 800 Raman spectrometer (Jobin Yvon, Horiba, France) at 632 nm red laser (NRS 1500 W).

4.4 Electrochemical Studies

The electrochemical analysis was carried out in an Auto-Lab Potentio-Galvanostat using a three-electrode system by using a glassy carbon electrode (GCE) as the working electrode, graphite rod and $Hg/HgSO_4$ as the counter and reference electrode, respectively. For the catalyst ink preparation, 10 mg of the P12 catalyst was dispersed in 1 ml solution of 3:1 ratio of IPA: water and 40 μl of 5 wt. % Nafion solution. 10 μl of the catalyst ink was drop coated on the glassy carbon electrode for the preparation of the working electrode and the coated surface was dried under an IR lamp to get the uniform coating on the electrode surface. 0.50 mg cm^{-2} loading of the catalyst was maintained on the glassy carbon electrode which is having an electrode area of 0.19625 cm^2. For comparison purpose, 40 wt. % Pt/C with a catalyst loading of 0.20 mg cm^{-2} was used in the half-cell studies. The linear sweep voltammograms (LSVs) were recorded by maintaining an electrode rotation speed of 1600 rpm and a voltage scan rate of 10 mV s^{-1} in oxygen saturated 0.5 M H_2SO_4 and 0.1 M KOH solution. For the accelerated durability test (ADT), cyclic voltammograms were recorded in between the potential range of 0.60 to 1.0 V *vs*. RHE at a voltage scan rate of 100 mV s^{-1} for 10000 potential cycling. Subsequent to the potential cycling, the LSV was measured at a voltage scan rate of 10 mV s^{-1} and the data was compared with the LSV profile obtained before performing the cycling studies.

4.4.1 Rotating Ring Disc Electrode (RRDE) Analysis

The RRDE study was performed at an electrode rotation rate of 1600 rpm in oxygen saturated 0.5 M H_2SO_4 at a scan rate of 10 mV s^{-1}. The ring potential was held at 1.5 V with respect to RHE. $K_3Fe(CN)_6$ solution was used for the measurement of the collection efficiency of the ring electrode. The measured collection efficiency is 0.37. To calculate the hydrogen peroxide percentage (mol %) and the number of electrons transferred during the reduction process, the following equation was used:

$$H_2O_2\% = \frac{\frac{200 \times I_R}{N}}{I_D + \frac{I_R}{N}} \tag{1}$$

$$n = \frac{(4 \times I_D)}{(I_D + \frac{I_R}{N})} \tag{2}$$

where, I_D is the disc current, I_R is the ring current and N is the collection efficiency.

4.4.2 Single-cell Analysis

A Nafion 212 membrane was used as the proton conducting membrane for fabricating the membrane electrode assembly (MEA). The pre-treatment of the membrane was performed by initially giving 30 % HNO_3 treatment at 80 ^{o}C for 1 h followed by DI water washing. The membrane was subsequently treated with 5 % H_2O_2 at 80 ^{o}C for 1 h followed by DI water washing. The final step involves treatment in 1 M H_2SO_4 for 1 h followed by DI water washing. The pre-treated membrane was stored in DI water for further use while assembling the MEA. The electrode was prepared by brush coating the catalyst slurry on the surface of a carbon gas diffusion layer (GDL). For the cathode, the catalyst slurry was prepared by mixing P12-900 and Nafion 20 wt. % (DuPont, USA) dispersion in isopropyl alcohol. A Nafion to catalyst ratio of 0.50 was maintained in the catalyst slurry. The slurry was applied onto the GDL (SGL, Germany). For the anode, Pt/C (40 wt. %) was used as the catalyst. The loadings of the catalyst in the anode and cathode are 0.50 and 2.0 mg cm^{-2}, respectively. The MEA was prepared by sandwiching the pretreated Nafion membrane between the anode and cathode electrodes by maintaining an active area of 4 cm^2. The assembly was hot pressed for 1 min at a temperature of 130 ^{o}C and a pressure of 0.25 ton. The single-cell evaluation of the MEA was performed by using a 4 cm^2 test fixture procured from Fuel Cell Technologies, Inc, USA, and by connecting to a fuel cell test station (Fuel Cell Technologies Inc, USA). Data acquisition was performed using LabView 5.1 software. 0.3 slpm of hydrogen and 0.2 slpm of oxygen were supplied to

the anode and cathode, respectively, without applying any back pressure. The measurement was performed under 100 % relative humidity condition by operating at a cell temperature of 60 °C.

4.4.3 Zinc-air Battery Analysis

For the fabrication of the zinc-air battery, P12-900 was used as the catalyst for the cathode. A dispersed solution of the catalyst in isopropyl alcohol was coated on to the porous carbon paper by keeping 1 cm^2 electrode active area to achieve the catalyst loading of 2 mg cm^{-2}. 6 M KOH was employed as the electrolyte and zinc powder was used as the anode. The anode and cathode compartments were separated with the help of a Celgard membrane. The battery testing was performed at room temperature by maintaining a continuous flow of oxygen on the cathode side. The setup was connected to an SP300 Biologic test station in order to measure the I-V polarization

4.5 Results and Discussion

4.5.1 XRD and Raman Analysis

Information on the textural and morphological features attained during the transformation of the polymer to the carbon phase has been gathered first by performing a powder X-ray diffraction analysis (PXRD) of P12-900 and P-900 (**Figure 4.1a**). In **Figure 4.1a**, both samples show a broad peak at a 2θ value of ~25.9° which corresponds to the (002) graphitic plane of the carbon. In the case of P12-900, additional peaks at 35.54°, 43.2°, and 65.54° (JCPDS No. 65-3356) (**Figure 4.2a**) appeared, which are attributed to the presence of the hexagonal metal sulfide (FeS) phase.[37]

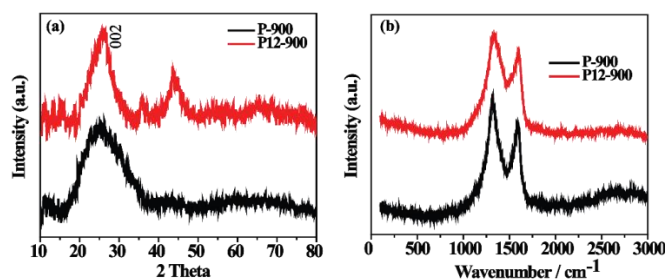**Figure 4.1** (a) X-ray diffraction (XRD) profiles and (b) Raman spectra of the P12-900 and P-900 electrocatalysts.

In contrast to the XRD results, the Raman spectrum of P12-900 (**Figure 4.1b**) does not show any peak corresponding to the FeS particles which is usually observed in these types of materials below 1000 cm^{-1}.[38] One possible reason for this is that the FeS nanoparticles are well

encapsulated within the graphene sheets. The D band (corresponding to the defective sites of carbon) and G band (representing the graphitization of the system) of P12-900 and P-900 are positioned at 1317 and 1593 cm^{-1}, respectively.[39] The I_D/I_G ratio (the intensity ratio of the D and G bands) of P-900 is less (1.13) compared to that of P12-900 (1.17). With respect
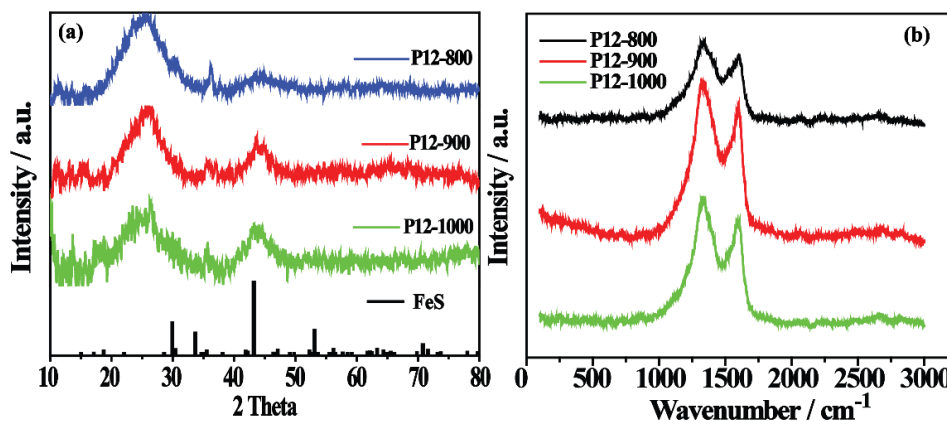
Figure 4.2 (a) X-ray diffraction (XRD) profiles and (b) Raman spectra of the P12 electrocatalysts prepared at different annealing temperatures.

to the increasing calcination temperature, the I_D/I_G ratio follows the order P12-800 (1.05) < P12-900 (1.17) < P12-1000 (1.21) (**Figure 4.2b**). At high temperature, the encapsulated FeS moieties decompose and produce sulphur gases. Expulsion of the sulphur gases from the graphene matrix may assist the doping of the graphene sheets with sulphur while inducing the defective sites.

4.5.2 SEM and TEM Analysis

Investigation of the material with the help of scanning electron microscopy (SEM) and transmission electron microscopy (TEM) revealed fine details on the morphology and microstructure of the materials. The SEM images of P12-900, as presented in **Figure 4.3a**, suggest the morphology of the material similar to buckled graphene nanosheets with large inherent porosity. Further analysis with the help of TEM provides more insightful information on the surface of the carbon layer (**Figure 4.3b-f**). For example, the TEM image shown in **Figure 4.3b** displays the scrolled nature of the carbon nanosheets possessing a transparent lamellar structure with wrinkles as in the case of the graphene sheets prepared by the conventional routes. On the other hand, **Figure 4.3c** shows the presence of the encapsulated FeS nanoparticles in the graphene sheet as indicated by the red arrows.
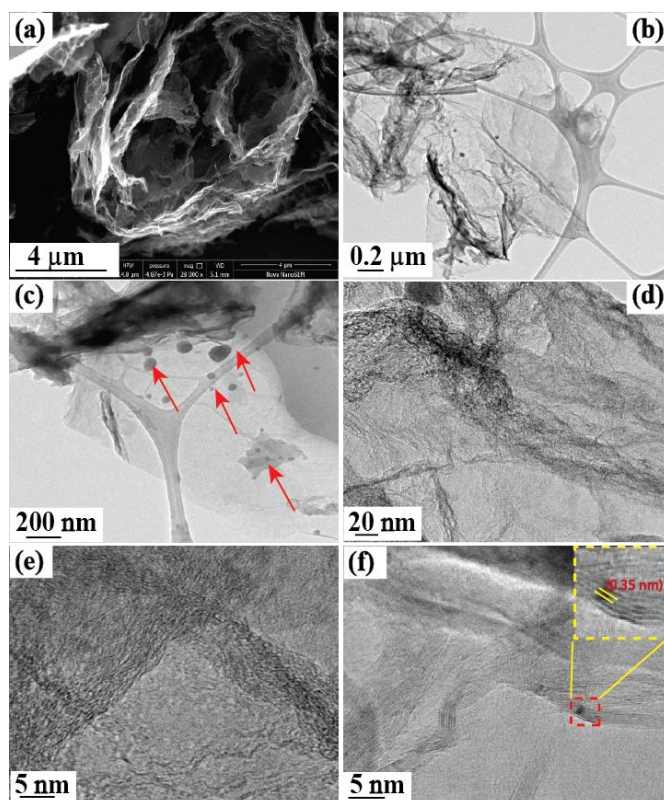
Figure 4.3 Morphological investigation of P12-900 with the help of SEM and TEM: (a) SEM image of P12-900 indicating the infolding of the PEDOT derived graphene; b) the TEM image of P12-900 displaying the transparent lamellar structure of the graphene sheet; c) the TEM image showing the presence of the encapsulated FeS nanoparticles by the graphene sheets; d) magnified TEM image of P12-900 displaying the scrolled nature of graphene; e and f) show the HRTEM images of the graphene sheets displaying the transparent graphene layers with the lattice fringes and their buckled nature due to heteroatom doping are clearly evident.

Most of these nanoparticles are well wrapped with the graphene sheets. **Figure 4.3d to f** correspond to the high-resolution TEM (HRTEM) images of P12-900, which show the presence of the disordered lattice fringes of the carbon. The d-spacing calculated from the HRTEM image corresponding to P12- 900 is 0.35 nm (**Figure 4.3f**), and it indicates effective graphitization of the carbon sheets. Buckling of the graphene layers is a characteristic feature of the heteroatom doped graphene systems, and the clear appearance of the disordered nature in the present case indicates effective doping of the heteroatoms in the sheets.[40] Interestingly, the SEM image of the P12-800 and P12-1000 electrocatalysts show the morphologies which differ from that of P12-900 (**Figure 4.4a, b**). It indicates that the morphology of the carbon derived from the polymer strongly depends on the annealing temperature. The elemental mapping gives a clear indication of the uniform distribution of the S and Fe present in the matrix of the graphene

nanosheet (**Figure 4.5**). The buckled graphene nanosheet is thereby believed to contain uniformly distributed S and Fe moieties.
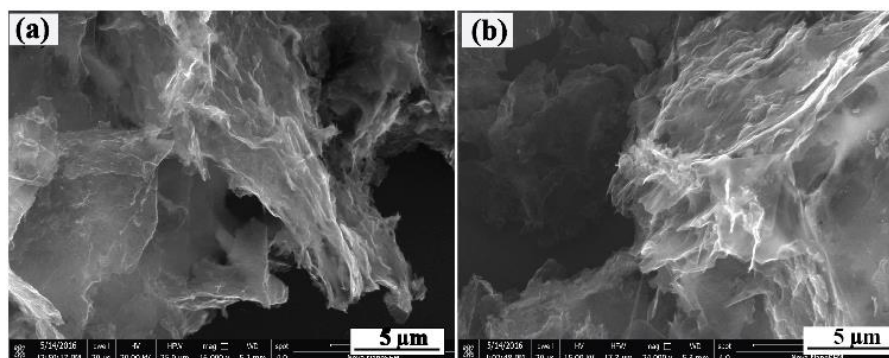
Figure 4.4. (a) P12-800 and (b) P12-1000.
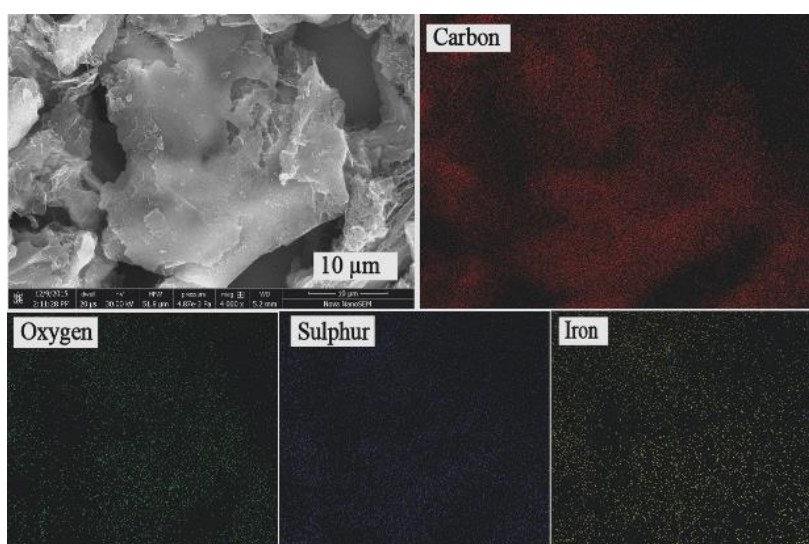
Figure 4.5. Elemental mapping of P12-900.

4.5.3 Surface Area Analysis

The Brunauer-Emmett-Teller (BET) surface area analysis of the samples calcined at different temperatures (**Figure 4.6a**) shows that as the annealing temperature increases, the BET surface area also concomitantly increases in the order P12-800 (1125 m^2 g^{-1}) < P12-900 (1684 m^2 g^{-1}) < P12-1000 (1860 m^2 g^{-1}). This trend is in accordance with the previously discussed differences in the morphologies of the materials as revealed through the SEM images of the samples prepared by calcining at different temperatures. The pore size of the P12 samples mainly lies between 1 to 4 nm (**Figure 4.6b**). The cumulative pore area of the P12 samples was found to increase with the increase in the pyrolysis temperature.
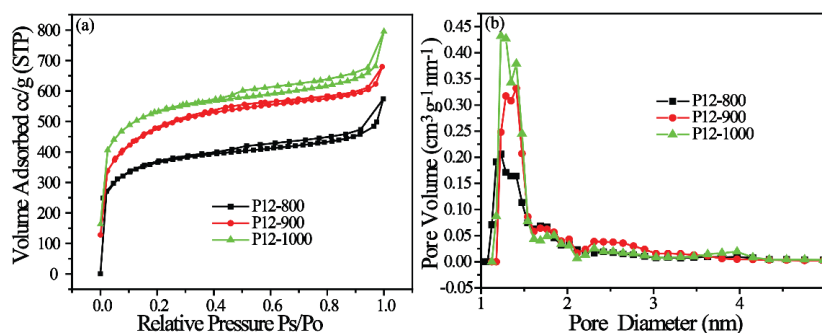
Figure 4.6 (a) N2 adsorption-desorption isotherms and (b) pore size distribution profiles of P12-800, P12-900, and P12-1000.

4.5.4 XPS Analysis
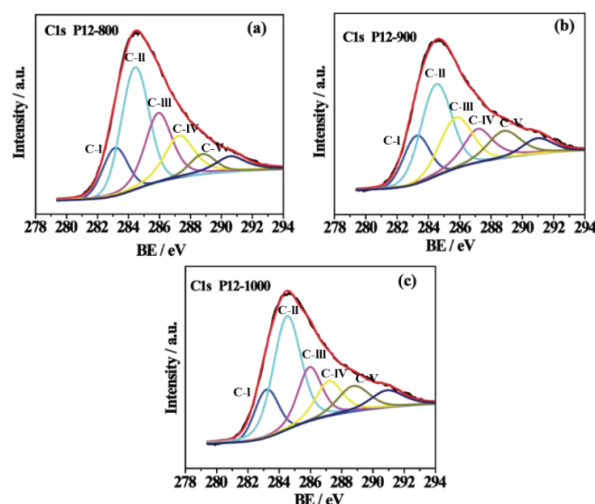
Figure 4.7 Fitted C1s spectra of (a) P12-800, (b) P12-900, and (c) P12-1000. Different carbon species are marked as C-I (metal carbide), C-II (C=C), C-III (C-S), C-IV (C=O) and C-V (-O-C=O).

The X-ray photoelectron spectroscopy (XPS) investigation gives information on the presence and nature of the coordination of carbon, oxygen, iron, and sulphur over the graphene sheet surface. The C 1s spectrum of P12-900 (**Figure 4.7b**) is fitted to gain insight on the different types of carbon bonding existing on the surface. The peak designated as C-I at 283.24 eV corresponds to the metal carbide, and the peak marked as C-II at 284.50 eV is attributed to the C=C coordinations.[41] Moreover, a strong indication of the presence of the C-S bond due to S doping is obtained from the peak represented as C-III at 285.74 eV.[42] The peaks denoted as C-IV and C-V are corresponding to the binding energy value of 287.16 and 288.83 eV of the fitted C 1s spectra, which also provide information on the C=O and -O-C=O type interactions of the carbon.[41] A similarity in peaks was also observed in the case of P12-800 and P12-1000 (**Figure 4.7a and c**).
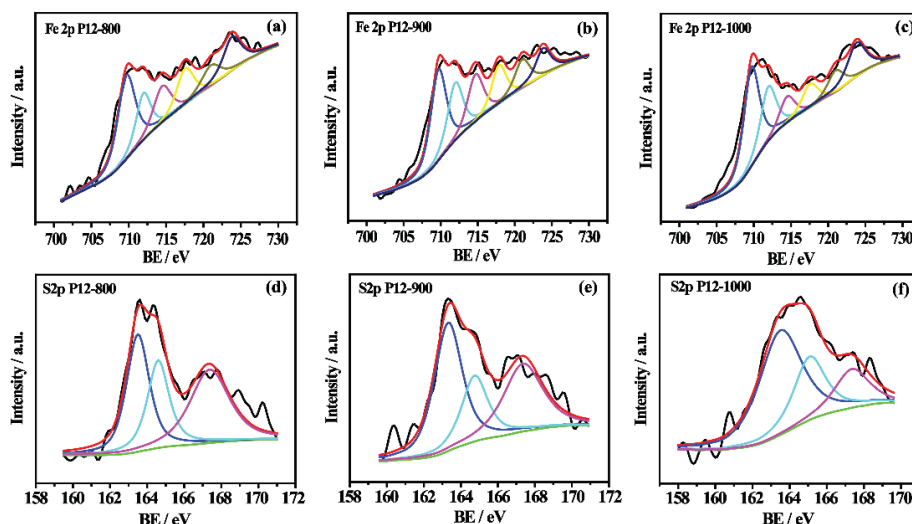
Figure 4.8 Fitted Fe 2p spectra of (a) P12-800, (b) P12-900, and (c) P12-1000; and the deconvoluted S 2p spectra of (d) P12-800, (e) P12-900, and (f) P12-1000.

Figure 4.8a-c shows the deconvoluted Fe 2p spectra of P12-800, P12-900, and P12-1000. The Fe $2p_{3/2}$ and Fe $2p_{1/2}$ peaks of lower binding energy (709.70 eV) and higher binding energy (721.01 eV) are ascribed to the +2 oxidation state of Fe in the Fe-S bond.[42-45] On the other hand, the peaks appearing at binding energies of 711.96 and the 723.83 eV represent the +3 oxidation state of Fe.[45,46] Since iron sulfide exhibits high reactivity toward oxygen, it is expected that the reaction with the oxygen present in PEDOT and iron sulfide can lead to the formation of iron oxide during the pyrolysis process. All the three samples display similar features in their Fe 2p spectral characteristics. **Figure 4.8d-f** shows the fitted S 2p spectra of the three P12 catalysts. The peaks appearing at around 163.5 and 164.74 eV represent the $2p_{3/2}$ and $2p_{1/2}$ states, respectively, of S, and the presence of these peaks suggests the major contribution by S^{2-}.[42,45,47] Another peak appearing at 167.36 eV indicates C-SO$_x$-C interactions.[41,42] Moreover, the peak expected at ~162.0 eV from the thiol groups is absent in the XPS spectra of all the samples.[48] This suggests that the sulphur doping is occurring mainly at the edges of the graphene sheets thereby facilitating efficient coordination with the iron moieties. The change in spin density of the carbon and sulphur is expected to play a crucial role in attaining improved ORR activity of these types of carbon catalysts.[34] Since the XPS spectra gave valid evidence for the existence of the Fe-S bonding along with the doping of iron and sulphur in the PEDOT derived graphene sheets, it is believed that the coexistence of these sites will act as efficient ORR active centers in these catalysts. Calculation of the atom percentage (at. %) of Fe and S from the XPS data for P12-900 gives 5.3 at. % of Fe and 2.44 at. % of S. It is interesting to note that the iron content in the P12 catalysts increases whereas the sulphur content decreases with the increase in the

annealing temperature (**Table 4.1**). This could be possibly caused by the partial removal of the less stable sulphur species at high temperature, leading to a proportional increase in the Fe content in the overall composition.

Table 4.1. The elemental composition of the surface of the P12 electrocatalyst calculated from XPS.

Sample	C (atom %)	O (atom %)	S (atom %)	Fe (atom %)
P12-800	78.91	13.63	2.69	4.76
P12-900	80.01	12.20	2.44	5.30
P12-1000	81.02	11.46	2.15	5.34

4.5.5 Electrochemical Analysis

The oxygen reduction reaction (ORR) activity of the P12 samples under acidic and basic pH conditions was evaluated by performing the rotating disc electrode (RDE) and rotating ring disk electrode (RRDE) techniques in 0.5 M H_2SO_4 and 0.1 M KOH solutions. The linear sweep voltammogram (LSV) was measured at a scan rate of 10 mV s^{-1} with different electrode rotation speeds (**Figure 4.9**). A glassy carbon electrode was used as the working electrode, and a graphite rod and reversible hydrogen electrode were used as the counter and reference electrodes, respectively.
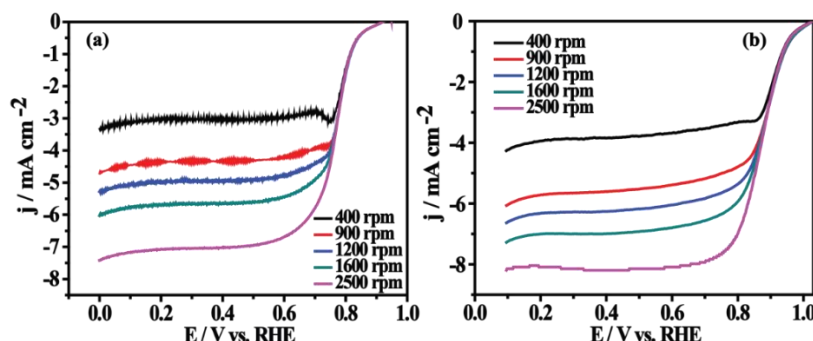
Figure 4.9 Linear sweep voltammograms (LSVs) of P12-900 measured at a scan rate 10 mV s^{-1} with different electrode rotation speeds: (a) in 0.5 M H_2SO_4 and (b) in 0.1 M KOH electrolyte.

Figure 4.10a shows the LSV profiles which were measured at an electrode rotation speed of 1600 rpm in 0.5 M H_2SO_4. The catalyst P12-900 shows an onset potential of 0.92 V (for Pt/C, the onset potential is 1.0 V) and a half-wave potential of 0.78 V (for Pt/C half-wave potential is 0.86 V) *vs.* RHE, which are more positive than that of P12-800 and P12-1000. The onset potentials of P12-800 and P12-1000 are observed at 0.90 V, each being 16 mV less compared to that of P12-900. Similarly, the half-wave potentials of P12-800 and P12-1000 are observed at 0.77 and 0.75 V, respectively. This is respectively 10 mV and 30 mV less compared to the

corresponding value of P12-900. P12-900 shows an overpotential difference of 80 mV for the onset and half-wave potentials compared to the commercial Pt/C (40 wt. %). It is also important to note that the ORR activity of the P12-900 catalyst is superior to the recently reported systems which are active in acidic medium. It also should be noted that the prepared control sample P-900, which contains only the doped S sites without coordinating to Fe, shows poor performance toward ORR under acidic conditions. This substantial difference in terms of the ORR performance of the P12 catalysts and their iron-free counterpart highlights the necessity of the generation of the Fe-S_x active centers to allow the system to be enabled to facilitate ORR under acidic conditions.

In order to differentiate how the Fe-S and Fe-N active centers differ in terms of the ORR activity under acidic conditions, the activity of P12-900 catalyst is compared with that of FeN/C-900 (prepared by the synthesis method used by Zelenay *et al.*[36,50]). FeN/C-900 displays onset and half-wave potentials at 0.89 and 0.75 V vs RHE, which confirmed that this catalyst is inferior to P12-900 by an overpotential of 30 mV each in the onset and half-wave potentials. It indicates that the Fe-Sx active sites in P12-900 are more efficient to facilitate ORR under acidic conditions compared to the Fe-N active sites present in FeN/C-900. The Tafel slope measured in the case of P12-900 is 61 mV decade^{-1}, which specifies that the dioxygen reduction mechanism is apparently similar to that of Pt/C (68 mV decade^{-1}). On the other hand, P12-800 (88 mV decade^{-1}) and P12-1000 (99 mV decade^{-1}) show much higher Tafel slope values, indicating less facile reactions in these cases compared to P12-900 (**Figure 4.10b**). The mass activity is calculated for all the catalysts at a fixed potential of 0.85 V *vs.* RHE. The activity estimated in the case of P12-900 is 0.833 A g^{-1}, which is superior to both P12-800 (0.630 A g^{-1}) and P12-1000 (0.530 A g^{-1}), respectively.

The number of electrons transferred and the hydrogen peroxide formation (H_2O_2 %) during ORR were measured using the rotating ring disk electrode (RRDE) studies. The RRDE voltammograms are recorded at a scan rate of 10 mV s^{-1} with an electrode rotation speed of 1600 rpm in oxygen saturated 0.5 M H_2SO_4. **Equations 1 and 2** were used to calculate the percentage of H_2O_2 and the number of electrons transferred during ORR. The P12-800, P12-900, and P12-1000 are found to show less than 3% peroxide yield compared to the substantial amount of ca. 64% recorded in the case of P-900 (**Figure 4.10c**). This certainly shows that the P12 catalysts possess the fertile surface with the right combination of active sites which are able to drive the dioxygen reduction kinetics through the preferred four-electron pathway. In particular, the drastic differences between P-900 and P12-900 in terms of their ORR activity and kinetic pathways clearly indicate the decisive role played by the Fe-S_x active sites in the

latter case to enable its functioning as a potential ORR electrocatalyst in an acid environment. The magnitude of the performance improvement accomplished simply by changing the nature
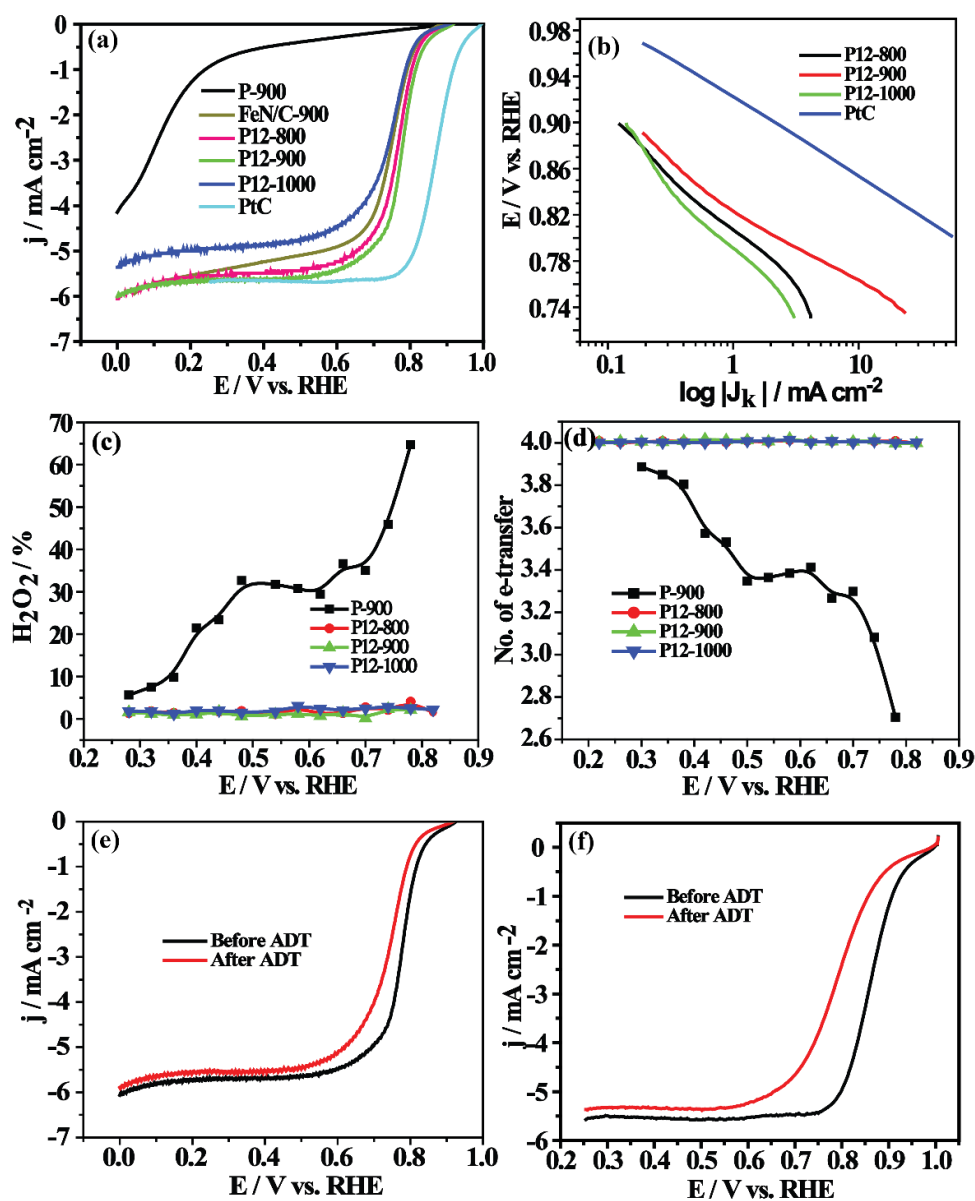
Figure 4.10 (a) The comparative LSVs of the different electrocatalysts measured under O_2 saturated 0.5 M H_2SO_4 at 10 mV s^{-1} scan rate using the electrode rotation rate of 1600 rpm., (b) the Tafel plots generated from the LSV profiles recorded for the P12 catalysts in 0.5 M H_2SO_4, (c) hydrogen peroxide yield, (d) the number of the electrons transferred in the case of the P12 electrocatalysts at different potentials in 0.5 M H_2SO_4 as calculated from RRDE, (e) LSVs of P12-900 before and after 10000 potential cycling, and (f) LSVs of Pt/C before and after ADT in 0.5 M $HClO_4$, recorded at a scan rate of 10 mV s^{-1} and an electrode rotation speed of 1600 rpm.

of the active sites suggests that the dependency of the ORR activity on the electrolyte pH is strongly a function of the nature of the active centers present in the case of the Pt-free

electrocatalysts. Once such active sites are created and their number density is maintained by strategically tuning the preparation protocols, the realization of the Pt-free catalysts with activity characteristics similar to those of the state-of-the-art Pt catalysts under proton exchange conditions is a clear possibility. The physically dispersed Fe moieties are vulnerable to leaching under the acid environment. Also, since these active sites are stitched on the carbon framework of the graphene, even carbon corrosion can remove some of the active sites with performance degradation. Hence, it is important to validate that the Fe-based active centers generated in the present case can survive the potential induced conditions under acid environments. This has been validated by performing an accelerated durability test (ADT) of P12-900 by maintaining an electrochemical condition which can accelerate the carbon corrosion. The material was subjected to 10000 potential cycles in the potential range 0.60 to 1.0 V *vs.* RHE. From the ADT profiles presented in **Figure 4.10e**, it can be seen that P12-900 suffers only a 30 mV potential shift in the half-wave potential with apparently no change in the onset potential. In comparison to P12-900, Pt/C suffers a 73 mV drop in the half-wave potential after subjection to 5000 potential cycles, (**Figure 4.10f**) accounting for the ~2.5 times higher degradation compared to P12-900. The morphology of P12-900 was investigated with the help of TEM analysis subsequent to ADT. The TEM images present in **Figure 4.11** show that the morphological features are more or less completely retained even after ADT. This high degree of retention of the morphological features and lower rate of performance loss subsequent to ADT correlate to the strong structural integrity possessed by the material, which plays a key role in maintaining the active sites intact under the drastic conditions of different pH and potential induced conditions.
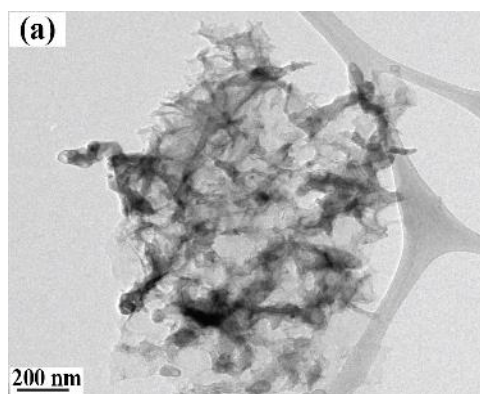
Figure 4.11 TEM images of P12-900 recorded after the 10000 ADT cycles in 0.5 M H_2SO_4.

Since the material shows excellent ORR activity in an acidic medium, as a realistic system-level validation, a single cell of PEMFC was assembled and tested by fabricating a membrane electrode assembly (MEA) in which P12-900 was employed as the cathode catalyst (2 mg cm⁻

^{2} loading). The commercial Nafion membrane was employed as the proton conducting electrolyte membrane. The anode was prepared by using the commercial Pt/C catalyst by maintaining a loading of 0.50 mg cm^{-2}. As can be seen from the current (I)-voltage (V) polarization plot presented in **Figure 4.12b**, the system displays an open circuit potential (OCV) of 0.89 V which is 30 mV lesser compared to the half-cell data.
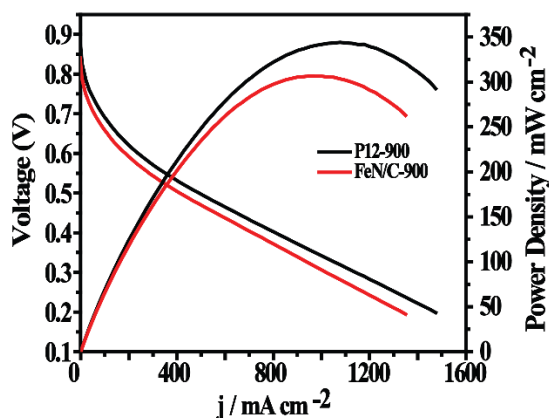
Figure 4.12 Comparison of the single-cell polarization plots of the MEAs fabricated by using P12-900 and FeN/C-900 as the cathode (2.0 mg cm^{-2}) catalyst and Pt/C (0.50 mg cm^{-2}) as the anode catalyst. The testing was carried out at a cell temperature of 60 $^{\circ}$C without applying any back pressure.

The polarization curve displays the standard features of the I-V plot in the case of the Pt-based MEAs, consisting of all three distinct overpotential regions corresponding to activation, ohmic and mass transfer. The system delivered a maximum power output of 345 mW cm^{-2} (at 0.32 V) and a maximum current density of 1.47 A cm^{-2} (at 0.2 V) without applying any back pressure. Thus, by looking at the performance profile based on the single-cell evaluation of the P12-900 catalyst-derived MEA, the catalyst as the cathode electrode can be seen as performing exceptionally well by delivering a power density value which is comparable to that reported to date for the non-Pt-based electrocatalysts in PEMFCs.[24,49] Furthermore, the performance of P12-900 is comparable to the electrocatalyst prepared using a silica template to obtain mesoporosity.[51] However, in this work, a high surface area and microporous structure are achieved without using any template. Thus, the intrinsic ORR activity of P12-900 as revealed through the half-cell studies could be translated in terms of power output in its realistic performance validation in a single cell mode by employing the catalyst as the cathode of the system. Even though the performance of this system is lower than that of the MEAs based on the Pt/C cathode, this is one of the best results obtained on a Pt-free system reported to date, offering new avenues for designing potential catalysts by logically developing strategies to enrich the Fe-S$_x$ active center density in the catalyst system. Similarly, for comparison, we have

fabricated an MEA by employing FeN/C-900 as the cathode catalyst (2 mg cm^{-2}, loading), and by maintaining the rest of the conditions as in the case of the P12-900 based MEA. The FeN/C-900 based MEA delivers a maximum power density of 306 mW cm^{-2} (at 0.32 V) and a current density of 1.35 A cm^{-2} (at 0.2 V) without applying any back pressure (**Figure 12b**). Thus, the comparison of the single-cell data in the above two cases substantiates the high intrinsic ORR activity displayed by P12-900 over FeN/C-900. A comparison of the single-cell data and analysis parameters of the present systems with the similar systems reported in the literature. The electrochemical stability of the single-cell fabricated from P12-900 was carried out, and the corresponding data are presented in **Figure 4.13**, by monitoring the current output from the MEA at a constant potential of 0.4 V for 12 h. The system delivered a current density of ~475 mA cm^{-2} without applying any back pressure at 60 °C under an H_2 and O_2 atmosphere and 100% humidification. The MEA displays stable performance once the cell reached 475 mA cm^{-2}, 4 h after the commencement of the test. It is observed from the stability data that the performance shows a gradual improvement in the initial hours and, thereafter, stabilizes by delivering a steady 475 mA cm^{-2} current. The initial improvement in the performance could be due to the activation of the catalyst under the electrochemical conditions.
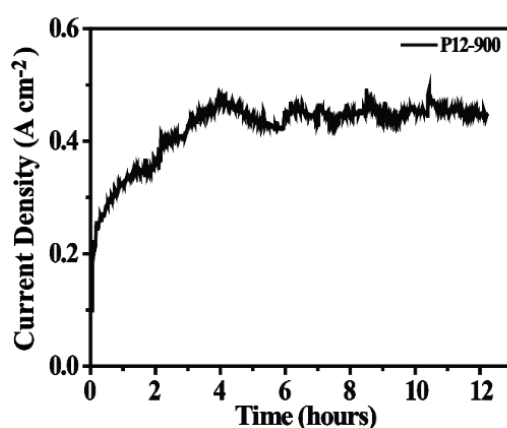
Figure 4.13 The plot indicating the stability of the PEMFC single cell derived from P12-900 (2 mg cm^{-2}) as the cathode catalyst and Pt/C (0.50 mg cm^{-2}) as the anode catalyst. The measurement was carried out under H_2 (anode) O_2 (cathode) feed conditions by maintaining the operating temperature of the cell at 60 °C. The operating potential of the cell was maintained at 0.40 V by without applying any back pressure.

Compared to the performance of the system in an acidic medium, under basic conditions (0.1 M KOH), P12-900 shows closely comparable ORR activity to that of the commercial Pt/C. P12-900 displays an onset potential of 1.02 V which is similar to the result obtained on 40 wt.

% Pt/C (1.04 V) (**Figure 4.14a**). Moreover, the half-wave potential (0.86 V *vs.* RHE) of the homemade catalyst is also comparable to its Pt/C counterpart (0.86 V *vs.* RHE). **Figure 4.14a** also shows that both P12-800 and P12-1000 show almost comparable onset (0.99 V *vs.* RHE) and half-wave potential (0.85 V *vs.* RHE) values. On the other hand, P-900, in which S is not coordinated with Fe, displays significantly high overpotential for both in terms of the onset and half-wave potential compared to its P12 counterparts. This result shows that, as in the case of
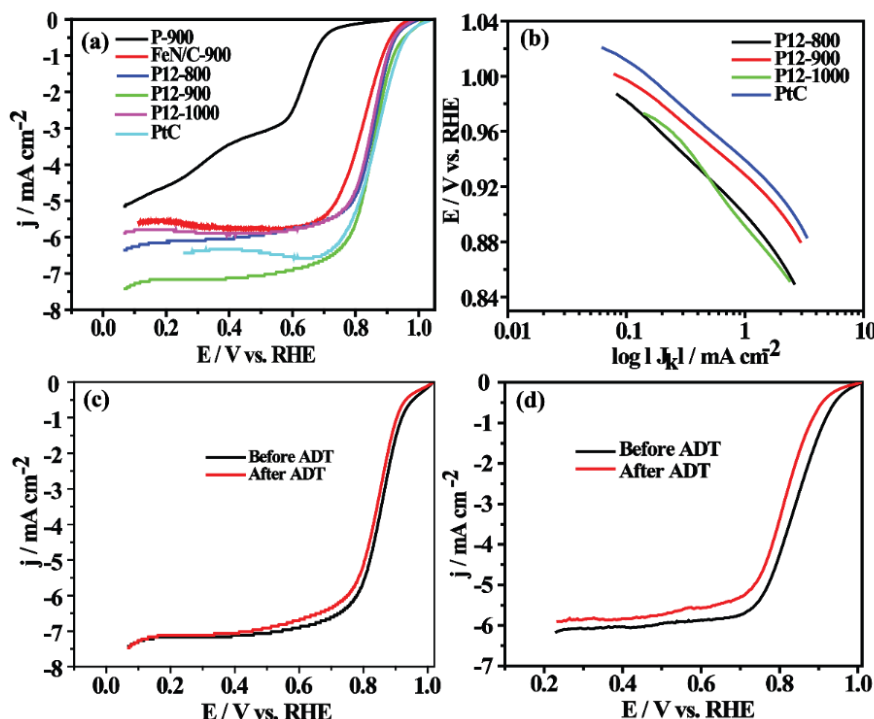
Figure 4.14 (a) The comparative LSVs of the different prepared catalysts recorded using O_2 saturated 0.1 M KOH at 10 mV s^{-1} scan rate under an electrode rotation rate of 1600 rpm, (b) the Tafel plots generated from the LSV profiles recorded for the P12 catalysts in 0.1 M KOH, (c) LSVs of P12-900 before and after 10000 potential cycling, and (d) LSVs of Pt/C before and after ADT in 0.1 M KOH, recorded at a scan rate of 10 mV s^{-1} and an electrode rotation speed of 1600 rpm.

the performance in the acid electrolyte, the Fe-S$_x$ active sites show exceptionally high performance under basic conditions as well. Since it is known that the Fe-N sites show high intrinsic activity toward ORR in basic electrolyte conditions, we compared the performance of P12-900 with FeN/C-900 which contains the Fe-N coordinated sites. The LSV profile of FeN/C-900 presented in **Figure 4.14a** shows the onset and half-wave potentials at 0.98 and 0.82 V *vs.* RHE, respectively. This result clearly indicates that the ORR activity of the P12-900 system, which holds the Fe-S$_x$ active sites, has a distinct advantage over the FeN/C-900 catalyst with the Fe-N active sites under alkaline conditions. The mass activity of the P12 catalysts

calculated at 0.85 V follows the order P12-900 (7.36 A g^{-1}) > P12-800 (6.49 A g^{-1}) > P12-1000 (5.9 A g^{-1}). The mass activity of the Pt/C catalyst at 0.85 V is estimated to be 7.55 A g^{-1}. Also, the Tafel slope of P12-900 (77 mV decade^{-1}) is found to be comparable to that of Pt/C (79 mV decade^{-1}) (**Figure 4.14b**). These results clearly emphasize that P12-900 in terms of its intrinsic ORR activity is closely comparable to the Pt-based catalyst under basic conditions. In order to investigate the durability aspect of P12-900 in a basic medium, ADT was carried out by following the procedure as illustrated before in the case of the acidic electrolyte. ADT induced a reduction in the half-wave potential by 11 mV without affecting the onset potential value (**Figure 4.14c**). The limiting current density is also found to be unaffected during ADT. On the other hand, ADT leads to a reduction in the half-wave potential by 35 mV in the case of Pt/C (**Figure 4.14d**). Thus, as in the case of the acidic conditions, P12-900 displays high activity and stability toward ORR in an alkaline environment as well.
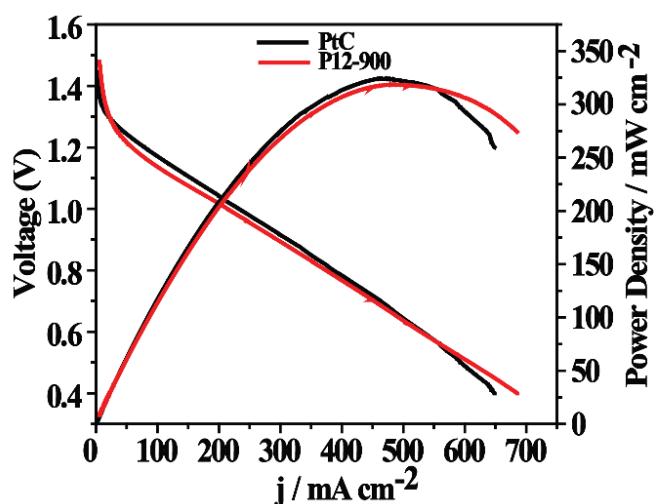
Figure 4.15 Polarization plots recorded on the ZABs based on P12-900 and Pt/C as the cathode catalysts.

Since a zinc-air battery (ZAB) works based on an alkaline electrolyte (KOH) and oxygen reduction catalyst as the cathode, the system level feasibility of P12-900 has been validated by fabricating a ZAB by utilizing it as the cathode in the cell. The anode of the cell was fabricated using zinc powder. The catalyst ink of P12-900 was prepared by maintaining a Nafion to catalyst ratio of 0.50 in isopropyl alcohol (IPA) solvent. The ink was applied on the gas diffusion layer by maintaining the P12-900 loading of 2.0 mg cm^{-2} to obtain the cathode. In the case of the control experiment using a Pt anode, the catalyst slurry containing 40 wt. % Pt/C and a Nafion to carbon ratio of 0.50 in IPA was coated on the gas diffusion layer to achieve a Pt loading of 1.0 mg cm^{-2}. The schematic representation of the ZAB assembly is shown in

Figure 4.15a. The performance of the cell was evaluated by using 6 M KOH as the electrolyte. To avoid electronic contact, a Celgard membrane was used as the separator. Subsequent to air purging on the cathode side of the cell, the P12-900-based system displays an onset potential of 1.47 V which is closely comparable to the value displayed by the Pt/C based cell (1.48 V) (**Figure 4.15b**). During polarization of the cell, close matching performance profiles have been displayed by the P12-900 and Pt/C. Both systems display a maximum power density of 320 mW cm^{-2}, justifying the comparable intrinsic activity characteristics obtained in the case of the P12-900 and Pt/C catalysts in the half-cell mode of measurements.

4.6 Conclusion

Here, Fe and S-doped graphene was prepared which displays exceptionally high ORR activity in both acidic and basic environments. The material derived from PEDOT after its controlled pyrolysis under an inert atmosphere possesses scrolled graphene structure with C-S and Fe-S active sites. The catalyst prepared by pyrolyzing at 900 °C (P12-900) displays ORR activity with substantially reduced overpotential under acidic and basic electrolyte conditions. Such performance characteristics displayed by a single system under two extreme pH conditions is a unique feature reported in these class of materials. In the basic medium, the ORR activity of P12-900 is found to be similar to that of the performance of 40 wt. % Pt/C in terms of the onset and half-wave potentials. Under acidic conditions, also the in-house system displays high ORR activity but lower than that of Pt/C by 80 mV in terms of the onset potential. During single-cell evaluation of a Nafion-based PEMFC, the P12-900-based cell delivered a maximum power density of 345 mW cm^{-2} at 60 °C in the absence of any applied back pressure. The zinc-air battery systems derived from P12-900 and standard Pt/C as the cathode catalysts and KOH as the electrolyte displayed nearly comparable performance profiles, delivering a maximum power density of 320 mW cm^{-2} in both cases. The prepared precious-metal-free catalyst enriched with the Fe and S-doped graphene can be thus considered as a promising alternative for the noble metal catalysts for PEMFCs and zinc-air battery systems with its unique capability to facilitate ORR under acidic and basic pH conditions of the electrolyte.

4.7 References

[1]. Yang, Z.; Nie, H.; Chen, X. a.; Chen, X.; Huang, S., Recent Progress in Doped Carbon Nanomaterials as Effective Cathode Catalysts for Fuel Cell Oxygen Reduction Reaction. *J. Power Sources* **2013**, *236*, 238-249.

[2]. Costa, R. A.; Camacho, J. R., The Dynamic and Steady State Behavior of a PEM Fuel Cell as an Electric Energy Source. *J. Power Sources* **2006**, *161*, 1176-1182.

[3]. Andújar, J. M.; Segura, F., Fuel Cells: History and Updating. A Walk Along Two Centuries. *Renewable and Sustainable Energy Reviews* **2009**, *13*, 2309-2322.

[4]. Yuan, C.; Wu, H. B.; Xie, Y.; Lou, X. W., Mixed Transition-Metal Oxides: Design, Synthesis, and Energy-Related Applications. *Angew Chem. Int. Ed.* **2014**, *53*, 1488-1504.

[5]. Wang, S.; Zhang, L.; Xia, Z.; Roy, A.; Chang, D. W.; Baek, J.-B.; Dai, L., BCN Graphene as Efficient Metal-Free Electrocatalyst for the Oxygen Reduction Reaction. *Angew. Chem. Int. Ed.* **2012**, *51*, 4209-4212.

[6]. Tse, E. C. M.; Gewirth, A. A., Effect of Temperature and Pressure on the Kinetics of the Oxygen Reduction Reaction. *J. Phys. Chem. A* **2015**, *119*, 1246-1255.

[7]. Kang, Y.; Murray, C. B., Synthesis and Electrocatalytic Properties of Cubic Mn-Pt Nanocrystals (Nanocubes). *J. Am. Chem. Soc.* **2010**, *132*, 7568-7569.

[8]. Zhang, J.; Dai, L., Heteroatom-Doped Graphitic Carbon Catalysts for Efficient Electrocatalysis of Oxygen Reduction Reaction. *ACS Catalysis* **2015**, *5*, 7244-7253.

[9]. Yang, L.; Jiang, S.; Zhao, Y.; Zhu, L.; Chen, S.; Wang, X.; Wu, Q.; Ma, J.; Ma, Y.; Hu, Z., Boron-Doped Carbon Nanotubes as Metal-Free Electrocatalysts for the Oxygen Reduction Reaction. *Angew. Chem.* **2011**, *123*, 7270-7273.

[10]. Gong, K.; Du, F.; Xia, Z.; Durstock, M.; Dai, L., Nitrogen-Doped Carbon Nanotube Arrays with High Electrocatalytic Activity for Oxygen Reduction. *Science* **2009**, *323*, 760-764.

[11]. Li, W.; Yang, D.; Chen, H.; Gao, Y.; Li, H., Sulfur-doped Carbon Nanotubes as Catalysts for the Oxygen Reduction Reaction in Alkaline Medium. *Electrochim. Acta* **2015**, *165*, 191-197.

[12]. Liu, Z.-W.; Peng, F.; Wang, H.-J.; Yu, H.; Zheng, W.-X.; Yang, J., Phosphorus-Doped Graphite Layers with High Electrocatalytic Activity for the O_2 Reduction in an Alkaline Medium. *Angew. Chem.* **2011**, *123*, 3315-3319.

[13]. Wohlgemuth, S.-A.; White, R. J.; Willinger, M.-G.; Titirici, M.-M.; Antonietti, M., A One-pot Hydrothermal Synthesis of Sulfur and Nitrogen Doped Carbon Aerogels with Enhanced Electrocatalytic Activity in the Oxygen Reduction Reaction. *Green Chem.* **2012**, *14*, 1515-1523.

[14]. Mo, Z.; Liao, S.; Zheng, Y.; Fu, Z., Preparation of Nitrogen-doped Carbon Nanotube Arrays and Their Catalysis Towards Cathodic Oxygen Reduction in Acidic and Alkaline Media. *Carbon* **2012**, *50*, 2620-2627.

[15]. Wei, W.; Liang, H.; Parvez, K.; Zhuang, X.; Feng, X.; Müllen, K., Nitrogen-Doped Carbon Nanosheets with Size-Defined Mesopores as Highly Efficient Metal-Free Catalyst for the Oxygen Reduction Reaction. *Angew. Chem.* **2014**, *126*, 1596-1600.

[16]. Yang, S.; Zhi, L.; Tang, K.; Feng, X.; Maier, J.; Müllen, K., Efficient Synthesis of Heteroatom (N or S)-Doped Graphene Based on Ultrathin Graphene Oxide-Porous Silica Sheets for Oxygen Reduction Reactions. *Adv. Funct. Mater.* **2012**, *22*, 3634-3640.

[17]. Wang , S.; Iyyamperumal , E.; Roy, A.; Xue, Y.; Yu, D.; Dai, L., Vertically Aligned BCN Nanotubes as Efficient Metal-Free Electrocatalysts for the Oxygen Reduction Reaction: A Synergetic Effect by Co-Doping with Boron and Nitrogen. *Angew. Chem.* **2011**, *123*, 11960-11964.

[18]. Dong, L.; Hu, C.; Huang, X.; Chen, N.; Qu, L., One-pot Synthesis of Nitrogen and Phosphorus Co-doped Graphene and Its Use as High-performance Electrocatalyst for Oxygen Reduction Reaction. *Chem. Asian J.* **2015**, *10*, 2609-2614.

[19]. Yu, D.; Xue, Y.; Dai, L., Vertically Aligned Carbon Nanotube Arrays Co-doped with Phosphorus and Nitrogen as Efficient Metal-Free Electrocatalysts for Oxygen Reduction. *J. Phys. Chem. Lett.* **2012**, *3*, 2863-2870.

[20]. Liang, W.; Chen, J.; Liu, Y.; Chen, S., Density-Functional-Theory Calculation Analysis of Active Sites for Four-Electron Reduction of O_2 on Fe/N-Doped Graphene. *ACS Catalysis* **2014**, *4*, 4170-4177.

[21]. Zhang, L.; Xia, Z., Mechanisms of Oxygen Reduction Reaction on Nitrogen-Doped Graphene for Fuel Cells. *J. Phys. Chem. C* **2011**, *115*, 11170-11176.

[22]. Rao, C. V.; Cabrera, C. R.; Ishikawa, Y., In Search of the Active Site in Nitrogen-Doped Carbon Nanotube Electrodes for the Oxygen Reduction Reaction. *J. Phys. Chem. Lett.* **2010**, *1*, 2622-2627.

[23]. Wu, G.; More, K. L.; Johnston, C. M.; Zelenay, P., High-Performance Electrocatalysts for Oxygen Reduction Derived from Polyaniline, Iron, and Cobalt. *Science* **2011**, *332*, 443-447.

[24]. Bashyam, R.; Zelenay, P., A Class of Non-precious Metal Composite Catalysts for Fuel Cells. *Nature* **2006**, *443*, 63-66.

[25]. Sa, Y. J.; Seo, D.-J.; Woo, J.; Lim, J. T.; Cheon, J. Y.; Yang, S. Y.; Lee, J. M.; Kang, D.; Shin, T. J.; Shin, H. S.; Jeong, H. Y.; Kim, C. S.; Kim, M. G.; Kim, T.-Y.; Joo, S. H., A General Approach to Preferential Formation of Active Fe–Nx Sites in Fe–N/C Electrocatalysts for Efficient Oxygen Reduction Reaction. *J. Am. Chem. Soc.* **2016**, *138*, 15046-15056.

[26]. Monteverde Videla, A. H. A.; Zhang, L.; Kim, J.; Zeng, J.; Francia, C.; Zhang, J.; Specchia, S., Mesoporous Carbons Supported Non-noble Metal Fe–N$_X$ Electrocatalysts for PEM Fuel Cell Oxygen Reduction Reaction. *J. Appl. Electrochem.* **2013**, *43*, 159-169.

[27]. Unni, S. M.; Illathvalappil, R.; Bhange, S. N.; Puthenpediakkal, H.; Kurungot, S., Carbon Nanohorn-Derived Graphene Nanotubes as a Platinum-Free Fuel Cell Cathode. *ACS Appl. Mater. Interfaces* **2015**, *7*, 24256-24264.

[28]. Kattel, S.; Atanassov, P.; Kiefer, B., A Density Functional Theory Study of Oxygen Reduction Reaction on Non-PGM Fe-Nx-C Electrocatalysts. *PCCP* **2014**, *16*, 13800-13806.

[29]. Lin, L.; Zhu, Q.; Xu, A.-W., Noble-Metal-Free Fe–N/C Catalyst for Highly Efficient Oxygen Reduction Reaction Under Both Alkaline and Acidic Conditions. *J. Am. Chem. Soc.* **2014**, *136*, 11027-11033.

[30]. Velázquez-Palenzuela, A.; Zhang, L.; Wang, L.; Cabot, P. L.; Brillas, E.; Tsay, K.; Zhang, J., Fe–Nx/C Electrocatalysts Synthesized by Pyrolysis of Fe(II)–2,3,5,6-tetra(2-pyridyl)pyrazine Complex for PEM Fuel Cell Oxygen Reduction Reaction. *Electrochim. Acta* **2011**, *56*, 4744-4752.

[31]. Singh, K. P.; Bae, E. J.; Yu, J.-S., Fe–P: A New Class of Electroactive Catalyst for Oxygen Reduction Reaction. *J. Am. Chem. Soc.* **2015**, *137*, 3165-3168.

[32]. Hu, K.; Tao, L.; Liu, D.; Huo, J.; Wang, S., Sulfur-Doped Fe/N/C Nanosheets as Highly Efficient Electrocatalysts for Oxygen Reduction Reaction. *ACS Appl. Mater. Interfaces* **2016**, *8*, 19379-19385.

[33]. Bhange, S. N.; Unni, S. M.; Kurungot, S., Nitrogen and Sulphur Co-doped Crumbled Graphene for the Oxygen Reduction Reaction with Improved Activity and Stability in Acidic Medium. *J. Mater. Chem. A* **2016**, *4*, 6014-6020.

[34]. Yang, Z.; Yao, Z.; Li, G.; Fang, G.; Nie, H.; Liu, Z.; Zhou, X.; Chen, X. a.; Huang, S., Sulfur-Doped Graphene as an Efficient Metal-free Cathode Catalyst for Oxygen Reduction. *ACS Nano* **2012**, *6*, 205-211.

[35]. Abraitis, P. K.; Pattrick, R. A. D.; Vaughan, D. J., Variations in the Compositional, Textural and Electrical Properties of Natural Pyrite: A Review. *Int. J. Miner. Process.* **2004**, *74*, 41-59.

[36]. Li, Q.; Wu, G.; Cullen, D. A.; More, K. L.; Mack, N. H.; Chung, H. T.; Zelenay, P., Phosphate-Tolerant Oxygen Reduction Catalysts. *ACS Catalysis* **2014**, *4*, 3193-3200.

[37]. Akhtar, M.; Malik, M. A.; Tuna, F.; O'Brien, P., The Synthesis of Iron Sulfide Nanocrystals From Tris(O-alkylxanthato)iron(iii) Complexes. *J. Mater. Chem. A* **2013**, *1*, 8766-8774.

[38]. Rémazeilles, C.; Saheb, M.; Neff, D.; Guilminot, E.; Tran, K.; Bourdoiseau, J.-A.; Sabot, R.; Jeannin, M.; Matthiesen, H.; Dillmann, P.; Refait, P., Microbiologically Influenced Corrosion of Archaeological Artefacts: Characterisation of Iron(II) Sulfides by Raman Spectroscopy. *J. Raman Spectrosc.* **2010**, *41*, 1425-1433.

[39]. Dhavale, V. M.; Gaikwad, S. S.; Kurungot, S., Activated Nitrogen Doped Graphene Shell Towards Electrochemical Oxygen Reduction Reaction by Its Encapsulation on Au Nanoparticle (Au@N-Gr) in Water-in-oil "Nanoreactors". *J. Mater. Chem. A* **2014**, *2*, 1383-1390.

[40]. Palaniselvam, T.; Kannan, R.; Kurungot, S., Facile Construction of Non-precious Iron Nitride-doped Carbon Nanofibers as Cathode Electrocatalysts for Proton Exchange Membrane Fuel Cells. *Chem. Commun.* **2011**, *47*, 2910-2912.

[41]. Wang, Z.; Dong, Y.; Li, H.; Zhao, Z.; Bin Wu, H.; Hao, C.; Liu, S.; Qiu, J.; Lou, X. W., Enhancing Lithium–sulphur Battery Performance by Strongly Binding the Discharge Products on Amino-functionalized Reduced Graphene Oxide. *Nature Commun.* **2014**, *5*, 5002.

[42]. Vinayan, B. P.; Diemant, T.; Behm, R. J.; Ramaprabhu, S., Iron Encapsulated Nitrogen and Sulfur Co-doped Few Layer Graphene as a Non-Precious ORR Catalyst for PEMFC Application. *RSC Advances* **2015,** *5*, 66494-66501.

[43]. Xu, X.; Dai, Y.; Yu, J.; Hao, L.; Duan, Y.; Sun, Y.; Zhang, Y.; Lin, Y.; Zou, J., Metallic State FeS Anchored (Fe)/Fe3O4/N-Doped Graphitic Carbon with Porous Spongelike Structure as Durable Catalysts for Enhancing Bioelectricity Generation. *ACS Appl. Mater. Interfaces* **2017**, *9*, 10777-10787.

[44]. Wang, M.; Xing, C.; Cao, K.; Zhang, L.; Liu, J.; Meng, L., Template-directed Synthesis of Pyrite (FeS_2) Nanorod Arrays with an Enhanced Photoresponse. *J. Mater. Chem. A* **2014**, *2*, 9496-9505.

[45]. Wang, X.; Xiang, Q.; Liu, B.; Wang, L.; Luo, T.; Chen, D.; Shen, G., TiO_2 Modified FeS Nanostructures with Enhanced Electrochemical Performance for Lithium-Ion Batteries. *Sci. Rep.* **2013**, *3*, 2007.

[46]. Li, B.; Huang, L.; Zhong, M.; Wei, Z.; Li, J., Electrical and Magnetic Properties of FeS_2 and $CuFeS_2$ Nanoplates. *RSC Adv.* **2015**, *5*, 91103-91107.

[47]. Kim, E.-J.; Kim, J.-H.; Azad, A.-M.; Chang, Y.-S., Facile Synthesis and Characterization of Fe/FeS Nanoparticles for Environmental Applications. *ACS Appl. Mater. Interfaces* **2011**, *3*, 1457-1462.

[48]. Castner, D. G.; Hinds, K.; Grainger, D. W., X-ray Photoelectron Spectroscopy Sulfur 2p Study of Organic Thiol and Disulfide Binding Interactions with Gold Surfaces. *Langmuir* **1996**, *12*, 5083-5086.

[49]. Proietti, E.; Jaouen, F.; Lefèvre, M.; Larouche, N.; Tian, J.; Herranz, J.; Dodelet, J.-P., Iron-based Cathode Catalyst with Enhanced Power Density in Polymer Electrolyte Membrane Fuel Cells. *Nature Commun.* **2011**, *2*, 416.

[50]. Wu, G.; More, K. L.; Xu, P.; Wang, H.-L.; Ferrandon, M.; Kropf, A. J.; Myers, D. J.; Ma, S.; Johnston, C. M.; Zelenay, P., A carbon-nanotube-supported graphene-rich non-precious metal oxygen reduction catalyst with enhanced performance durability. *Chem. Commun.* **2013,** *49*, 3291-3293.

[51]. Kwak, D.-H.; Han, S.-B.; Lee, Y.-W.; Park, H.-S.; Choi, I.-A.; Ma, K.-B.; Kim, M.-C.; Kim, S.-J.; Kim, D.-H.; Sohn, J.-I.; Park, K.-W., Fe/N/S-doped mesoporous carbon nanostructures as electrocatalysts for oxygen reduction reaction in acid medium. *Applied Catalysis B: Environmental* **2017,** *203* (Supplement C), 889-898.

[52]. Ren, H.; Wang, Y.; Yang, Y.; Tang, X.; Peng, Y.; Peng, H.; Xiao, L.; Lu, J.; Abruña, H. D.; Zhuang, L., Fe/N/C Nanotubes with Atomic Fe Sites: A Highly Active Cathode Catalyst for Alkaline Polymer Electrolyte Fuel Cells. *ACS Catalysis* **2017,** *7*, 6485-6492.

Chapter-5

FeN$_x$/FeS$_x$-Anchored Carbon Sheet-Carbon Nanotube Composite Electrocatalyst for Oxygen Reduction

Even though various Pt-free electrocatalysts for oxygen reduction reaction (ORR) have been introduced, many of them are found to be active only in alkaline conditions. Considering Nafion, phosphoric acid doped polybenzimidazole (PBI) and so on as the prominent ionomer membranes used in the commercially available polymer electrolyte membrane fuel cells (PEMFCs), it becomes important that any development on the Pt-free catalysts should ensure better ORR performance under acidic conditions. The work detailed in this chapter is dedicated to tackle this issue, where an ORR-based catalyst could be prepared with simultaneous incorporation of both Fe-N and Fe-S active sites on *in situ* generated carbon sheets which are spatially separated by a network created by means of carbon nanotube (CNT). This catalyst shows ability to perform under both the acidic and basic conditions. This has been achieved by growing a polyethylenedioxythiophene polymer network in the presence of

CNT and melamine followed by its pyrolysis under inert atmosphere. The catalyst formed at 900 °C (PMCNT-900) displays an onset potential of 0.94 V for ORR under acidic electrolyte conditions, which corresponds to 60 mV overpotential compared to its 40 wt % Pt/C counterpart. Interestingly, in single cell demonstration of a Nafion-based PEMFC with PMCNT-900 as the cathode catalyst, the system delivered a maximum power density (PD) of 500 and 275 mW cm^{-2} at 60 °C under H$_2$-O$_2$ and H$_2$-Air feed conditions, respectively. On the other hand, in a single cell test in the anion exchange membrane fuel cell (AEMFC) mode, a maximum power density of 65 mW cm^{-2} at 50 °C could be achieved with the same cathode catalyst, which is a comparable value obtained while employing Pt/C as the cathode. These results, thus, infer to the efficiency of the catalyst to facilitate ORR under the extreme pH conditions, and, particularly, its performance under acidic condition reveals its prospect as a potential Pt-free electrocatalyst to serve in the Nafion based systems.

5.1 Introduction

Even though polymer electrolyte membrane fuel cells (PEMFCs) are being inducted for various domestic and commercial applications in recent days, a wide spread penetration of these systems in the energy market can be realized only by making them cost-effective with desirable activity and durability.[1-3] Among the various cost contributing factors, use of platinum (Pt) as the electrocatalyst to tackle the sluggish oxygen reduction reaction (ORR) kinetics at the cathode is the major stumbling block in the efforts targeted for cost reduction.[4] To realize the goal of achieving PEMFCs free of Pt, various types of non-noble metal-based electrocatalysts are being proposed and demonstrated as viable alternatives to the Pt-based electrocatalysts.[5-7] Various class of materials including heteroatom doped carbons, metal-porphyrin systems, metal oxide-based systems etc have been widely explored in this direction.[8-13] Of these, a breakthrough discovery is the ORR catalysts based on the non-noble metal phthalocyanine complexes, which display significantly reduced overpotential compared to many of its counterpart Pt-free systems explored in the literature.[14] Another landmark revelation was made by Yeager *et. al*. in 1989, who prepared carbon containing M-N_x systems (where, 'M' stands for the non-noble metal atom) by the pyrolysis of polyacrylonitrile mixed with Fe(II) and Co(II) salts.[15] Since then, various non-noble metal carbon-based catalysts obtained through high temperature have been demonstrated as ORR catalysts.[16-21] As compared to the high temperature pyrolysis synthesis routes, Xu *et. al.* have also prepared an FeN$_x$/C catalyst with fast heating system which also contributes to the ORR activity with selective formation of the highly active sites.[22] In terms of the onset and half-wave potentials, which are the two key performance indicators in defining the intrinsic activity towards ORR, many of these systems display promising trends. However, the ORR performance of such systems is found to be highly sensitive to the pH of the electrolytes and majority are reported to be more active in basic pH conditions. Ma *et. al.* prepared FeN$_x$-decorated carbon nanotube at high temperature through sacrificial template method, which displays catalytic activity both in the acidic and basic media.[23]

Among the noble-metal-free ORR catalysts which display performance in the acidic pH conditions, the systems based on Fe-N_x moieties embedded in the carbon matrix are the most versatile ones with activity comparable to the state-of-the-art Pt/C catalyst.[24-27] Recently, Fe-S_x engrafted carbon is also reported to be displaying activity comparable to Pt/C in the acidic medium.[28] Pyrolysis of different precursors like metal organic frameworks,[29-31] conducting polymers,[32-34] nitrogen and sulphur containing organic compounds,[35-36] organic waste,[37] etc. has been adopted to prepare carbons engrafted with Fe-N_x and Fe-S_x linkages. Amongst the

different precursors used for this purpose, the conducting polymer (polyaniline, polypyrrole, polythiophene, etc.) derived catalysts show better performance compared to those derived from the other precursors.[38] Conducting polymers possess extended conjugation, ring structure and well-defined metal atom-heteroatom binding, which upon pyrolysis yields catalyst with high conductivity and surface area along with uniformly distributed active sites throughout the matrix. Along with this, low cost and easy methodologies available for the synthesis make them cost-effective compared to many of the counterpart systems. Even though such systems display promising ORR activity characteristics in single electrode modes, many of them often fail to match with the performance of Pt/C and its alloys[39] during real fuel cell device level demonstration.[40] Among the various issues which contribute towards this reduced system level performance of the Fe-N and Fe-S based systems, the factors like low conductivity, embedded inaccessible active sites and restricted diffusion of the reactant gases to the ORR active sites in the membrane electrode assemblies (MEAs) are the most crucial ones. If the electrodes in the MEAs fail to meet the requisites in terms of conductivity, utilization of the active sites and availability of the reactant gases, there can be a significant mismatch between the intrinsic activity of the catalyst and its system level performance.

As a way to address these issues, we have developed a system by using carbon nanotube (CNT) as a spacer, which separates the layers of the polymer derived carbon sheets bearing the Fe-N and Fe-S ORR active sites. This has been accomplished by the pyrolysis of *in-situ* formed polyethylenedioxythiophene (PEDOT) in presence of melamine with CNT, which generates spatially separated thin carbon sheets in the spacer network of CNT. Thus formed carbon sheets are embedded with the active sites of Fe-N and Fe-S moieties in the matrix. The source of Fe is the FeCl$_3$, which was also used as the oxidizing agent for facilitating polymerization of the monomer ethylenedioxythiophene (EDOT) to PEDOT. While the combination of Fe-N and Fe-S works synergistically to favor the intrinsic activity for ORR in acidic environment, the CNT network concomitantly plays a critical role to prevent aggregation of the sheets by acting as spacers. Such a strategy considering the electrode level requirement is essential to deal with these types of heteroatom doped carbon structures in order to prevent aggregation of the particles while making the catalyst ink with ionomers in the course of electrode preparation. CNT as a spacer plays a critical role to maintain the structural integrity of the matrix, to expose the active sites to the reactants and also to assist current collection by providing efficient conducting network in the system. The results discussed in the manuscript reveal how this strategy of tuning material properties and bringing in the required structural aspects has worked favourably to achieve efficient noble-metal-free catalysts which display high ORR

performance in acidic conditions and leads to the successful demonstration of a single cell of PEMFCs by delivering promising power outputs.

5.2: Experimental Method

5.2.1 Synthesis of PMCNT

In a typical synthesis, 80 mg of the functionalized carbon nanotube (CNT) was dispersed in 40 ml of acetonitrile solution through bath sonication for 1 h. Subsequently, 600 mg of melamine was added in the above solution and stirred for 30 min. After that, 400 mg of EDOT monomer was added in 10 ml of acetonitrile; this solution was then added into the dispersed CNT. A solution of oxidizing agent was prepared by dissolving 5.475 g of iron chloride in 20 ml of acetonitrile. Subsequently, the oxidizing solution was added drop wise in the solution containing CNT and EDOT under continuous stirring. The solution was stirred for 24 h. The recovered material (precursor) was dried at 80 $^{\circ}$C, and pyrolyzed at 800, 900, and 1000 $^{\circ}$C for 1 h in an inert atmosphere. After pyrolysis, the material obtained was washed in 0.5 M H_2SO_4 for 8 h at 80 $^{\circ}$C. It was then filtered and washed with copious amount of DI water and dried at 80 $^{\circ}$C for 12 h. The second round of pyrolysis was carried out at the same temperature for 1 h, and the corresponding catalysts are named as PMCNT-800, PMCNT-900 and PMCNT-1000. Similarly, the control sample was also prepared by using $FeCl_3$ as the oxidizing agent at 900 $^{\circ}$C by adopting the similar procedure as above without incorporating CNT, which is designated as PM-900.

5.3 Materials Characterization

Transmission electron microscope (TEM) Tecnai-T 20 model at an acceleration voltage of 200 kV was used for the analysis of the morphology of the synthesized materials. The sample for the TEM scanning was prepared by dispersing the catalyst sample in isopropyl alcohol and drop coating on the carbon coated Cu grid followed by drying. For X-ray diffraction, a Rigaku Smartlab diffractometer was used, and the scan rate was maintained as 2° min^{-1}. A VG Microtech Multilab ESCA 3000 spectrometer was used for the X-ray photoelectron spectroscopic (XPS) investigation of the catalysts. Raman study was performed using an HR 800 Raman spectrometer (Jobin Yvon, Horiba, France) at 632 nm red laser.

5.4. Electrochemical Characterization

5.4.1 Electrochemical Analysis

The electrochemical studies were carried out in a Bio-logic (SP-300) instrument connected with a three-electrode system having a glassy carbon electrode (GCE) as the working electrode, graphite rod as the counter and $Hg/HgSO_4$ as the reference electrode. Preparation of the ink was done by taking 10 mg of the PMCNT catalyst and 40 µl of 5 wt. % Nafion solution dispersed in 1 ml solution of 3:1 ratio of IPA:water. For the preparation of the working electrode, the 10 µl of the catalyst ink was drop coated on the glassy carbon electrode and the coated surface was dried under an IR lamp. The maintained loading of the catalyst on the electrode was 0.50 mg cm^{-2}, which is having an electrode area of 0.19625 cm^2. For comparison purpose, 40 wt. % Pt/C with a catalyst loading of 0.25 mg cm^{-2} was used in the half-cell studies. The linear sweep voltammograms (LSVs) were recorded at 1600 rpm of the electrode rotation speed and a voltage scan rate of 10 mV s^{-1} in O_2 saturated 0.5 M H_2SO_4 and 0.1 M KOH solution. For the accelerated durability test (ADT), cyclic voltammograms were recorded in between the potential range of 0.60 to 1.0 V *vs.* RHE at a voltage scan rate of 100 mV s^{-1} for 10000 potential cycling. Subsequent to the potential cycling, the LSV was measured at a voltage scan rate of 10 mV s^{-1} and the data was compared with the LSV profile obtained before performing the cycling studies.

The effective electrochemical surface area S_a (m^2 g^{-1}) of all the obtained electrocatalysts can be calculated by using the formula:[26-27]

$$S_a = \frac{C}{C_{GC}} \tag{1}$$

where, C is the gravimetric double layer capacitance (Fg^{-1}) of the catalyst and C_{GC} is the double layer capacitance (Fm^{-2}) of the glassy carbon electrode which is 0.2 Fm^{-2}.[28]

5.4.2 Rotating Ring Disc Electrode (RRDE) Analysis

To calculate the H_2O_2 percentage and number of electron transfer, the RRDE study was performed at an electrode rotation speed of 1600 rpm in O_2 saturated 0.5 M H_2SO_4 and 0.1 M KOH at a scan rate of 10 mV s^{-1}. The ring potential was held at 1.5 V with respect to RHE. $K_3Fe(CN)_6$ solution was used for the measurement of the collection efficiency of the ring electrode. The measured collection efficiency is 0.37. For the calculation of the H_2O_2 percentage and the number of electrons transferred during the reduction process, the following equations were used:

$$H_2O_2\% = \frac{\frac{200 \times I_R}{N}}{I_D + \frac{I_R}{N}} \qquad (2)$$

$$n = \frac{(4 \times I_D)}{(I_D + \frac{I_R}{N})} \qquad (3)$$

where, N is the collection efficiency, I_D is the disc current and I_R is the ring current.

5.4.3 Single Cell Analysis

5.4.3.1 PEMFCs

For fabricating the membrane electrode assembly (MEA), the proton conducting membrane was fabricated by using Nafion 212 membrane. The pre-treatment of the membrane was performed by using a reported procedure.[3] The pre-treated membrane was stored in DI water for further use while assembling the MEA. The electrode was prepared by doing the brush coating of the catalyst slurry on the top surface of a carbon gas diffusion layer (GDL). For the cathode, the catalyst ink was made by mixing PMCNT-900 and 20 wt. % Nafion dispersion in IPA. A Nafion to catalyst ratio of 0.50 was kept in the catalyst ink. The ink was applied onto the GDL. For the anode, Pt/C (40 wt. %) was used as the catalyst. The loadings of the catalyst for both the anode and cathode were measured to be 0.50 and 3.0 mg cm^{-2}, respectively. The MEA was prepared by using the pre-treated Nafion membrane between the anode and cathode electrodes by maintaining an active area of 4 cm^2. The assembly was hot pressed with a pressure of 0.25 ton for 1 min at temperature of 130 °C. The single cell performance of the prepared MEA was assessed by using a 4 cm^2 test fixture procured from Fuel Cell Technologies, Inc, USA, by connecting to a fuel cell test station. 0.3 slpm of hydrogen and 0.2 slpm of oxygen were supplied to the anode and cathode, respectively, without applying any back pressure. The complete measurement has been done under 100 % relative humidity condition by operating at a cell temperature of 60 °C.

5.4.3.2 AEMFCs

The slurry was prepared by using PMCNT-900 as the cathode catalyst and Fumion as the binder by keeping the binder to catalyst ratio constant as 0.50. The loading of the catalyst on the GDL surface was maintained as 2.0 mg cm^{-2}, while the loading of the commercial Pt/C as the anode catalyst was kept as 0.80 mg cm^{-2}. The MEA was made by using these two electrodes with the FuMA Tech-FAA membrane as the alkaline exchange membrane with an active area of 4 cm^2.

5.5 Result and Discussion
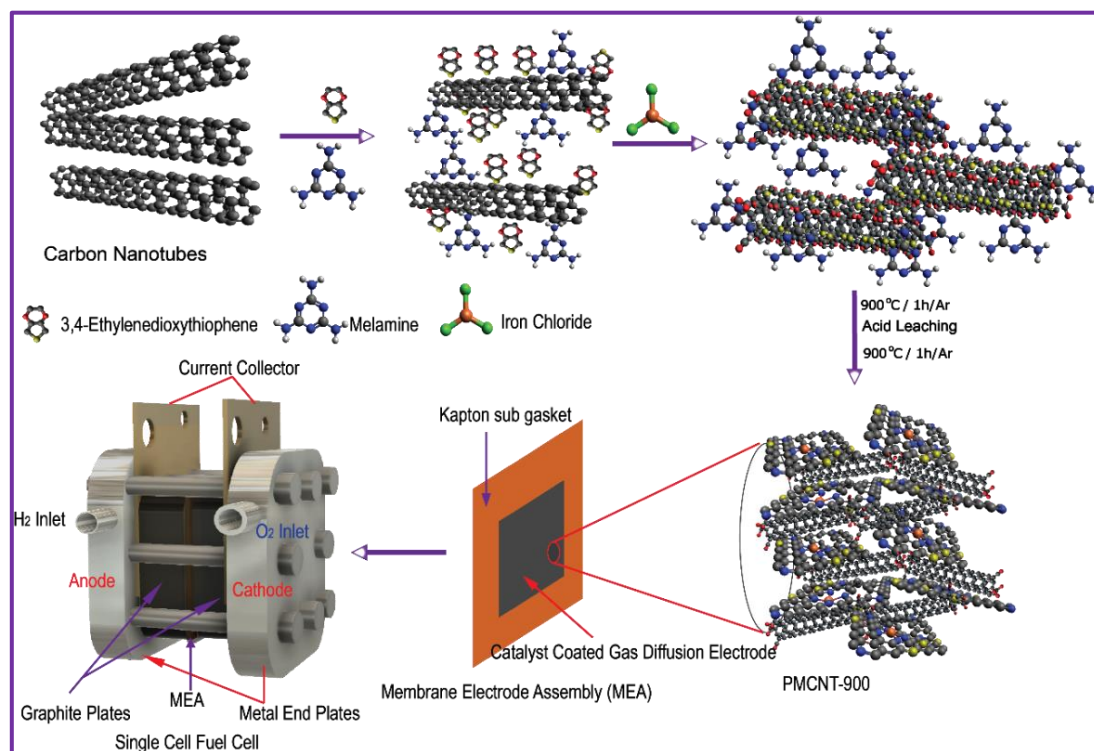
Scheme 5.1 Schematic representation of the processes involved in the synthesis of the PMCNT-900 electrocatalyst followed by its system level demonstration for PEMFC by utilizing it as the cathode electrode of the system.

Scheme 5.1 highlights the steps involved in the material preparation followed by the system level demonstration by utilizing the prepared catalyst as the cathode of the cell. EDOT, melamine and the oxidizing agent $FeCl_3$ were mixed in acetonitrile with CNT to get an optimal weight ratio between the PEDOT and CNT so that essentially bulk polymerization occurs in a controllable way along with the formation of PEDOT on the CNT surface. The PEDOT formed on the CNT surface from the initially anchored EDOT moieties essentially interconnects the bulk polymerized PEDOT, thereby serving as the building block for providing the right carbon textural features after the pyrolysis process. Pyrolysis of the mixture of PEDOT, CNT and melamine at high temperature under inert atmosphere gives sheet-like structure with interpenetrated CNTs in the matrix. The pyrolysis facilitates formation and embedment of FeN_x and FeS_x active sites not only on the carbon sheets derived from PEDOT but also on the surface of the CNTs. This ultimately increases the number density of the catalytic sites available to the reactants. Based on the samples prepared at the pyrolysis temperatures of 800, 900 and 1000 °C, the obtained catalysts are designated respectively as PMCNT-800, PMCNT-900, and

PMCNT-1000. A control sample was also prepared by removing CNT from the mixture which was pyrolyzed at temperature 900 °C (PM-900).

5.5.1 Field Emission Scanning Electron Microscopy (FESEM) Analysis
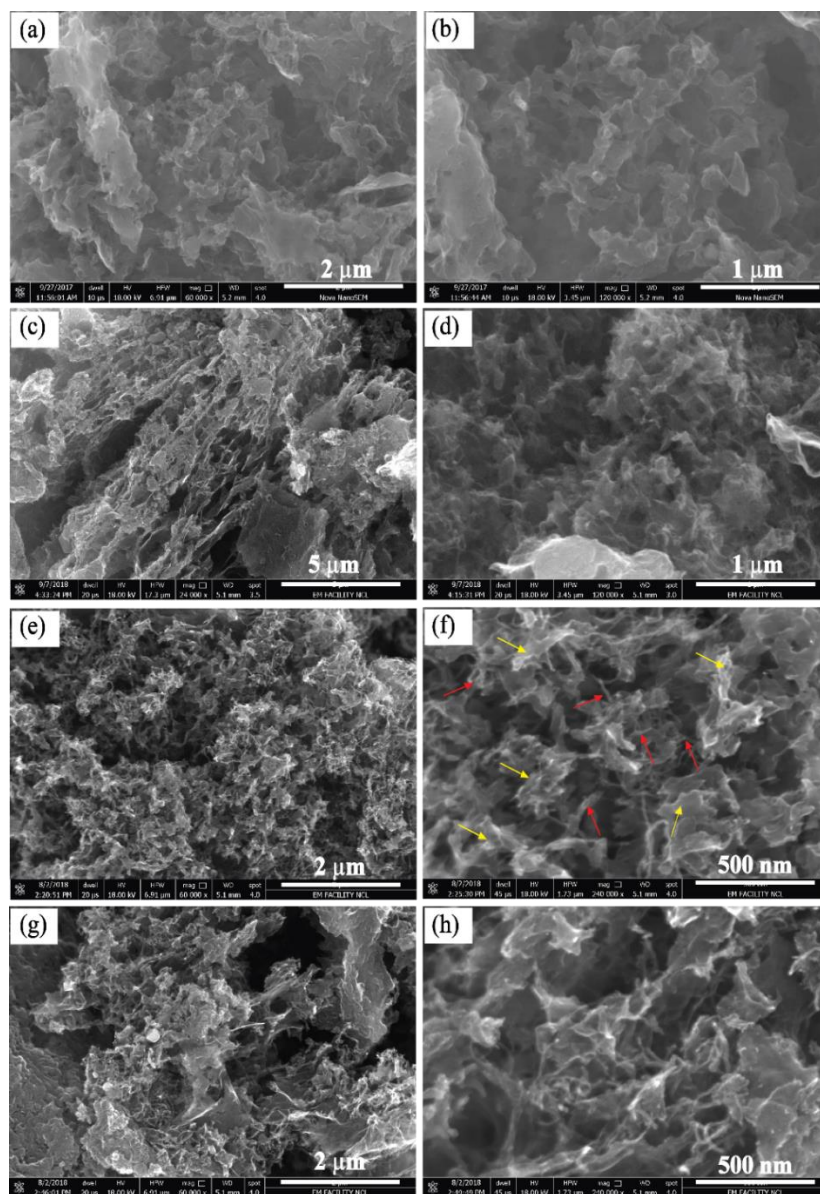
Figure 5.1 Field Emission Scanning electron microscopy (SEM) images recorded at different magnifications, (a) and (b) for PM-900, (c) and (d) for PMCNT-800, (e) and (f) for PMCNT-900 and (g) and (h) for PMCNT-1000.

Field Emission Scanning Electron Microscopic (FESEM) analysis was performed to understand the morphological features of the prepared materials. Accordingly, **Figure 5.1a-h** show the images recorded for PM-900, PMCNT-800, PMCNT-900, and PMCNT-1000. The role of CNT to accomplish the desired morphological fine tuning is clearly evident from the

figures, particularly by looking at the differences in the textural characteristics of PM-900 (**Figure 5.1a-b**), which does not contain CNT in the matrix, and its CNT containing counterpart systems (**Figure 5.1c-h**). While PM-900 gives very compact structures with thicker and denser sheets, with apparently reduced porosity, the CNT composites display much porous architecture possessing thin sheet like morphologies of reduced particle sizes distributed between the interconnected network of CNTs. Among the various CNT-based samples, PMCNT-900 (**Figure 5.1e-f**) shows highly porous textural characteristics with very clear weaving network of CNTs. This type of interconnected CNT network is expected to play a key role in establishing the structural integrity of these types of highly porous textures. Contrary to PMCNT-900, a comparatively thicker sheet distribution with reduced porosity has been observed in the case of PMCNT-1000.

5.5.2 Transmission Electron Microscopy

A better close look on the interpenetration of the CNTs in PMCNT-900 is possible in the TEM images of the sample presented in **Figure 5.2**. CNTs of ~10-15 nm in diameter are clearly seen encompassing the carbon sheets which are surrounding the CNTs. The images clearly validate the role of CNT as a spacer preventing the sheet stacking and clustering. Also, a thin layer of carbon is found to be covered on the surface of CNT (**Figure 5.2e**), which is formed from the PEDOT layer grown on the CNT surface during its surface aligned polymerization from the anchored EDOT moieties. This difference at the surface of the CNT due to the carbon layer formation can be understood by comparing the TEM image of the surface of the pristine CNT presented in **Figure 5.2f**. The thin carbon layer along the CNT further makes the CNT surface enriched with the ORR active FeN_x and FeS_x sites. The EDS mapping presented in **Figure 5.2g** clearly indicates the presence and uniform distribution of C, N, S, Fe and O elements in the carbon tube as well as the sheet. Thus, the rigid and conducting network of CNT brings in the features of better structural integrity and porosity to the composite which consists of the carbon sheets bearing the noble metal-free ORR sites along with its ability to further enhance the active site distribution by acting as a substrate for holding the PEDOT-derived carbon layer. These features can be taken as important prerequisites for effectively converting the nanoparticles to electrodes, where a controlled interplay of the activity of the catalyst along with the process requirements such as mass transfer, reactant accessibility and conductivity is considered to be important in achieving system level performance.
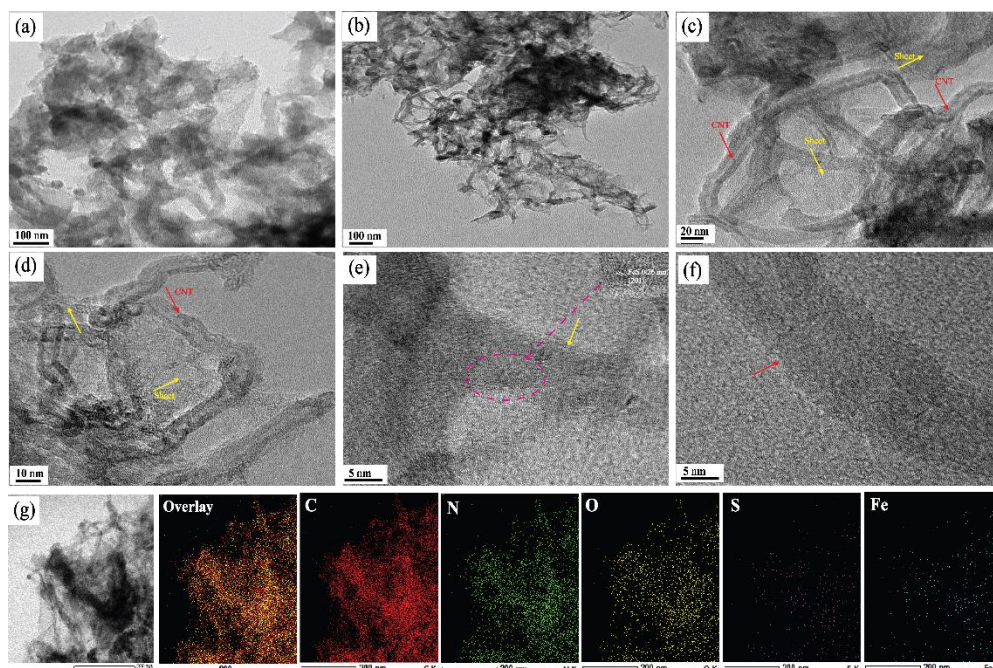
Figure 5.2 (a) TEM image of PM-900, (b-d) TEM images recorded at different magnifications for PMCNT-900, (e-f) HRTEM image of PMCNT-900 and pristine CNT and (g) elemental mapping of PMCNT-900.

5.5.3 BET Surface Area Analysis
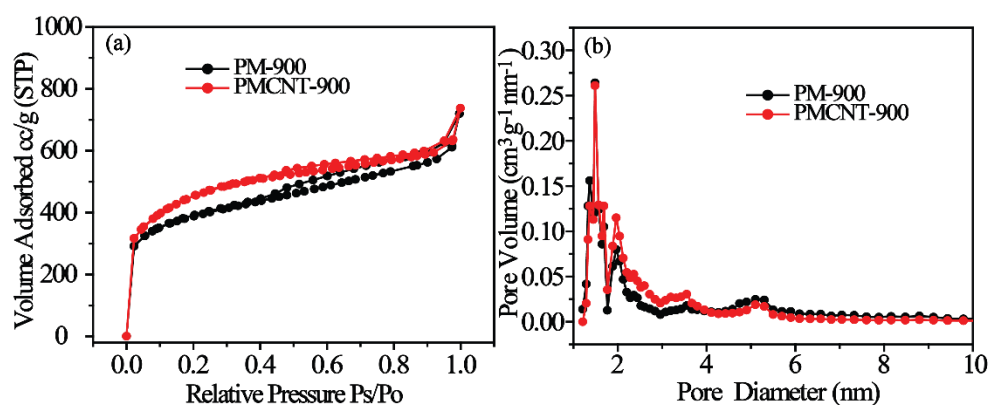
Figure 5.3 (a) N_2 adsorption-desorption isotherms recorded to measure the BET surface area and (b) pore size distribution profiles of PM-900 and PMCNT-900.

To demonstrate the synergistic effect of CNT on the surface properties of PMCNT-900, we compared the BET surface area values of both PM-900 and PMCNT-900 (**Figure 5.3a**). The surface area of PMCNT-900 has been increased to 1645 m^2 g^{-1} with the incorporation of CNT as the spacer to prevent the stacking of the carbon sheets in PM-900, which exhibits the surface area of 1388 m^2 g^{-1}. Along with this, the appearance of higher density of pore with

diameter below 6 nm, as indicated in the pore size distribution curves presented in **Figure 5.3b**, clearly indicates the existence of both micro and mesopores in these catalysts. The role of CNT has also been revealed through the pore size distribution curve with the appearance of higher pore volume value with in the pore diameter of 2-4 nm for PMCNT-900 (**Figure 5.3b**).

5.5.4 Thermogravimetric Analysis:

Metal content in the different samples was estimated by thermogravimetric analysis (TGA) and the corresponding data is presented in **Figure 5.4**. The TGA profiles of the four samples display two plateaus, one at a comparatively low temperature range (300-370 °C) and the other at a higher temperature range (370-400 °C). The low temperature plateau is expected to be due to the loss of sulphur from the system[41] and this plateau is found to be progressively shifted to higher temperature with increase in the pyrolysis temperature. Such a shift is attributed to the different surrounding environments of the sulphur in the different samples, affected by the temperature of pyrolysis. The other plateau at a slightly higher temperature indicates the carbonization of the polymer. All the TGA curves show an initial weight loss up to 100 °C due to the loss of water. The residue content present in PMCNT-800 is 6.9 wt.%, which is decreased to nearly 3 wt.% for PMCNT-900 and PMCNT-1000, and this residue is expected to be primarily originated from the metallic moieties in the system. PM-900 contains even a lesser residue content of 1.4 wt. %. To validate the difference in the metal content of
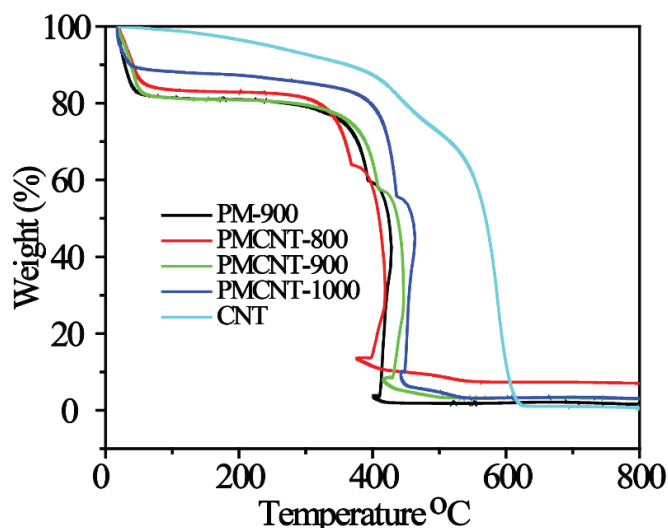

Figure 5.4 Thermogravimetric analysis (TGA) of the PMCNT and PM electrocatalysts.

PM-900 and its CNT containing counterparts, TGA of pristine CNT is also compared, which shows a residue content of 0.63 %. Hence, the difference in the residue content of these samples is attributed to the non-combustible impurities present in CNT. Further, the decrease in the

metal content with the increase in the pyrolysis temperature (*i.e.*, PMCNT-800, PMCNT-900 and PMCNT-1000) is attributed to the decrease in the number of the metal coordination sites.

5.5.5 X-ray Diffraction and Raman Analyses

The materials were further investigated with the help of powder X-ray diffraction (PXRD) and Raman analyses to get more insightful information about the textural and morphological features accomplished during the transformation of the CNT polymer to the CNT carbon phase (**Figure 5.5**). As can be seen from the XRD profiles in **Figure 5.5a**, all the samples display a broad peak at a 2θ value of ~26°, which corresponds to the (002) graphitic plane of the carbon.[42] Moreover, the XRD profiles designate the appearance of peaks at 29.9, 35.2, 43.6, 44.4 and 56.9° in PM-900, PMCNT-800, PMCNT-900 and PMCNT-1000. These peaks are attributed to the formation of FeS ((ICDD#01-089-6272) and Fe_3N (ICDD#00-001-1236) crystalline phases marked by the symbol '*' and '°' respectively. The appearance of the peak at 43.86° in PM-900 sample has been assigned to the Fe_3C (ICDD#01-089-2867) phase along with the Fe_3N and FeS phases.

Raman spectra recorded for PM-900 and PMCNT-900 (**Figure 5.5b**) do not show any peak corresponding to the FeS and FeN_x moieties which are usually observed below 1000 cm^{-1}; this suggests that the thin carbon sheet present in the systems shields the metal sites from their detection in Raman analysis.[43] The D band and G band of PM-900 and PMCNT-900 are positioned at 1317 and 1593 cm^{-1}, respectively.[44] The ratio of the intensities of these two peaks (I_D/I_G ratio) of PM-900 is less (1.08) compared to that of PMCNT-900 (1.11), indicating the presence of a higher degree of defects in PMCNT-900 as a result of higher packing density of CNT.
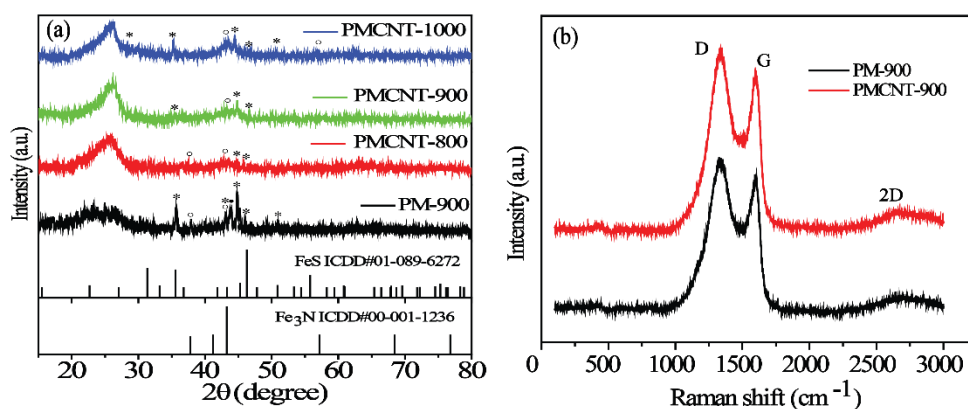

Figure 5.5 (a) Comparison of the X-ray diffraction (XRD) patterns recorded for the different composite catalysts, and (b) comparison of the Raman spectra recorded on PMCNT-900 and PM-900.

5.5.6 EDAX Analysis and Elemental Mapping
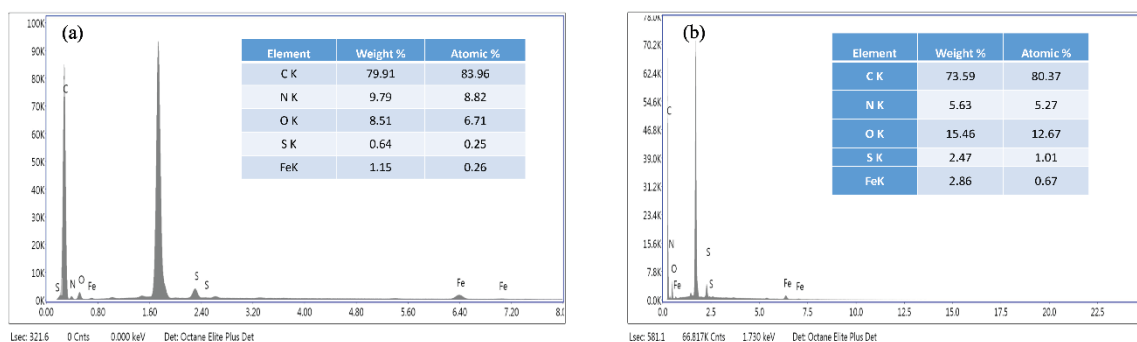
Figure 5.6 EDAX analysis of (a) PMCNT-900, and (b) PM-900.

An investigation on the bulk composition of PMCNT-900 and PM-900 was performed through EDAX measurement; the corresponding data is given in **Figure 5.6a and 5.6b**, respectively. EDAX of PMCNT-900 show the presence of carbon (83.96 at. %), nitrogen (8.82 at. %), oxygen (6.71 (at. %), sulphur (0.25 at. %) and iron (0.26 at. %). A higher content of nitrogen (8.82 at. %) indicates that along with the formation of Fe-N moiety, a substantial amount of nitrogen gets doped in the carbon framework. It is advantageous as the nitrogen-doped carbon possess significant ORR activity.[45-46] Also, a comparatively low percentage of oxygen in the system indicates the presence of less oxidized carbon, which is essential for achieving good electrical conductivity for the electrocatalyst. In contrast to PMCNT-900, PM-900 shows low content of both carbon (80.4 at. %) and nitrogen (5.3 at. %) with a higher contribution of oxygen (12.7 at. %), which points towards the highly oxidized nature of the carbon. PM-900 also displays the presence of sulphur (1.0 at. %) and iron (0.67 at. %).

5.5.7 XPS Analysis

In addition to the bulk composition, a detailed XPS analysis was performed to understand the nature of the surface composition. The survey spectra of the four samples, *viz*., PM-900, PMCNT-800, PMCNT-900 and PMCNT-1000, given in **Figure 5.7a**, show the presence of carbon, oxygen, nitrogen, sulphur and iron in all the samples. The contents of the different elements present in the samples are listed in **Table 5.1**. In corroboration to the EDAX results, the XPS of PMCNT-900 shows higher content of carbon compared to PM-900, ascribed to the presence of CNTs. Among the different PMCNT catalysts, the percentage of nitrogen, sulphur and oxygen is observed to be decreased with the increase in the pyrolysis temperature, and this trend is in agreement to the results obtained in some of the previously reported studies.[32, 47-48] The content of iron also got decreased with the pyrolysis temperature, which goes along
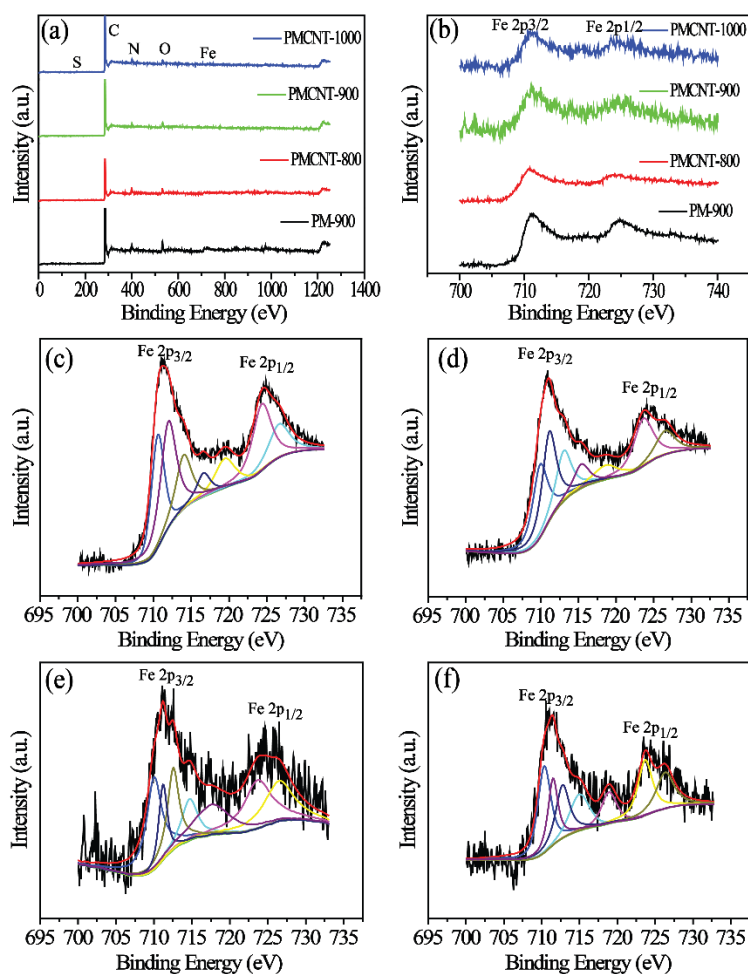
Figure 5.7 X-ray photoelectron spectroscopy (XPS) analysis: (a) shows the survey spectra of the PMCNT catalysts obtained at different temperatures and PM-900, (b) Fe 2p spectra of the four different catalysts and (c-f) the deconvoluted Fe 2p spectra of PM-900, PMCNT-800, PMCNT-900 and PMCNT-1000, respectively.

Table 5.1 Surface composition of the elements present on the PMCNT and PM electrocatalysts calculated from XPS.

Sample	Carbon (%)	Nitrogen (%)	Oxygen (%)	Sulphur (%)	Iron (%)
PM-900	78.26	5.59	5.86	0.54	1.72
PMCNT-800	83.34	9.5	4.99	0.86	0.94
PMCNT-900	89.10	5.36	4.53	0.65	0.35
PMCNT-1000	91.94	3.30	3.85	0.60	0.29

with the fact that the higher pyrolysis temperature results in the reduction of the amount of hetero atoms doped in the system which act as the binding sites for iron. PMCNT-900 has shown the best electrochemical activity among all the three composite catalysts, as can be seen in a subsequent section, inferring to the optimum composition of the different elements acquired by this system. The XPS spectra of Fe 2p for all prepared samples has been shown in **Figure 5.7b**, which attribute the existence of Fe $2p_{3/2}$ and Fe $2p_{1/2}$ corresponds to lower and higher binding energy respectively. The deconvoluted XPS spectra of Fe 2p for all catalysts are shown in **Figure 5.7c-f**, which attribute to the signals at the binding energies of 710.0 and 713.0 eV corresponding to the $2p_{3/2}$ state of Fe^{2+} and Fe^{3+}, respectively. While, the peaks at 723.6 and 726.5 eV can be assigned to the $2p_{1/2}$ state of Fe^{2+} and Fe^{3+}, respectively.[49] The appearance of the peaks corresponding to Fe^{2+} can be attributed to the formation of iron sulfides.[50] The appearance of peak at 711.2 eV in the deconvoluted spectra confirms the formation of Fe-N in all the catalysts.[51] Hence, this analysis indicates that, in all the prepared catalysts, both Fe^{2+} and Fe^{3+} oxidation states coexist with the formation of Fe-N/Fe-S moieties.

The deconvolution of N 1s spectra shows the presence of five different types of nitrogen, namely, pyridinic, pyrrolic, graphitic, N-oxide and nitrogen coordinated to Fe (Fe-N) in the composite catalysts and the control sample. The deconvoluted N 1s spectra of PM-900, PMCNT-800, PMCNT-900 and PMCNT-1000 are given in **Figure 5.8a, c, e and g**, respectively.

Table 5.2 Percentage composition of the different types of nitrogen present in the catalysts prepared at different temperatures.

	PM-900	PMCNT-800	PMCNT-900	PMCNT-1000
Pyridinic-N	16.69	32.46	15.26	6.03
Fe-N$_x$	11.55	8.63	13.19	8.86
Pyrrolic-N	10.71	16.88	11.93	13.11
Graphitic-N	50.67	30.32	40.18	67.29
Oxidised-N	10.27	11.68	19.41	4.68

and their relative percentage are listed in **Table 5.2**. The Fe-N$_x$ moiety, which is the most prominent ORR active site, is present in all the prepared catalysts along with the other ORR active sites based on the graphitic and pyridinic nitrogen coordinated centres. A close look at the N 1s spectra of the different PMCNT catalysts reveal that the content of the graphitic N
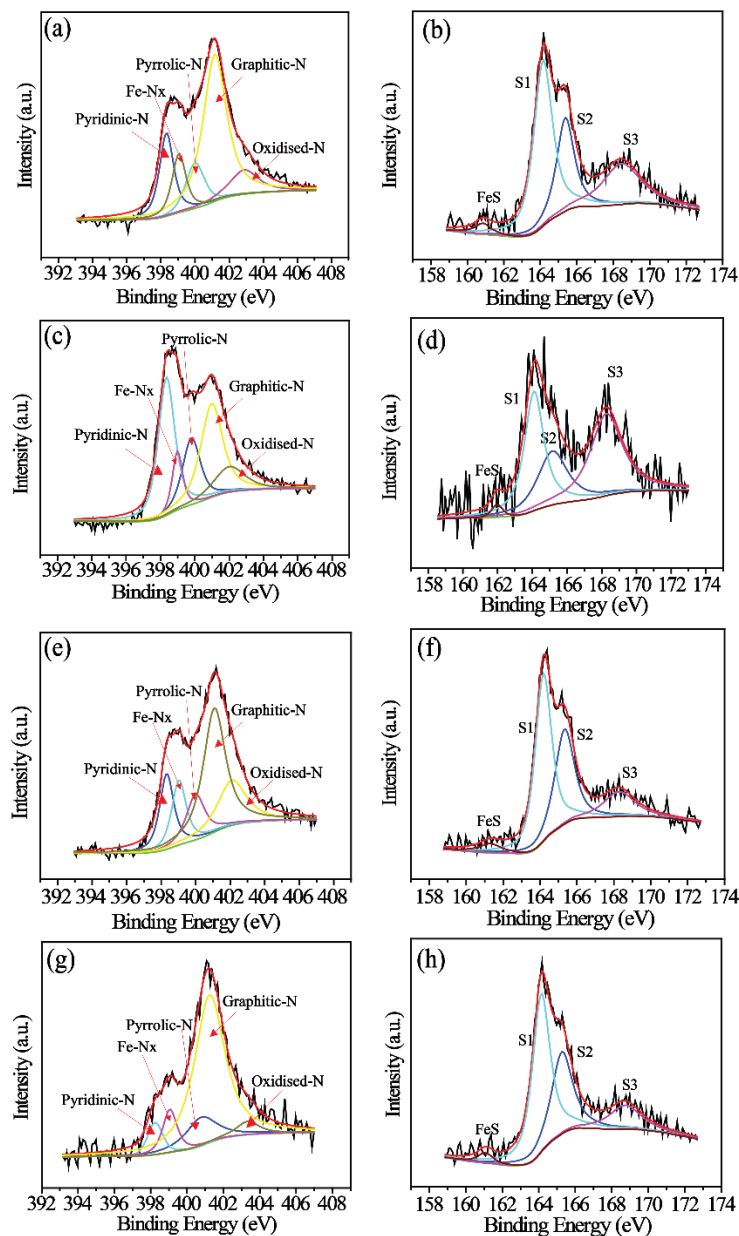
Figure 5.8 Deconvoluted N 1s and S 2p XPS of (a) and (b) PM-900, (c) and (d) PMCNT-800, (e) and (f) PMCNT-900 and (g) and (h) PMCNT-1000.

increases with a reduction in the pyridinic N content with the pyrolysis temperature. PMCNT-900, being a system with optimal contents of the graphic and pyridinic nitrogen along with the coordinated $Fe-N_x$ sites, thus outperformed better than the other systems in terms of the ORR performance. The deconvolution of the S 2p spectra of the catalysts (**Figure 5.8b, d, f, h**) leads to the peaks corresponding to S $2p_{3/2}$ and S $2p_{1/2}$ caused by the spin-orbital coupling and a peak towards a high binding energy caused by the oxidized form of the sulphur, *i.e.*, SO_x.[52-53] Also, it should be noted that the content of SO_x is found to be decreased with the increase in the pyrolysis temperature of the composites. The peak at ~161.5 eV in the S 2p

spectra indicates the formation of the Fe-S bond in all the samples.[54-55] Along with the presence of the active sites, a uniform distribution of the catalytic sites is also critical to achieve high performance from an electrocatalyst. These parameters significantly influence on governing the half-wave potential and power densities at the potential regions where the system performances are usually recorded. Accordingly, the EDS mapping recorded for PMCNT-900 and PM-900 as given in **Figure 5.6a and 5.6b**, respectively, points towards a uniform distribution of all the elements in the two samples over the measured area.

5.5.8 Electrochemical Characterization:

5.5.8.1 Evaluation of the ORR Performance in Acidic and Alkaline Media

As a first step to understand the electrochemical ORR characteristics of the prepared materials, the electrochemically active surface area (S_a) was calculated following Equation 1 by initially calculating the electrochemical double layer capacitance (C) of the catalysts. A detailed discussion on the calculation of S_a and the associated experimental procedure is included in the abovementioned electrochemical analysis section. The cyclic voltammograms recorded for the four catalysts in 0.5 M H_2SO_4 electrolyte are given in **Figure 5.9**. The C values obtained from the slope between the current *vs.* scan rate plots at a potential of 1.0 V *vs.* RHE (**Figure 5.10**) follow the order PMCNT-900 (111.5 F g^{-1}) > PM-900 (104.5 F g^{-1}) > PMCNT-1000 (83.5 F g^{-1}) > PMCNT-800 (81.2F g^{-1}). This corresponds to the S_a values as 558 m^2 g^{-1} (PMCNT-900) > 523 m^2 g^{-1} (PM-900) > 418 m^2 g^{-1} (PMCNT-1000) > 406 m^2 g^{-1} (PMCNT-800). Thus, in terms of ESA, PMCNT-900 has turned out to be the best one of the series.
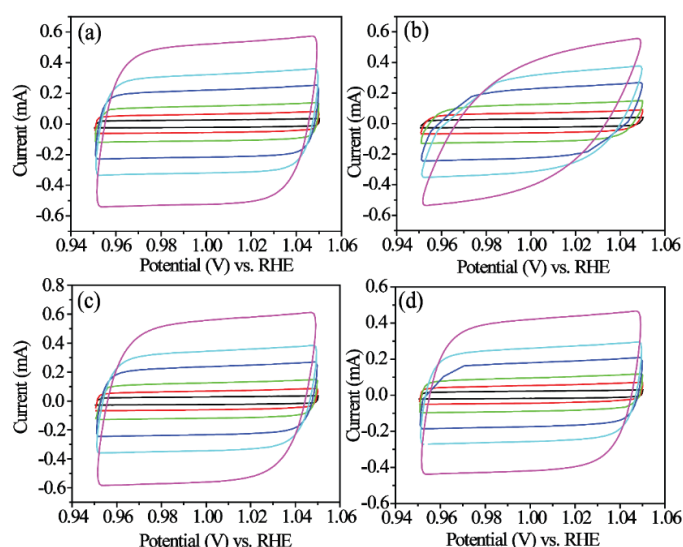
Figure 5.9 Capacitive CV profiles recorded at different scan rates in the non-faradic region in N_2 saturated 0.5 M H_2SO_4: (a) PM-900, (b) PMCNT-800, (c) PMCNT-900 and (d) PMCNT-1000.
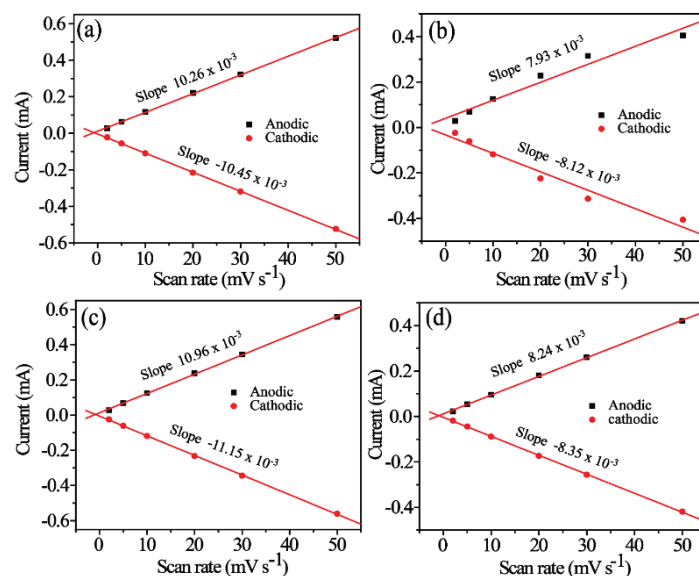
Figure 5.10 Cathodic and anodic current (mA) *vs.* scan rate (mV s^{-1}) obtained from the CV at 0.10 V *vs* RHE: (a) PM-900, (b) PMCNT-800, (c) PMCNT-900 and (d) PMCNT-1000.

The linear sweep voltammogram (LSV) profiles recorded for all the catalysts in 0.5 M H_2SO_4 at a scan rate of 10 mV s^{-1} are presented in **Figure 5.11a**. As can be seen, the highest onset and half-wave potentials are exhibited by PMCNT-900. The overpotential with respect to Pt/C for this catalyst is 60 mV, which is better than the many Fe-N_x-C systems reported for acidic media. The better onset potential achieved in the case of PMCNT-900 compared to PM-900 suggests that the addition of CNT has brought in favourable activity modulation to the system. This might be originated from a controlled interplay of many coexisting factors such as the increased number of the available catalytic sites, better reactant accessibility to the catalytic sites and increased electrical conductivity affected by the interconnecting networks of CNTs. However, to relate the effect of the number density of the active sites and the mass transfer advantages achieved by the presence of CNT as a spacer, a close look at the half-wave potential ($E_{1/2}$) characteristics will be more useful. Among the catalysts, PMCNT-900 shows an $E_{1/2}$ of 0.78 V compared to 0.84 V displayed by the state-of-the-art Pt/C catalyst. The other catalysts display higher overpotential compared to PMCNT-900. This close matching performance of PMCNT-900 with Pt/C and the way through which the ORR performance of PMCNT-900 gets improved as compared to its CNT-free PM-900 counterpart (which displays an onset potential of 0.91 V and $E_{1/2}$ of 0.76 V) confirm that the addition of CNT could help the system to make available more number of the active sites for facilitating the reaction. This increased utilization of the

active sites is further confirmed from the highest limiting current value obtained for PMCNT-900 (**Figure 5.11a**), which is even higher than that of Pt/C. As a more general quantitative performance indicator to compare the intrinsic activity of PMCNT-900 with Pt/C, the Tafel slope values are compared from the Tafel plots generated (**Figure 5.11b**). The Tafel slope values of PMCNT-900 (63 mV decade^{-1}) and Pt/C (66 mV decade^{-1}) are nearly comparable, inferring towards similar ORR kinetics and feasibility on these two systems. On the other hand, PM-900 shows a higher Tafel slope of 70 mV decade^{-1}.

The divergence in the ORR kinetic can arise due to the difference in the nature of the active sites such as those in Pt/C and the PMCNT systems. An insightful information on this has been achieved through the rotating ring disc electrode (RRDE) voltamograms recorded at 1600 rpm at a scan rate of 10 mV s^{-1} in 0.5 M H_2SO_4 electrolyte. The number of electrons involved in the ORR kinetics as well as the percentage of H_2O_2 formed has been calculated using **Equations 2 and 3**. The calculated number of electrons transferred is found to be close to 4 for PMCNT-900 (**Figure 5.11c**), which indicates the dioxygen reduction through the direct 4 e-reduction pathway as compared to the other samples which display relatively lower electron transfer
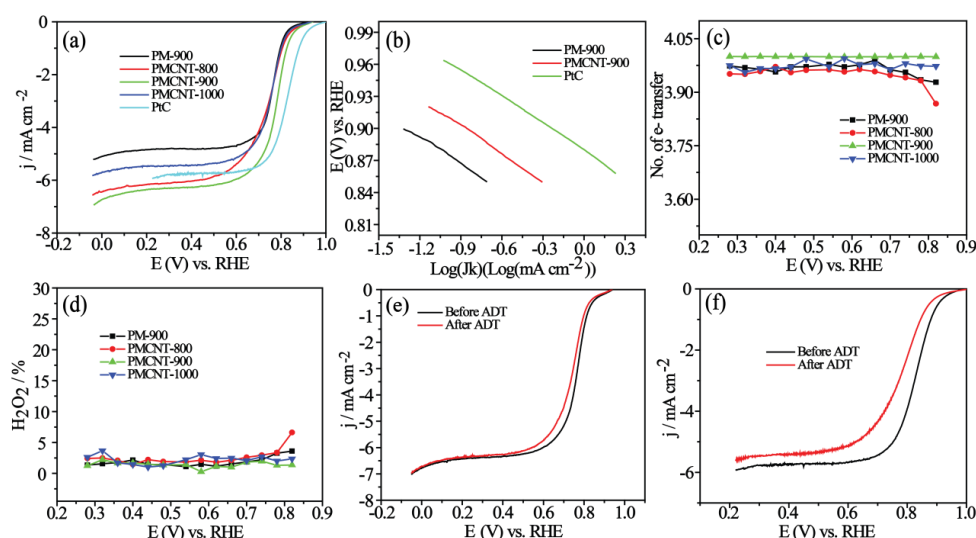
Figure 5.11 Electrochemical performance under acidic pH conditions of the electrolyte (0.5 M H_2SO_4): (a) comparison of the linear sweep voltammograms (LSVs) of the Pt/C, PMCNT and PM catalysts recorded at a rotating speed of 1600 rpm of the working electrode at 10 mV s^{-1} scan rate, (b) Tafel plots of Pt/C, PMCNT-900 and PM-900, (c) the number of electrons transferred for ORR in case of the PMCNT and PM catalysts as recorded through RRDE, (d) the hydrogen peroxide yield recorded on the PMCNT and PM catalysts, (e) LSVs of PMCNT-900 recorded before and after the 10000 potential cycling during ADT in 0.5 M H_2SO_4, and (f) LSVs of Pt/C recorded before and after the 5000 potential cycling in 0.1 M $HClO_4$.

numbers. The amount of H_2O_2 recorded in all the samples as a function of the potential are plotted in **Figure 5.11d**, which clearly shows the negligible amount accounted by all the systems.

Since the active sites are distributed along the carbon matrix in the system, the stability of the active sites is directly related to the integrity of the carbon matrix. Factors like carbon corrosion etc. can deteriorate the performance since corrosion can remove or destroy the active centers. As a means to look into the structural integrity of the carbon framework, an accelerated durability test (ADT) was performed on PMCNT-900 by sweeping the potential between 0.6 to 1.0 V *vs*. RHE for 10000 times under O_2 enriched condition in 0.5 M H_2SO_4. The condition mimics an activated corrosive environment, where, by looking at the changes incurred on $E_{1/2}$ subsequently due to ADT provide important information on the durability characteristics of the carbon. The corresponding results are shown in **Figure 5.11e** for PMCNT-900, which incurred only 19 mV negative shift in $E_{1/2}$ after 10000 cycles of ADT and thus demonstrates its high structural integrity and resilience of active sites in the carbon framework. The Pt/C catalyst, on the other hand, displays an $E_{1/2}$ shift by 46 mV just after 5000 potential cycles in 0.1 M $HClO_4$ (**Figure 5.11f**). Interestingly, PM-900 shows even a larger degree of degradation (32 mV) in performance in acidic medium after 10000 cycles (**Figure 5.12**), inferring to the important role played by the CNT network in bringing in the overall structural integrity for PMCNT-900.
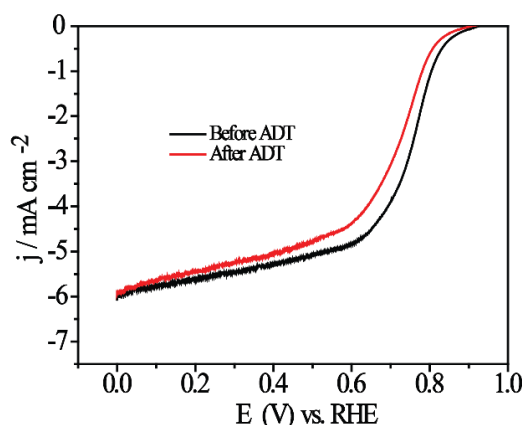
Figure 5.12 ADT of PM-900 in 0.5 M H_2SO_4.

The performance and stability aspects of the catalysts are also investigated in the basic environment. The corresponding LSV curves recorded in 0.1 M KOH for all the catalysts are given Figure 5.13a. It is important to note that, in alkaline medium, although all the PMCNT catalysts display better onset and $E_{1/2}$ potential values compared to Pt/C, PMCNT-900 fares better in the series in terms of the onset potential (1.06 V) as compared to Pt/C (1.03 V) displaying a performance which is comparable to how it performed in the acidic medium. This

extraordinary performance of PMNCT-900 both in acidic and basic conditions can be attributed to the unique architecture of the composite catalyst where CNTs are laid horizontally between the carbon sheets as observed in the TEM images. This architecture helps to improve the catalyst site utilization apart from increasing the electronic conductivity and facilitating mass transfer. The high ORR activity in the basic medium of PMCNT-900 is complemented with higher $E_{1/2}$ potential ($E_{1/2}$ of 0.88 V) as compared to that of Pt/C ($E_{1/2}$ of 0.84 V). As a result, PMCNT-900 has been exposed as one of the best catalysts for ORR activity in acidic as well as in basic media among transition metal based electrocatalysts.

The ability to facilitate ORR in the activation polarization region within the basic condition is further confirmed from Tafel analysis (**Figure 5.13b**). As in the case of the acidic conditions, the Tafel slope value obtained for PMCNT-900 (74 mV decade^{-1}) is found to be comparable to Pt/C (76 mV decade^{-1}). Also, in terms of the number of electrons involved for the ORR process (**Figure 5.13c**) and the amount of H_2O_2 recorded (**Figure 5.13d**), in the basic media also, PMCNT-900 is found to be the better choice among the group and closely matching with the characteristics to that of the Pt/C catalyst. It should be noted that, compared to the acidic
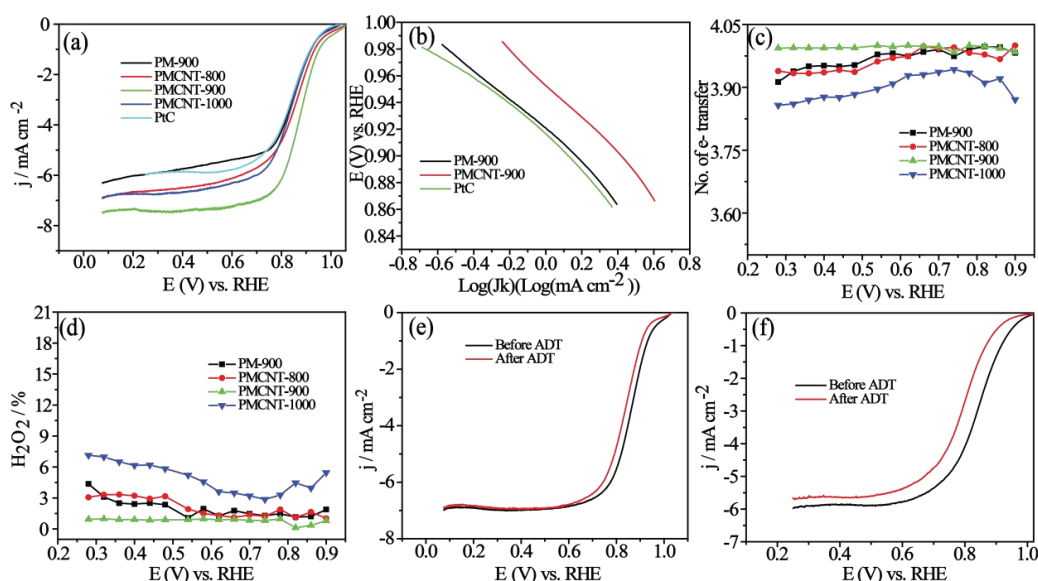
Figure 5.13 Electrochemical performance under basic pH conditions of the electrolyte (0.1 M KOH): (a) comparison of the LSVs of the Pt/C, PMCNT and PM catalysts recorded at a rotating speed of 1600 rpm of the working electrode and a scan rate of 10 mV s^{-1}, (b) Tafel plots of the catalysts, (c) the number of electrons transferred for ORR in case of the PMCNT and PM catalysts as recorded through RRDE, (d) the hydrogen peroxide yield recorded on the PMCNT and PM catalysts, (e) LSVs of PMCNT-900 recorded before and after the 10000 potential cycling in 0.1 M KOH and (f) LSVs of Pt/C recorded before and after the 5000 potential cycling in 0.1 M KOH.

environment, the basic condition triggers more H_2O_2 production and on PMCNT-1000, an amount as high as 8% has been observed. The electrochemical endurance of PMCNT-900 in the basic medium is also found to be good as in the acidic conditions because the ADT leads to only 25 mV negative shift in $E_{1/2}$ during 10000 potential cycles (**Figure 5.13e**) compared to 40 mV shift displayed by Pt/C after 5000 potential cycles (**Figure 5.13f**).

5.5.8.2 PMCNT-900 as a Cathode in PEMFC and AEMFC

The efficacy of PMCNT-900 as the cathode for a single cell in a PEMFC and AEMFC has been validated by fabricating and testing the respective membrane electrode assemblies (MEAs) of 4 cm^2 active area. In both the cases, the anodes were made by employing 40 wt. % Pt/C by maintaining a loading of 0.50 mg cm^{-2}. For comparative purpose, the cells based on Pt/C in the both cathode and anode were also prepared and tested. **Figure 5.14a** represents the comparative I-V polarization plots recorded for the MEAs based on PMCNT-900 and Pt/C as the cathode catalysts under H_2-O_2 feed conditions. While the conventional Pt/C based system exhibits a peak power density of 650 mW cm^{-2}, the PMCNT-900 based cell displays a value of 500 mW cm^{-2}. For practical applications, the cell performance needs to be evaluated at the operating potentials rather than that based on the peak power densities. At the most widely used operating potential of 0.60 V, the current densities delivered by the PTCNT-900 and Pt/C based systems are 202 mA cm^{-2} and 612 mA cm^{-2}, respectively. Even though the performance of the cell based on the in-house MEA is lower than that of its counterpart Pt/C based system, the value obtained is significant by considering the reported values based on the precious metal-free ORR electrocatalysts.[24,44,47-49] Also, it should be noted that the essential characteristics of both the I-V polarization plots retain the same features starting from the nearly comparable open circuit potential (OCV) to the nature of the behavior of the cells in the regions corresponding to activation, ohmic and mass-transfer polarizations. The I-V polarization plots were further plotted by switching over to air instead of O_2, since performance under air feed condition is important to consider the practical operability of PEMFCs. The corresponding data presented in **Figure 5.14b** indicates that the trend in the performance characteristics is retained similar in both the MEAs and as expected both the systems displayed reduced performance under this diluted O_2 condition.

To get a more insightful information on the processes occurring at different time scales in the MEAs, the cells were further investigated with the help of electrochemical impedance spectroscopy (EIS) at the potential regions of OCV, 0.80 V (activation polarization region), 0.60 V (conventional operating potential region) and 0.40 V (mass transfer region) along the

polarization plots (**Figure 5.14c**). It can be seen that the basic nature of the Nyquist plots is same in both the types of MEAs even though there are notable differences in terms of the charge transfer resistance (CTR) occurring at the different voltages. The CTR values obtained in the case of the MEA based on PMCNT-900 cathode are 0.812, 0.180 and 0.055 Ω at 0.80, 0.60 and 0.40 V, respectively. The corresponding values in the case of the Pt/C based system

Figure 5.14 (a) The I-V polarization plots recorded during the single cell evaluation of the PEMFCs based on PMCNT-900 and Pt/C as the cathode catalysts under H_2 and O_2 feed conditions; (b) comparative I-V polarization plots of the MEAs based on PMCNT-900 and Pt/C as the cathode catalysts in H_2 and air feed condition; (c) the impedance plots recorded for the MEA based on PMCNT-900 as the cathode catalyst at different potentials along with the corresponding data obtained for the Pt/C based MEA in the inset image when the test was conducted in H_2-O_2 feed condition; (d) the impedance plots recorded for the MEA based on PMCNT-900 as the cathode catalyst at different potentials along with the corresponding data obtained for the Pt/C based MEA in the inset i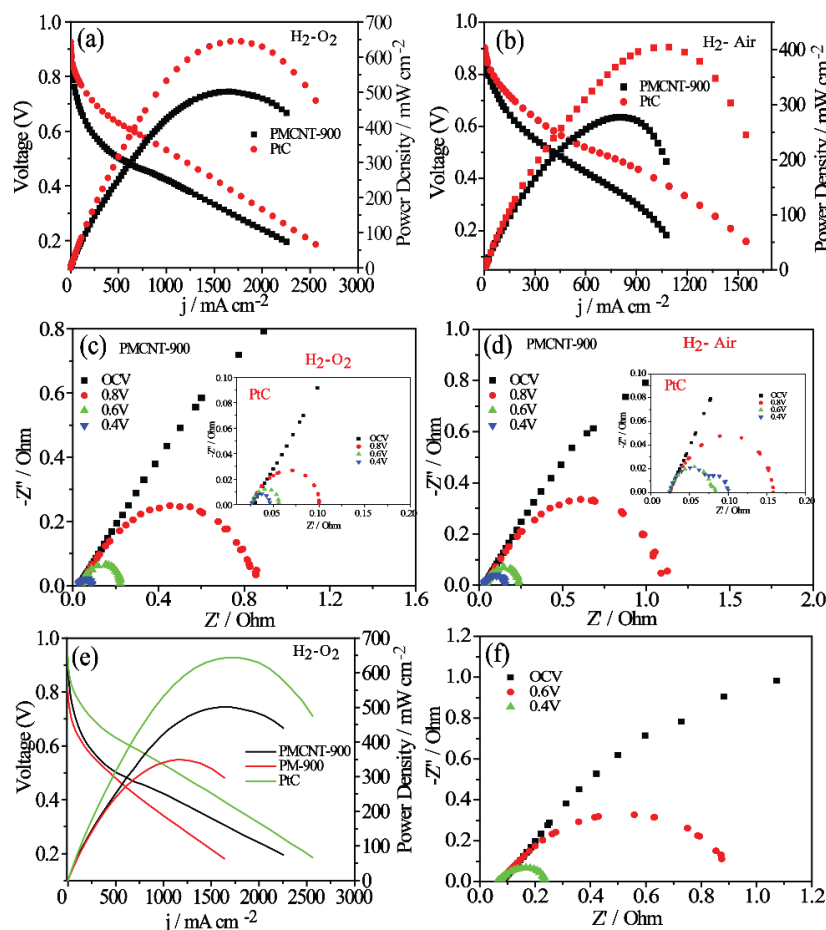mage when the test was done in H_2 and air feed condition; (e) comparative I-V polarization plots recorded during the single cell testing of the MEAs based of PMCNT-900, PM-900 and Pt/C as the cathode catalysts under H_2-O_2 feed condition; (f) impedance analysis of the MEA based on PM-900 as the cathode catalyst recorded at different potentials in H_2 and O_2.

are 0.066, 0.028 and 0.019 Ω, indicating that the trend follows the basic nature of the differences in terms of the intrinsic ORR activity characteristics of the systems as detailed in the previous few sections. It should be noted that EIS loops recorded under H_2-O_2 feed conditions do not show any indication of mass transfer issues (Warburg impedance) in both the systems even at the high current dragging states (such as the case at 0.40 V).

However, when the EIS was recorded under H_2-Air feed conditions (**Figure 5.14d**), the mass transfer issue which is evident as a shoulder in the low frequency region of the EIS loop recorded at 0.40 V for the Pt/C based system is clearly absent in the case of the cell based on PMCNT-900. The efficiency of the MEA based on the homemade catalyst to tackle the mass transfer issue is presumably originated due to the presence of CNT as a spacer in the electrode. The entangled CNT networks can create open channels and spaces for reactant distribution and product water dissipation in a better way compared to the Vulcan type of carbon present in the Pt/C based system. Such channels also help to improve the accessibility of the reactant gases to the active sites, leading to an improved performance output from the cell as evident from **Figure 5.14e**, where the performance of a cell based on PM-900 (which does not contain the CNT spacer) is clearly inferior to its counterpart system based on PMCNT-900. The Nyquist plots recorded for PM-900 based cell is presented in **Figure 5.14f**, which displays an ESR value of 0.072 Ω compared to 0.03 Ω at OCV for the PMCNT-900 based cell. This difference in ESR between the system inferring to the controlled property and activity modulations incurred by the system in the electrode level due to the presence of the weaving network of CNT while employing PMCNT-900 as the ORR catalyst.
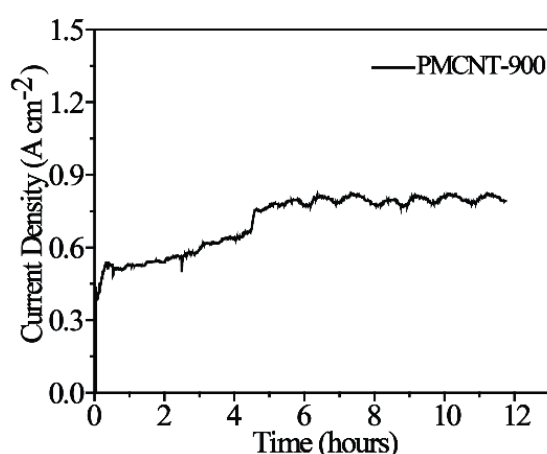

Figure 5.15. The life-test data for 12 h recorded in the PEMFCs single cell mode by employing PMCNT-900 and Pt/C as the cathode and anode catalysts, respectively, in H_2 and O_2 atmosphere at 60 ºC. The analysis was performed at a constant potential of 0.40 V without applying any back pressure.

The stability test of PMCNT-900 in single cell has also been carried out by monitoring the performance at a constant potential of 0.40 V for the 12 h, which has delivered a current density of ~790 mA cm^{-2} at 60 °C in H$_2$ and O$_2$ atmosphere with 100 % humidification as shown in Figure 5.15. It is observed from this life-test data that the performance is gradually getting improved initially and becoming stable in the remaining period. The initial continuous improvement in the performance of PMCNT-900 could be due to the activation of the catalyst. From the short-term life-test data, it is confirmed that PMCNT-900 is highly stable in the single cell testing condition under the period of investigation.
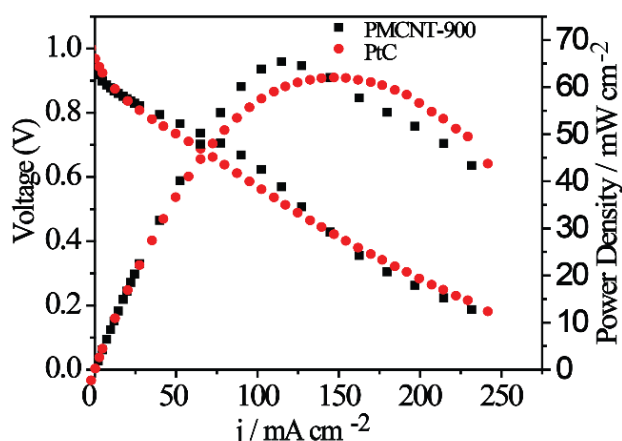
Figure 5.16 The I-V polarization plot recorded under H$_2$ and O$_2$ feed conditions during the single cell testing of the AEMFC based PMCNT-900 as the cathode catalyst in the MEA.

Since PMCNT-900 is displaying comparable ORR characteristics to that of Pt/C in basic medium, testing of a 4 cm^2 MEA in a single cell mode was done in anion exchange membrane fuel cell (AEMFC) by using KOH doped Fumapem FAA membrane by employing PMCNT-900 as the cathode of the cell. The corresponding polarization plot is presented in comparison to a similar data generated on the cell based on Pt/C as the cathode in **Figure 5.16**. The PMCNT-900 and Pt/C based cells deliver maximum power densities of 65 mW cm^{-2} and 62 mW cm^{-2}, respectively, inferring only to a slight performance difference between the systems. It should be noted that, unlike PEMFCs, the performance in AEMFCs is largely limited by the quality of the anion exchange membrane in terms of its conductivity and durability. The KOH doped membranes possess the issue of alkali leaching out from the polymer matrix, leading to a reduction in performance with time. Still, the nearly comparable performance obtained in the case of the cell based on PMCNT-900 to its counterpart system based on Pt/C points towards the efficiency of the Pt-free catalyst to facilitate ORR in a realistic system level demonstration and the result goes in agreement with the comparable ORR characteristics displayed by the

system during the single electrode studies in KOH medium. Hence, PMCNT-900 has demonstrated the comparable activity to the reported literature based transition metal electrocatalyst for PEMFCs and AEMFCs.

5.6 Conclusion

In summary, a noble metal-free ORR electrocatalyst containing both nitrogen and sulphur on carbon sheets which are spatially separated by the CNT network could be successfully synthesized and the catalyst is found to be working exceptionally well both under acidic and basic pH conditions. This has been achieved by controlled pyrolysis of a combination of the *in-situ* grown PEDOT with CNT and melamine, which leads to the formation of the carbon sheets bearing the Fe-N and Fe-S active sites all the while acquiring desirable spatial distribution facilitated by the CNT network. The catalyst prepared by pyrolyzing at 900 $^{\circ}$C (PMCNT-900) displays ORR activity with substantially reduced overpotential in both acidic and basic electrolyte conditions. In the acidic medium, PMCNT-900 shows high ORR activity, which is lower than that of Pt/C in terms of the onset as well as half-wave potential. However, in case of the basic condition, the PMCNT-900 catalyst shows better activity compared to the 40 wt.% Pt/C in terms of the onset as well as half-wave potential. While employing PMCNT-900 as the cathode catalyst in a single cell of Nafion-based PEMFC, the system delivered a maximum power density (PD) of 500 and 275 mW cm^{-2} at 60 $^{\circ}$C without applying any back-pressure under H$_2$-O$_2$ and H$_2$-Air feed conditions, respectively. On the other hand, a corresponding test in the anion exchange membrane fuel cell (AEMFCs) mode resulted to a power density of 65 mW cm^{-2} at 50 $^{\circ}$C, which is a comparable value obtained while employing Pt/C as the cathode. Thus PMCNT-900 evolves as a strong contender as a Pt-free electrocatalyst to facilitate ORR under the extreme pH conditions.

5.7 References

[1]. Feng, Y.; Alonso-Vante, N. Nonprecious Metal Catalysts for the Molecular Oxygen-Reduction Reaction. *phys. status solidi (b)* **2008,** *245*, 1792-1806.

[2]. Yang, L.; Su, Y.; Li, W.; Kan, X. Fe/N/C Electrocatalysts for Oxygen Reduction Reaction in PEM Fuel Cells Using Nitrogen-Rich Ligand as Precursor. *J. Phy. Chem. C* **2015,** *119*, 11311-11319.

[3]. Tian, X. L.; Wang, L.; Deng, P.; Chen, Y.; Xia, B. Y., Research Advances in Unsupported Pt-based Catalysts for Electrochemical Methanol Oxidation. *J. Energy Chem.* **2017,** *26*, 1067-1076.

[4]. Tse, E. C. M.; Gewirth, A. A. Effect of Temperature and Pressure on the Kinetics of the Oxygen Reduction Reaction. *J. Phy. Chem. A* **2015,** *119*, 1246-1255.

[5]. Guo, X.; Jia, X.; Song, P.; Liu, J.; Li, E.; Ruan, M.; Xu, W. Ultrahigh Pressure Synthesis of Highly Efficient FeNx/C Electrocatalysts for the Oxygen Reduction Reaction. *J. Mater. Chem. A* **2017,** *5*, 17470-17475.

[6]. Jaouen, F.; Proietti, E.; Lefèvre, M.; Chenitz, R.; Dodelet, J.-P.; Wu, G.; Chung, H. T.; Johnston, C. M.; Zelenay, P., Recent Advances in Non-precious Metal Catalysis for Oxygen-Reduction Reaction in Polymer Electrolyte Fuel Cells. *Energy Environ. Sci.* **2011,** *4*, 114-130.

[7]. Byon, H. R.; Suntivich, J.; Shao-Horn, Y., Graphene-Based Non-Noble-Metal Catalysts for Oxygen Reduction Reaction in Acid. *Chem. Mater.* **2011,** *23*, 3421-3428.

[8]. Zhang, J.; Dai, L., Heteroatom-Doped Graphitic Carbon Catalysts for Efficient Electrocatalysis of Oxygen Reduction Reaction. *ACS Catal.* **2015,** *5*, 7244-7253.

[9]. Cheng, N.; Kutz, R.; Kemna, C.; Wieckowski, A., Enhanced ORR Activity of Cobalt Porphyrin Co-deposited with Transition Metal Oxides on Au and C Electrodes. The ORR Threshold Data. *J. Electroanal. Chem.* **2013,** *705*, 8-12.

[10]. Morozan, A.; Campidelli, S.; Filoramo, A.; Jousselme, B.; Palacin, S., Catalytic Activity of Cobalt and Iron Phthalocyanines or Porphyrins Supported on Different Carbon Nanotubes Towards Oxygen Reduction Reaction. *Carbon* **2011,** *49*, 4839-4847.

[11]. Wang, Y.; Li, J.; Wei, Z., Transition-Metal-Oxide-Based Catalysts for the Oxygen Reduction Reaction. *J. Mater. Chem. A* **2018,** *6*, 8194-8209.

[12]. Liu, X.; Dai, L., Carbon-based Metal-free Catalysts. *Nat. Rev. Mater.* **2016,** *1*, 16064.

[13]. Hu, C.; Dai, L., Carbon-Based Metal-Free Catalysts for Electrocatalysis Beyond the ORR. *Angew. Chem. Int. Ed.* **2016,** *55*, 11736-11758.

[14]. Vasudevan, P.; Santosh; Mann, N.; Tyagi, S., Transition Metal Complexes of Porphyrins and Phthalocyanines as Eectrocatalysts for Dioxygen Reduction. *Transit. Metal Chem.* **1990,** *15*, 81-90.

[15]. Yeager, E. Dioxygen Electrocatalysis: Mechanisms in Relation to Catalyst Structure. *J. Mol. Catal.* **1986,** *38*, 5-25.

[16]. Jaouen, F.; Herranz, J.; Lefèvre, M.; Dodelet, J.-P.; Kramm, U. I.; Herrmann, I.; Bogdanoff, P.; Maruyama, J.; Nagaoka, T.; Garsuch, A.; Dahn, J. R.; Olson, T.; Pylypenko, S.; Atanassov, P.; Ustinov, E. A. Cross-Laboratory Experimental Study of

Non-Noble-Metal Electrocatalysts for the Oxygen Reduction Reaction. *ACS Appl. Mater. Interfaces* **2009,** *1*, 1623-1639.

[17]. Byon, H. R.; Suntivich, J.; Shao-Horn, Y. Graphene-Based Non-Noble-Metal Catalysts for Oxygen Reduction Reaction in Acid. *Chem. Mater.* **2011,** *23*, 3421-3428.

[18]. Li, S.; Zhang, L.; Kim, J.; Pan, M.; Shi, Z.; Zhang, J. Synthesis of Carbon-supported Binary FeCo–N Non-Noble Metal Electrocatalysts for the Oxygen Reduction Reaction. *Electrochim. Acta* **2010,** *55*, 7346-7353.

[19]. Cao, R.; Lee, J.-S.; Liu, M.; Cho, J. Recent Progress in Non-Precious Catalysts for Metal-Air Batteries. *Adv. Energy Mater.* **2012,** *2*, 816-829.

[20]. Othman, R.; Dicks, A. L.; Zhu, Z. Non Precious Metal Catalysts for the PEM Fuel Cell Cathode. *Int. J. Hydrogen Energy* **2012,** *37*, 357-372.

[21]. Xu, H.; Ci, S.; Ding, Y.; Wang, G.; Wen, Z., Recent Advances in Precious Metal-free Bifunctional Catalysts for Electrochemical Conversion Systems. *J. Mater. Chem. A* **2019,** *7*, 8006-8029.

[22]. Guo, X.; Jia, X.; Song, P.; Liu, J.; Li, E.; Ruan, M.; Xu, W., Ultrahigh Pressure Synthesis of Highly Efficient FeNx/C Electrocatalysts for the Oxygen Reduction Reaction. *J. Mater. Chem. A* **2017,** *5*, 17470-17475.

[23]. Li, Y.; Huang, H.; Chen, S.; Wang, C.; Ma, T., Nanowire-Templated Synthesis of FeNx-Decorated Carbon Nanotubes as Highly Efficient, Universal-pH, Oxygen Reduction Reaction Catalysts. *Chem. : Eur. J.* **2019,** *25*, 2637-2644.

[24]. Wang, M.-Q.; Yang, W.-H.; Wang, H.-H.; Chen, C.; Zhou, Z.-Y.; Sun, S.-G. Pyrolyzed Fe–N–C Composite as an Efficient Non-precious Metal Catalyst for Oxygen Reduction Reaction in Acidic Medium. *ACS Catal.* **2014,** *4*, 3928-3936.

[25]. Lai, Q.; Zheng, L.; Liang, Y.; He, J.; Zhao, J.; Chen, J. Metal–Organic-Framework-Derived Fe-N/C Electrocatalyst with Five-Coordinated Fe-Nx Sites for Advanced Oxygen Reduction in Acid Media. *ACS Catal.* **2017,** *7*, 1655-1663.

[26]. Ren, P.; Ci, S.; Ding, Y.; Wen, Z., Molten-Salt-Mediated Synthesis of Porous Fe-containing N-doped Carbon as Efficient Cathode Catalysts for Microbial Fuel Cells. *Appl. Surf. Sci.* **2019,** *481*, 1206-1212.

[27]. Li, Y.; Huang, J.; Hu, X.; Bi, L.; Cai, P.; Jia, J.; Chai, G.; Wei, S.; Dai, L.; Wen, Z., Fe Vacancies Induced Surface FeO6 in Nanoarchitectures of N-Doped Graphene Protected β-FeOOH: Effective Active Sites for pH-Universal Electrocatalytic Oxygen Reduction. *Adv. Funct. Mater.* **2018,** *28*, 1803330.

[28]. Bhange, S. N.; Unni, S. M.; Kurungot, S. Graphene with Fe and S Coordinated Active Centers: An Active Competitor for the Fe–N–C Active Center for Oxygen Reduction Reaction in Acidic and Basic pH Conditions. *ACS Appl. Energy Mater.* **2018,** *1*, 368-376.

[29]. Wang, X.; Zhou, J.; Fu, H.; Li, W.; Fan, X.; Xin, G.; Zheng, J.; Li, X. MOF Derived Catalysts for Electrochemical Oxygen Reduction. *J. Mater. Chem. A* **2014,** *2*, 14064-14070.

[30]. Aiyappa, H. B.; Bhange, S. N.; Sivasankaran, V. P.; Kurungot, S. Single Cell Fabrication Towards the Realistic Evaluation of a CNT-Strung ZIF-Derived Electrocatalyst as a Cathode Material in Alkaline Fuel Cells and Metal−Air Batteries. *ChemElectroChem* **2017,** *4*, 2928-2933.

[31]. Zhang, H.; Hwang, S.; Wang, M.; Feng, Z.; Karakalos, S.; Luo, L.; Qiao, Z.; Xie, X.; Wang, C.; Su, D.; Shao, Y.; Wu, G. Single Atomic Iron Catalysts for Oxygen Reduction in Acidic Media: Particle Size Control and Thermal Activation. *J. Am. Chem. Soc.* **2017,** *139*, 14143-14149.

[32]. Bhange, S. N.; Unni, S. M.; Kurungot, S. Nitrogen and Sulphur Co-doped Crumbled Graphene for the Oxygen Reduction Reaction with Improved Activity and Stability in Acidic Medium. *J. Mater. Chem. A* **2016,** *4*, 6014-6020.

[33]. Wu, G.; More, K. L.; Johnston, C. M.; Zelenay, P. High-Performance Electrocatalysts for Oxygen Reduction Derived from Polyaniline, Iron, and Cobalt. *Science* **2011,** *332*, 443-447.

[34]. Chlistunoff, J. RRDE and Voltammetric Study of ORR on Pyrolyzed Fe/Polyaniline Catalyst. On the Origins of Variable Tafel Slopes. *J. Phy. Chem. C* **2011,** *115*, 6496-6507.

[35]. Wu, Z.-S.; Yang, S.; Sun, Y.; Parvez, K.; Feng, X.; Müllen, K. 3D Nitrogen-Doped Graphene Aerogel-Supported Fe3O4 Nanoparticles as Efficient Electrocatalysts for the Oxygen Reduction Reaction. *J. Am. Chem. Soc.* **2012,** *134*, 9082-9085.

[36]. You, C.; Jiang, X.; Wang, X.; Hua, Y.; Wang, C.; Lin, Q.; Liao, S. Nitrogen, Sulfur Co-doped Carbon Derived from Naphthalene-Based Covalent Organic Framework as an Efficient Catalyst for Oxygen Reduction. *ACS Appl. Energy Mater.* **2018,** *1*, 161-166.

[37]. Unni, S. M.; George, L.; Bhange, S. N.; Devi, R. N.; Kurungot, S. Valorization of Coffee Bean Waste: A Coffee Bean Waste Derived Multifunctional Catalyst for

Photocatalytic Hydrogen Production and Electrocatalytic Oxygen Reduction Reactions. *RSC Adv.* **2016,** *6*, 82103-82111.

[38]. Liang, J.; Jiao, Y.; Jaroniec, M.; Qiao, S. Z. Sulfur and Nitrogen Dual-Doped Mesoporous Graphene Electrocatalyst for Oxygen Reduction with Synergistically Enhanced Performance. *Angew. Chem.* **2012,** *124*, 11664-11668.

[39]. Tian, X.; Zhao, X.; Su, Y.-Q.; Wang, L.; Wang, H.; Dang, D.; Chi, B.; Liu, H.; Hensen, E. J. M.; Lou, X. W.; Xia, B. Y., Engineering Bunched Pt-Ni Alloy Nanocages for Efficient Oxygen Reduction in Practical Fuel Cells. *Science* **2019,** *366*, 850-856

[40]. Chung, H. T.; Cullen, D. A.; Higgins, D.; Sneed, B. T.; Holby, E. F.; More, K. L.; Zelenay, P. Direct Atomic-Level Insight into the Active Sites of a High-Performance PGM-free ORR Catalyst. *Science* **2017,** *357*, 479-484.

[41]. Zhang, S., 127. Understanding of Sulfurized Polyacrylonitrile for Superior Performance Lithium/Sulfur Battery. *Energies* **2014,** *7*, 4588-4600.

[42]. Li, Z. Q.; Lu, C. J.; Xia, Z. P.; Zhou, Y.; Luo, Z., X-ray Diffraction Patterns of Graphite and Turbostratic Carbon. *Carbon* **2007,** *45*, 1686-1695.

[43]. Rémazeilles, C.; Saheb, M.; Neff, D.; Guilminot, E.; Tran, K.; Bourdoiseau, J.-A.; Sabot, R.; Jeannin, M.; Matthiesen, H.; Dillmann, P.; Refait, P. Microbiologically Influenced Corrosion of Archaeological Artefacts: Characterisation of Iron(II) Sulfides by Raman Spectroscopy. *J. Raman Spectrosc.* **2010,** *41*, 1425-1433.

[44]. Dhavale, V. M.; Gaikwad, S. S.; Kurungot, S. Activated Nitrogen Doped Graphene Shell Towards Electrochemical Oxygen Reduction Reaction by its Encapsulation on Au Nanoparticle (Au@N-Gr) in Water-in-oil "Nanoreactors". *J. Mater. Chem. A* **2014,** *2*, 1383-1390.

[45]. Yin, H.; Zhang, C.; Liu, F.; Hou, Y. Hybrid of Iron Nitride and Nitrogen-Doped Graphene Aerogel as Synergistic Catalyst for Oxygen Reduction Reaction. *Adv. Funct. Mater.* **2014,** *24*, 2930-2937.

[46]. Lv, Q.; Si, W.; He, J.; Sun, L.; Zhang, C.; Wang, N.; Yang, Z.; Li, X.; Wang, X.; Deng, W.; Long, Y.; Huang, C.; Li, Y., Selectively Nitrogen-doped Carbon Materials as Superior Metal-free Catalysts for Oxygen Reduction. *Nat. Commun.* **2018,** *9*, 3376.

[47]. Unni, S. M.; Bhange, S. N.; Illathvalappil, R.; Mutneja, N.; Patil, K. R.; Kurungot, S., Nitrogen-Induced Surface Area and Conductivity Modulation of Carbon Nanohorn and Its Function as an Efficient Metal-Free Oxygen Reduction Electrocatalyst for Anion-Exchange Membrane Fuel Cells. *Small* **2015,** *11*, 352-360.
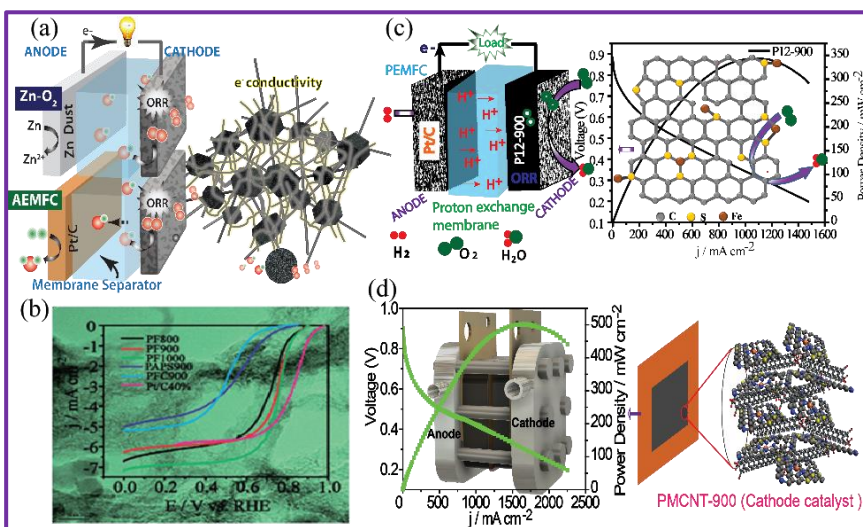
[48]. Zhang, H.; Hwang, S.; Wang, M.; Feng, Z.; Karakalos, S.; Luo, L.; Qiao, Z.; Xie, X.; Wang, C.; Su, D.; Shao, Y.; Wu, G., Single Atomic Iron Catalysts for Oxygen Reduction in Acidic Media: Particle Size Control and Thermal Activation. *J. Am. Chem. Soc.* **2017,** *139*, 14143-14149.

[49]. Tran, T.-N.; Song, M. Y.; Singh, K. P.; Yang, D.-S.; Yu, J.-S., Iron–polypyrrole Electrocatalyst with Remarkable Activity and Stability for ORR in Both Alkaline and Acidic Conditions: A Comprehensive Assessment of Catalyst Preparation Sequence. *J. Mater. Chem. A* **2016,** *4*, 8645-8657.

[50]. Vinayan, B. P.; Diemant, T.; Behm, R. J.; Ramaprabhu, S., Iron encapsulated nitrogen and sulfur co-doped few layer graphene as a non-precious ORR catalyst for PEMFC application. *RSC Advances* **2015,** *5*, 66494-66501.

[51]. Eissa, A. A.; Peera, S. G.; Kim, N. H.; Lee, J. H., g-C3N4 templated synthesis of the Fe3C@NSC electrocatalyst enriched with Fe–Nx active sites for efficient oxygen reduction reaction. *J. Mater. Chem. A* **2019,** *7*, 16920-16936.

[52]. Li, W.; Yang, D.; Chen, H.; Gao, Y.; Li, H. Sulfur-doped Carbon Nanotubes as Catalysts for the Oxygen Reduction Reaction in Alkaline Medium. *Electrochim. Acta* **2015,** *165*, 191-197.

[53]. Shi, J.; Zhou, X.; Xu, P.; Qiao, J.; Chen, Z.; Liu, Y. Nitrogen and Sulfur Co-doped Mesoporous Carbon Materials as Highly Efficient Electrocatalysts for Oxygen Reduction Reaction. *Electrochim. Acta* **2014,** *145*, 259-269.

[54]. Park, J.-e.; Jang, Y. J.; Kim, Y. J.; Song, M.-s.; Yoon, S.; Kim, D. H.; Kim, S.-J., Sulfur-doped graphene as a potential alternative metal-free electrocatalyst and Pt-catalyst supporting material for oxygen reduction reaction. *Physical Chemistry Chemical Physics* **2014,** *16* (1), 103-109.

[55]. Smart, R. S. C.; Skinner, W. M.; Gerson, A. R., XPS of sulphide mineral surfaces: metal-deficient, polysulphides, defects and elemental sulphur. *Surface and Interface Analysis* **1999,** *28* (1), 101-105.

[56]. Bashyam, R.; Zelenay, P. A Class of Non-precious Metal Composite Catalysts for Fuel Cells. *Nature* **2006,** *443*, 63-66.

[57]. Unni, S. M.; Illathvalappil, R.; Bhange, S. N.; Puthenpediakkal, H.; Kurungot, S. Carbon Nanohorn-Derived Graphene Nanotubes as a Platinum-Free Fuel Cell Cathode. *ACS Appl. Mater. Interfaces* **2015,** *7*, 24256-24264.

[58]. Proietti, E.; Jaouen, F.; Lefèvre, M.; Larouche, N.; Tian, J.; Herranz, J.; Dodelet, J.-P. Iron-based Cathode Catalyst with Enhanced Power Density in Polymer Electrolyte Membrane Fuel Cells. *Nat. Commun.* **2011,** *2*, 416.

[59]. Tian, X. L.; Wang, L.; Chi, B.; Xu, Y.; Zaman, S.; Qi, K.; Liu, H.; Liao, S.; Xia, B. Y., Formation of a Tubular Assembly by Ultrathin Ti0.8Co0.2N Nanosheets as Efficient Oxygen Reduction Electrocatalysts for Hydrogen–/Metal–Air Fuel Cells. *ACS Catal.* **2018,** *8*, 8970-8975

Chapter-6

Summary

This chapter summarizes the main successes and results of the previous chapters compiled in this thesis. Chapter 1 discusses about the global energy scenario, green technology devices like polymer electrolyte membrane fuel cells (PEMFCs), and zinc-air battery (ZAB) and the existing material level and system level challenges. The significance of electrocatalyst development and literature discussion on Pt-free electrocatalysts for oxygen reduction reaction (ORR) are also included in this chapter. The high cost and poor durability of the commercial Pt/C catalyst in ORR restrict the wide application of PEMFCs and ZABs. Hence, the primary target of the present study is to develop strategies and synthesis protocols to realize the full potential of the electrode materials for ORR in PEMFCs and ZABs in a cost-effective manner. To achieve this, in one case, the Co-based ZIF

was found to be acting as a non-precious 'self-sacrificial' template for deriving Cobalt-embedded highly porous carbon, while MWCNT was found to largely impart high electrical conductivity and corrosion resistance to the catalyst system. The electrocatalyst is found to consistently perform in par with that of the standard Pt/C electrocatalyst when implemented in both the ZAB and anion exchange membrane fuel cell (AEMFC) systems and the results are summarized in Chapter 2. As the next advancement, the micro/mesoporous nitrogen and sulphur dual doped crumbled graphene possessing a high surface area and accessible active sites could be prepared from a single precursor, PEDOT, through high-temperature annealing under an inert atmosphere. The results of this development are summarized in Chapter 3. Chapter 4 deals with the development of Fe- and S-doped graphene, which displays exceptionally high ORR activity in both acidic and basic environments. The material derived from PEDOT after its controlled pyrolysis under an inert atmosphere possesses a scrolled graphene structure with C-S and Fe-S active sites. The catalyst prepared by pyrolyzing at 900

°C displays ORR activity with substantially reduced overpotential under acidic and basic electrolyte conditions. Chapter 5 illustrates how a noble metal-free ORR electrocatalyst containing both nitrogen and sulphur on carbon sheets which are spatially separated by the CNT network could be successfully synthesized, which is found to be working exceptionally well both under acidic and basic pH conditions. This has been achieved by controlled pyrolysis of a combination of *in-situ* grown PEDOT with CNT and melamine, which leads to the formation of the carbon sheets bearing the Fe-N and Fe-S active sites all the while acquiring desirable spatial distribution facilitated by the CNT network. Lastly, the thesis concluded with this chapter, which includes the discussion of future scope, prospects, and importance of the works detailed in this thesis in the development of the PEMFCs and ZAB systems.

The major accomplishments of the thesis work are summarized below:

6.1. Single Cell Fabrication of CNT Strung ZIF-derived Electrocatalyst as a Cathode Material in Alkaline Fuel Cell and Metal-air Battery

In any electrochemical system involving gaseous reactants like fuel cell and metal-air battery systems, the active catalytic site must have simultaneous and liberal access to the three-phase interface, *i.e.*, gas, electron-conducting medium, and proton-conducting medium. Therefore, an ideal electrode configuration should concurrently balance the transport process of all these three phases effectively. Thus, it is very likely that the key requisites of a fuel cell electrocatalyst are high porosity, surface area, high conductivity, strong ORR activity and good electrochemical stability. In this direction, a cobalt based ZIF stringed CNT is used to derive a nanostructured, non-precious catalyst which is observed to effectively catalyze ORR showing remarkably on par performance with that of the commercial 40% Pt/C catalyst when employed in both AEMFC and primary ZAB systems.

The work showcases the following unique features:

- The as-synthesized electrocatalyst is found to possess at least 16 times higher electron conductivity compared to that of plain ZIF derived carbon (without CNT).
- In the half cell study, CoNC-900 is found to display an ORR activity with a half-wave potential ($E_{1/2}$) difference of just 30 mV and a much smaller Tafel slope compared to that of the standard Pt/C catalyst. The slight negative shift of only 6 mV at the end of the accelerated durability test (ADT) reveals the superior support stability of CNT, over that of the Vulcan carbon support in Pt/C.

- Maximum power densities of 296 mW cm^{-2} and 60 mW cm^{-2} in the single-cells of ZAB and AEMFC, respectively, establish the practical proficiency of the systems as the cathode electrocatalyst for real-world energy applications.
- The stand out performance of CoNC-900 could be observed to be a beneficial effect of its high surface area, which is expected to assist facile mass diffusion and ready access to the active sites. It could also be a contributing effect of the presence of CNT in the backbone, which is known to be a better electron conductor and corrosion resistor than the Vulcan$^{®}$ XC-72 carbon support used in the commercial Pt/C.

6.2. Nitrogen and Sulphur co-doped Crumbled Graphene for the Oxygen Reduction Reaction with Improved Activity and Stability in Acidic Medium

Non-precious dioxygen reduction electrocatalysts have attracted significant attention currently for the development of stable, cost-effective PEMFCs. In line with this requirement, a Pt-free oxygen reduction electrocatalyst based on nitrogen and sulphur co-doped crumbled graphene with trace amounts of iron could be developed. The co-doped crumbled graphene structure was obtained by simple oxidative polymerization of ethylenedioxythiophene in aqueous solution followed by an annealing process under an inert atmosphere.

The work showcases the following unique features:

- The study deals with a strategy wherein micro/mesoporous nitrogen and sulphur dual doped crumbled graphene possessing a high surface area and accessible active sites could be prepared from a single precursor, PEDOT, through high-temperature annealing under an inert atmosphere. PEDOT annealed at 1000°C (PF-1000) displays a surface area of 800 m^2 g^{-1}, which is higher compared to that of the PEDOT annealed at 900 and 800°C.
- XPS analysis reveals the presence of three different types of active reaction centers, *viz.* graphitic nitrogen coordination, sulphur–carbon interaction, and Fe–Nx. Both PF-900 and PF-1000 show similar onset and half-wave potentials in 0.5 M H$_2$SO$_4$, and the overpotential with respect to 40 wt% Pt/C is only 0.1 V.
- Only 27 mV reduction in the half-wave potential is observed for PF-1000, compared to 80 mV shift in the case of Pt/C, after 5000 ADT cycles. This validates the better electrochemical stability possessed by PF-1000.
- A single-cell analysis using PF-1000 as the cathode catalyst provides a well-defined voltage-current polarization plot with a maximum power density of 193 mW cm^{-2} without applying any backpressure. Thus, the intrinsic activity as measured through the half-cell

measurements of PF-1000, could be fairly well translated in terms of a single cell performance under realistic cell testing conditions.

6.3. Graphene with Fe and S Coordinated Active Centers: An Active Competitor for the Fe−N−C Active Center for ORR

This work discusses the development of an ORR electrocatalyst comprised of S-doped graphene enriched with the Fe-S_x coordinated sites, which displays exceptionally high activity in both acidic and basic environments. The material is derived from the conducting polymer polyethylenedioxythiophene after its controlled pyrolysis under an inert atmosphere, which leads to the formation of scrolled graphene structures with the Fe-S_x active sites. The residual iron chloride retained by the polymer matrix, which was employed as the oxidizing agent for the polymerization reaction, plays a critical role in generating the potential ORR active sites based on the Fe-S_x coordination in the system.

This work showcases the following unique features:

- The Pt-free catalyst enriched with the Fe- and S-doped graphene coordinated sites (P12-900) prepared *via* annealing of PEDOT acts as a potential oxygen reduction electrocatalyst, which could perform equally well under acidic and basic electrolyte conditions.

- The Fe-S_x coordination sites originated by the intervention of the residual iron chloride retained by the polymer matrix, which was employed as the oxidizing agent for the polymerization reaction, plays a critical role in achieving the unique activity characteristics of the system.

- In the basic medium, P12-900 displays an ORR activity, which is similar to that of the performance of 40 wt. % Pt/C, whereas, under acidic conditions, the inhouse system displays only 80 mV overpotential in the onset potential compared to the Pt counterpart.

- The chapter also includes data on the realistic system-level validations of the catalyst considering its ORR activity under acidic (single-cell demonstration of PEMFC) and basic (single-cell evaluation of Zn-air battery system) conditions. Both the systems performed fairly well, justifying the intrinsic activity characteristics of the system evaluated under the acidic and basic electrolyte conditions through single electrode studies.

6.4. FeN$_x$/FeS$_x$-Anchored Carbon Sheet-Carbon Nanotube Composite Electrocatalyst for Oxygen Reduction

In this work, the development of an ORR electrocatalyst comprised of co-existing FeN$_x$/FeS$_x$ active site bearing carbon sheets which are spatially separated by a network of carbon nanotubes (CNTs) for facilitating ORR both under acidic and basic pH conditions is reported. The material is derived from the *in-situ* grown conducting polymer polyethylenedioxythiophene (PEDOT) in the presence of CNT and melamine upon controlled pyrolysis under an inert atmosphere, which facilitates the formation of this electrocatalyst having the desirable characteristics of spatial separation of the active site-bearing carbon sheets with the help of the CNT network. The residual iron chloride retained by the polymer matrix, which was employed as the oxidizing agent for the polymerization reaction, plays a critical role in generating the potential ORR active sites based on the Fe-N$_x$ and Fe-S$_x$ coordination in the system.

The salient features of the work are listed below:

- The Pt-free catalyst with the coexisting Fe-N$_x$/Fe-S$_x$ active sites anchored on spatially separated carbon sheets with the help of the CNT network as the spacer (PMCNT-900), shows good ORR performance both in acidic and basic pH conditions. This strategy of controlling both the nature of the active sites and architectural features appears to be an important step towards realizing a catalyst which can facilitate ORR irrespective of the pH of the medium.

- In the basic medium, PMCNT-900 displays an ORR activity which is better than that of the performance of 40 wt. % Pt/C, whereas, under acidic condition, the catalyst displays a performance with only 60 mV overpotential in the onset potential compared to the Pt counterpart. The catalyst is found to be facilitating ORR through the preferred 4-electron reduction pathway in both the pH conditions and the structural integrity under these two extreme pH conditions is also commendable.

- The work also includes data on the realistic system-level validations of the catalyst considering its ORR activity under acidic (single-cell demonstration of PEMFC) and basic (single-cell evaluation of AEMFC) conditions. Both the systems performed fairly well, justifying the intrinsic activity characteristics of the system evaluated under the acidic and basic electrolyte conditions through single electrode studies.

- Considering the appealing performance towards ORR in acidic and basic pH conditions under single electrode studies and the justifiable performance under the system level validation in a single-cell mode of PEMFC and AEMFC, the present system will be

interesting to those who are deeply involved in the fuel cell catalyst development. Considering the scarcity of such systems which can display pH-independent ORR activity in the electrochemistry literature, the present finding will have a wide-spread impact in the fuel cell and related fields.

6.5 Future Scope and Prospects

The ideas and strategies demonstrated in this dissertation are focused on developing ORR active electrocatalysts for PEMFC and metal air battery fields. The performance of any electrochemical system largely depends on the exposure and number of the active centres present in the electrocatalysts. In this direction, various strategies related to creation of non-noble metal based active sites and morphological fine tuning of the electrocatalyst to tackle the existing issues related to mass transfer and active site utilization were adopted. In general, the works illustrated in this thesis give strong evidence on how well the coordinated heteroatom (nitrogen/sulphur) in graphitic carbon with transition metal and strategically designed morphological features can favourably tune the efficiency of the catalysts for the practical applications in PEMFCs and metal-air batteries. Hence, the same strategies can be adopted in developing suitable electrocatalysts for addressing many other challenging issues associated with the systems for energy generation and conversion. These include various types of batteries, fuel cells and supercapacitors. Further, even though reasonably good performance could be obtained in the case of PEMFCs with the catalysts developed during this study, the system level performance can be further improved by developing catalyst specific electrode fabrication processes rather than following the conventional methodologies. The issues related to effective building of the active "triple phase boundary", reduction of the charge transfer resistance etc. need to be considered based on the nature and morphology of the new catalysts designed and appropriate electrode fabrication protocols should be developed to address such issues. Hence, the works summarized in this thesis open up great opportunities for further exploration both in the material and system level to make further advancements in developing cost effective and high performing energy generation and conversion systems.

List of Publications

Journal Articles

1. **Siddheshwar N. Bhange**, Roby Soni, Gourav Singla, T. G. Ajithkumar, and Sreekumar Kurungot, FeNx/FeSx-Anchored Carbon Sheet–Carbon Nanotube Composite Electrocatalysts for Oxygen Reduction, *ACS Appl. Nano mater.* **2020**, 3, 3, 2234-2245.

2. Sachin Kumar, **Siddheshwar N. Bhange**, Roby Soni, and Sreekumar Kurungot, WO_3 Nanorods Bearing Interconnected Pt Nanoparticle Units as an Activity Modulated and Corrosion Resistant Carbon-free System for PEMFCs, *ACS appl. Energy Mater*. **2020**, 3, 2, 1908-1921.

3. Pranav K Gangadharan, **Siddheshwar N. Bhange**, Nasrin Kabeer, Rajith Illathvalappil, and Sreekumar Kurungot, $NiCo_2O_4$ nanoarray on CNT sponge: a bifunctional oxygen electrode material for rechargeable Zn–air batteries, *Nanoscale Advances*, **2019**, 1, 3243-3251.

4. Roby Soni, **Siddheshwar N. Bhange**,* and Sreekumar Kurungot, A 3-D nanoribbon-like Pt-free oxygen reduction reaction electrocatalyst derived from waste leather for anion exchange membrane fuel cells and zinc-air batteries, *Nanoscale*, **2019**, 11, 7893-7902.

5. Roby Soni, **Siddheshwar N. Bhange**,* E. Athira, Rashmi Chetry, and Sreekumar Kurungot, Synthesis of Ultrathin PEDOT on Carbon Nanotubes and Shear Thinning Xanthan Gum-H2SO4 Gel Electrolyte for Supercapacitors, *ChemElectroChem* **2019**,6, 1861–1869.

6. Himadri Sekhar Sasmal, Harshitha Barike Aiyappa, **Siddheshwar N. Bhange**, Suvendu Karak, Arjun Halder, Sreekumar Kurungot, and Rahul Banerjee, Superprotonic Conductivity in Flexible Porous Covalent Organic Framework Membranes, *Angewandte Chemie,* **2018**, 57, 10894-10898.

7. **Siddheshwar N. Bhange**, SM Unni, and S Kurungot, Graphene with Fe and S Coordinated Active Centers: An Active Competitor for the Fe–N–C Active Center for Oxygen Reduction Reaction in Acidic and Basic pH Conditions, *ACS Applied Energy Materials,* **2018**, 1, 368-376.

*** Equal contribution**

8. Santosh K Singh, Varchaswal Kashyap, Narugopal Manna, **Siddheshwar N. Bhange**, Roby Soni, Rabah Boukherroub, Sabine Szunerits, Sreekumar Kurungot, Efficient and Durable Oxygen Reduction Electrocatalyst Based on CoMn Alloy Oxide Nanoparticles Supported Over N-doped Porous Graphene, *ACS Catalysis*, **2017**, 7, 6700-6710.

9. R. Illathvalappil, VM Dhavale, **Siddheshwar N. Bhange**, and S Kurungot, Nitrogen-doped graphene anchored with mixed growth patterns of CuPt alloy nanoparticles as a highly efficient and durable electrocatalyst for the oxygen reduction reaction in an alkaline medium, *Nanoscale*, **2017**, 9, 9009-9017.

10. BJ Waghmode, **Siddheshwar N. Bhange**, SM Unni, KR Patil, DD Malkhede, In situ grown nickel nanoparticles in a calixarene nanoreactor on a graphene–MoS_2 support for efficient water electrolysis, *Sustainable Energy & Fuels*, **2017**, 1, 1329-1338.

11. HB Aiyappa, **Siddheshwar N. Bhange**,* VP Sivasankaran, S Kurungot, Single-cell fabrication towards realistic evaluation of CNT strung ZIF-derived electrocatalyst as cathode material in alkaline fuel cell and metal-air battery, *ChemElectroChem*, 2017, 4, 2928–2933.

12. Sreekuttan M. Unni, Leena K. George, **Siddheshwar N. Bhange**, Nandini Devi, Kurungot Sreekumar, Valorization of Coffee Bean Waste: Coffee Bean Waste Derived Multifunctional Catalyst for Photocatalytic Hydrogen Production and Electrocatalytic Oxygen Reduction Reactions, *RSC Advances*, **2016**, 82103-82111.

13. **Siddheshwar N. Bhange**, Sreekuttan M. Unni, and Sreekumar Kurungot, Nitrogen and Sulphur Co-doped Crumbled Graphene for Oxygen Reduction Reaction with Improved Activity and Stability in Acidic Medium, *J. Mater. Chem. A*, **2016**, 4, 6014-6020.

14. T. Palaniselvam, V. Kashyap, **Siddheshwar N. Bhange** J. B. Baek, and S. Kurungot, Nanoporous graphene enriched with Fe/Co-N active sites as a promising oxygen reduction electrocatalyst for anion exchange membrane fuel cells, , *Adv. Funct. Mater.* **2016**, 26, 2150–2162.

15. Sreekuttan M. Unni, Rajith Illathvalappil, **Siddheshwar N. Bhange**, Hasana Puthenpediakkal, and Sreekumar Kurungot, Carbon Nanohorn-Derived Graphene Nanotubes as a Platinum-Free Fuel Cell Cathode, *ACS Appl. Mater. Interfaces*, **2015**, 7, 43, 24256-24264.

16. Sreekuttan M. Unni, **Siddheshwar N. Bhange**, Rajith Illathvalappil, Nisha Mutneja, Kasinath R. Patil, and Sreekumar Kurungot, Nitrogen-induced surface area and conductivity modulation of carbon nanohorns and its function as an efficient metal-free oxygen reduction electrocatalysts for anion-exchange membrane fuel cells, *Small,* **2015**, 11, 352-360.

17. Bihag Anothumakkool, Roby Soni, **Siddheshwar N. Bhange** and Sreekumar Kurungot, Novel scalable synthesis of highly conducting and robust PEDOT paper for a high performance flexible solid supercapacitor, *Energy Environ. Sci.*, **2015**, 8, 1339-1347.

18. Sreekuttan M. Unni, Sarath Ramadas, Rajith Illathvalappil, **Siddheswar N. Bhange** and Sreekumar Kurungot, Surface Modified Single Wall Carbon Nanohorn as an Efficient Electrocatalyst for Platinum-Free Fuel Cell Cathode, *J. Mater. Chem. A*, **2015**, 3, 4361-4367.

19. Sreekuttan M. Unni, Rajith Illathvalapil, Pranav K. Gangadharan, **Siddheswar N. Bhange,** and Sreekumar Kurungot, Layer-separated distribution of nitrogen-doped graphene by wrapping on carbon nitride tetrapods for enhanced oxygen reduction reaction in acid medium, *Chem. Commun.,* **2014**, 50, 13769-13772.

20. Chamundi P Jijil, **Siddheshwar N. Bhange**, Sreekumar Kurungot, and R. Nandini Devi, Effect of B Site Coordination Environment in the ORR Activity in Disordered Brownmillerites $Ba_2In_{2-x}Ce_xO_{5+\delta}$, *ACS Appl. Mater. Interfaces*, **2015**, 7, 3041-3049.

21. Bihag Anothumakkool, Arun Torris A. T, **Siddheshwar N. Bhange**, Manohar V. Badiger, and Sreekumar Kurungot, Electrodeposited Polyethylenedioxythiophene with Infiltrated Gel Electrolyte Interface: A Close Contest of an All-Solid-State Supercapacitor with its Liquid-State Counterpart. *Nanoscale*, **2014**, 6, 5944-5952.

22. Bihag Anothumakkool, Onkar Game, **Siddheshwar N. Bhange**, Tanya Kumari, Satishchandra Ogale, and Sreekumar Kurungot, Enhanced Catalytic Activity of Polyethylenedioxythiophene towards Tri-iodide Reduction in DSSC via 1-Dimensional Alignment Using Hollow Carbon Nanofiber, *Nanoscale*, **2014**, 6, 10332-10339.

23. Bihag Anothumakkool, Arun Torris A. T., **Siddheshwar N. Bhange**, Sreekuttan M. Unni, Manohar V. Badiger, and Sreekumar Kurungot, Design of a High Performance Thin All-Solid-State Supercapacitor Mimicking the Active Interface of Its Liquid-State Counterpart, *ACS Appl. Mater. Interfaces*, **2013**, 5, 13397−13404.

24. Sreekuttan M. Unni, **Siddheshwar N. Bhange**, Bihag Anothumakkool, and Sreekumar Kurungot, Redox-Mediated Synthesis of Functionalised Graphene: A Strategy towards 2D Multifunctional Electrocatalysts for Energy Conversion Applications, *Chempluschem*, **2013**, 78, 1296-1303.

25. Bihag Anothumakkool, Ishita Agrawal, **Siddheshwar N. Bhange**, Roby Soni, Onkar Game, Satishchandra Ogale, and Sreekumar Kurungot, Pt- and TCO-free flexible cathode for DSSC from highly conducting and flexible PEDOT paper prepared via in-situ interfacial polymerization, *ACS Appl. Mater. Interfaces,* **2016,** *8*, 553–562.

26. B. Anothumukkool, **Siddheshwar N. Bhange**, S. M. Unni and S. Kurungot, 1-Dimensionally aligned porous polyethylenedioxythiophene using carbon nanofiber as an efficient charge storage material, *RSC Adv.*, **2013**, 3, 11877-11887.

27. Liuqing Pang, **Siddheshwar N. Bhange**, Alexandre Barras, Ahmed Addad, Pascal Roussel, Mohammed Amin, Sreekumar Kurungot, Sabine Szunerits, Rabah Boukherroub, The ultimate limit of Pt electrocatalytic activity in PtRu/nitrogen and sulphur co-doped crumbled graphene in acid and alkaline media, **(Communicated).**

28. Gourav Singla, **Siddheshwar N. Bhange**,* Kurungot, Sreekumar, Facile Synthesis of CNT Interconnected PVP-ZIF-8 Derived Hierarchical Porous Zn/N Co-doped Carbon Frameworks for Oxygen Reduction, **(Communicated).**

Patent

1. A process for the preparation of PBI based membrane electrode assembly (MEA) with improved fuel cell performance and stability, S Kurungot, R Illathvalappil, **Siddheshwar N Bhange**, SM Unni, *US Patent*, 10,361,446.

Erratum